DFIG-BASED SPLIT-SHAFT WIND ENERGY CONVERSION SYSTEMS

by

Rasoul Akbari

A Dissertation

Submitted to the Faculty of Purdue University

In Partial Fulfillment of the Requirements for the degree of

Doctor of Philosophy

Department of Electrical and Computer Engineering

Indianapolis, Indiana

August 2022

THE PURDUE UNIVERSITY GRADUATE SCHOOL
STATEMENT OF COMMITTEE APPROVAL

Dr. Afshin Izadian, Co-Chair

Department of Engineering Technology

Dr. Euzeli Dos Santos, Co-Chair

Department of Electrical and Computer Engineering

Dr. Robert S. Weissbach

Department of Engineering Technology

Dr. Brian King

Department of Electrical and Computer Engineering

Approved by:

Dr. Brian King

To my parents, whose dedication and endless support motivated me throughout my education

ACKNOWLEDGMENTS

I owe my gratitude to my supervisor, Dr. Afshin Izadian, for all the support and encouragement he devoted to me from the first day of my Ph.D. His valuable advice directed me to complete productive research. I thank Dr. Robert Weissbach for his support and collaboration with this research. I want to thank my committee Co-chair, Dr. Euzeli Dos Santos, for helpful comments and suggestions to enhance the quality of my research. I also want to thank Dr. Brian King, my committee member.

I am thankful to the Department of Engineering and Technology, the Department of Electrical and Computer Engineering, and the office of the Dean for funding my Ph.D. and research. Finally, I am grateful to the Department of Electrical and Computer Engineering administrative staff at IUPUI, especially Ms. Sherrie Tucker, who kindly helped me on many occasions.

TABLE OF CONTENTS

LIST OF TABLES

LIST OF FIGURES

LIST OF SYMBOLS

Greek symbols:

β	Pitch angle
β_f	Bulk modulus of the fluid
η_{tm}	Torque efficiency of the hydraulic motor
η_{vm}	Volumetric efficiency of the hydraulic motor
η_{tp}	Torque efficiency of the hydraulic pump
η_{vp}	Volumetric efficiency of the hydraulic pump
η_v	Volumetric efficiency of the hydraulic drivetrain
λ_o	Optimal tip speed ratio
λ	Tip speed ratio
μ	Dynamic viscosity of the fluid
ρ_{air}	Air density
$\tau_{\mathrm{e}}, \tau_r$	Electrical and wind turbine torques
τ_{hp}	Torque of hydraulic pump
τ_{bp}, τ_{bm}	Breakaway torque of hydraulic pump and motor
τ_f	Time constant of the low-pass filter
ω_p, ω_m	Pump and motor angular speeds
ω_{max}	Maximum speed of the DFIG
ω_{min}	Minimum speed of the DFIG
ω_s	Synchronous angular velocity of the DFIG

Latin symbols:

C_p	Power capacity of the wind turbine
C_{max}	Maximum power capacity of the wind turbine
C_{fp}, C_{fm}	Coulomb friction coefficient of the hydraulic pump and motor
C_{sp}, C_{sm}	Slippage coefficient of the hydraulic pump and motor
C_{vp}, C_{vm}	Viscous drag coefficient of the hydraulic pump and motor
D_p, D_m	Hydraulic pump and motor displacements
D_{po}	Optimal pump displacement

E	Energy capacity of the energy storage system
E_{max}	Maximum energy of the energy storage system
E_{min}	Minimum energy of the energy storage system
H_t	Inertia constant of the generator and hydraulic motor combined
I_{m0}	Magnetizing current of the DFIG
I_{qr}	Quadrature component of rotor current
J_r	Wind rotor-hydraulic pump inertia
J_m	Generator-hydraulic motor inertia
J_v	Virtual inertia
L_s, L_m	Stator and magnetizing inductance
P_f	Pressure of the pipeline
p	Pole number of the DFIG
P_a	Aerodynamic power of the wind turbine
P_{reg}	Regulated output power injected into the grid
P_{hm}	Mechanical power of the hydraulic motor
P_{hp}	Mechanical power of the hydraulic pump
P_s, P_r	Stator and rotor powers of the DFIG
P_{e}	Electrical power of the DFIG
P_{loss-m}	Torque Loss of the hydraulic motor
Q_p, Q_m	The flow of hydraulic pump and motor
R	The radius of the rotor of the wind turbine
s_{max}	Maximum slip of the DFIG
s_{min}	Minimum slip of the DFIG
s	Laplace variable
V_f	The volume of the fluid
v_w	Wind velocity

ABBREVIATIONS

BESS	Battery Energy Storage System
CF	Capacity Factor
DFIG	Doubly-Fed Induction Generator
ESS	Energy Storage System
FESS	Flywheel Energy Storage System
GSC	Grid-Side Converter
HESS	Hybrid Energy Storage System
HTS	Hydraulic Transmission System
LCOE	Levelized Cost of Energy
LVRT	Low Voltage Ride Through
MPPT	Maximum Power Point Tracking
OMDC	Optimal Motor Displacement Control
OTC	Optimal Torque Control
OPDC	Optimal Pump Displacement Control
RSC	Rotor-Side Converter
RSM	Response Surface Method
SCESS	Super-capacitor Energy Storage System
SoC	State of Charge
SMES	Superconducting Magnetic Energy Storage
SS-WECS	Split-Shaft Wind Energy Conversion System
TSR	Tip Speed Ratio
VDM	Variable-Displacement Motor
VDP	Variable-Displacement Pump

ABSTRACT

In this research, a Split-Shaft Wind Energy Conversion System (SS-WECS) is investigated to improve the performance and cost of the system and reduce the wind power uncertainty influences on the power grid. This system utilizes a lightweight Hydraulic Transmission System (HTS) instead of the traditional gearbox and uses a Doubly-Fed Induction Generator (DFIG) instead of a synchronous generator. This type of wind turbine provides several benefits, including decoupling the shaft speed controls at the turbine and the generator. Hence, maintaining the generator's frequency and seeking maximum power point can be accomplished independently. The frequency control relies on the mechanical torque adjustment on the hydraulic motor that is coupled with the generator. This research provides modeling of an SS-WECS to show its dependence on mechanical torque and a control technique to realize the mechanical torque adjustments utilizing a Doubly-Fed Induction Generator (DFIG). To this end, a vector control technique is employed, and the generator electrical torque is controlled to adjust the frequency while the wind turbine dynamics influence the system operation. The results demonstrate that the generator's frequency is maintained under any wind speed experienced at the turbine.

Next, to reduce the size of power converters required for controlling DFIG, this research introduces a control technique that allows achieving MPPT in a narrow window of generator speed in an SS-WECS. Consequently, the size of the power converters is reduced significantly. The proposed configuration is investigated by analytical calculations and simulations to demonstrate the reduced size of the converter and dynamic performance of the power generation. Furthermore, a new configuration is proposed to eliminate the Grid-Side Converter (GSC). This configuration employs only a reduced-size Rotor-Side Converter (RSC) in tandem with a supercapacitor. This is accomplished by employing the hydraulic transmission system (HTS) as a continuously variable and shaft decoupling transmission unit. In this configuration, the speed of the DFIG is controlled by the RSC to regulate the supercapacitor voltage without GSC. The proposed system is investigated and simulated in MATLAB Simulink at various wind speeds to validate the results.

Next, to reduce the wind power uncertainty, this research introduces an SS-WECS where

the system's inertia is adjusted to store the energy. Accordingly, a flywheel is mechanically coupled with the rotor of the DFIG. Employing the HTS in such a configuration allows the turbine controller to track the point of maximum power (MPPT) while the generator controller can adjust the generator speed. As a result, the flywheel, which is directly connected to the shaft of the generator, can be charged and discharged by controlling the generator speed. In this process, the flywheel energy can be used to modify the electric power generation of the generator on-demand. This improves the quality of injected power to the grid. Furthermore, the structure of the flywheel energy storage is simplified by removing its dedicated motor/generator and the power electronics driver. Two separate supervisory controllers are developed using fuzzy logic regulators to generate a real-time output power reference. Furthermore, small-signal models are developed to analyze and improve the MPPT controller. Extensive simulation results demonstrate the feasibility of such a system and its improved quality of power generation.

Next, an integrated Hybrid Energy Storage System (HESS) is developed to support the new DFIG excitation system in the SS-WECS. The goal is to improve the power quality while significantly reducing the generator excitation power rating and component counts. Therefore, the rotor excitation circuit is modified to add the storage to its DC link directly. In this configuration, the output power fluctuation is attenuated solely by utilizing the RSC, making it self-sufficient from the grid connection. The storage characteristics are identified based on several system design parameters, including the system inertia, inverter capacity, and energy storage capacity. The obtained power generation characteristics suggest an energy storage system as a mix of fast-acting types and a high energy capacity with moderate acting time. Then, a feedback controller is designed to maintain the charge in the storage within the required limits. Additionally, an adaptive model-predictive controller is developed to reduce power generation fluctuations. The proposed system is investigated and simulated in MATLAB Simulink at various wind speeds to validate the results and demonstrate the system's dynamic performance. It is shown that the system's inertia is critical to damping the high-frequency oscillations of the wind power fluctuations. Then, an optimization approach using the Response Surface Method (RSM) is conducted to minimize the annualized cost of the Hybrid Energy Storage System (HESS); consisting of a flywheel, supercapaci-

tor, and battery. The goal is to smooth out the output power fluctuations by the optimal size of the HESS. Thus, a 1.5 MW hydraulic wind turbine is simulated, and the HESS is configured and optimized. The direct connection of the flywheel allows reaching a suitable level of smoothness at a reasonable cost. The proposed configuration is compared with the conventional storage, and the results demonstrate that the proposed integrated HESS can decrease the annualized storage cost by 71 %.

Finally, this research investigates the effects of the reduced-size RSC on the Low Voltage Ride Through (LVRT) capabilities required from all wind turbines. One of the significant achievements of an SS-WECS is the reduced size excitation circuit. The grid side converter is eliminated, and the size of the rotor side converter (RSC) can be safely reduced to a fraction of a full-size excitation. Therefore, this low-power-rated converter operates at low voltage and handles the regular operation well. However, the fault conditions may expose conditions on the converter and push it to its limits. Therefore, four different protection circuits are employed, and their effects are investigated and compared to evaluate their performance. These four protection circuits include the active crowbar, active crowbar along a resistor-inductor circuit (C-RL), series dynamic resistor (SDR), and new-bridge fault current limiter (NBFCL). The wind turbine controllers are also adapted to reduce the impact of the fault on the power electronic converters. One of the effective methods is to store the excess energy in the generator's rotor. Finally, the proposed LVRT strategies are simulated in MATLAB Simulink to validate the results and demonstrate their effectiveness and functionality.

1. INTRODUCTION

With the depletion of conventional energy sources such as coal, oil, and gas in the future, the need for reliable, cheap energy sources seems necessary [1], [2]. To have sustainable energy sources, renewable energy such as wind energy can be a proper alternative due to its geographically wide distribution, abundance, and pollution-free nature [3], [4]. However, due to its intermittent nature, deep penetration of wind energy can impose serious challenges such as instability, voltage fluctuation, and power fluctuation in the power grid [3]–[7]. To make wind energy more reliable and limit the impact of its intermittent nature, employing decentralized energy storage in power grids can be effective [8]–[10]. Stand-alone energy storage could be an alternative. However, this needs their extra supporting hardware like inverter, transformer, etc. Energy Storage Systems (ESS) integrated with a power generation unit without additional supporting hardware can meet the demand at a lower cost.

Meanwhile, the cost of wind energy production is relatively high, especially for offshore wind turbines, due to their expensive structure [5], [11]. Therefore, to have more cost-effective and reliable Wind Energy Conversion Systems (WECS), the conventional gearbox drivetrain can be replaced with a split-shaft drivetrain such as a hydraulic transmission system (HTS) [12]. However, the Synchronous Generator (SG) employed with these SS-WECSs is not an appropriate option for such an uncontrollable intermittent resource. Therefore, this research proposes and investigates a new configuration with SS-WECS and a DFIG to decrease the size and number of required components for energy storage by integrating them into the WECS. In addition, the size and number of converters of the DFIG are reduced to have cheaper and more flexible generators than SGs that are also reliable in the case of faults.

1.1 Reduction of the Power Converters' Size and Number

The split-shaft hydraulic technology can be a suitable solution to overcome the challenges of the traditional gearbox-based method of harvesting power from wind turbines. These challenges include high maintenance costs, long downtime in case of gearbox failure, high installation costs, and the need for a strong tower [13]–[17]. For instance, [18] shows that the weight of the nacelle could be decreased by 33-50% simply by relocating the generator

and other subassemblies to the ground level. Then, by using an analytical technique and investigating the natural frequencies of the tower for a 5-MW hydraulic wind powertrain, the weight of the tower itself compared with the conventional wind turbine can be cut to 50%, and the capital cost of the wind energy reduced by 4%. The result of [12] demonstrates the reduction of 35.5% in mass of the nacelle due to employing a hydraulic drivetrain, and an average installed cost saving of 5.36-24.0% can occur for offshore wind. Despite the lower efficiency of HTS, which is about 85-88% [19], [20], the HTS could reduce the overall cost of the system and lower the Levelized Cost of Energy (LCOE) by 3.92-18.8% [12], and improve the Capacity Factor (CF) of the wind turbine [21]. Given a tower structure, the rotor speed of a wind turbine with HTS could be restricted to a higher speed resulting in harvesting about 17% more energy and compensating for its losses [22]. Therefore, employing the HTS can decrease the overall cost and lead to cheaper energy production.

In a split-shaft drivetrain like the HTS, synchronous generators (SGs) have been utilized to convert mechanical energy to electrical energy [23]–[33]. Generally, the governor control is employed to control the input power and balance the power swing equations of the SG. However, in WECSs, the input power is out of control and depends on the wind speed. Therefore, the application of the governor would be quite complex since the controller would need to simultaneously consider feedback from both the input source (the wind) and the output load. To mitigate this problem, two strategies have been applied to maintain the SG at synchronous speed with a small allowed variation and subsequently control the frequency: first, relying on the damping factor of the SG [23]–[26], and second, inserting an energy buffer between the wind turbine and SG [27]–[33]. The former strategies can further reduce the efficiency of the synchronous generator due to the ever-changing nature of wind speed, and the latter necessitates the application of other extra subassemblies. Unlike an SG, in which the mechanical swing is defined by its primary mover power and damping factors, the speed of DFIGs can be controlled actively, and its active and reactive powers can be controlled in a decoupled manner [34]–[36]. Despite the controllability of the DFIG, this generator needs two power converters with a size of about 25-30% of the generator's rated power [37], [38]. Therefore, this challenge should be managed to move toward having economical and reliable energy production.

1.2 Integration of Hybrid Energy Storage System

Two approaches have been taken to overcome challenges about deep penetration of WECSs in the power grid and mitigate the power fluctuation of the WECS [8]: first, utilizing the inherent features of the WECS, including pitch angle control, employing the energy of the inertia of wind turbines, and employing the energy of DC-link capacitor [39]–[45], and second, employing Energy Storage Systems (ESS) [46]–[49]. The former strategies could make the output power smooth to some extent, but they only can attenuate short-term power fluctuation because of their limited energy storage capability. Unlike these intrinsic strategies, the application of EESs could effectively provide more energy and mitigate the power fluctuation for a longer duration.

Various ESS types have been utilized with the power grid, including Conventional storage units are battery Energy Storage System (BESS) [50], Superconducting Magnetic Energy Storage System (SMESS) [50]–[52], Super capacitor Energy Storage System (SCESS) [53], [54], Flywheel Energy Storage System (FESS) [47], Compressed Air Energy Storage System (CAESS) [55], Pumped Hydro Energy Storage System (PHESS) [56], and Thermal Energy Storage System (TESS) [57]. These systems exhibit different characteristics, making them more favorable for various applications. ESSs are characterized by their round trip efficiency, response time, energy and power density, life cycles, self-discharge rate, investment cost, and environmental impacts [58], [59]. For example, FESS and SCESS have high efficiency, low impact on the environment, high specific power, high power density, long life cycle, fast charging and discharging response, and low maintenance cost. However, the primary drawbacks of these ESSs are high investment costs and low energy densities [60], [61]. Furthermore, FESSs have a high self-discharge rate and are not proper for long-term energy storage [61], [62]. On the other hand, BESSs, such as lithium-ion batteries, have a high energy density, fast response, and low investment cost but suffer from limited cycles and lifetime. This could be more problematic in the applications that need frequent charge and discharge by dramatically reducing the lifetime of the BESS.

Hybrid ESSs (HESSs) turn out to be one of the promising solutions to take full advantage of various characteristics of different types of ESSs and improve the performance

of the ESS [63], [64]. For example, by directing the short-term power fluctuations to another form of energy storage such as SCESS [65], [66] or FESS [67], [68], the lifetime of the BESS can be prolonged. These HESSs have the advantage of the high-power density of the SCESS and FESS and the high energy density of the BESS. Different combinations of HESSs such as BESS-SCESS, BESS-SMESS, and BESS-FESS have been utilized in various applications [64]. One of the main applications of HESSs in sustainable power grids with RESs is to smooth power fluctuations and reduce the uncertainties of RESs [69].

To this end, two aspects of HESS should be considered: 1) the power allocation or energy management methods and 2) optimal sizing [70]. The available power allocation can be categorized broadly into two main groups [64]: 1) classical methods such as low-pass filter decomposition [70] and rule-based control [71], and 2) intelligent methods such as fuzzy control [72]–[74], artificial neural network (ANN) [75], model predictive control (MPC) [76], [77], which has demonstrated exemplary performance [78], [79]. Another aspect of the HESS is to determine the appropriate storage capacity. Various methods have been proposed to determine the HESS capacity, such as analytical and statistical methods considering the total cost, reliability, and performance [64].

However, the application of any of these storage units requires employing dedicated power converters and other supporting hardware to functionalize the storage. For example, FESSs are connected either to the point of common coupling (PCC) [46], [47] or to the DC link of the back-to-back converter [48], [49]. The former is mainly employed with a back-to-back power converter; the latter only needs an AC/DC inverter. Furthermore, the FESS requires a dedicated motor-generator to exchange electrical and mechanical power. In all of these methods, an extra power electronic converter and additional motor-generator are necessary to operationalize the storage. Consequently, the cost of power production is increased. Therefore, integration of storage with the power production units with minimal additional hardware can be a cheaper solution to make a reliable power grid.

1.3 Low Voltage Ride Through

DFIG has the disadvantage of high vulnerability to grid disturbances, especially low voltage and short circuit cases [80], [81]. Generally, enhancement approaches to the LVRT capability of DFIG can be divided into three categories: control strategies [82]–[88], reactive power injection devices [89]–[92], and protection circuits [93]–[104]. Control approaches improve the LVRT capability of the DFIG without additional hardware. In [83], the stator current during the fault is fed back as the rotor current reference to suppress the post fault rotor current. In [84], a demagnetizing control method is proposed to control rotor current such that it contains both transient and harmful sequence components. A partially demagnetizing control method is proposed in [85] by controlling the rotor''' flux to track the stator flux with a certain proportion. The virtual resistance control methods and virtual impedance control methods are introduced in [86] and [87] to increase the system damping by adding another feedback loop to the current control loop. In [88], the RSC is controlled to emulate an inductance for suppressing post-fault rotor current. However, these methods can be effective in moderate voltage dips but require high voltage at the RSC to offset the rotor's electromotive force (EMF) voltage in case of severe voltage drops. Also, reactive power injection methods, including dynamic voltage restorer (DVR) [89], [90], superconducting fault current limiters [91], and static synchronous compensator (STATCOM) [92], could be expensive solutions with adding extra components and complexity to the system [105].

On the other hand, many pieces of research have been conducted to analyze the low voltage situations in DFIG that rely on protection circuits, including the crowbar circuit, rotor fault current limiters, and stator fault current limiters. In the simplest form, the crowbar circuit [93] short-circuits the rotor winding of the DFIG to divert the high rotor current from the RSC. However, in this situation, the DFIG turns into an equivalent squirrel-cage induction generator (SCIG) and draws a sizeable magnetizing current during the fault and voltage build-up. In [94], the GSC is controlled to compensate for the consumed reactive power. However, the generator is still absorbing the reactive power. An active crowbar scheme is presented in [95] to prevent losing control of the DFIG during the fault. In [96], [97], new vector control methods are proposed to enhance the crowbar circuit performance

and minimize the length of the crowbar application period.

Additionally, to avoid the disconnection of the RSC during a fault, [98] suggests employing a series dynamic resistor (SDR) along with a crowbar. In [99], the crowbar is replaced by a modified vector control with an R-L circuit connected with the RSC. In addition, some series protection circuits are connected to the stator terminals to limit the fault current. These methods are including series dynamic braking resistor (SDBR) [100], new bridge-type fault current limiter (NBFCL) [101], capacitive bridge type fault current limiter (CBFCL) [102], and inductive–resistive-type solid-state fault current limiter (SSFCL-LR) [103]. In [104], the performance of these series methods was compared, and it was demonstrated that the NBFCL outperformed the others. This research investigates the LVRT capability for a hydraulic DFIG-based WECS. Four strategies based on the active crowbar, crowbar with series resistor-inductor (C-RL), SDR, and NBFCL are adopted for the system, and the results are compared.

2. PROBLEM STATEMENT AND RESEARCH OBJECTIVES

The energy depletion curve shown in Figure 2.1 demonstrates that primary today's resources, including coal, oil, gas, and Uranium, will be depleted in the future [1], [2]. Therefore, replacing such energy resources with clean and renewable energy resources is a genuine concern. Renewable energy such as wind and photovoltaic energies are safe, environmentally clean, and replenishable and can provide the whole energy required worldwide [106], [107]. Consequently, these sources could be appropriate options for the future. However, due to their uncertainty, it might be farfetched to have a power grid entirely supplied from renewable sources such as wind energy. To allow deeper penetration of renewable sources, the energy captured from these sources should be more reliable and economical. Therefore, the uncertainty of these resources should be managed by utilizing a combination of these renewable sources in tandem with ESS. Commonly, extracting power from the areas with more reliable wind speed, such as offshore, is more expensive.

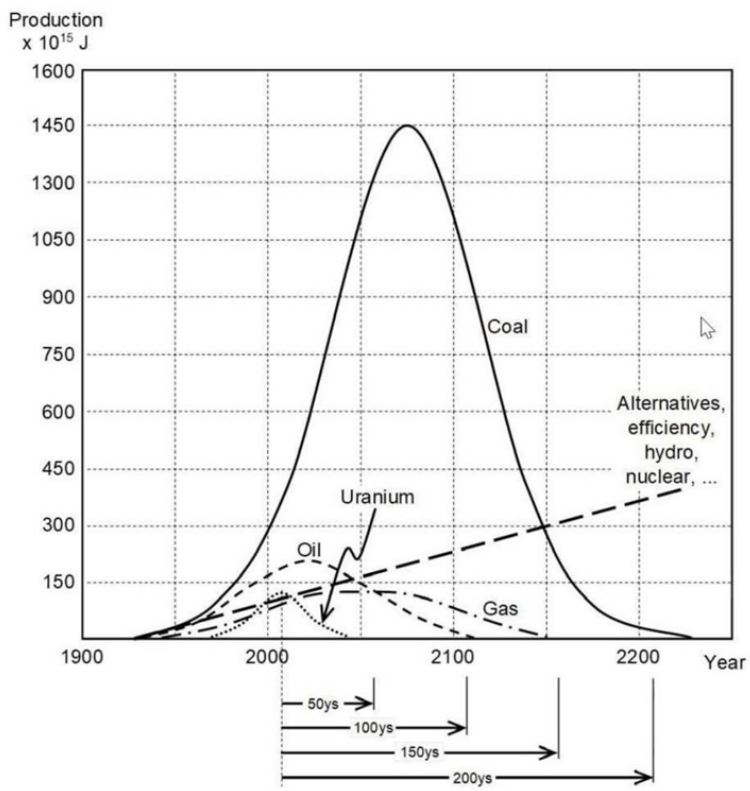

Figure 2.1. Energy depletion Curves

Meanwhile, employing the distributed ESS to the power grid can be costly and make the whole system complex. Therefore, this research suggests utilizing a configuration that allows the integration of energy storage into the system with minimal supporting hardware. This configuration consists of a split-shaft drivetrain, an HTS in this research, and DFIG as a generator that allows flexibility. As mentioned earlier, DFIG needs two power converters with the size of 30% and has a poor performance under low voltage faults. Therefore, to introduce a flexible WECS, this research aims to evaluate the proposed configuration in several aspects, including component sizing of the excitation circuit, integration of storage to improve power quality, and evaluation of such a system under low voltage faults. Therefore, the objectives of this research are as follows:

2.1 Objective 1: Component Sizing of DFIG Excitation Circuit

The split-shaft HTS can improve the performance of the WECS by eliminating the gearbox and relocating most of the sub-assemblies at the ground level. In such a system, the HTS could provide a decoupled transmission system. Many studies have been conducted on different HTSs and use this property to employ a conventional synchronous generator (SG) and eliminate the power converters. However, the SG is hard to control with an uncontrollable intermittent prime mover like a wind turbine. On the other hand, the DFIG is a popular generator in WECSs in which the power electronic interface controls the rotor current at various speeds. In the DFIG, the power electronic converters only process the DFIG rotor power, which offers the advantages of controlling the speed with reduced cost and losses. To take advantage of the hydraulic transmission system (HTS) and the DFIG, a DFIG-based SS-WECS is investigated in this research. However, the size and number of power converters required to control the DFIG are still large compared to the SG, which does not need any power converter. The DFIG needs two power converters with a size of 30%. Therefore, decreasing the size and number of the power converters is an objective of this research. Accordingly, to realize such an objective, several tasks should be accomplished.

2.1.1 Task 1: HTS Model and MPPT Control Strategies

The purpose of an SS-WECS is to separate the speed control of the wind turbine from the speed control of the generator. This can be done in several ways, one of which is an HTS. In an HTS, the wind power captured by the turbine rotor is converted to a high pressurized fluid by a hydraulic pump. Then this power is transferred to the generator through a hydraulic motor at the ground level. In this drivetrain, the high transmission ratio can easily be achieved by changing the displacement ratio of the pump and/or the motor. Therefore, a variable-displacement pump or motor (or both) can achieve the Continuously Variable Transmission (CVT). Various HTSs have been investigated in the literature [108]. Herein, two configurations variable-displacement-pump fixed-displacement motor (VDP) and fixed-displacement-pump variable-displacement motor (VDM) are modeled and controlled. In the HTS, the Maximum Power Point Tracking (MPPT) is achieved by controlling the displacement of the hydraulic machinery. Therefore, the MPPT control strategies employed for the HTS should be elaborated.

2.1.2 Task 2: DFIG Excitation Model

The DFIG is a three-phase wound-rotor induction generator where the stator windings are directly connected to the electrical grid. Its rotor windings are indirectly supplied through a back-to-back converter consisting of the Rotor Side Converter (RSC) and Grid Side Converter (GSC), connected through a DC link. The RSC is responsible for controlling the DFIG, while the GSC regulates the DC-link voltage. Therefore, the DFIG model considering the dynamic of its rotor and stator in dq frame is explained, and the decoupled vector control is elaborated. The main feature of this generator that allows such a size reduction is that the power passing the DFIG rotor is proportional to its slip. By employing this feature, the GSC can be eliminated. In the case of eliminating the GSC, the DFIG excitation circuit is formed by the RSC and a supercapacitor. This excitation circuit will be elaborated to understand the performance of such a system.

2.1.3 Task 3: Controller Design of the DFIG Excitation Circuit

Since, in the HTS, the MPPT is achieved by controlling the displacement of the hydraulic machinery, the speed of the DFIG can be controlled independently. This degree of freedom can be used to reduce the size and number of power converters required for the DFIG.

Design to Reduce the Size of Power Converters

It is proven that the power passing through the DFIG's RSC is proportional to the generator slip [36], [37]. By taking advantage of the decoupling transmission that the HTS can provide, the speed of the DFIG can be limited in a narrow window close to the synchronous speed. Therefore, the power passing through the rotor windings of the DFIG can be limited, and consequently, the size of the power converters can be reduced. Therefore, the proper controller should be designed to achieve this objective.

Controller Design to Reduce the Number of Power Converters

To further improve the system's performance, a new configuration of the DFIG-based WECS can be proposed that is employing only a reduced-size RSC in tandem with a capacitor. The objective of such a configuration is to eliminate the grid side converter (GSC) utilized in conventional DFIG-based WECSs. Employing the HTS as a continuously variable and shaft decoupling transmission unit provides an opportunity to control the power flow through the generator's rotor circuit regardless of the wind turbine's shaft speed. This feature of the HTS can be utilized to control the RSC power and ultimately regulate the capacitor voltage without a need for GSC. In this case, the new controller should be designed to control the capacitor voltage and generator speed by controlling the current of the DFIG rotor.

2.2 Objective 2: Storage Integration with DFIG-Based SS-WECS

Coupling WECS and storage technologies help to have a more sustainable and reliable way of harvesting wind energy. The reason is that wind energy is not always produced when

energy is needed most. For example, peak power usage often occurs during the afternoons and evenings while wind energy is falling. The wind speed can be high at night when the power usage is minimal. Storage helps WECSs contribute to the electricity supply even when the wind is not blowing. It can also help smooth out fluctuations of wind power created by wind speed variations. Storage allows the flexible use of energy at different times and can increase the system efficiency and resilience and improve the power quality. Therefore, in this research, the proposed DFIG-based split shaft WECS is investigated to integrate different energy storage systems with minimal additional hardware. To this end, several tasks should be accomplished.

2.2.1 Task 1: Integration of Mechanical Storage into DFIG-Based SS-WECS

To take advantage of full control over the speed of the generator, flywheel storage is integrated into the WECS and charged and discharged on-demand. A flywheel is a heavy wheel attached to a rotating shaft. Charging and discharging energy can be done by increasing and decreasing the flywheel speed. This energy can be extracted by connecting the wheel to an electrical generator, which uses electromagnetism to slow the wheel down and produce electricity. To this end, the rotating mass of the flywheel can be mechanically coupled with the rotor of the DFIG, and its energy can be controlled by controlling the DFIG. Consequently, the structure of the Flywheel Energy Storage System (FESS) can be simplified, and the supporting power electronics and its dedicated motor-generator can be eliminated.

2.2.2 Task 2: Integration of Hybrid Storage into DFIG-Based SS-WECS

To improve the power quality while significantly reducing the generator excitation power rating and its component counts, the rotor excitation circuit can be modified to include a Hybrid Energy Storage System (HESS) to its DC link and the DFIG rotor directly. The output power fluctuations can be attenuated solely by utilizing the RSC, making it self-sufficient from the grid connection. Three energy storage types seemed suitable for such a system, namely Flywheel Energy Storage System (FESS), Super-capacitor Energy Storage

System (SCESS), and Battery Energy Storage System (BESS). BESS and SCESS can be directly integrated into the DC link of RSC, and FESS can be coupled directly to the shaft of the generator. Characteristics of these storage units needed to be considered. The impact of each type of storage, including FESS, SCESS, and BESS, on the output power fluctuation will be determined.

2.2.3 Task 3: Energy Management of the Storage

Any Energy Storage System (ESS) has a limited capacity to store or deliver energy. Therefore, in order to prevent the saturation of the ESS, the energy level of the storage, the State of Charge (SoC) of the storage, should be managed by a supervisory controller.

Supervisory Controller for Mechanical Storage

In the case of integrating mechanical storage like a flywheel, the supervisory controllers are investigated to determine the output power reference such that it decreases the output power fluctuation and maintains the speed of the generator within a permissible range. Since the speed of the flywheel is an indicator of its SoC, controlling the speed within its limits prevents the saturation of the storage. Therefore, A supervisory controller based on fuzzy logic and a low-pass filter is employed to attenuate the output power fluctuations and keep storage operational.

Supervisory Controller for the HESS

In the case of integrating the HESS, managing the SoC of the hybrid storage will be a complex task. It is necessary to design a supervisory controller that keeps the SoC of all storage within the permissible range. As mentioned earlier, the hybrid storage that is compatible with such a WECS are mechanical like FESS and electrical storage like BESS and SCESS. An SoC feedback controller will be designed to manage the SoC of the electrical storage, and an SoC controller based on a model-based predictive controller (MPC) will be employed to manage the mechanical SoC and smooth out the output power.

2.2.4 Task 4: Optimization of the HESS

Application of the hybrid energy storage can help to take advantage of the characteristics of all storage systems. For instance, BESSs are suitable for applications that need low power storage with high energy capacity. However, FESS and SCESS can provide high power in a short time, but their energy capacities are much smaller than BESS [109], [110]. Therefore, finding the proper combinations of these hybrid storage systems to achieve a cheaper and better performance is necessary.

2.3 Objective 3: Fault Tolerance of DFIG-Based SS-WECS

Due to the direct integration of the DFIG stator to the power grid, large currents are drawn to demagnetize the machine when a short circuit or voltage sag happens at the grid side. These transient demagnetizing currents last for several cycles, and consequently, large voltages are induced in the rotor windings. Consequently, highly induced transient currents are generated in the rotor windings, which flow towards the back-to-back power converters and may cause damage to the DC-link capacitor and RSC [80], [81]. It is worth mentioning that the thermal time constant of the DFIG itself is large enough, and the DFIG can handle the fault transient current. Additionally, this overcurrent can result in an oscillation of generator torque and cause damage to mechanical parts, and in the long run, can deteriorate the wind turbine performance [99], [111], [112]. In the case of reducing the size of the converter or eliminating the GSC, the low voltage ride-through capabilities of DFIGs can be challenging. Different protection circuits are investigated to adapt them for such a system such that the DFIG safely rides through low-voltage situations and meets the current grid code requirements.

Recent grid codes cover many topics such as frequency operating range, power factor regulating, and low voltage ride-through capability that wind turbines must meet when connecting to the power grid [110], [113]–[117]. According to these grid codes [114]–[117], wind turbine generators should stay connected to grids and withstand grid voltage dip to a certain percentage of nominal voltage for a certain time since disconnection might degrade voltage restoration after faults and have severe effects on transient and steady-state stability

of power system operation [118]. This requirement is shown in Figure 2.2 for different countries. For example, in the USA, the power generation unit must withstand the fault with a voltage drop of 15% for 0.625 seconds without tripping off. Furthermore, some transmission system operators expect the power generation unit to inject reactive power into the grid during a fault to improve voltage recovery. The amount of this reactive current is defined based on the voltage dip, as shown in Figure 2.2 [116].

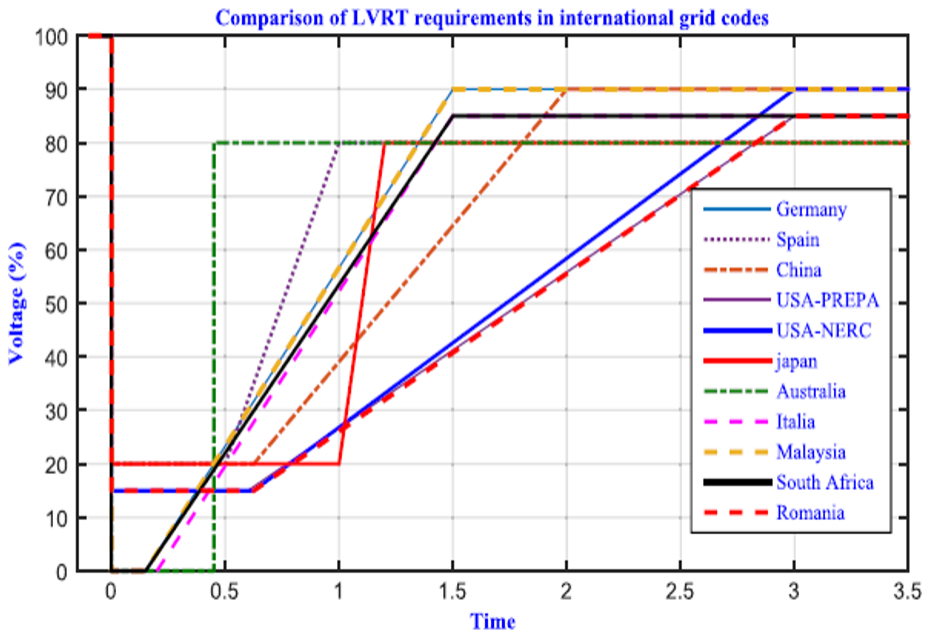

Figure 2.2. LVRT requirement for different countries [114]

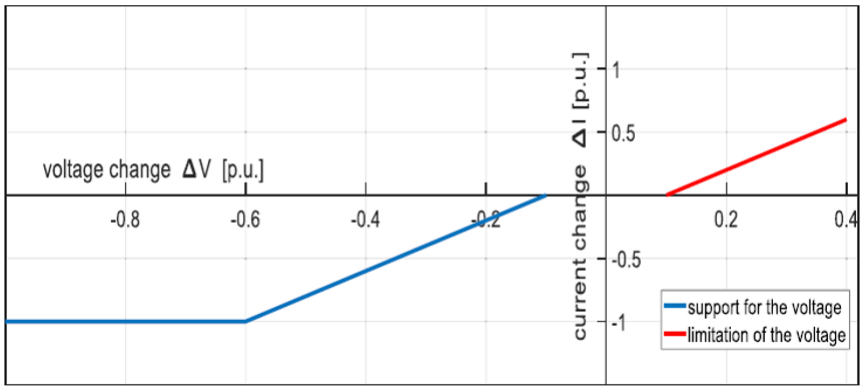

Figure 2.3. Reactive current injection during fault [116]

Under normal conditions, a power system operates under balanced conditions with all equipment carrying normal currents and the bus voltages within the prescribed limits. This condition can be disrupted due to a fault in the system. A fault in a circuit is a failure that interferes with the normal flow of current. A short circuit fault occurs when the system's insulation fails, resulting in a low impedance path either between phases or phase(s) to the ground. This causes excessively high currents to flow in the circuit, requiring the operation of protective equipment to prevent damage to equipment. The short circuit faults can be classified as symmetrical and unsymmetrical faults.

In symmetrical faults, all the phases are short-circuited to each other and often to the earth. Such a fault is balanced in the sense that the system remains symmetrical. It is the most severe type of fault involving the largest current, but it occurs rarely. This type of fault can be of two types: 1) line to line to line to ground (LLLG) or 2) line to line to line (LLL). In WECS, only LLL is typically evaluated since from the grid side, there is no way to pass the zero-sequence current. In this case, the current consists of two components: the positive sequence and the transient natural term. Therefore, the performance of the system should be evaluated under the symmetrical faults.

2.4 Dissertation Outline

Following studies have been conducted to address the tasks listed in previous sections:

- In Chapter 3, the principles of DFIG-based SS-WECS are explained. In this chapter, different configurations of the HTS and their approach to achieving MPPT, the efficiency of the HTS, and the model of the DFIG excitation circuit are explained in detail.

- The scalability and the electrical equivalent circuit of the SS-WECS are elaborated on in Chapter 4 to help understand better the performance of such a system.

- In Chapter 5, the feasibility of DFIG-based SS-WECS and the methodology to design reduced-size power converters are expressed. Then, the proposed configuration is investigated by analytical calculations as well as a simulation at different wind speeds to

demonstrate the reduced size of the converter and dynamic performance of the power generation.

- In Chapter 6, a configuration that allows the integration of flywheel energy storage with SS-WECS is introduced. Then, a control strategy using fuzzy logic regulators is developed to smooth out the output power and prevent the flywheel storage system from saturation.

- In Chapter 7, a configuration of DFIG-based SS-WECS is developed that only uses the RSC to control the system. First, the proposed configuration and its active and reactive power control methods are elaborated. Then, the design nuances of the proposed method are explained.

- In Chapter 8, a configuration of DFIG-based SS-WECS is proposed to integrate a HESS consisting of SCESS, BESS, and FESS. Then, the principle of this configuration is elaborated, and a control strategy to manage the energy of the HESS is adapted and explained in detail.

- In Chapter 9, an optimization is conducted to define the optimal size of the HESS. Then, the cost of the HESS consisting of SCESS, BESS, and FESS is modeled and optimized.

- In Chapter 10, the capability of the configuration proposed in Chapter 7 to ride through low voltage and the faulty situation is evaluated. Furthermore, this chapter compares the performance of various protection circuits. Also, a control strategy is developed for such a system in faulty situations.

- In Chapter 11, the conclusion of the research and the future study direction are explained.

3. PRINCIPLES OF SPLIT-SHAFT WIND ENERGY CONVERSION SYSTEM

The wind turbine is used to capture the kinetic energy from the wind to generate electricity. The wind turbine efficiency, the portion of captured power to wind power known as the power coefficient, is theoretically confined to the Betz limit [119]. The wind turbine power, which is a function of the wind power and power coefficient C_p, is as follows:

$$P_T = P_{wind} C_p(\lambda, \beta) = \frac{1}{2} \rho_{air} A v_w^3 C_p(\lambda, \beta) \tag{3.1}$$

where the power coefficient C_p is a function of pitch angle, β, and Tip Speed Ratio (TSR), λ, for each wind turbine. The power coefficient reaches its maximum only if the TSR is equal to the optimal TSR, λ_o, for a given pitch angle. In other words, the closer to λ_o, the higher C_p. The maximum power of the wind turbine can be calculated as a cubic function of turbine angular velocity as follows:

$$P_T^{opt} = \frac{1}{2} \rho_{air} A \omega_t^3 = k_{opt} \omega_t^3 \tag{3.2}$$

where ρ_{air}, A, R, and ω_t are the air density, cross-section area of the wind turbine, radius of the wind turbine, and angular velocity of the wind turbine, respectively. The characteristics of a $1.5MW$ wind rotor are shown in Figure 3.1. The curve $A'BCD'$ in Figure 3.1 demonstrates this cubic function when the pitch angle is zero. In an active pitch angle control region, when the wind speed is higher than its nominal, the pitch angle is increased to keep the output power at nominal. For wind speed below the nominal, the TSR is kept at λ_o to follow the MPPT. However, the angular velocity of the wind turbine is restricted by multiple factors, including mechanical stresses, noise restrictions, and electrical system limitations; and it is not practical to follow the MPPT completely. Noise restriction and mechanical stresses define the upper limit of the turbine speed (ω_n) as shown in Figure 3.1. For wind speeds higher than this point (C), The turbine angular velocity is kept constant at ω_n, and the torque is increased up to the nominal power. In a gearbox drivetrain, the turbine shaft

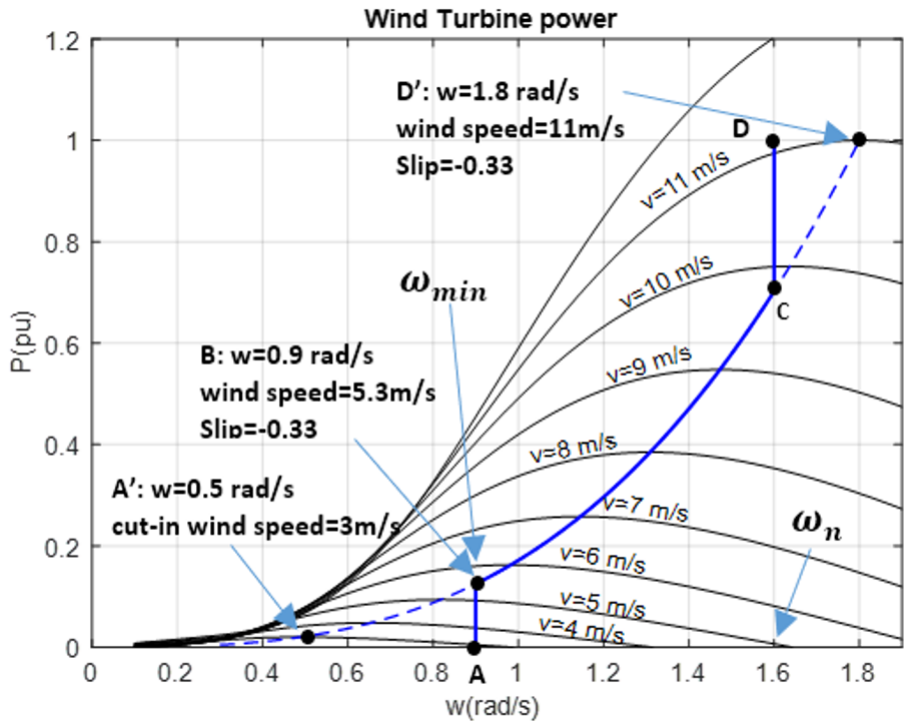

Figure 3.1. Captured power of a $1.5MW$ wind turbine in different wind speeds and wind turbine speed

is coupled to the generator shaft through the gearbox. Therefore, in region II (line $B - C$), MPPT requires maintaining λ_o at different wind speeds, which means that the turbine and generator speeds must reach ω_o. Tracking MPPT in low wind speed needs a larger DFIG slip. Consequently, it leads to an over-designed converters size in low-power wind speeds. Therefore, the lower limit of the DFIG shaft angular velocity is kept at a minimum turbine angular velocity (ω_{min}) [37], [119].

3.1 Hydraulic Transmission System (HTS)

The diagrams of the decoupled SS-WECS with an HTS are shown in Figure 3.2 and Figure 3.3. The nacelle contains a hydraulic pump that is driven by the turbine shaft. As the wind turbine turns, it turns the pump, and the transmission fluid is pressurized. The high-pressure fluid is circulated in a hydraulic system that reaches a hydraulic motor located at ground level. As the wind speed increases, the hydraulic pump causes the pressure to

increase at the inlet of the hydraulic motor. Consequently, the motor produces more torque to drive the generator. In the following subsections, the dynamic of each system element is explained [108], [120], [121].

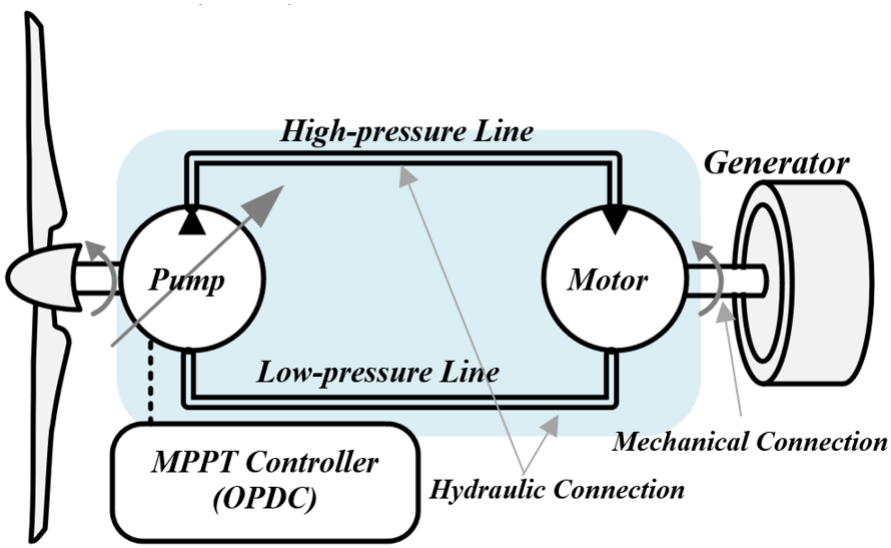

Figure 3.2. Configuration of the hydraulic wind turbine with a variable-displacement pump (VDP)

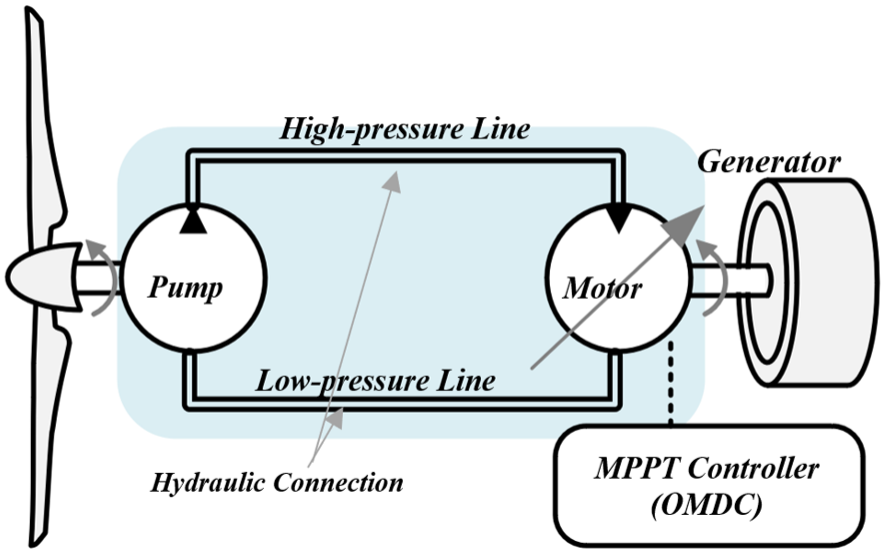

Figure 3.3. Configuration of the hydraulic wind turbine with a variable-displacement motor (VDM)

3.1.1 Wind Turbine Rotor Dynamic

The wind turbine rotor captures a portion of wind energy. This power produces a lift force on turbine blades and rotates the turbine rotor. Then, this driving torque of the turbine rotor, τ_r, turns the shaft of the hydraulic pump. The hydraulic pump shaft creates a braking torque, τ_{sh}, by pressurizing the hydraulic fluid. Herein, the most popular two-mass model of turbine rotor has been employed [122]. The governing equations of wind turbine rotor dynamic in the frequency domain are as follows:

$$\tau_r - \tau_{sh} = J_r s\omega_r + D_r\omega_r \tag{3.3}$$

$$\tau_{sh} = (\omega_r - \omega_p)\,(K_{sh}/s + D_{sh}) \tag{3.4}$$

where, D_r, D_{sh}, and K_{sh} are wind rotor damping coefficient, shaft damping coefficient, and shaft stiffness coefficient, respectively.

3.1.2 Hydraulic Pump Dynamic

The governing equations of the hydraulic pump are two types: torque and flow equations. The rotation of the pump, ω_p, creates a flow of fluid in the hydraulic pipeline, Q_p, as stated in 3.5. The value of this flow depends mainly on pump displacement and speed. Some portion of this flow leaks back to the low-pressure side of the hydraulic pump through the clearance of pump mechanical parts. The amount of leaking flow is proportionate to pressure and pump spillage coefficient, C_{sp}. According to 3.6 and 3.7, As the pressure of the fluid at the pump side, P_p, increases, the pump braking torque (τ_p) and its driving torque can be balanced, and the pump reaches a steady angular velocity.

$$Q_p = D_p\omega_p - \frac{C_{sp}}{\mu} D_p P_f \tag{3.5}$$

$$J_p s\omega_p = \tau_{sh} - \tau_p \tag{3.6}$$

$$\tau_p = D_p P_p + \mu C_{vp} D_p \omega_p + C_{fp} D_p P_f + \tau_{bp} \tag{3.7}$$

The coefficient C_{fp} represents the opposing friction torque of the pump, which is proportional to the displacement and pressure. Viscous damping coefficient, C_{vp}, represents viscous torque required to shear fluid in the small clearance of hydraulic machinery. Also, μ is the absolute viscosity of the fluid. When a more viscous liquid is employed, it is harder to shear the fluid, and the torque loss is more considerable.

3.1.3 Hydraulic Pipeline Dynamic

The pipeline dynamic is expressed in 3.8-3.12 by considering fluid compressibility and pressure drop along the pipeline. Due to the pump flow, Q_p, the operating pressure increases based on mass conservation principles and the definition of bulk modulus 3.8. A hydraulic fluid with a lower buck modulus is more compressible. Pressure loss along the pipeline can be calculated based on 3.9 and 3.10.

$$sP_f = \frac{\beta_f}{V_f}(Q_p - Q_m) \tag{3.8}$$

$$\Delta P_p = (P_p - P_f) = f\frac{L\rho_f}{2D_{\text{pipe}}A_{\text{pipe}}^2}Q_p|Q_p| \tag{3.9}$$

$$\Delta P_m = (P_f - P_m) = f\frac{L\rho_f}{2D_{\text{pipe}}A_{\text{pipe}}^2}Q_m|Q_m| \tag{3.10}$$

where P_f, P_p, and P_m are the fluid pressure at the middle point, pump side, and motor side of the pipeline. The coefficient f is calculated based on the Reynolds coefficient as follows:

$$R_{\text{e}} = \frac{QD_{\text{pipe}}}{v_f A_{\text{pipe}}} \tag{3.11}$$

$$f = \begin{cases} K_s/R_{\text{e}} & R_{\text{e}} \leq R_{\text{e}_L} \\ f_L + \frac{f_T - f_L}{R_{\text{e}_T} - R_{\text{e}_L}}(R_{\text{e}} - R_{\text{e}_L}) & R_{\text{e}_L} < R_{\text{e}} < R_{\text{e}_T} \\ 1/(-1.8\log(\frac{6.9}{R_{\text{e}}} + (\frac{r/D_H}{3.7})^{1.11}))^2 & R_{\text{e}_T} \leq R_{\text{e}} \end{cases} \tag{3.12}$$

In Equations 3.11 and 3.12, v, ρ, A_H, D_H, and r are fluid kinematic viscosity, fluid density, the pipeline cross-section, pipeline inner diameter, and roughness of the pipeline wall, respectively. Depending on the Reynolds coefficient, the performance of the fluid can be

laminar or turbulent. When flow is turbulent, the pressure loss is noticeable larger than laminar flow.

3.1.4 Hydraulic Motor Dynamic

Similar to the hydraulic pump, hydraulic motor flow and torque equations are the same as follows:

$$Q_m = D_m\omega_m + \frac{C_{sm}}{\mu}D_mP_m \tag{3.13}$$

$$J_m s\omega_m + D_g\omega_m = \tau_m - \tau_{\mathrm{e}} \tag{3.14}$$

$$\tau_m = D_mP_m - \mu C_{vm}D_m\omega_m - C_{fm}D_mP_m - \tau_{bm} \tag{3.15}$$

The volumetric loss of motor flow passes through the clearance of the mechanical parts without creating an effective power. The effective part of the flow depends on the displacement and speed of the hydraulic motor. The pressurized fluid reaches the hydraulic motor and creates a driving torque to drive the generator. Similar to pump equations, the hydraulic motor has some torque losses.

3.1.5 MPPT Approaches in SS-WECSs

In an SS-WECS, a hydraulic power transmission system decoupled the wind turbine angular velocity and the generator speed. In steady-state, dP_f/dt in 3.8 becomes zero, and by neglecting the losses, the speed turn ratio of the hydraulic transmission is obtained as $\omega_m/\omega_p = D_p/D_m$. By changing the displacement of the pump or motor, the hydraulic drivetrain behaves as a Continuously Variable Transmission (CVT) and could provide decoupled power transmission. That means the generator speed can be controlled independently of the turbine speed. In such systems, achieving MPPT depends on the different types of HTS.

Optimal Pump Displacement Control (OPDC)

The configuration shown in Figure 3.2 has a variable-displacement pump housed in the nacelle driven by the turbine shaft and a fixed-displacement hydraulic motor located at ground level. The pump speed is controlled through the pump displacement to obtain the maximum power coefficient (C_{max}) for different wind speeds. In this configuration, the optimal pump displacement is obtained as follows [123]:

$$D_{po} = \left(\frac{1}{2\lambda_o^3 P}\right) \eta_m \rho \pi R^5 C_{\max} \omega_p^2 = k_{opt} \omega_p^2 / P_f \tag{3.16}$$

Optimal Motor Displacement Control (OMDC)

The configuration shown in Figure 3.3 has a fixed-displacement pump housed in the nacelle driven by the turbine shaft and a variable-displacement hydraulic motor located at ground level. The optimal power production of the wind turbine is achieved by optimizing the drivetrain operating points such that the optimal TSR is obtained in a combination of speed and pressure. To this end, the optimal motor displacement to obtain the maximum power coefficient (C_{max}) is obtained as follows [20]:

$$D_m = \frac{\eta_v}{\omega_m} \sqrt{\frac{2(D_p \lambda_o)^3}{\eta_{mp} \rho_{air} \pi R^5 C_{\max}}} \sqrt{P_f} \tag{3.17}$$

Optimal Pressure Control of Hydraulic Motor

In the case of a variable-displacement motor, there is another approach to follow MPPT. This control strategy is to follow the optimal pressure. The optimum pressure can be followed by controlling the displacement of the hydraulic motor to get the maximum power coefficient (C_{max}). The optimal pressure is obtained as follows:

$$P_{fo} = \left(\frac{1}{2\lambda_o^3 D_p}\right) \eta_{tp} \rho_{air} \pi R^5 C_{max} \omega_p^2 \tag{3.18}$$

3.2 Energy Conversion Efficiency and Power Flow

Hydraulic machinery utilized in the HTS has two types of loss, volumetric and torque losses. Also, the pipeline loss is due to the pressure loss along the pipeline.

3.2.1 HTS Efficiency

For the hydraulic pump, the input power is $P_{sh} = \omega_p \tau_p$ and the output power is $P_{hp} = Q_p P_p$. Also, for the hydraulic motor, the input power is $P_{\text{in}}^m = Q_m P_m$, and the output power is $P_{hm} = \omega_m \tau_m$. Using the equations of these elements, the volumetric efficiency of the hydraulic pump and motor is obtained as follows:

$$\eta_{vp} = 1 - \frac{C_{sp}}{A_p} \tag{3.19}$$

$$\eta_{vm} = \frac{1}{1 + C_{sm}/A_m} \tag{3.20}$$

where $A_p = \mu\omega_p/P_p$ and $A_m = \mu\omega_m/P_m$. $_{vp}$ and $_{vm}$ are the volumetric efficiency of the pump and motor, respectively. Moreover, the torque efficiency of the pump and motor is achieved as follows:

$$\eta_{tp} = \frac{1}{1 + C_{fp} + C_{vp}A_p - \tau_{bp}/(D_p P_f)} \tag{3.21}$$

$$\eta_{tm} = 1 - C_{fm} - C_{vm}A_m - \tau_{bm}/(D_m P_f) \tag{3.22}$$

where η_{tp} and η_{tm} are the torque efficiency of the pump and motor, respectively. The overall efficiency of the hydraulic machinery is the product of the torque and volumetric efficiencies.

$$\eta_p = \eta_{tp}\eta_{vp} \tag{3.23}$$

$$\eta_m = \eta_{tm}\eta_{vm} \tag{3.24}$$

where η_p and η_m are the overall pump and motor efficiencies, respectively. The power loss of the pipeline is as follows:

$$P_{lp} = \Delta P_p Q_p + \Delta P_m Q_m \tag{3.25}$$

3.2.2 Power Flow in Split-Shaft WECS

The relation between the input and output power of hydraulic machinery can be calculated using the equation of the system as follows:

$$Q_p = D_p \omega_p \eta_{vp} \tag{3.26}$$

$$P_{hp} = \eta_{tp} \eta_{vp} P_{sh} = D_p \omega_p P_p \eta_{vp} \tag{3.27}$$

$$Q_m = D_m \omega_m / \eta_{vm} \tag{3.28}$$

$$P_{hm} = \eta_{tm} \eta_{vm} P_{\text{in}}^m = D_m \omega_m P_m \eta_{tm} \tag{3.29}$$

The power flow diagram of the HTS is demonstrated in Figure 3.4.

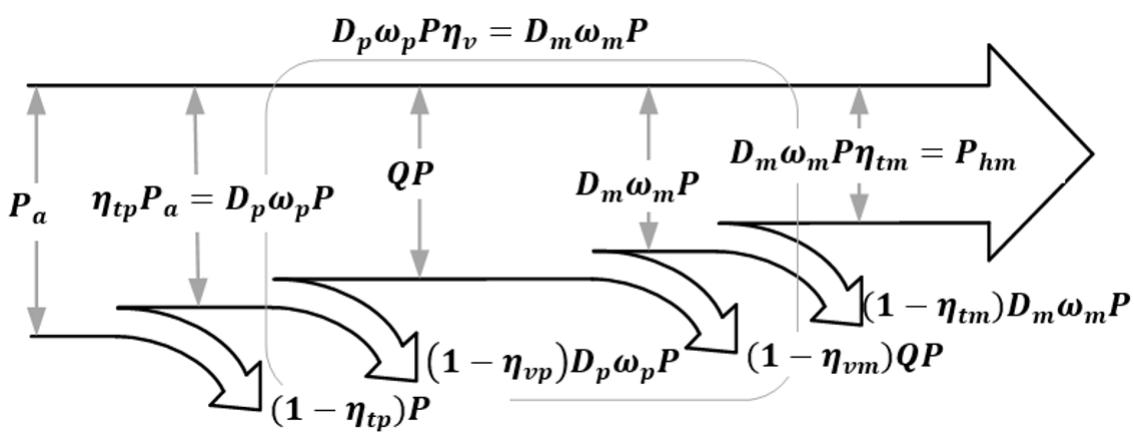

Figure 3.4. Power Flow of the HTS

The torque loss of the pump causes the input power of the pump, P_{sh}, cut to $D_p \omega_p P_p$. A portion of this power becomes the volumetric loss, $(1 - \eta_{vp})\ D_p \omega_p P_p$. The remaining power is the input power of the pressurized pipeline that equals to $Q_p P_p$. The pipeline delivers the power of $Q_m P_m$ to the hydraulic motor. Similarly, the volumetric efficiency of the motor cut

the pressurized power of the fluid to $D_m\omega_m P_m$. Finally, the torque efficiency of the hydraulic motor reduces the term $D_m\omega_m P_m$ to the output power P_{hm}.

To demonstrate the efficiencies of the hydraulic machinery and the pipeline, a SS-WECS with SG is simulated in MATLAB. The data of such a system is given in Table 3.1. The efficiency of the pump and motor are shown in Figure 3.5 and Figure 3.6. The efficiency of various elements of the HTS for the given wind turbine, from cut-in speed to nominal power, is demonstrated in Figure 3.7.

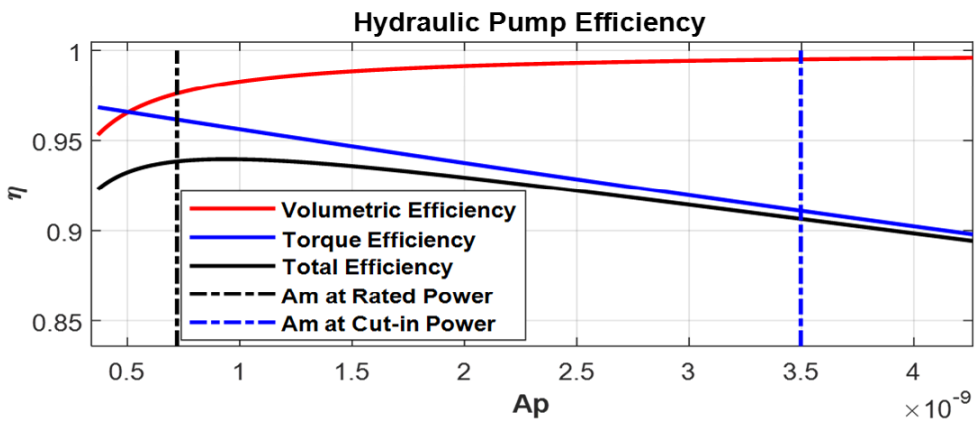

Figure 3.5. Hydraulic pump efficiencies

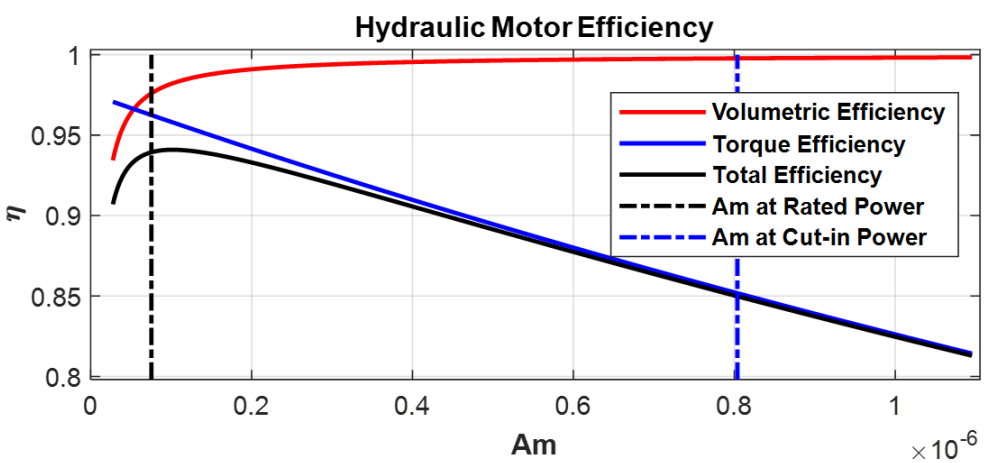

Figure 3.6. Hydraulic motor efficiencies

At low wind speed, the efficiency of the pipeline decreased noticeably to 95%. This is because the operating pressure is low at low wind speeds, so the portion of pressure loss is

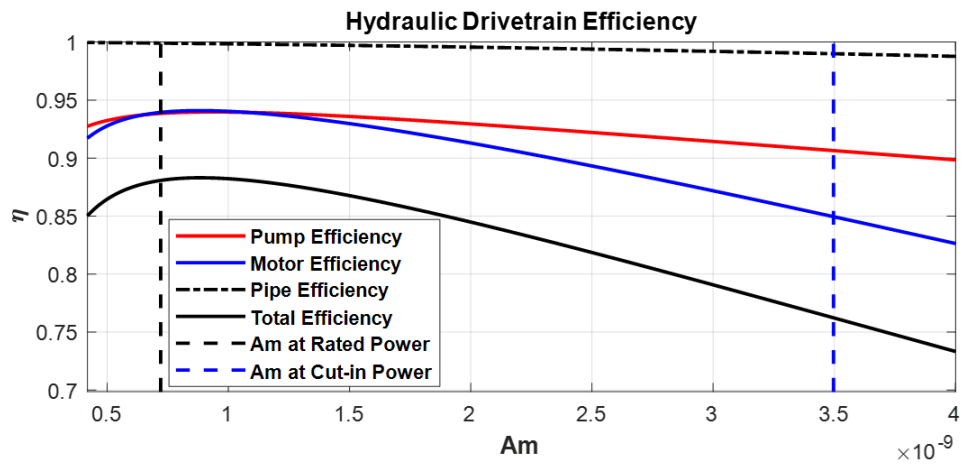

Figure 3.7. HTS efficiency

higher. Generally, the displacement of the hydraulic machinery can be controlled to improve the efficiency of HTS at low wind speed. At low wind speeds, the torque loss is dominant in hydraulic machinery. However, at very high pressure, Full load, the dominant loss of the system is the volumetric loss of the hydraulic machinery. In other words, in very high pressure, the leaking flow is the main reason for having low efficiency.

3.3 DFIG Model

In conventional gearbox-driven DFIG-based WECSs, the DFIG shaft is mechanically coupled to the wind turbine shaft. Therefore, its speed must be controlled proportionally to the wind speed to maintain the TSR close to the optimal TSR. As a result, to obtain MPPT, the generator's optimal speed must be controlled within a wide range of $\mp 30\%$, and the converters' power rating must be chosen accordingly. By considering the dynamic of the stator and rotor, the rotor and stator voltage equations in the dq frame are as follows [99]:

$$\begin{bmatrix} V_{qr} \\ V_{dr} \end{bmatrix} = \begin{bmatrix} R_r & 0 \\ 0 & R_r \end{bmatrix} \begin{bmatrix} I_{qr} \\ I_{dr} \end{bmatrix} + \begin{bmatrix} \mathrm{d}/\,\mathrm{d}t & s\omega_s \\ -s\omega_s & \mathrm{d}/\,\mathrm{d}t \end{bmatrix} \begin{bmatrix} \lambda_{qr} \\ \lambda_{dr} \end{bmatrix} \tag{3.30}$$

$$\begin{bmatrix} V_{qs} \\ V_{ds} \end{bmatrix} = \begin{bmatrix} R_s & 0 \\ 0 & R_s \end{bmatrix} \begin{bmatrix} I_{qs} \\ I_{ds} \end{bmatrix} + \begin{bmatrix} \mathrm{d}/\,\mathrm{d}t & \omega_s \\ -\omega_s & \mathrm{d}/\,\mathrm{d}t \end{bmatrix} \begin{bmatrix} \lambda_{qs} \\ \lambda_{ds} \end{bmatrix} \tag{3.31}$$

where variables V, I, λ, s, ω_s are voltage, current, flux, slip, and synchronous speed, respectively. Subscripts qr, qs ,dr, ds are the quadrature components of rotor and stator variables and direct components of the rotor and stator variables, respectively. Flux equations of the DFIG are calculated as follows:

$$\begin{bmatrix} \lambda_{qs} \\ \lambda_{ds} \end{bmatrix} = \begin{bmatrix} L_s & 0 \\ 0 & L_s \end{bmatrix} \begin{bmatrix} I_{qs} \\ I_{ds} \end{bmatrix} + \begin{bmatrix} L_m & 0 \\ 0 & L_m \end{bmatrix} \begin{bmatrix} I_{qr} \\ I_{dr} \end{bmatrix} \tag{3.32}$$

$$\begin{bmatrix} \lambda_{qr} \\ \lambda_{dr} \end{bmatrix} = \begin{bmatrix} L_m & 0 \\ 0 & L_m \end{bmatrix} \begin{bmatrix} I_{qs} \\ I_{ds} \end{bmatrix} + \begin{bmatrix} L_r & 0 \\ 0 & L_r \end{bmatrix} \begin{bmatrix} I_{qr} \\ I_{dr} \end{bmatrix} \tag{3.33}$$

By eliminating the stator current from rotor flux Equations 3.33 using 3.32 and replacing the flux equations of the rotor in 3.30, the rotor voltage equations can be rewritten as follows:

$$\begin{bmatrix} V_{qr} \\ V_{dr} \end{bmatrix} = \begin{bmatrix} R_r + \sigma L_r \, \mathrm{d}/\mathrm{d}t & s\omega_s \sigma L_r \\ -s\omega_s \sigma L_r & R_r + \sigma L_r \, \mathrm{d}/\mathrm{d}t \end{bmatrix} \begin{bmatrix} I_{qr} \\ I_{dr} \end{bmatrix} + L_m/L_s \begin{bmatrix} V_{qs} - (1-s)\omega_s \lambda_{ds} \\ V_{ds} + (1-s)\omega_s \lambda_{qs} \end{bmatrix} \tag{3.34}$$

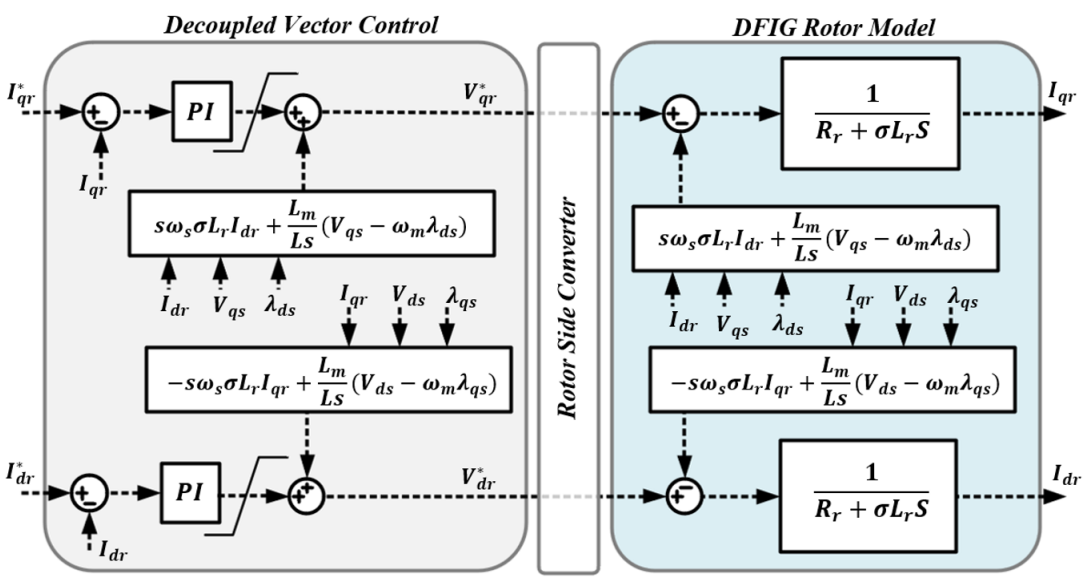

Figure 3.8. Decoupled vector control and DFIG model

By using 3.34, the model of the DFIG rotor can be achieved, as shown in Figure 3.8. Furthermore, the decoupled vector control can be achieved by eliminating the coupling link.

This decoupled vector control is shown in Figure 3.8. The converter dynamic is considered much faster in this research than the machine and control strategy response time. The active power of the stator and rotor of the DFIG can be calculated as follows:

$$\begin{aligned} P_s = \frac{3}{2}(V_{qs}I_{qs} + V_{ds}I_{ds}) &= \frac{3}{2}R_s(I_{qs}^2 + I_{ds}^2) + \frac{3}{2}\omega_s L_m(I_{dr}I_{qs} - I_{qr}I_{ds}) \\ &= \frac{3}{2}R_s(I_{qs}^2 + I_{ds}^2) + \frac{3}{2}(\frac{\omega_s L_m}{\sigma L_r L_s})(\lambda_{dr}\lambda_{qs} - \lambda_{qr}\lambda_{ds}) \end{aligned} \tag{3.35}$$

$$\begin{aligned} P_r = \frac{3}{2}(V_{qr}I_{qr} + V_{dr}I_{dr}) &= \frac{3}{2}R_r(I_{qr}^2 + I_{dr}^2) + \frac{3}{2}L_m s\omega_s(I_{ds}I_{qr} - I_{qs}I_{dr}) \\ &= \frac{3}{2}R_r(I_{qr}^2 + I_{dr}^2) + \frac{3}{2}(\frac{s\omega_s L_m}{\sigma L_r L_s})(\lambda_{ds}\lambda_{qr} - \lambda_{qs}\lambda_{dr}) \end{aligned} \tag{3.36}$$

By neglecting the losses, the relation between stator and rotor powers can be achieved as follows:

$$P_r = -sP_s \tag{3.37}$$

Equation 3.37 indicates that the power passing through the DFIG rotor is proportional to the slip of the generator. This feature has been utilized to decrease the size and number of power converters.

3.3.1 Steady-State Model

Assuming the stator and rotor resistance are negligible, the steady-state DFIG flux and voltages equations in the stator flux-oriented frame, in which the quadrature of the stator flux is zero, are as follows:

$$\lambda_{sq} = L_s \mathrm{i}_{sq} + L_m \mathrm{i}_{rq} = 0, \qquad \lambda_{sd} = L_s \mathrm{i}_{sd} + L_m \mathrm{i}_{rd} = L_m \mathrm{i}_{m0} \tag{3.38}$$

$$\lambda_{rq} = \sigma L_r \mathrm{i}_{rq}, \qquad \lambda_{rd} = \sigma L_r \mathrm{i}_{rd} + L_0 \mathrm{i}_{m0} \tag{3.39}$$

$$V_{sq} = \omega_s \lambda_{sd}, \qquad V_{sd} = 0 \tag{3.40}$$

$$V_{rq} = s\omega_s \lambda_{rd}, \qquad V_{rd} = -s\omega_s \lambda_{rq} \tag{3.41}$$

where $\sigma = 1 - L_m^2/(L_r L_s)$, and $I_m 0 = V_{sq}/(\omega_s L_m)$ is the magnetizing current. The equations of DFIG expressed in per-unit help understand the DFIG equations better. To this end, stator nominal power and phase voltage are chosen as per-unit bases:

$$V_b = V_{s-ph} \tag{3.42}$$

$$P_b = P_{sn} = \frac{P_{\text{mech}}}{1 + s_{\max}} \tag{3.43}$$

$$P_b = 3V_b I_b = \frac{3}{2} V_b^{dq} I_b^{dq} \tag{3.44}$$

V_b and I_b are the base voltage and current of the stator for the *abc* frame, respectively. Similarly, V_b^{dq}, I_b^{dq} are the base voltage and current in the *dq* frames. By using these bases, the equations in per unit can be calculated as follows:

$$V_{pu}^s = 1 \tag{3.45}$$

$$I_{pu}^{sd} = \mathrm{i}_{m0-pu} - I_{pu}^{rd}, \qquad I_{pu}^{rq} = -I_{pu}^{sq} \tag{3.46}$$

$$P_{r-pu} = -sP_{s-pu} = sI_{pu}^{rq} \tag{3.47}$$

$$Q_{s-pu} = I_{pu}^{sd}, \qquad Q_{r-pu} = sI_{pu}^{rd} \tag{3.48}$$

$$T_{\text{e}-pu} = -I_{pu}^{rq} \tag{3.49}$$

At the rotor, apparent power, voltage, and current are obtained as follows:

$$S_{pu}^r \approx |s|\sqrt{(I_{pu}^{rq})^2 + (I_{pu}^{rd})^2} \tag{3.50}$$

$$V_{pu}^r \approx |s| \tag{3.51}$$

$$I_{pu}^r = \sqrt{(I_{pu}^{rq})^2 + (I_{pu}^{rd})^2} \tag{3.52}$$

The performance of the DFIG using these equations is more understandable. Equation 3.45 demonstrates that the power flow through the rotor is proportional to the rotor slip. Above the synchronous speed, the slip is negative. Consequently, the power of the rotor is positive, which means the rotor is also delivering power to the grid through the converter. Similarly, the rotor voltage is equal to the absolute value of the slip. Figure 3.9 demonstrates

the voltage and current of the DFIG rotor when the reactive power of the stator is equal to zero, $Q_s = 0$, and operating points move on the $ABCD$ curve shown in Figure 3.1. The amount of the steady-state voltage depends on the slip of the generator, as stated in 3.49. However, the current of the DFIG rotor depends on the active power and magnetizing current of the rotor.

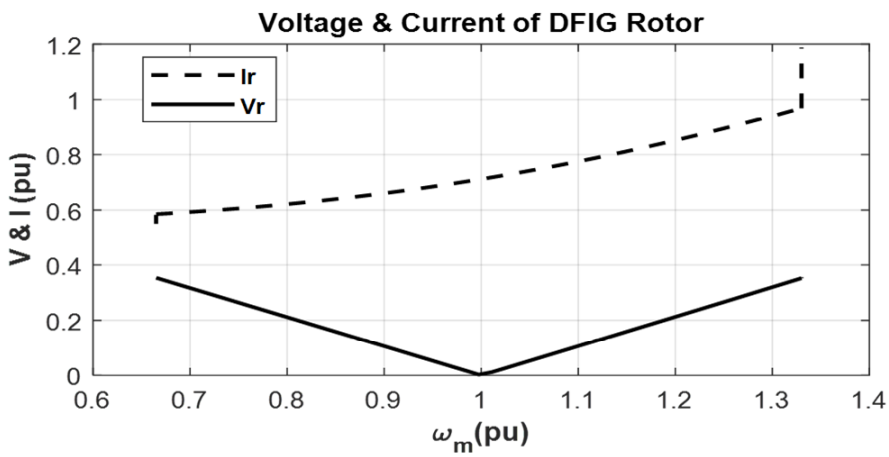

Figure 3.9. Operating voltage and current of the DFIG rotor at different speeds when $Q_s = 0$ for operating points on the $ABCD$ curve shown in Figure 3.1

For a conventional gearbox-driven DFIG, the power injected into the grid $(P_s + P_r)$ is shown in Figure 3.10 for operating points on the $ABCD$ curve. The data used for simulation are given in Table 3.1. It has shown that the power of the rotor for sub-synchronous speed is negative. This means that the rotor absorbs power at those speeds. But the summation of the stator and rotor powers is equal to the mechanical power of the prime mover.

Figure 3.11 demonstrates the maximum power of the rotor based on the maximum slip of the generator. This power would be the rating of the RSC.

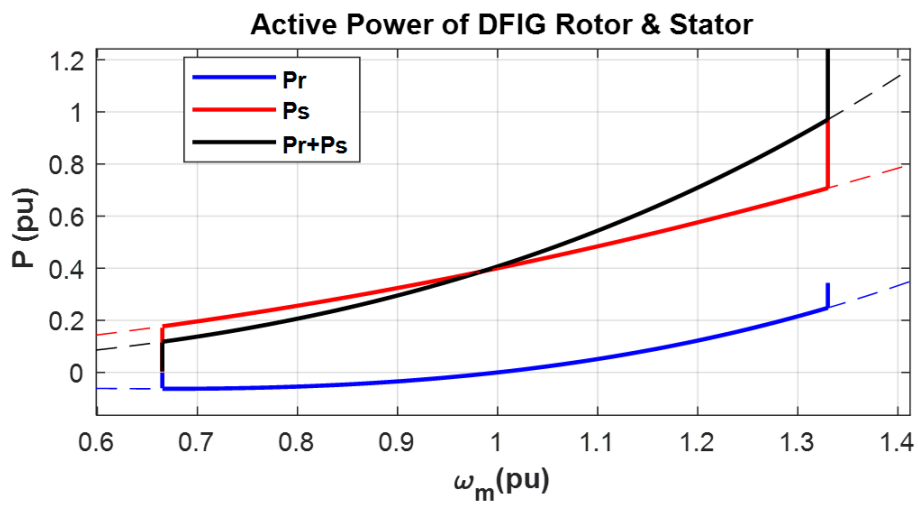

Figure 3.10. Stator and rotor power injected into the power grid at different speeds for operating points on the $ABCD$ curve shown in Figure 3.1

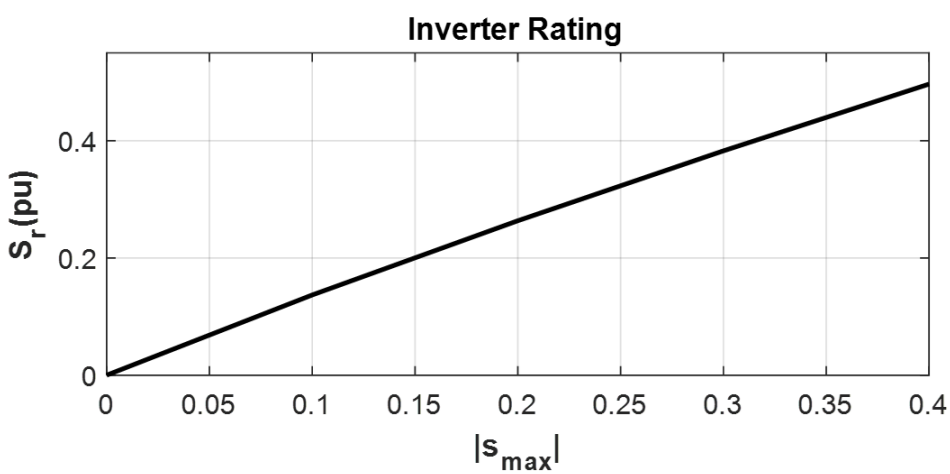

Figure 3.11. Rating of RSC

Table 3.1. Characteristics of the Split-Shaft HTS

	Generator Data	
P_g	Generator Rated Power	1.5 MW
Vs	Grid Voltage (Line)	690 V
L_{ls}/L_{lr}	Stator/Rotor Inductance	0.167 mH
L_m	Magnetizing Inductance	5.48 mH
R_s	Stator Resistance	2.65 $m\Omega$
R_r	Rotor Resistance	2.63 $m\Omega$
P	Generator Pole Pairs	1
	Turbine Data	
R	Blade Diameter	68.45 m
ρ_{air}	Air Density	1.225 kg/m^3
v_w	Nominal Wind Speed	11 m/s
λ_o	Nominal Tip Speed Ratio	9.94
C_{max}	Maximum Power Coefficient	0.5
H_t	Wind Turbine Inertia Constant	4.32 s
	Hydraulic Transmission System	
P_f	Pressure Base	4×10^7 Pa
D_p	Nominal Displacement of Pump	0.0208 m^3/rad
D_m	Nominal Displacement of Motor	9.95×10^{-5} m^3/rad
ω_p	Nominal Turbine Speed	17.2 rpm
ω_m	Nominal Motor Speed	3600 rpm
Q	Nominal Flow	0.0375 m^3/s
β_f	Bulk Modulus	1.2×10^9 Pa
V_f	Fluid Volume	0.864 m^3
C_{sp}	Pump Slippage Coefficient	1.7302×10^{-11}
C_{sm}	Motor Slippage Coefficient	3.6238×10^{-9}
C_{fp}	Pump Coulomb Friction Coefficient	0.025
C_{fm}	Motor Coulomb Friction Coefficient	0.025
C_{vp}	Pump Viscous Drag Coefficient	2.0806×10^7
C_{vm}	Motor Viscous Drag Coefficient	92720
μ	Dynamic Viscosity of Fluid	0.0160 $Pa.s$
v_f	Kinematic Viscosity of Fluid	18.786×10^{-6} m^2/s

4. SCALABILITY AND ELECTRICAL EQUIVALENT OF SS-WECS

In this chapter, the electrical equivalent circuit of each element is obtained to help understand better the system performance. In the equivalent circuit, the performance of each mechanical and hydraulic element is explained with the equivalent electrical components. Furthermore, large-scale SS-WECSs based on HTS require low-speed high-displacement hydraulic pumps and can be challenging. To deal with this challenge, some researchers proposed a new concept of hydraulic machinery that can provide low-speed high-displacement pumps, such as the rotating hydraulic cylinder concept proposed in [124]. Another way is to employ a one-stage low-turn-ratio gearbox between the wind turbine and the hydraulic pump. Furthermore, the number of the generator pole pairs, which reflect the speed of the generator, can affect the HTS performance and efficiency. Therefore, this chapter presents a methodology to evaluate the impact of these variables and parameters on the displacement of hydraulic machinery and component selection.

4.1 Electrical Equivalent Circuit of HTS

Understanding the performance of the SS-WECS for most electrical engineers is not entirely sensible. However, comparing the performance of these types of hydraulic machinery to the performance of the electrical elements could help to have a deeper understanding of such a system. Therefore, the equivalent circuit of the whole system is obtained using the system's equations. The equations of the system shown in Figure 4.1 are stated in the previous chapter. In this figure the two-mass model of the shaft is demonstrated. Based on the equations of the system, the torque and pressure of each element are equivalent to the voltage of the circuit nodes, and the angular velocity and fluid flow are considered as the current of components of the equivalent circuit. Resistor, inductor, and capacitor represent losses and damping factors, inertia, shaft stiffness, and fluid compressibility. These equivalent elements and variables are summarized in Table 4.1.

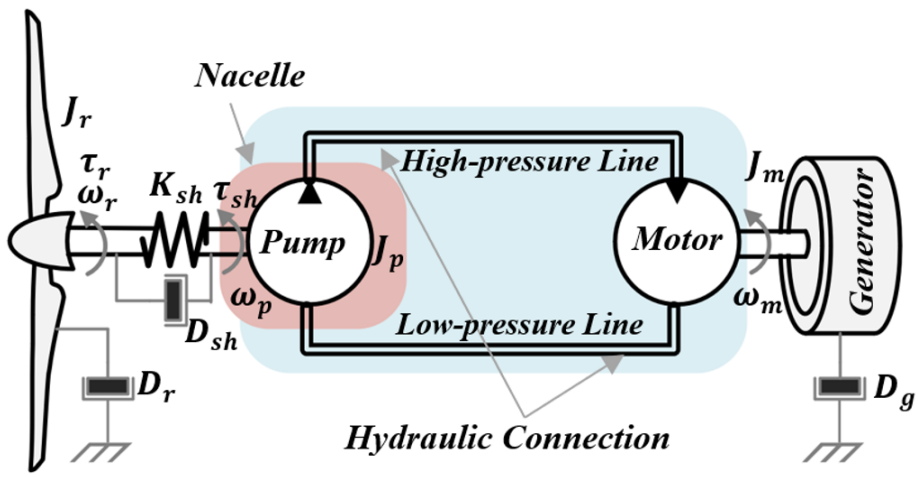

Figure 4.1. Configuration of the split-shaft WECS

Table 4.1. Equivalent Parameters and Variables

Electrical	**Mechanical**	**Hydraulic**
Voltage	Torque	Pressure
Current	Angular Speed	Flow
Resistor	All Losses	Pipeline loss
Inductor	Inertia	
Capacitor	Shaft Stiffness	Fluid Compressibility
DC Voltage Source	Breakaway torque	

The equivalent electrical models of the HTS are shown in Figure 4.2 and Figure 4.3. In the pump model, there are two dependent voltage and current sources, one that depends on the pressure of the fluid and shows hydraulic torque at the turbine shaft side, and the other represents the flow at the pipeline side. At the turbine side, torque and angular velocities are the voltage and current at each point, respectively. Similarly, pressure and flow act like voltage and current in the pipeline-sided model. The torque losses of the pump are represented by a resistor and a DC voltage source (τ_{bp}) at the turbine shaft side. The volumetric loss of the pump is represented by a resistor with the value of μ/C_{sp}. The behavior of the hydraulic motor and its equivalent circuit is similar to the pump equivalent circuit.

The compressibility of the pipeline behaves like a capacitor with a value of $V_f/_f$. This demonstrates that the lower bulk modulus of the fluid means that the size of the capacitor is

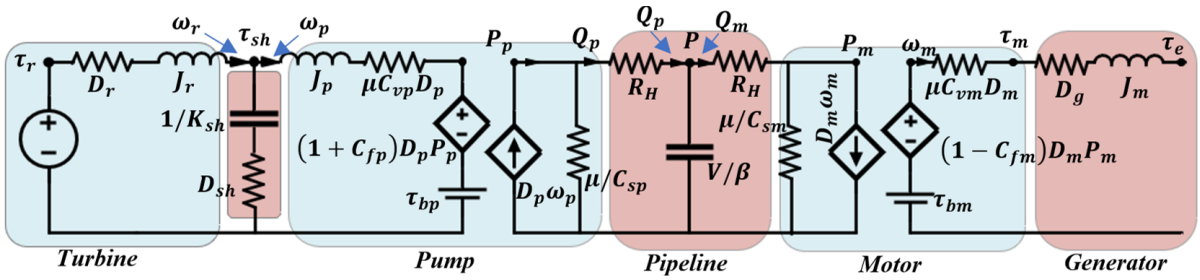

Figure 4.2. The equivalent of the split-shaft WECS

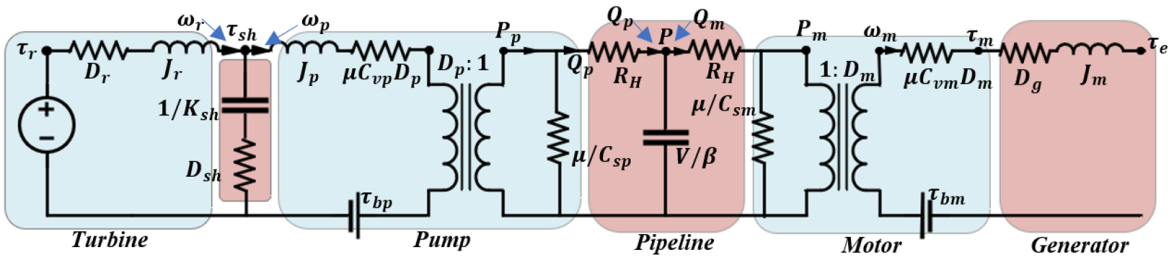

Figure 4.3. The equivalent of the split-shaft WECS neglecting Coulomb friction coefficient of hydraulic types of machinery

more extensive, and the pressures at the middle point of the pipeline change in a smoother manner. The pipeline pressure loss behaves as a nonlinear resistor, R_H, with the value of ΔP_p and ΔP_m. The pipeline model is comparable with the T model of electrical lines. In electrical lines, having a higher voltage level with a given nominal power, the current operating point is lower, and consequently, the loss of the line is smaller. Similarly, in designing a pipeline, having a larger pressure operating point with a given nominal power, the pipeline flow is smaller, and the fluid is laminar. Consequently, the pipeline loss becomes smaller.

Furthermore, the effect of the pipeline diameter on its power loss is similar to the impact of the line cross-section on its power loss in an electrical grid. Therefore, the line's pressure losses can be regarded as negligible by considering the proper pipe diameter size [27]. By neglecting the Coulomb friction coefficient of the hydraulic machinery, the electrical equivalent of the system is shown in Figure 4.3. In this model, the hydraulic machinery behaves such a transformer in the electrical circuit, and its function is to transfer power from one form to another (from rotational power to hydraulic power).

4.2 Scalability and Components Selection

The diagram of an SS-WECS with an HTS is shown in Figure 4.4. The nacelle contains a hydraulic pump and probable one-stage gearbox driven by the turbine shaft. A multi-stage gearbox with a high turn ratio (70-100) is commonly employed in WECS. These gearbox types have lower efficiency and lifetime compared to a one-stage gearbox with a lower turn ratio (2-10). Therefore, employing a one-stage gearbox with the HTS can be justified. A 1.5 MW hydraulic wind turbine is considered as a base model to evaluate the impact of the system parameters on the efficiency and performance of the system. Furthermore, the scalability of the HTS is evaluated for different power scales. The wind power captured by the wind turbine is assumed to be transferred to the generator by an HTS whose data is given in Table 3.1. The output of the HTS is connected to a synchronous generator whose speed is close to 1 per unit. In this section, the effects of various parameters on the performance and efficiency of the system are investigated.

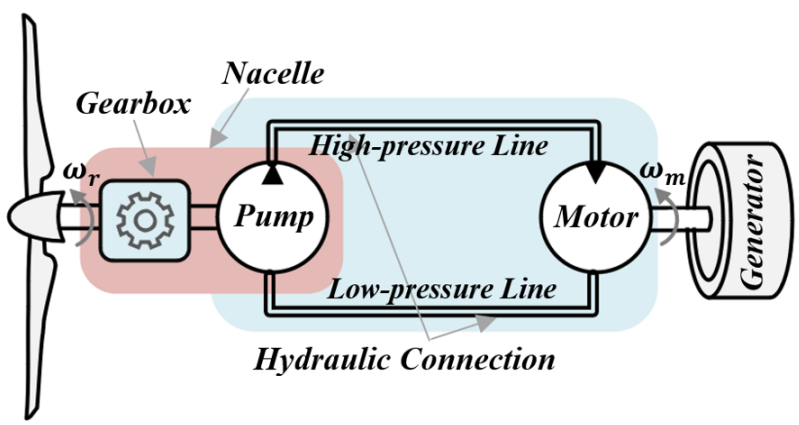

Figure 4.4. Configuration of the split-shaft WECS

4.2.1 Pipeline Length and Diameter Impacts on Pressure Loss

The impact of pipeline parameters on the pressure loss across the pipeline is shown in Figure 4.5-Figure 4.7. As demonstrated in Figure 4.5, the percent of the pressure drop across the pipeline increases noticeably when the diameter of the pipeline is small. This is because

the Reynolds coefficient increases with a small pipe diameter. Therefore, the fluid becomes turbulent, and its loss increases. However, the length of the pipeline is linearly correlated to the loss of the pipeline.

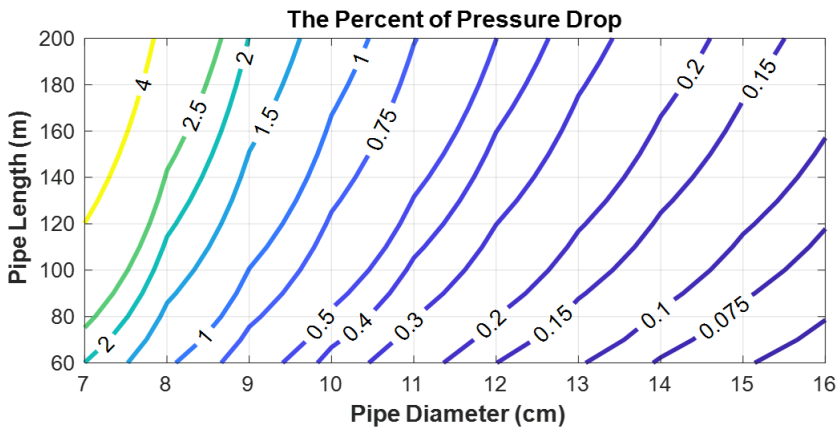

Figure 4.5. The percent of pressure drop for the base WECS in various pipeline lengths and diameters

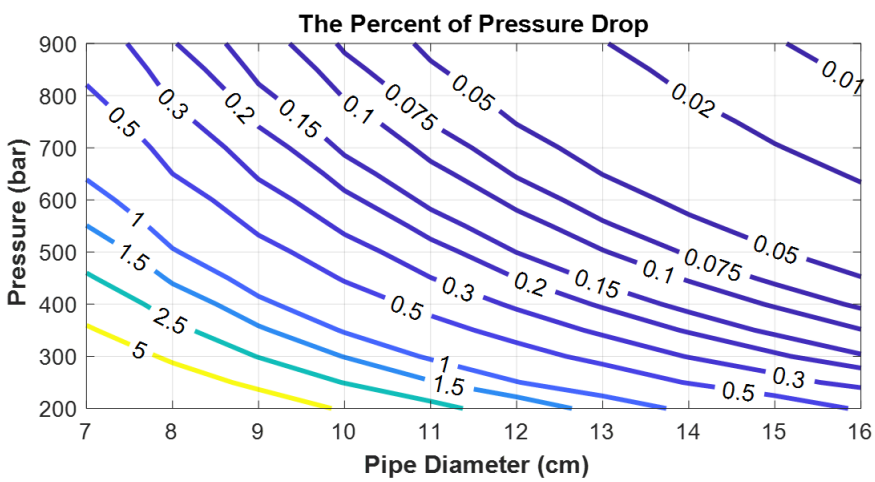

Figure 4.6. The percent of pressure drop for the base WECS in various nominal pressure points and pipeline diameters

The effect of the nominal pressure point is demonstrated in Figure 4.6. As shown in this figure, choosing a higher pressure point results in lower pressure loss with the same diameter. This is because, at the same nominal power, the nominal flow becomes smaller with higher nominal pressure. Therefore, smaller flow results in smaller pipeline loss. The

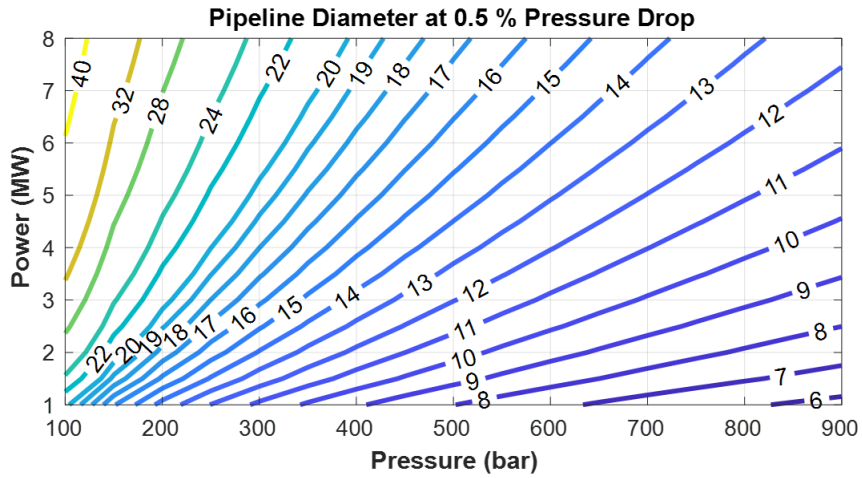

Figure 4.7. Pipeline diameter (cm) for various nominal power and pressure points

scalability of the pipeline and the proper diameter with 0.5% loss for various nominal power and pressure points are shown in Figure 4.7. As this figure demonstrates, choosing a high nominal pressure for large-scale wind turbine results in a smaller pipeline diameter to realize 0.5% pressure loss. By considering the proper size of pipe diameter, the line's pressure losses can be regarded as negligible [27].

4.2.2 Impacts of Nominal Pressure and Speed Points on Pump Displacement

The selection of a higher nominal pressure for a given nominal power results in a pump selection with a smaller displacement, as shown in Figure 4.8. In this figure, the displacement of the pump is given in per unit based on the base wind turbine. For instance, at 5 MW nominal power, choosing the nominal pressure as 400 and 900 bar results in a pump with a nominal displacement of 3.5 and 1.5 per unit, respectively. The impact of nominal pressure and pump speed on pump displacement is shown in Figure 4.9. As shown in this figure, to have a pump with smaller displacement, the turn ratio of the one-stage gearbox can be increased. The one-stage gearbox with a low-speed turn ratio is cheap, light, and reliable. Therefore, adding this to the HTS cannot decrease its reliability or increase its cost significantly. In large-scale WECS choosing a high nominal pressure and adding a one-stage

gearbox can help in a smaller displacement selection. However, choosing a very high nominal pressure increase the volumetric loss of the hydraulic machinery.

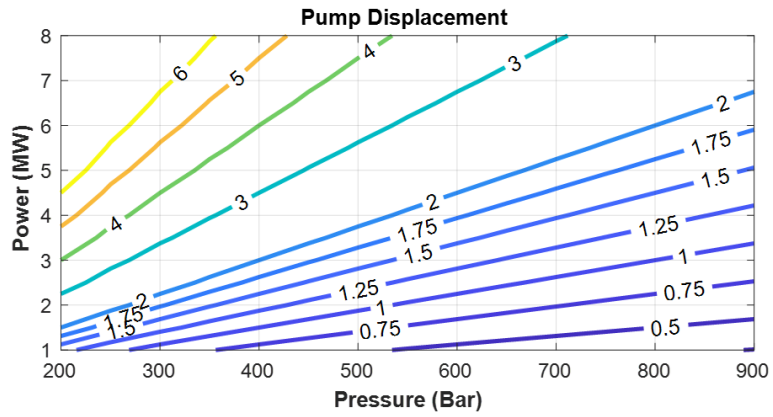

Figure 4.8. Pump displacement (pu) for various nominal power and pressure points

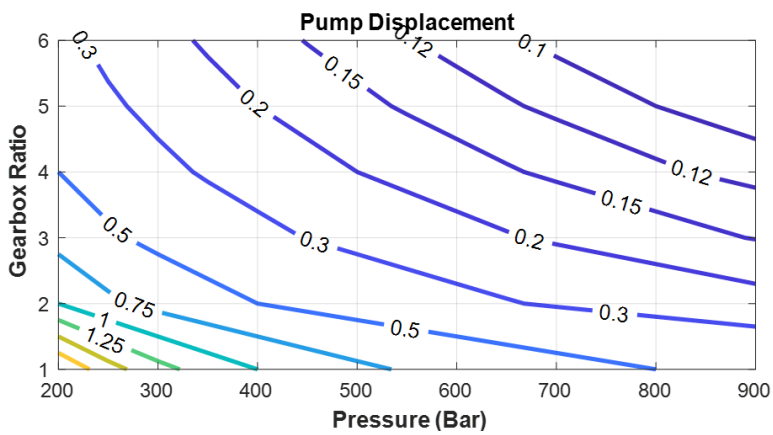

Figure 4.9. Pump displacement (pu) for various nominal pressure points and gearbox turn ratios

4.2.3 Impacts of Nominal Pressure and Speed Points on Motor Displacement

Choosing a higher nominal pressure impacts motor displacement similar to pump displacement, as shown in Figure 4.10. The impact of nominal pressure and generator speed on motor displacement is demonstrated in Figure 4.11. As shown in this figure, A motor

with smaller displacement can be employed with a lower number of generator pole pairs. Commonly, the displacement of the hydraulic motor is small due to its high speed.

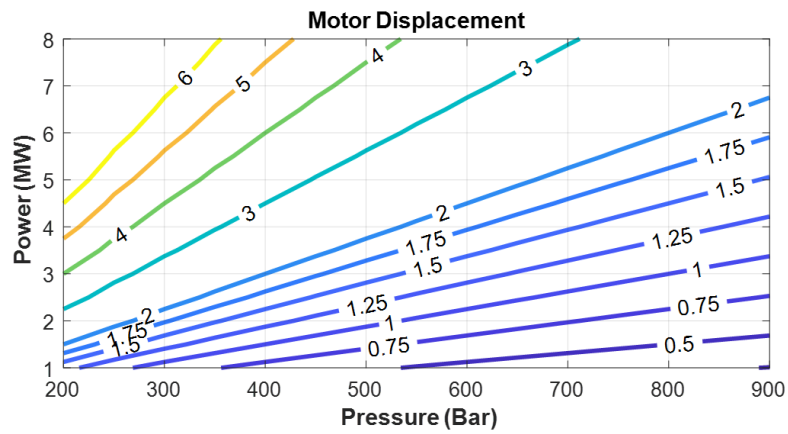

Figure 4.10. Motor displacement (pu) for various nominal power and pressure points

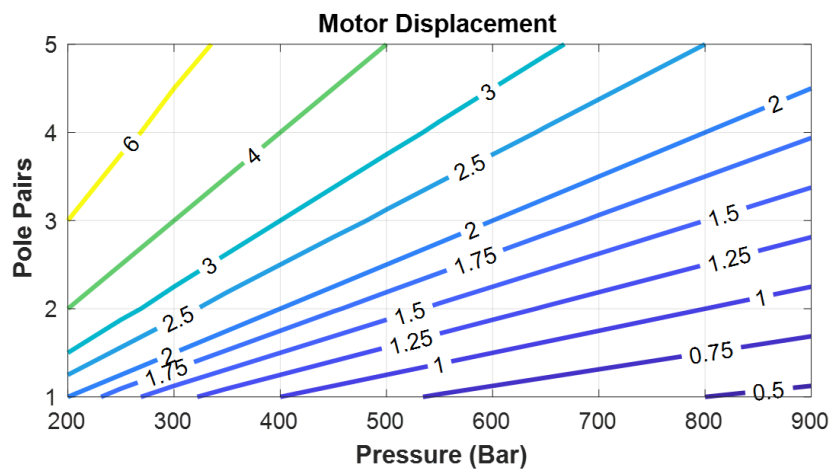

Figure 4.11. Motor displacement (pu) for various nominal pressure points and generator pole pairs

4.2.4 Efficiency of HTS

Figures 4.12 and 4.13 demonstrate the efficiency of the base HTS in various nominal pressure and generator pole pairs. For the base model, when the pressure and pole pairs are chosen too large, the efficiency of the HTS is decreased. This is because the value

of A_m and A_p is decreased too much and that result in large volumetric loss. For the base model, choosing 400 bar nominal pressure with pole pairs of two can result in higher nominal efficiency.

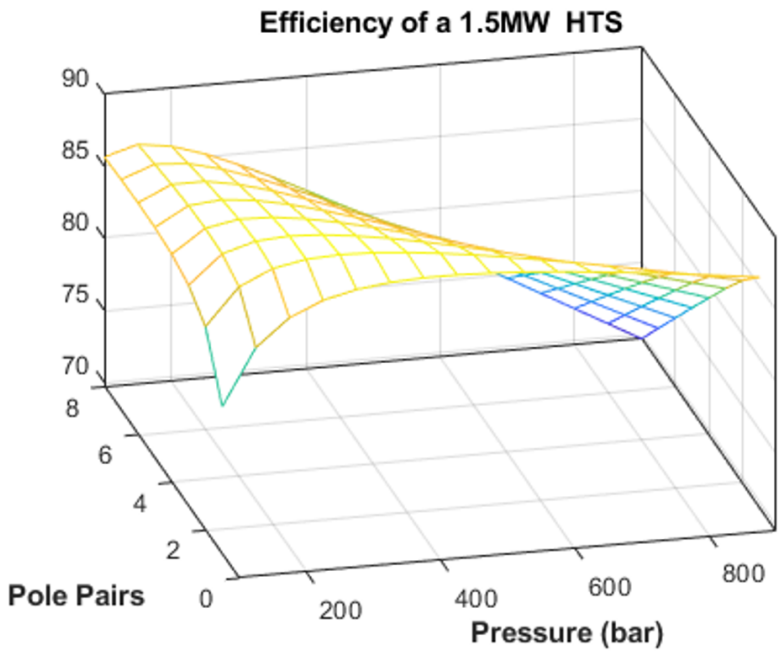

Figure 4.12. Efficiency (%) of base HTS in various nominal pressure and generator pole pairs

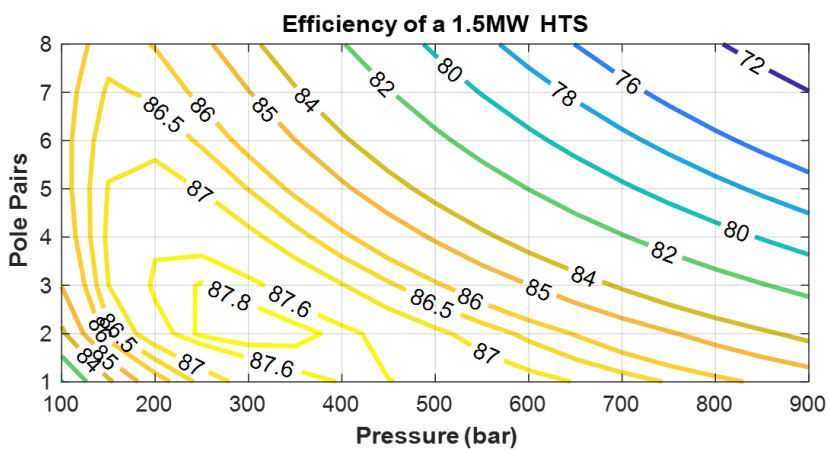

Figure 4.13. Efficiency (%) of base HTS in various nominal pressure and generator pole pairs

Figure 4.14 and Figure 4.15 demonstrate the efficiency of the base HTS in various nominal

pressure and gearbox. For the base model, when low pressure and high-speed operating points are chosen, the efficiency of the HTS is decreased. This is because the value of A_m and A_p is increased too much and that result in large torque loss.

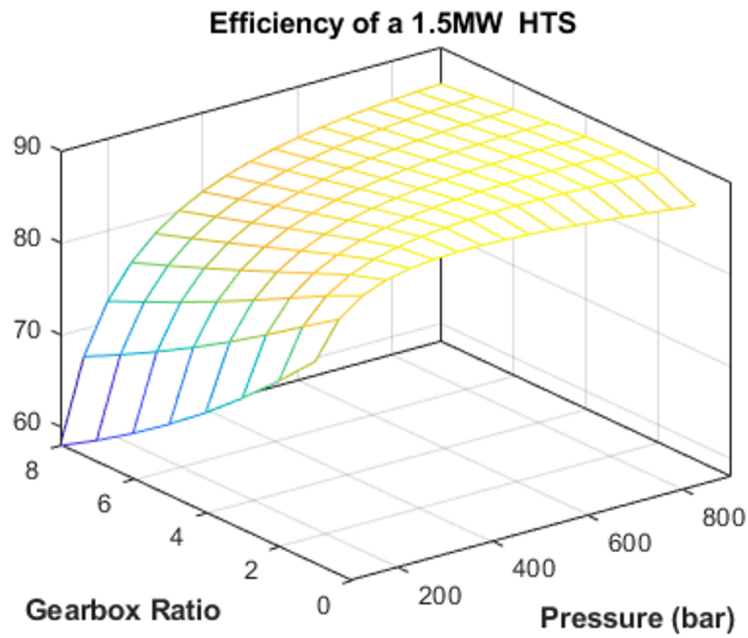

Figure 4.14. Efficiency (%) of base HTS in various nominal pressure and generator pole pairs

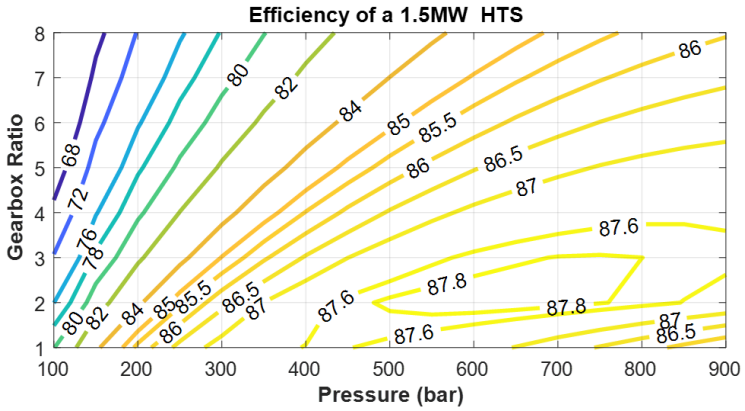

Figure 4.15. Efficiency (%) of base HTS in various nominal pressure and generator pole pairs

5. REDUCTION OF CONVERTERS SIZE IN DFIG-BASED SS-WECS

5.1 DFIG-Based Split-Shaft WECS

Various configurations of the HTS and their efficiency are investigated in the literature, including variable displacement pump and fixed displacement hydraulic motor (VDP)[123], fixed displacement pump, variable displacement motor (VDM) [20], and variable displacement pump/variable displacement hydraulic motor [23]. The mechanical structure of all these configurations allows for multiple degrees of freedom and decoupling of the turbine shaft and the generator shaft. This unique feature of the hydraulic power transmission opens a window of opportunity to control the speed of the DFIG independently. The configuration of a DFIG-based SS-WECS with the VDP HTS is shown in Figure 5.1.

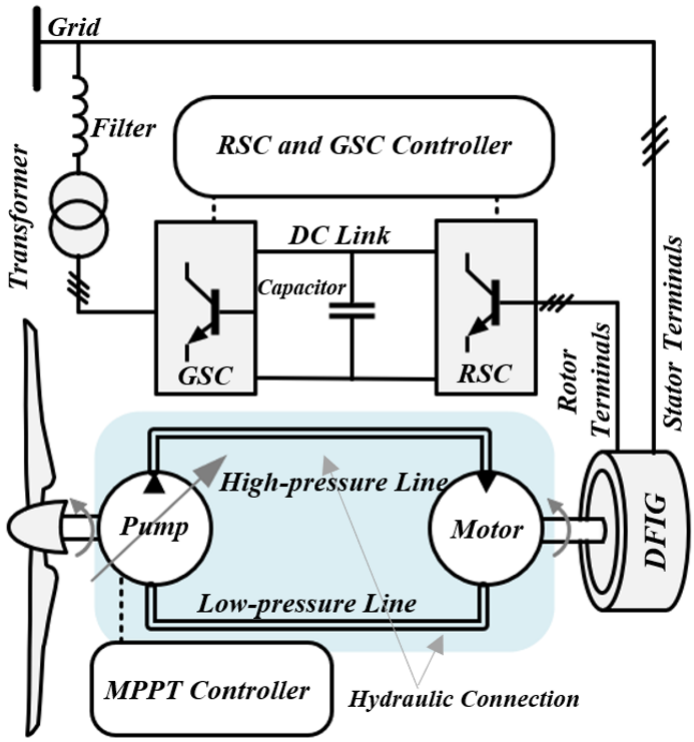

Figure 5.1. Configuration of the hydraulic wind turbine and the generator controller

This configuration has a variable displacement pump housed in the nacelle that is driven by the turbine shaft. The objective of this section is to investigate the feasibility of such

a system. The generator is controlled to have a constant speed as a conventional SG. The quadrature component of the DFIG rotor current is controlled to adjust the torque of the generator and ultimately to keep the speed of the generator at a constant reference. This control strategy is shown in Figure 5.2.

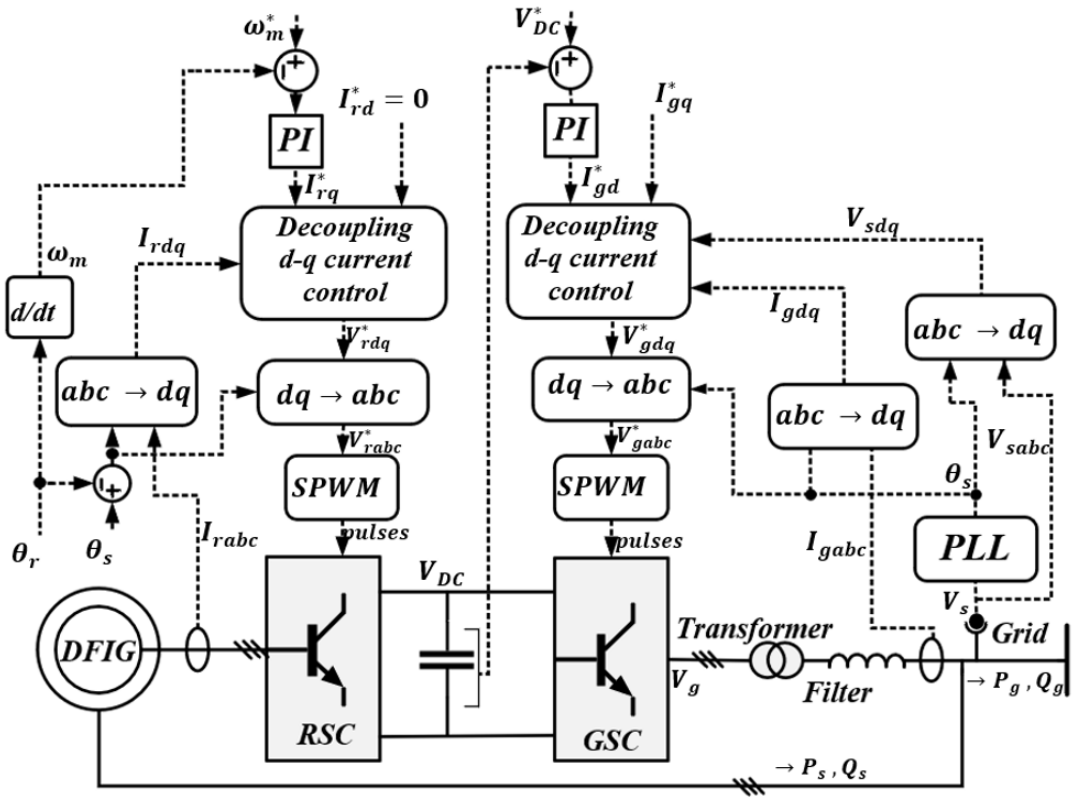

Figure 5.2. DFIG controller

The performance of the torque controller in tracking the desired reference speed is evaluated through simulation in MATLAB Simulink. Throughout this research, a 1.5-MW wind turbine is investigated as a test bench. The parameters of the WECS are listed in Table 3.1. The wind speed profile, as shown in Figure 5.3 (a), introduces a severe variation in four steps. First, the performance of the generator's controller to maintain DFIG speed due to variability of the wind speed is shown in Figure 5.3 (b). As seen in this figure, the DFIG can adequately track the reference value of speed. The wind speed variations introduce a mechanical power swing at the turbine shaft. The generator is controlled to track the desired speed reference. Power generation from the wind turbine, shown in Figure 5.3 (c),

follows the wind profile very closely. As the wind speed increases, the amount of harvested power transferred to the generator increases. The normalized power coefficient is shown in Figure 5.3 (d), indicating that MPPT is achieved. The MPPT is achieved by controlling the displacement of the pump, as stated in 3.16. The normalized displacement is shown in Figure 5.4 (a). Since the speed of the generator is kept constant, and the displacement of the hydraulic motor is also constant, the pressure is proportional to cubic of wind speed, $P \propto v_w^3$, as shown in Figure 5.4 (b). Consequently, the displacement of the pump is proportional to the inverse of the wind speed according to 3.16, $D_p \propto 1/v_w$, as demonstrated in Figure 5.4 (a). The electrical torque is shown in Figure 5.4 (c).

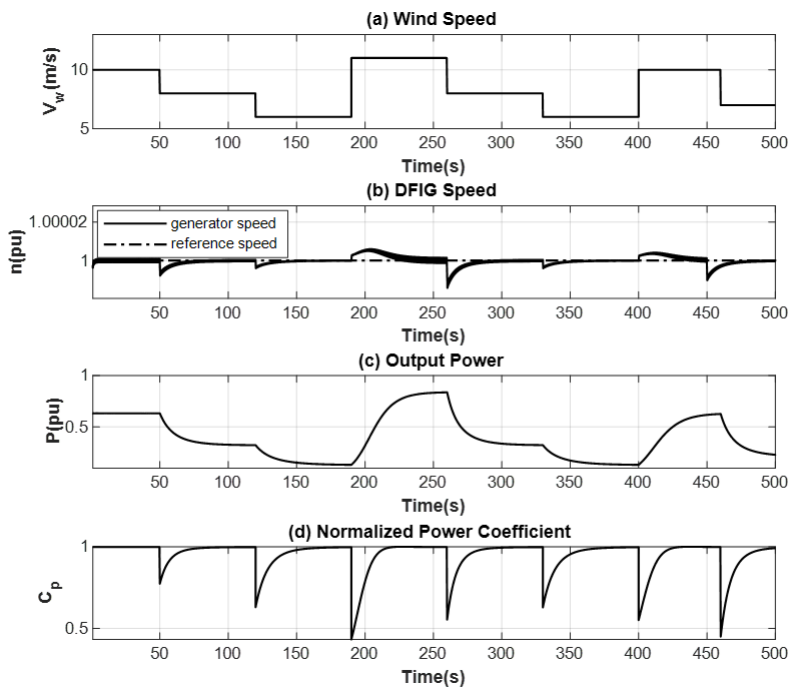

The w

Figure 5.3. Wind speed profile applied to the turbine of the hydraulic power-train

5.2 Reduction of Converters' Size

The configuration shown in Figure 5.1 is investigated to reduce the size of power converters. In the previous section, it was shown that the speed of the generator could be controlled close to synchronous speed irrespective of the wind speed. Meanwhile, the size

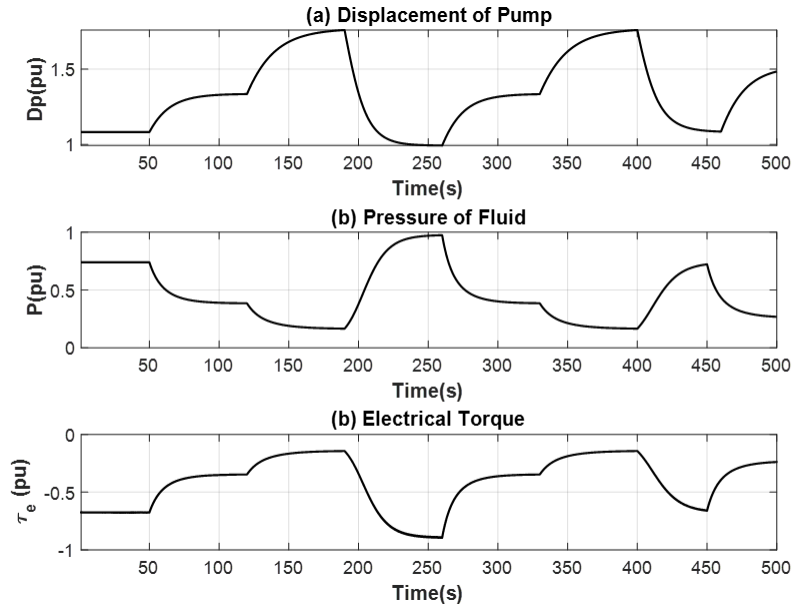

Figure 5.4. Generator speed (rpm). The figure shows that the generator speed remains at the reference speed. The steps in wind speed had no significant speed deviation from the reference.

of the converter is proportional to the maximum permissible slip of the DFIG, as shown in Figure 3.11. Therefore, the size of power converters could be decreased.

5.2.1 System Design to Decrease the Size of Power Converters

To design the power converters, some criteria like the DC-link voltage, current rating, and voltage rating of the power electronic devices are crucial. The installed power rating of the converter is obtained as 5.1. V_{con}^{max} and I_{con}^{max} are the maximum voltage and maximum current of the DFIG rotor for all operating points, respectively. However, the actual power that passes through the converter might be less than the installed power rating because the maximum voltage and current might not happen simultaneously.

$$S_{con} = 3V_{con}^{max} I_{con}^{max} \tag{5.1}$$

DC-Link Voltage Selection in Back-to-Back Power Converter

To be able to inject power into the grid, the DC-link voltage should be as follows [37], [125]:

$$V_{dc} \geq 2\sqrt{2}V_b/n_t \tag{5.2}$$

where n_t is the transformer turn ratio. The modulation index is considered as one. On the other hand, to be able to deliver power to the rotor, the DC-link voltage is determined as follows:

$$V_{dc} \geq 2\sqrt{2}V_r^{'max} \approx \frac{s_{max}}{n}2\sqrt{2}V_b \tag{5.3}$$

where $V_r^{'max}$ is the maximum rotor voltage transferred to the rotor side, and n is the stator to rotor winding turn ratio. s_max is the maximum of the absolute value of the rotor slip. From 5.2 and 5.3 the DC-link can be obtained as follows:

$$V_{dc} \geq \max\left(2\sqrt{2}\frac{V_b}{n_t}, \frac{s_{max}}{n}2\sqrt{2}V_b\right) \tag{5.4}$$

To prevent the over-designing of the RSC, it is better to choose n_t as close as to the n/s_{max}. Therefore, the DC voltage is as follows:

$$V_{dc} \geq \left(2\sqrt{2}\frac{V_b}{n_t} = \frac{s_{max}}{n}2\sqrt{2}V_b\right) \tag{5.5}$$

Voltage and Current Rating of Power Electronic Devices

The switching power electronic devices and diodes should withstand the DC-link voltage. Therefore, considering the DC-link voltage expressed in 5.5, the maximum RMS of phase voltage of both converters, RSC and GSC, is calculated as follows:

$$V_{RSC}^{'max} = V_{GSC}^{'max} = \frac{1}{n_t}V_b = \frac{s_{max}}{n}V_b \tag{5.6}$$

Using 5.1, $I_{pu-rq}^{max} = 1$ when the stator power is maximum. Since the current of the rotor is equal to the RSC current, the current rating for RSC can be obtained as follows:

$$I_{RSC}^{'max} = nI_b\sqrt{(1 + (\mathrm{i}_{m0-pu})^2} \tag{5.7}$$

where $I_{RSC-max}^{'}$ is the current of the rotor transferred to the rotor side. The GSC should inject the active power of the rotor into the grid at the steady-state condition to keep the DC-link voltage constant. The reactive power for GSC is zero. Therefore, the rating of the GSC can be achieved as follow:

$$I_{GSC}^{'max} = n_t s_{max} I_b = nI_b \tag{5.8}$$

For simplicity and modularity, the rating current of both inverters is considered as in 5.7.

Power Rating of Rotor Side and Grid Side Converters

Substituting 5.6 and 5.7 into 5.1, the power rating of the RSC and GSC can be calculated as follows:

$$S_{pu-RSC}^{max} = S_{pu-GSC}^{max} = s_{max}\sqrt{1 + \mathrm{i}_{m0-pu}^2} \tag{5.9}$$

In gearbox-driven wind turbines, the maximum voltage and maximum current happen at the same time when the wind speed is reaching the nominal or higher. Thus, this power also passes through the transformer, and the rating power of the transformer should define based on 5.9. However, in the SS-WECS, the slip is controlled at a given slip s_c, and maximum voltage and current does not happen at the same time. So then, similar to 5.9, the rating of the transformer for the SS-WECS is as follows:

$$S_{pu-Trans}^{H} = s_c\sqrt{1 + I_{m0-pu}^2} \tag{5.10}$$

5.2.2 Case Study for Evaluation of Converters Size Reduction

A 1.5-MW wind turbine, shown in Figure 3.1, is used to run simulations and compare the benefits of decoupling the shafts of the turbine and that of the generator. The performance of the conventional DFIG-based WECS and SS-WECS has been compared analytically and verified through simulations. In a gearbox-driven wind turbine, the maximum slip is chosen to be $\mp 33\%$. In the hydraulic-driven DFIG, the steady-state slip of -0.025% is chosen to avoid working in synchronous speed and unbalanced thermal stresses [126]. In addition, a 5% maximum slip is chosen to extend the system maneuverability and controllability.

First, the rating of the converters for both configurations can be achieved based on the analytical approach. These values are shown in Table 5.1. It can be seen that the DC-link voltage and the power rating for the hydraulic-driven DFIG have decreased considerably from 390V to 60V and from $386\,kVA$ to $73\,kVA$, respectively. Furthermore, the power rating of the transformer has been decreased from $386\,kVA$ to $37\,kVA$. To validate the

Table 5.1. Comparison of Two DFIGs

	Conventional DFIG	**Decoupled WECS**
$P_s(kVA)$	1127	1428
$S_{con}(kVA)$	386	73
$V_{DC}(V)$	390	60
$S_t(kVA)$	386	37
n_t	3.18	21
$V_r^{'max}(phase)$	138	21
$I_r^{'max}$	990	1255

design and analyze the performance of the proposed system, simulations of both structures are conducted.

Simulation Results for Size Reduction of Power Converters

The wind turbine is simulated for both gearbox-driven and hydraulic-driven WECS. The losses of power transmission are considered insignificant in the simulation. The wind speed shown in Figure 5.5 (a) is considered the same for both simulations, and it ranges from 5.3

to $11\,m/s$. The wind speed is considered to fluctuate drastically within the range to better express the performance of the systems. For the gearbox-driven, the optimal torque control (OTC) method is used to track MPPT [127]. 3.1.

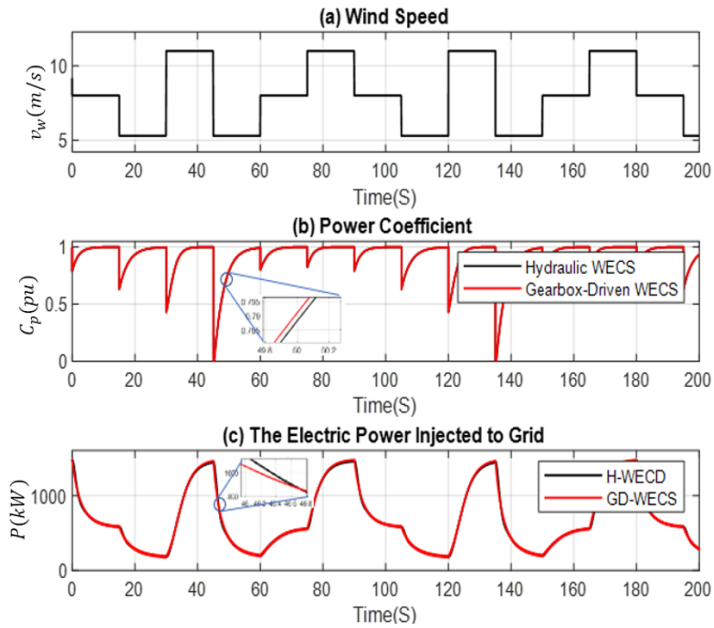

Figure 5.5. a) Wind speed (b) Normalized power coefficient (c) output power

The normalized power coefficient shown in Figure 5.5 (b) demonstrates that the MPPT achieved by controlling the pump displacement for Hydraulic WECS (H-WECS) and controlling Speed for Gearbox-driven DFIG (GD-DFIG) are the same. Consequently, the output power shown in Figure 5.5 (c) is the same as well. At wind speed of $11\,m/s$, the output power reaches its nominal, as shown in Figure 3.1.

The speed of the DFIG for Gearbox-driven WECS is controlled to follow MPPT, as shown in Figure 5.6 (a). When the wind speed reaches $11\,m/s$, the speed reaches its maximum of $1.33\omega_s$ and at $5.3\,m/s$ it reaches its minimum of $0.67\omega_s$. While for hydraulic WECS, the speed of DFIG is controlled to be at $s_c = 1.025\omega_s$. As shown in Figure 5.6 (b), the speed remains in the range of $0.95\omega_s$ to $1.05\omega_s$. The active, reactive, and apparent power of the rotor for both structures are shown in Figure 5.7. For GD-WECS, the maximum apparent power passed through the rotor, which is equal to the RSC power rating, is equal to $386\,kVA$ calculated in Table 5.1. The GSC and transformer rating power, which is equal

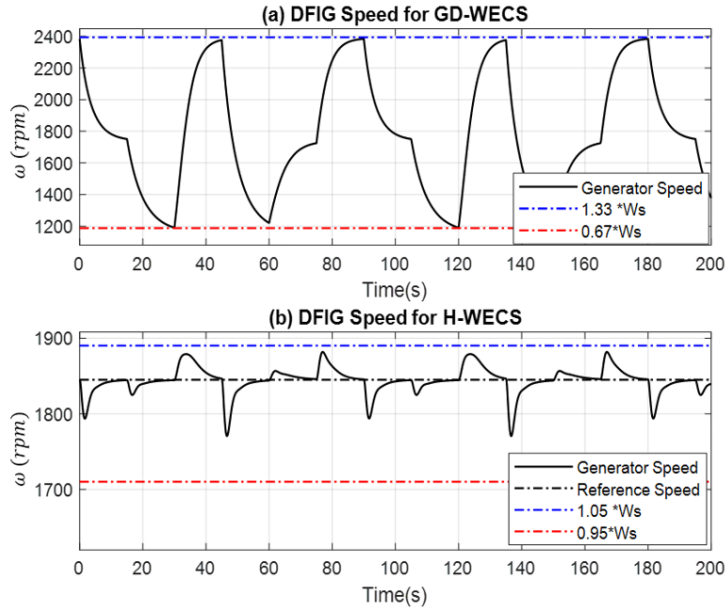

Figure 5.6. DFIG speed for (a) gearbox-driven WECS (b) hydraulic WECS

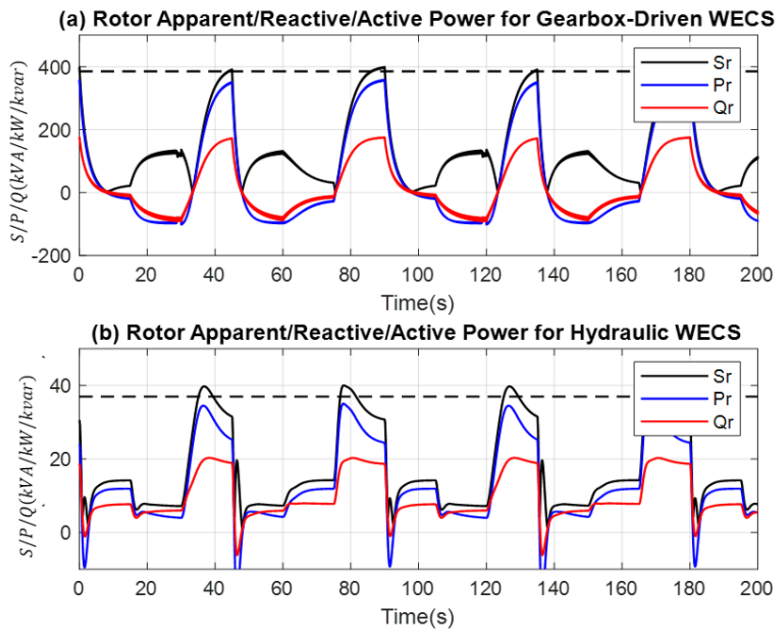

Figure 5.7. Rotor apparent power, active power, and reactive power for (a) gearbox-driven WECS (b) hydraulic WECS

to the maximum active power of the rotor, remain in the calculated range. However, rotor losses might result in small errors. On the other hand, the apparent power of the rotor for

H-WECS is less than $37\,kVA$. This is because the GSC and transformer only deliver the active power of the rotor. The rotor voltages are generated with PWM switching. However, the equation obtained in the previous section is the main component of the output voltages of the converters. Therefore, the main components of the rotor voltages are filtered out and shown in Figure 5.8. According to Table 5.1, the maximum RMS value of the main component of the rotor voltage is $V_r^{'} = 21\,volts$ and $V_r^{'} = 138\,volts$ for H-WECS and GD-WECS, respectively. Therefore, the peak value of the rotor voltage should be smaller than $21\sqrt{2}$ and $138\sqrt{2}$ as shown in Figure 5.8. The rotor voltage, as mentioned in 3.38, is proportional to slip.

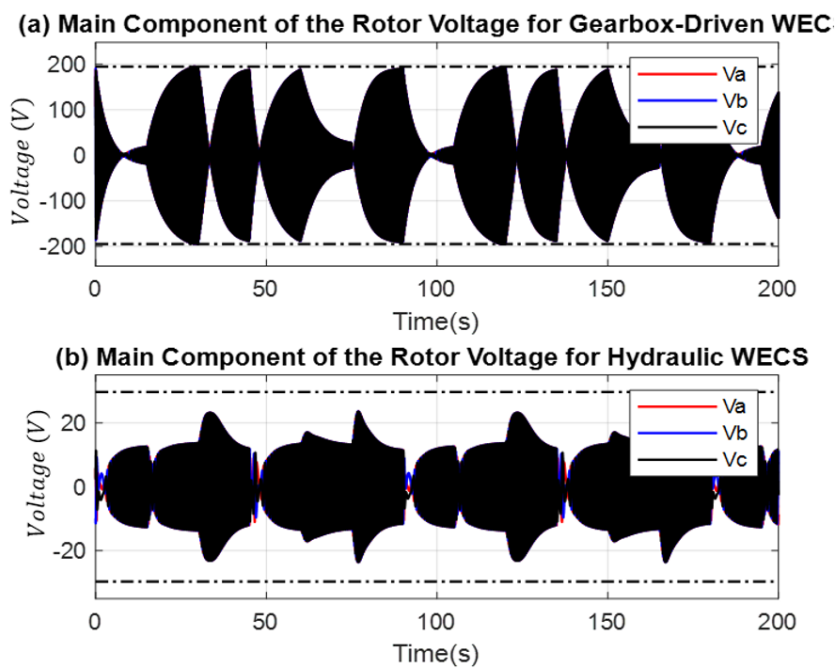

Figure 5.8. DFIG rotor voltage for (a) gearbox-driven WECS (b) hydraulic WECS

The currents of the rotor for both drivetrains are shown in Figure 5.9. Both structures are simulated for the same mechanical power; the amplitude of the rotor current for hydraulic DFIG is higher than that of gearbox-driven DFIG. As mentioned in Table 5.1 the $I_r^{'} = 990(A)$ and $I_r^{'} = 990(A)$ for H-WECS and GD-WECS, respectively. Therefore, the peak value of the rotor current should be smaller than $1255\sqrt{2}$ and $990\sqrt{2}$.

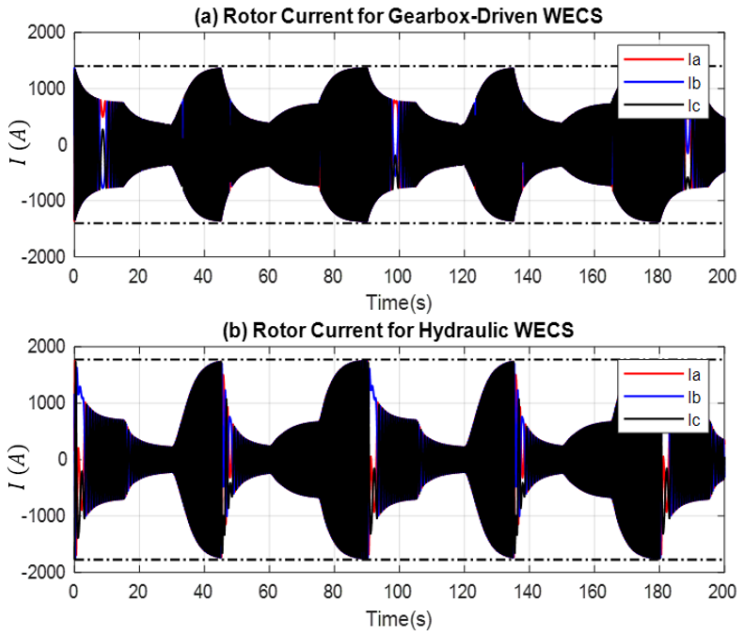

Figure 5.9. DFIG rotor current for (a) gearbox-driven WECS (b) hydraulic WECS

5.3 Summary

In this chapter, a DFIG-based SS-WECS employed an HTS with a VPD system instead of the gearbox was simulated to validate the feasibility of such a configuration. The simulation results showed that the HTS system allowed for decoupling the speed of the generator and wind turbine, consequently, resulting in an independent control over the speed of the generator and MPPT. Then, this degree of freedom was used to reduce the size of both RSC and GSC converters, the size of the transformer, and the DC-link voltage. Finally, the functionality of the proposed structures was investigated through analytical deduction and MATLAB simulation. The reduction of the size of power converters and DC-link voltage leads to a more reliable, low-cost SS-WECS. Furthermore, lower DC-link voltage allowed the use of less expensive capacitors and decreased the voltage stresses on power electronic devices, resulting in higher reliability and efficiency.

6. INTEGRATION OF FLYWHEEL ENERGY STORAGE WITH SS-WECS

Flywheel energy storage system (FESS) stores the energy in a rotating mass. The kinetic energy of the flywheel can increase or decrease in the charge and discharge process, respectively. Generally, the power converter of the energy storage sends or receives the energy to/from the motor/generator, converting the electrical to mechanical energy and vice versa. To directly connect a FESS to the generator shaft, an HTS can be utilized. In this configuration, the speed of the generator shaft can be controlled in a wide range independent of the turbine's rotational speed. This range of speed and its independence from the wind turbine provides an extra degree of freedom in the controller that can be used to store energy directly through the rotor of the DFIG. Furthermore, in this arrangement, as shown in Figure 6.1, the generator and converters are located at the ground level. Consequently, connecting the flywheel to the generator does not increase the weight of the nacelle. The power generated from the wind turbine can be stored in the flywheel and released on demand to control the power profile injected into the grid. In this system, the energy stored in rotating parts can be expressed as follow:

$$E = \frac{1}{2} J_m \omega_m^2 \tag{6.1}$$

where J_m is the sum of DFIG rotor inertia, hydraulic motor inertia, and flywheel inertia. The amount of energy stored in a flywheel is proportional to the square of its angular velocity. Therefore, to increase the capacity of the proposed configuration, the flywheel can be connected to the DFIG shaft by a speed step-up gearbox. However, herein, the flywheel is connected directly to the shaft of the generator for the sake of simplicity. The energy storage capacity of FESS is given by:

$$\Delta E = E_{max} - E_{min} = \frac{1}{2} J_m \left(\omega_{max}^2 - \omega_{min}^2 \right) \tag{6.2}$$

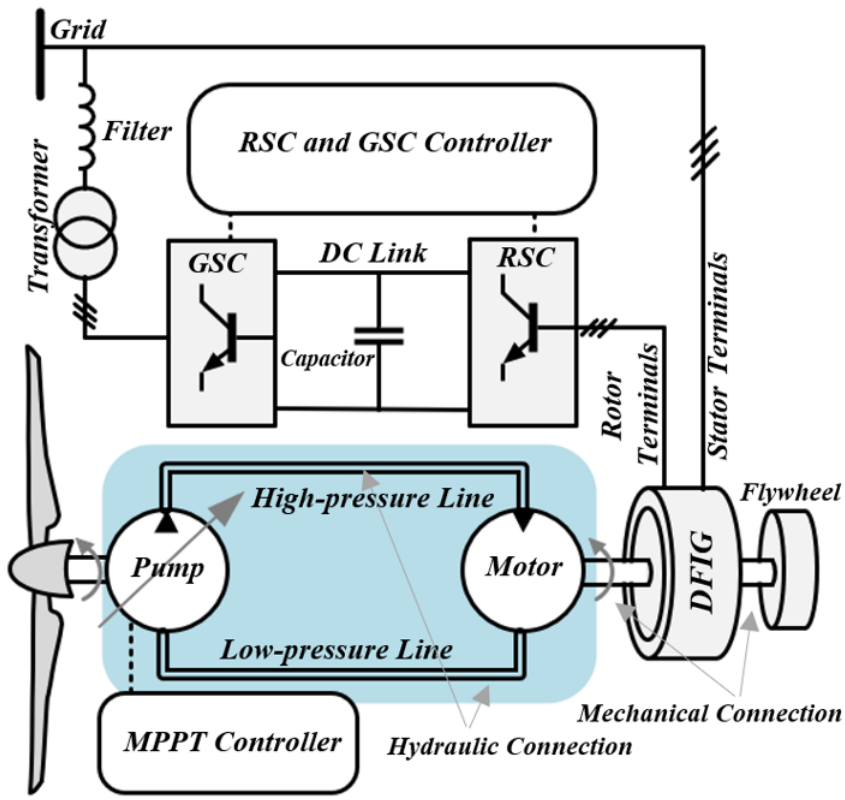

Figure 6.1. Split-shaft hydraulic drive-trains decouple the shaft of the turbine from the shaft of the generator. It makes the direct integration of the FESS to the generator

.

where E_{max} and E_{min} are the maximum and minimum of stored energy at the maximum and minimum speed of the generator. The maximum and minimum speed can be obtained as:

$$\omega_{max} = 2\left(1 - s_{max}\right)\frac{\omega_{max}}{p} \tag{6.3}$$

$$\omega_{min} = 2\left(1 - s_{min}\right)\frac{\omega_{min}}{p} \tag{6.4}$$

where s_{max} and s_{min} are the generator slip percentage at maximum and minimum speed, p is the number of poles in the generators, and ω_s is the synchronous speed. In an optimal converter design, the slip range is chosen to be symmetric [37]. Hence:

$$s_{min} = -s_{max} \tag{6.5}$$

Using 6.1 and substituting 6.3 and 6.4 into 6.2, the energy storage capacity of this system is obtained as follows:

$$\Delta E = \frac{8}{p^2} J_m \omega_s^2 s_{min} \tag{6.6}$$

As 6.6 shows, the energy storage capacity depends on the maximum slip and the equivalent inertia of the storage system. Similar to a conventional DFIG, the maximum slip of the DFIG is considered to be $\mp 30\%$ in this section. This configuration does not need an extra power electronics converter and even does not need its own electric motor/generator. A control strategy is developed to improve the quality of the generated power.

6.1 Control Strategy

The control strategy of the whole system consists of two parts. They are first, controlling the DFIG to charge and discharge the storage on demand and inject smoothed electrical power into the power grid. Second, the pump displacement control is employed to maintain the MPPT. In the DFIG control strategy shown in Figure 6.2, a supervisory controller defines the current reference for the generator such that the output power fluctuations are attenuated, and the speed of the generator remains within the permissible range. This current reference creates the desired outcome power of the generator. In addition, the FESS controller is intrinsically accomplished through generator control.

6.1.1 Generator Control

In the proposed configuration, the GSC is conventionally controlled to maintain the DC-link voltage by a vector control approach shown in Figure 6.2. Considering the fast dynamic of the GSC, this converter can rapidly exchange the power of the rotor windings with the grid through the rotor-side converter and DC-link. As a result, the total power injected into the grid from the generator is the sum of the rotor and the stator power as follows:

$$P_{\mathrm{e}} = P_s + P_r = \omega_m \tau_{\mathrm{e}} \tag{6.7}$$

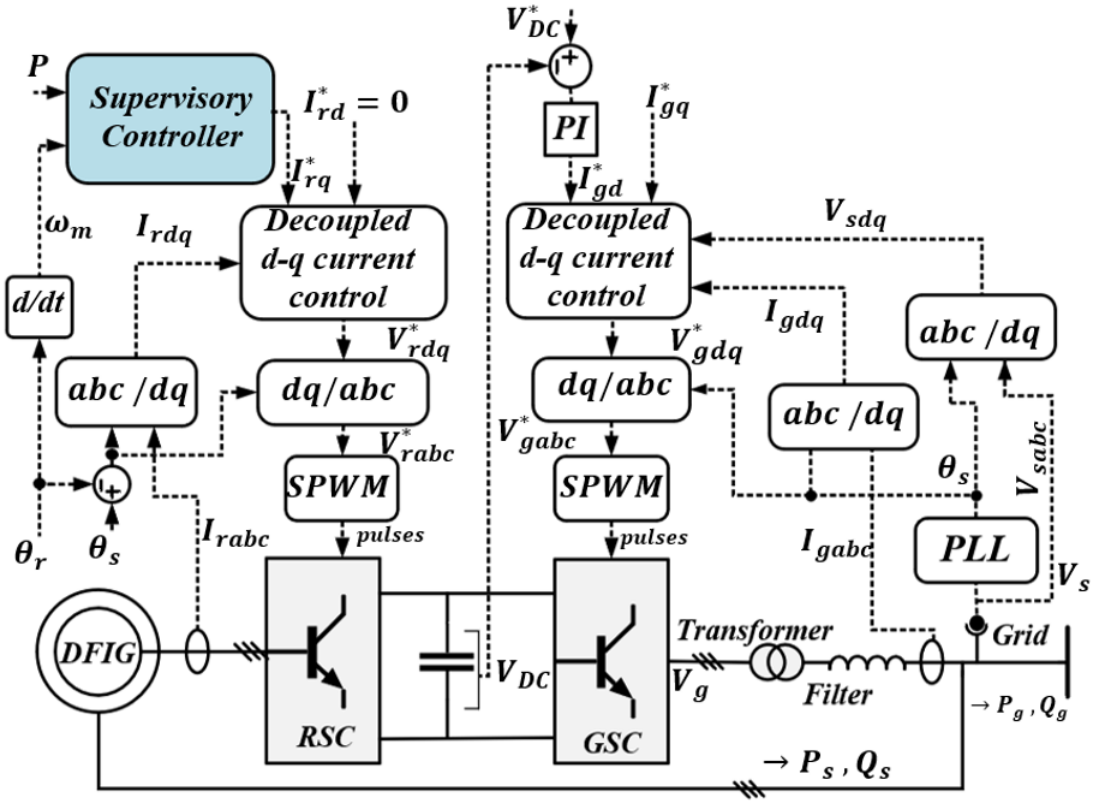

Figure 6.2. The vector control diagram of the proposed configuration.

here, P_{e} and τ_{e} are the electrical power injected into the grid and electrical torque, respectively. The electrical torque, τ_{e}, can be obtained in the dq frame. Accordingly, by controlling the quadrature component of the rotor current I_{rq}, the electrical torque and P_{e} can be controlled as follows:

$$\tau_{\mathrm{e}} = -\frac{3}{4} p L_0 I_{m0} I_{rq} \tag{6.8}$$

where $L_0 = L_m^2/L_s$, and I_{m0} is the magnetizing current of the generator. The electrical power is controlled by adjusting the reference, I^*_{rq}, through the RSC. The GSC is controlled to maintain the voltage of the DC-link constant, as shown in Figure 6.2.

6.1.2 Supervisory Controller

The supervisory controller shown in Figure 6.2 is responsible for managing the amount of energy exchanged with the storage system by determining the desired power profile and

the reference current. Herein, two supervisory controllers are employed. The first is based on a low-pass filter to define the desired output power directly. The second strategy is based on controlling the kinetic energy of the FESS connected to the DFIG.

Direct Power-Averaging Technique

A general supervisory control structure for FESSs [46]–[49] based on average power measurement is shown in Figure 6.3 (b). In conventional applications, the FESS is a unit independent from the WECS, as shown in Figure 6.3 (a); consequently, the power provided by the FESS, P_{ref}, should be the balance of the wind turbine power, P_w, and the regulated power, P_{reg}. In other words, to inject the desired output power (P_{reg}), the FESS should inject/absorb the high-frequency variations of wind turbine power. However, in the proposed configuration shown in Figure 6.1, the FESS is incorporated into the WECS that becomes one compound unit, and the output power of the SS-WECS can be regulated directly, as

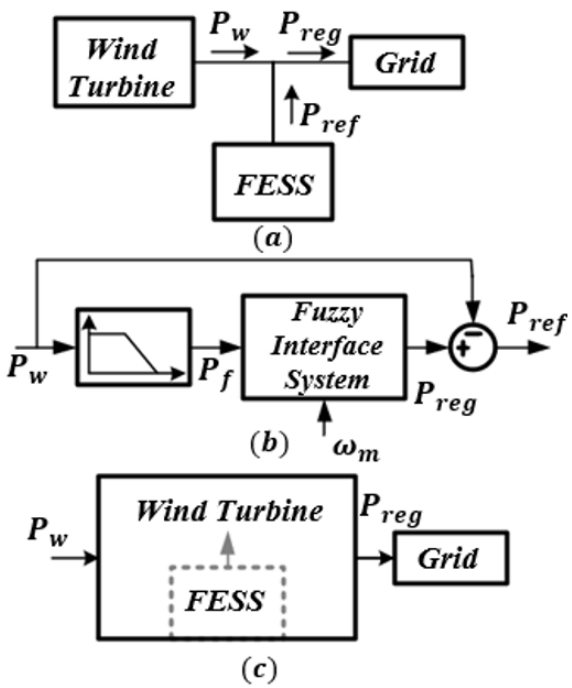

Figure 6.3. (a) The schematic of power flow in conventional FESSs (b) supervisory controller based on the power-averaging technique in conventional FESSs (c) the schematic power flow in the proposed HTS WECS.

shown in Figure 6.3 (c). Therefore, a supervisory controller can be adapted by utilizing direct average power calculations illustrated in Figure 6.4. The fuzzy logic regulator prevents the saturation of the FESS, which limits the extent of power profile controls [47]. The mechanical power of the hydraulic motor, which is the power reaching the hydraulic motor (P_{hm}), is a function of its angular velocity, the displacement, and the pressure of the system, which is obtained as follows:

$$P_{hm} = PD_m\omega_m - P_{loss-m} \tag{6.9}$$

The mechanical loss of the hydraulic motor is denoted by P_{loss-m}. The supervisory controller must compute the value of the P_{reg} to maintain the flywheel speed within its upper and lower speed limits. As Figure 6.4 illustrates, a Fuzzy Interface System (FIS) is utilized to define the desired reference power, P_{reg}. Inputs to the FIS are the filtered value of P_{hm}, which is denoted as P_f, and the speed of the generator ω_m. Then, the reference current, I^*_{rq}, can be calculated using 6.7 and 6.8. In the HTS, the desired output power can be obtained without knowing the wind speed based on 6.9.

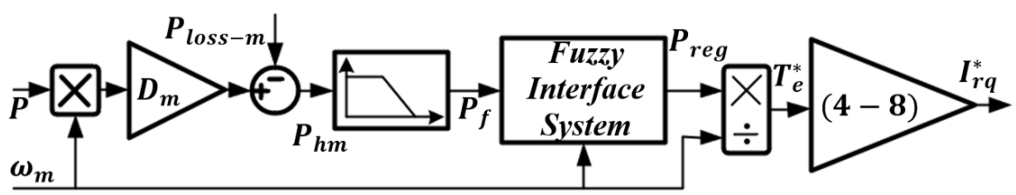

Figure 6.4. Supervisory controller based on the direct power-averaging technique

Flywheel Kinetic-Energy Management

A supervisory control strategy could be based on the energy of the rotating inertia [43], [44]. In Figure 6.5, ΔP, the difference between the instantaneous mechanical power of the hydraulic motor and the regulated output power is the amount of power that should be

stored into or recovered from the flywheel's kinetic energy. The amount of stored energy in a flywheel, to mitigate the output power, is as follows:

$$\Delta E^* = \int \Delta P dt \tag{6.10}$$

ΔE^* contains the high-frequency variation of wind power. Therefore, the reference energy for the FESS is obtained as:

$$E^* = \Delta E^* + \frac{1}{2} J_m \omega_0^2 \tag{6.11}$$

where ω_0 is the initial angular velocity of the FESS. The speed reference for the flywheel as well as the generator speed is obtained as follows:

$$\omega_m^* = \sqrt{\frac{2E^*}{J_m}} \tag{6.12}$$

By having the reference speed ω_m^*, I_{rq}^* can be achieved through a PI controller, as shown in Figure 6.5.

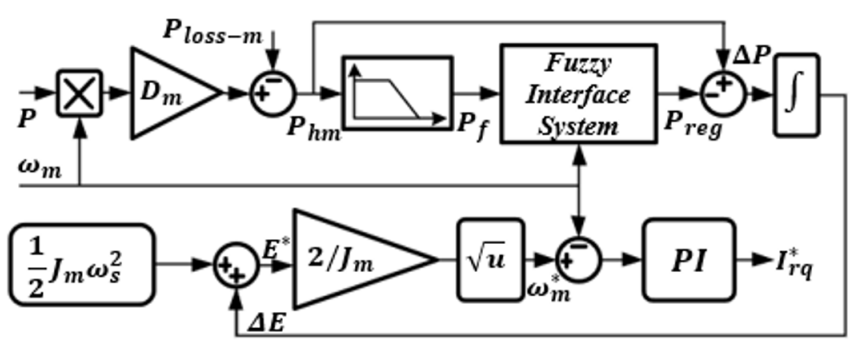

Figure 6.5. Supervisory controller based on flywheel kinetic-energy Management

Fuzzy Interface System

A fuzzy logic controller needs to prevent storage from saturation. The application of an averaging low-pass filter may lead to saturation in a variant average wind speed [47]. Furthermore, the power profile enhancement is extremely dependent on the time constant of the filter. In other words, at a larger time constant or lower bandwidth, the output power

shows less variations; however, the storage saturation probability is very high. Conversely, a high-bandwidth low-pass filter can prevent saturation but results in a higher power fluctuation. Fuzzy logic regulators can improve the storage availability by allowing slightly more variations than an output power fluctuation of a low-pass filter but provides better performance in all wind speed profiles.

The fuzzy regulator, employed in Figure 6.4 and Figure 6.5, has two inputs from the angular velocity and averaged power,P_f. Therefore, both inputs should be mapped to the output via membership functions. Each input can be defined by five fuzzy sets, and the output is defined by seven fuzzy sets, as shown in Figure 6.6. Fuzzy rules are shown in Table 6.1. The surface created by the FIS is shown in Figure 6.7.

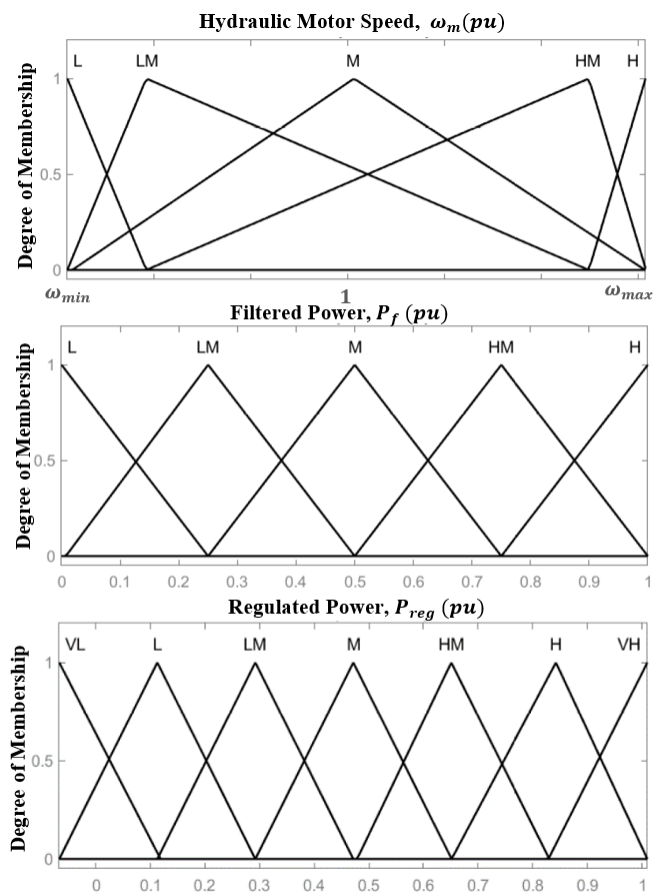

Figure 6.6. Fuzzy sets the membership function for (a) speed input (b) filtered power input (c) regulated power.

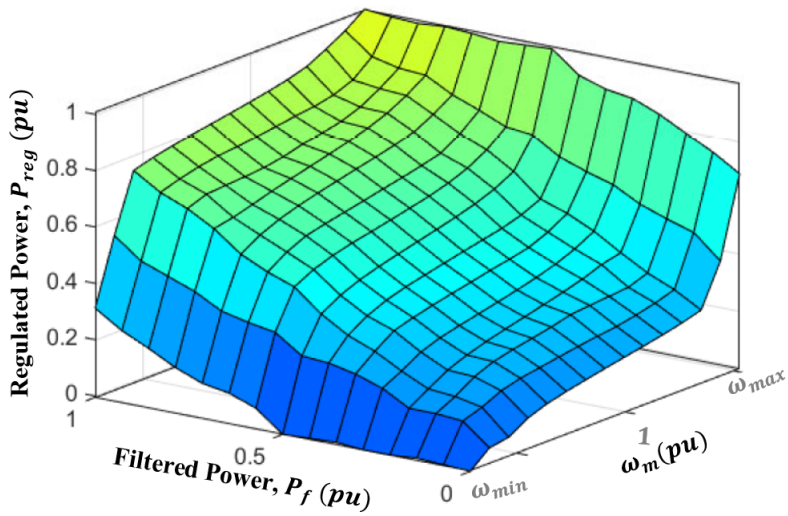

Figure 6.7. Regulated power P_reg obtained by fuzzy logic regulator

Table 6.1. Fuzzy rules

ω_m / P_f	**L**	**LM**	**M**	**HM**	**H**
L	VL	VL	VL	L	LM
LM	VL	L	LM	M	HM
M	L	LM	M	HM	H
HM	LM	M	HM	H	VH
H	M	HM	H	VH	VH

6.1.3 MPPT Control

There are several algorithms to achieve MPPT in conventional gearbox-driven DFIG-based wind turbines, including TSR control and optimal torque control (OTC) [127]. The TSR method is fast and efficient, but it results in a non-minimum phase control method [128]. In addition, the main drawback of TSR is that the value of wind speed is required. On the other hand, OTC does not need wind speeds but is slower since the MPPT is achieved using the steady-state equations [129], [130]. The MPPT control of the SS-WECS can be achieved by controlling the pump displacement. Herein, two MPPT control methods for the hydraulic WECS are studied.

Optimal Pump Displacement Control (OPDC)

A common approach to follow MPPT in the HTS is controlling the torque of the hydraulic pump by using steady-state equations as stated in 3.16. The performance of the OPDC is similar to that of the OTC in conventional WECSs and shows a slow response. The diagram of the OPDC is shown in Figure 6.8. The inertia of the wind turbine can be adjusted virtually to increase the speed of reach of the MPPT.

Virtual Inertia Adjustment

Using the steady-state equations results in a slow response in the reach of the MPPT. One way to track the maximum power point and increase the captured power from the wind is to decrease the wind turbine's inertia virtually [131]. This can be accomplished by modifying the optimum pump displacement with a virtual torque term such as $J_v\omega_p^{'}$, as shown in the blue shaded area in Figure 6.8. Therefore, 3.11 can be re-written as follows:

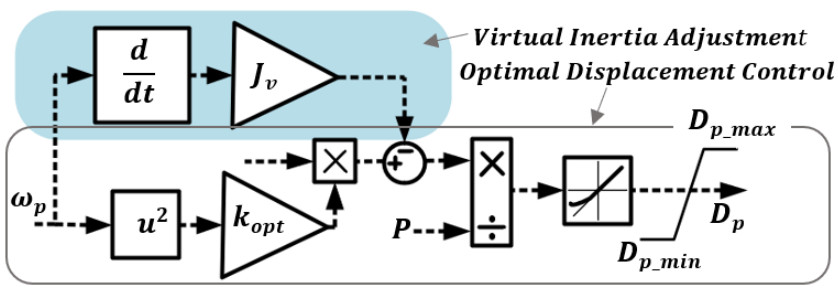

Figure 6.8. Displacement control to achieve MPPT

$$D_{op} = \frac{k_{opt}\omega_p^2 - J_v\omega_p^{'}}{P_f} \tag{6.13}$$

where J_v is a portion of the wind turbine-pump inertia. In [131], results showed that the use of virtual inertia to speed up the MPPT process might potentially increase the output power fluctuation in a conventional WECS. However, in the proposed SS-WECS, there is energy storage integrated into the system, and the power fluctuations added to the system due to

the virtual inertia can be eliminated. To analyze the effect of virtual inertia, a small-signal analysis has been done.

6.1.4 Small Signal Model of Integrated Flywheel and Split-Shaft WECS

In this section, a closed-loop small-signal model of the system is evaluated. Considering negligible mechanical losses, multiplying the ω_p and ω_m on both sides of 3.6 and 3.7 respectively and linearizing them at operating points results in 6.14-6.16:

$$J_r\omega_p\frac{\mathrm{d}\Delta\omega_p}{\mathrm{d}t} = \Delta P_a - \Delta P_{hp} \tag{6.14}$$

$$J_m\omega_m\frac{\mathrm{d}\Delta\omega_m}{\mathrm{d}t} = \Delta P_{hm} - \Delta P_{\mathrm{e}} \tag{6.15}$$

$$\frac{\mathrm{d}\Delta P_f}{\mathrm{d}t} = \frac{\beta_f}{V_f}(\Delta Q_p - \Delta Q_m) \tag{6.16}$$

where small disturbances are applied to aerodynamic power (ΔP_a), pump hydraulic power (ΔP_{hp}), motor hydraulic power (ΔP_{hm}), and electrical power (ΔP_{e}). The components of the ΔP_a are linearized around the operating point (OP) as follows:

$$\Delta P_a = \frac{\partial P_a}{\partial v_w}\mid_{op}\Delta v_w + \frac{\partial P_a}{\partial \omega_p}\mid_{op}\Delta\omega_p + \frac{\partial P_a}{\partial \beta}\mid_{op}\Delta\beta \tag{6.17}$$

where v_w is the wind speed. In the MPPT region, the pitch angle variation is zero, $\Delta\beta = 0$. The power equation of a wind turbine is presented as follows:

$$P_a = 0.5\rho_{air}\pi R^2 C_p(\lambda,\beta)v_w^3 = k_a C_p(\lambda,\beta)v_w^3 \tag{6.18}$$

where $C_p(\lambda,\beta)$ is the power coefficient of the wind turbine, which is a function of tip speed ratio (λ) and pitch angle (β), and $k_a = 0.5\rho_{air}\pi R^2$. By taking the partial derivative of the aerodynamic power, P_a, the components of ΔP_a are obtained as follows:

$$\begin{cases} \frac{\partial P_a}{\partial v_w}\mid_{op} = 3k_a C_p\mid_{op} v_{w0}^2 - R\omega_{p0}k_a v_{w0}\frac{\partial C_p}{\partial \lambda}\mid_{op} \\ \frac{\partial P_a}{\partial \omega_p}\mid_{op} = Rk_a v_{w0}^2\frac{\partial C_p}{\partial \lambda}\mid_{op} \end{cases} \tag{6.19}$$

The subscript 0 that is added to variables indicates the value of the variables at the operating point. Small signal variation at the point of MPPT can be recognized as $\frac{\partial C_p}{\partial \lambda} \mid op$ and $C_p \mid_{op} = C_{max}$. Then, ΔP_a can be re-written as follows:

$$\Delta P_a = 3k_a C_{max} v_{w0}^2 \Delta v_w \tag{6.20}$$

From the displacement control signal 6.13 and using the torque of a hydraulic pump as $\tau_{hp} = D_p P_f$, the term ΔP_{hp} is obtained as follows:

$$\Delta P_{hp} = 3k_{opt}\omega_{p0}^2 \Delta\omega_p - J_v \omega_{p0} \frac{\mathrm{d}\Delta\omega_p}{\mathrm{d}t} \tag{6.21}$$

$$D_p \Delta P + P \Delta D_p = 2k_{opt}\omega_{p0}\Delta\omega_p - J_v \frac{\mathrm{d}\Delta\omega_p}{\mathrm{d}t} \tag{6.22}$$

At the hydraulic motor side, the displacement of the hydraulic motor is fixed. Therefore, the small-signal model of 6.9 results in:

$$\Delta P_{hm} = D_m \omega_m \Delta P + P D_m \Delta\omega_m \tag{6.23}$$

The electrical power generated from the generator receives a filtered version of the power that reaches the hydraulic motor. To be able to linearize the model without loss of generality, the fuzzy regulator is neglected, and the low-pass filter is considered as a first-order low pass filter with a time constant τ_f. Hence:

$$\tau_f \frac{\mathrm{d}\Delta P_\mathrm{e}}{\mathrm{d}t} + \Delta P_\mathrm{e} = \Delta P_{hm} \tag{6.24}$$

The linear small-signal model of the hydraulic flow through the pump and motor from 3.5 and 3.13 are obtained as follows:

$$\Delta Q_p = \omega_{p0}\Delta D_p + D_{p0}\Delta\omega_p \tag{6.25}$$

$$\Delta Q_m = D_m \Delta\omega_m \tag{6.26}$$

Using 6.20-6.26, the dependency of small-signal output power model $\Delta P_{\mathrm{e}}/\Delta v_w$ is calculated in 6.27. Now that we have achieved the transfer function, we need to analyze the impact of wind speed on the electrical power at various levels of the flywheel and virtual inertia.

$$\frac{\Delta P_{\mathrm{e}}}{\Delta v_w} = \frac{3k_a C_{max} v_{w0}^2 \beta_f D_m J_m \omega_m^2 (2K_{opt}\omega_p^2 + D_p P_f - \omega_p J_v s)}{\omega_p (3K_{opt}\omega_p + (J_r - J_v)s)(\beta_f \tau_f D_m P_f (\omega_m D_m - \omega_p D_p) - \tau_f V_f D_m P_f^2 s + J_m V_f \omega_m P_f (\tau_f s^2 + s) + \beta_f D_p J_m \omega_m \omega_p (1 + \tau_f s))} \tag{6.27}$$

6.2 Simulation Results and Discussion

A 1.5 MW wind turbine with an HTS and flywheel attached to the generator shaft was simulated in MATLAB Simulink. The wind speed varied from 5 to 11 m/s, as shown in Figure 6.9. The maximum slip of the DFIG is considered to be $\mp 30\%$, and consequently, the size of the converters is 30% of the rated power. The generator has two pole-pairs, and the inertia of the flywheel is considered to be 1100 Kgm^2. The rest of the system data is given in Table 3.1.

6.2.1 Small Signal Analysis of Integrated Flywheel and SS-WECS

The bode diagram of the normalized $\Delta P_{\mathrm{e}}/\Delta v_w$ is shown in Figure 6.10, in which four cases at different filter time constants τ_f and virtual inertia J_v are analyzed respectively. Two extreme cases of $\tau_f = 0\,s$ and $\tau_f = 20\,s$ are compared with extreme consideration of virtual inertia at $J_v = 0$ and $J_v \neq 0$.

- $\tau_f = 0\,s$ means no flywheel and $\tau_f = 20\,s$ means a large flywheel.
- $J_v = 0$ means no virtual inertia, and $J_v \neq 0$ means a virtual percentage is reduced from the system inertia.

The Bode diagram of the transfer function 6.27, shown in Figure 6.10 at the combination of extreme cases, shows that the system without a flywheel is impacted by virtual inertia adjustment. The bandwidth of the system when $\tau_f = 20\,s$ and $\tau_f = 0\,s$ are about $\frac{1}{2(H_t+\tau_f)}$ and $1/(2H_t)$, respectively. H_t is the inertia constant of the wind turbine.

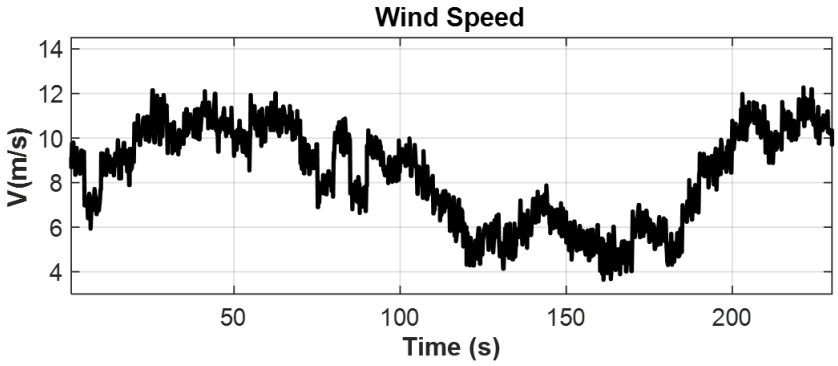

Figure 6.9. Wind speed profile

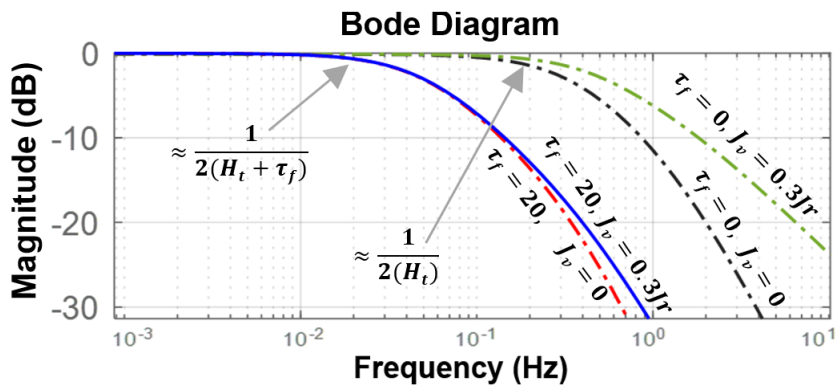

Figure 6.10. Bode diagram for the system

According to this figure, the bandwidth increase is an indication of accepting more high-frequency fluctuations. As a result, the power profile exhibits more variation. However, the output power is not affected by the virtual inertia when a flywheel is employed. The bandwidth with and without virtual inertia is the same. This indicates that the virtual inertia does not decrease the power profile smoothness while speeding up the reach of MPPT. To evaluate the performance of the proposed configurations, two indicators of maximum power production (P_{max}) and the output power leveling (P_{level}) are analyzed [43]. In the SS-WECS,

P_{max} is defined as the integral of the mechanical power that reaches the hydraulic motor. To evaluate the power profile smoothness, the P_{level} is defined as follows:

$$P_{max} = \int P_{hm} dt \tag{6.28}$$

$$P_{level} = \int \left| \frac{\mathrm{d}P_{\mathrm{e}}}{\mathrm{d}t} \right| \mathrm{d}t \tag{6.29}$$

According to these equations, it can be observed that the lower the P_{level} , the less the output power fluctuations.

6.2.2 Evaluation of Supervisory Controllers

In this section, three cases with the same MPPT control strategy are simulated to evaluate the performance of the supervisory controllers. These cases are as follow:

- **Case 1:** when the supervisory controller in Figure 6.4 is employed (direct power-averaging technique) with the OPDC shown in Figure 6.8 ($J_v = 0$).
- **Case 2:** when the supervisory controller in Figure 6.5 is employed (flywheel kinetic-energy Management) with the OPDC shown in Figure 6.8 ($J_v = 0$).
- **w/o FIS:** when the supervisory controller in Figure 6.5 is employed with the OPDC shown in Figure 6.8 ($J_v = 0$) while the FIS is deleted.

Figure 6.11 (a) demonstrates the normalized power coefficient for all cases. This figure indicates that all cases are capable of tracking the MPPT. Figure 6.11 (b) shows the electric power generated from the system. Simulation results illustrate that both supervisory controllers, cases 1 and 2, have a similar performance and can mitigate the power profile and prevent the saturation of the storage. However, the control system without the FIS cannot avoid storage saturation. When the storage becomes saturated, the speed of the generator hits a lower limit, and the power injected into the grid drops to the aerodynamic power of the wind turbine (Figure 6.11 (b)) to prevent a further decrease in generator speed that results in losing the generator control. It stays in this form until the wind speed picks up and more energy is injected into the system (Figure 6.11 (c)).

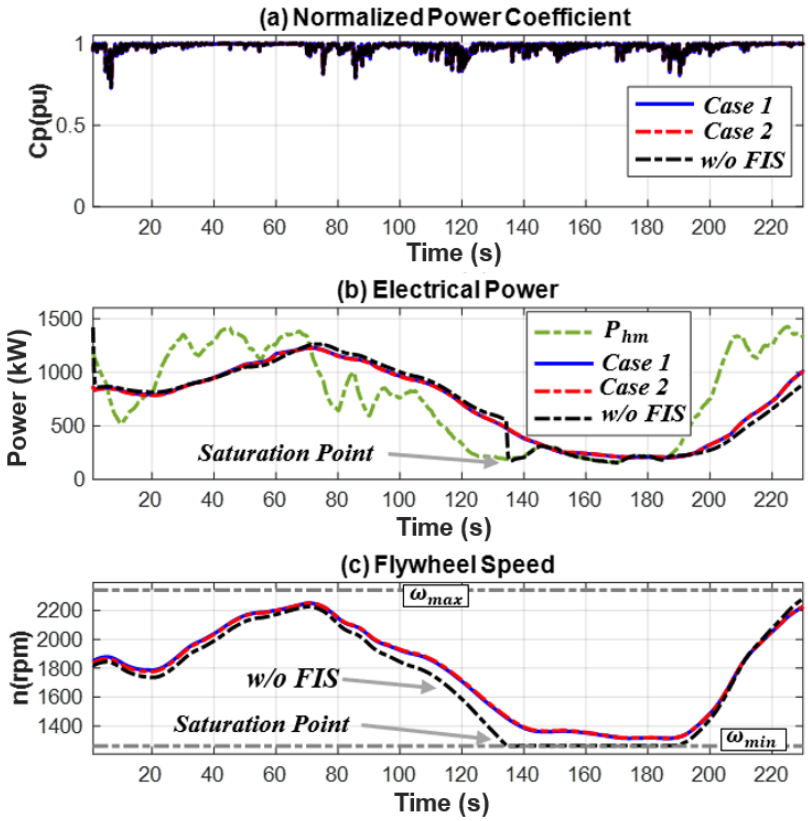

Figure 6.11. (a) Normalized power coefficient (b) output power (c) flywheel speed for case 1, Case 2, and w/o FIS.

Table 6.2. Power Leveling and Maximum Energy Function for Case 1, Case 2, and w/o FIS at the End of the Period

	Case 1	**Case 2**	**w/o FIS**
$P_{max}(J)$	1.7268×10^8	1.7268×10^8	1.7268×10^8
P_{Level}	3.7935×10^6	3.7995×10^6	4.5800×10^6

When the storage becomes saturated, the controller cannot utilize the storage, and this results in an increase in power swings (Figure 6.11 (b)). In this period, the output power of the system matches the aerodynamic power of the wind turbine with all the fluctuations. The values of P_{max}, and P_{Level} are tabulated in Table 6.2 for three cases. It can be seen that the amount of energy captured at the end of the period is the same for all cases. However, without the FIS, the power fluctuations of the system are much higher than two other cases.

6.2.3 Evolution of Virtual Inertia and Flywheel Effects

The effect of virtual inertia is shown on the J_v value in two cases of $(0, 0.3J_r)$ combined with the system without FESS, i.e., $(\tau_f = 0\,s)$ and the system with FESS, i.e., $(\tau_f = 20\,s)$. The results for these four cases were examined with the supervisory controller of case 2 because the performance of both supervisory controllers was nearly similar. The normalized power coefficient of four cases is shown in Figure 6.12. These results show that decreasing the inertia of the wind turbine virtually speeds up the dynamic of the wind turbine. On the other hand, the flywheel (τ_f) does not affect the dynamic of the wind turbine. Analysis of Figure 6.13 reveals a detailed analysis of the power fluctuations and the output power at various inertia levels.

Figure 6.13 (a) show the output power fluctuations. It can be observed that when $\tau_f = 0$ (No FESS), there is a significantly more fluctuation of the wind turbine power when the virtual inertia adjustment method $(J_v = 0.3J_r)$ is employed than when OPDC is utilized $(J_v = 0)$. However, for the system with $\tau_f = 20\,s$ (with FESS), the output powers are similar, and imposing virtual inertia has negligible effects on the fluctuation of the output power (Figure 6.13 (c)). This is because of the amount of the added fluctuation of aerodynamic power in case of having virtual inertia turned into more flywheel speed oscillation, as shown in Figure 6.13 (b). In other words, the flywheel captured those fluctuations and prevented them from being injected into the grid. This confirms the results of the small-signal analysis demonstrated in Figure 6.10. It shows that imposing virtual inertia did not affect the output power fluctuations when a significant FESS is utilized. When $\tau_f = 0\,s$, the ΔP in the

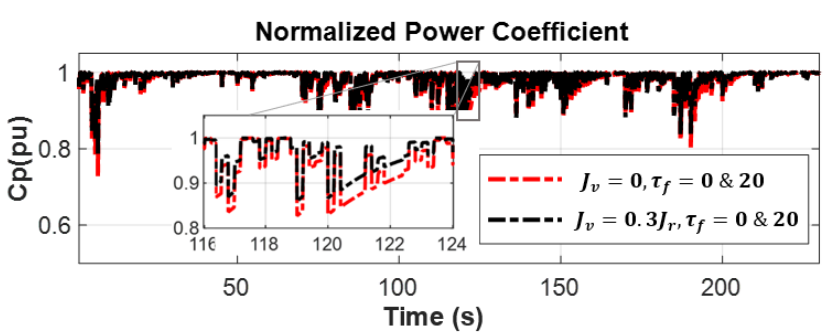

Figure 6.12. Normalized power coefficient for different J_v and τ_f.

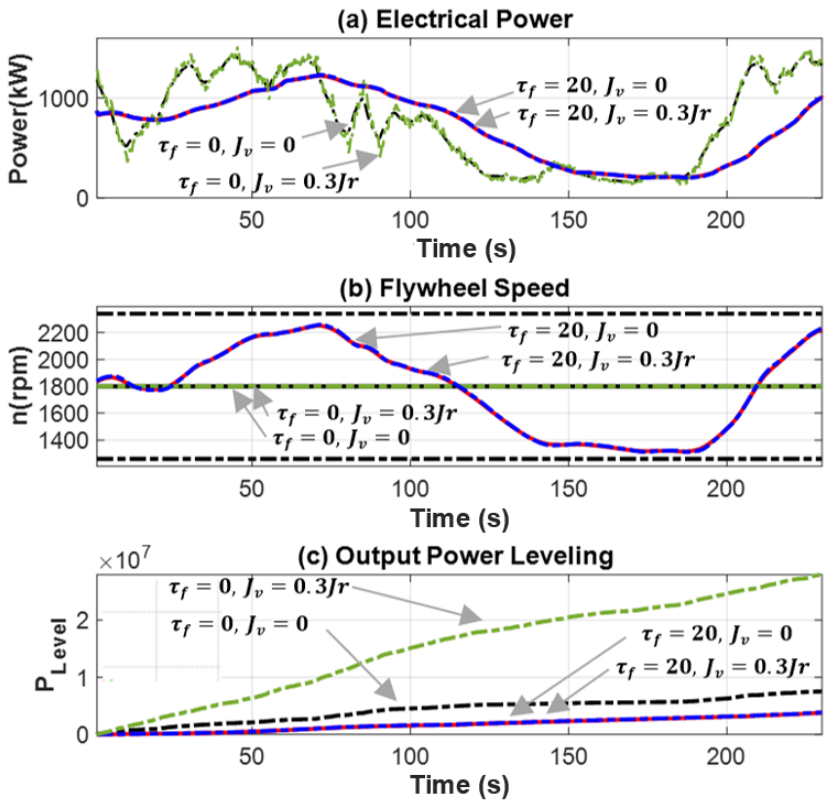

Figure 6.13. (a) Output power (b) flywheel speed (c) Power leveling function for different J_v and τ_f.

supervisory controller, becomes zero. This indicates that the controller kept the generator speed constant at ω_0, as shown in Figure 6.13 (b). In other words, no flywheel shows no oscillations of the generator speed since the output power becomes similar to the power that reaches the hydraulic motor. However, in the case of the flywheel, the speed of the generator varies to absorb the fluctuation of the aerodynamic power (Figure 6.13 (b)).

Table 6.3. Power Leveling and Maximum Energy Function for different Virtual Inertia at the End of the Period

	$\tau_f = 0$, $J_v = 0$	$\tau_f = 20$, $J_v = 0$	$\tau_f = 0$, $J_v = 0.3$	$\tau_f = 20$, $J_v = 0.3$
$P_{max}(J)$	1.7268×10^8	1.7268×10^8	1.7319×10^8	1.7319×10^8
P_{Level}	7.5413×10^6	3.7995×10^6	2.7961×10^7	3.8552×10^6

The values of P_{max}, and P_{Level} are tabulated in Table 6.3 for different τ_f and J_v. It can

be seen that the amount of the energy captured at the end of the period is dependent on the virtual inertia (changing τ_f with the same J_v does not change the P_{max}). However, with the flywheel, the power fluctuations of the system are similarly small. When the $J_v = 0.3J_r$, the energy which was captured over 230 seconds increased by $0.5\,MJ$. Therefore, on average, the system with virtually adjusted inertia not only had superior performance it also increased the capacity of the captured energy by $55\,kWh$ per day.

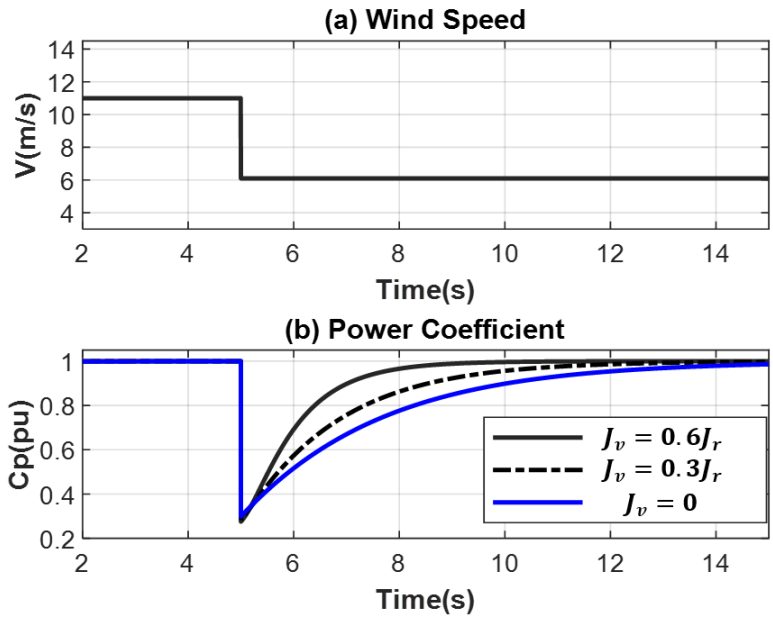

Figure 6.14. (a) Wind speed (b) normalized power coefficient

6.2.4 Step Response and Virtual Inertia

Figure 6.14 shows the effect of adding virtual inertia at two different magnitudes. A step response analysis shows that the MPPT dynamics becomes faster as the amount of J_v increases. The advantage of this approach over TSR control is that there is no need for prior knowledge of wind speed. Besides, the fluctuations of the captured mechanical power (aerodynamics) are reduced when the FESS is connected directly to the DFIG rotor, and the effects of the non-minimum phase of TSR do not appear in the output power.

6.3 Summary

This chapter introduced an integrated flywheel energy storage with the generator of an SS-WECS. The configuration removed the need for a dedicated power electronic converter and a motor/generator for the FESS. Then, two power quality control techniques were developed, including the direct power-averaging control method and the flywheel kinetic-energy control method. Simulation results demonstrated that both methods controlled the system properly. Furthermore, two MPPT control strategies were investigated, namely the optimal displacement control (ODC) and the virtual inertia adjustment. The effect of virtually decreasing the inertia of the wind turbine was analyzed analytically by small-signal analysis. The results of utilizing virtual inertia showed an increase in the amount of harvested energy and increased system dynamics. It was also demonstrated that the output power fluctuations which were caused by intermittent wind speeds were eliminated effectively.

7. REDUCTION OF THE NUMBER OF POWER CONVERTERS IN SS-WECS

This section introduces a new reconfiguration for the hydraulic wind turbine that allows the elimination of the GSC. The proposed configuration is shown in Figure 7.1. This configuration has a variable-displacement pump housed in the nacelle driven by the turbine shaft and a hydraulic motor located at ground level.

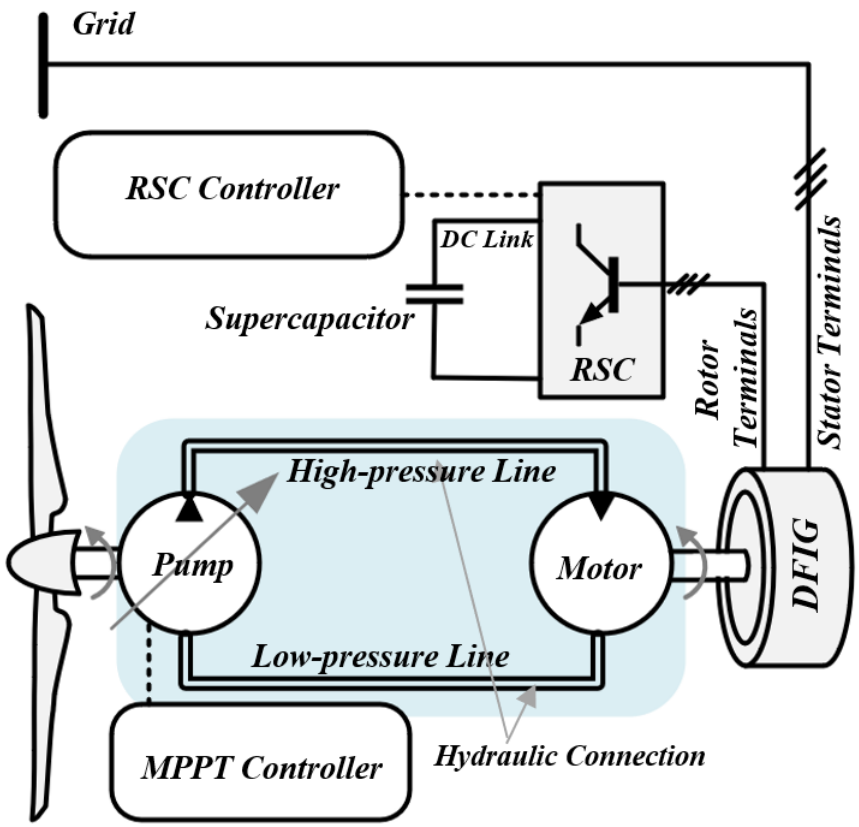

Figure 7.1. Configuration of the SS-WECS and the generator controller

7.1 Proposed Configuration and Control Strategy

In the configuration shown in Figure 7.1, the power flowing through the RSC can be independently controlled irrespective of the wind speed and turbine angular velocity by controlling the generator speed [123]. Consequently, the GSC can be eliminated, and the

rotor terminals can be supplied by only the RSC in conjunction with a capacitor. In this configuration, the rotor side converter (RSC) should only process the system's losses since the net power at the DC-link terminal should be zero. However, since this amount of power constitutes only a small portion of the system power rating, the power rating of the converter, which is only RSC, reduces noticeably.

7.1.1 Control Strategy

Active Power Control

The rotor power equation can be achieved as follow:

$$P_r = \frac{3}{2}R_r\left(I_{qr}^2 + I_{dr}^2\right) + \frac{3}{2}s_g\omega_s L_0 I_{m0} I_{qr} = P_{lr} + P_{ar} \tag{7.1}$$

The calculated power P_r is the amount of power injected into the rotor windings at their terminals. The first term in 7.1 represents the rotor windings losses, $P_l r$, and the second term stands for the power transferred to the airgap, P_{ar}, which depends on the generator slip. The stator power, similarly, can be divided into two terms as follows:

$$P_s = \frac{3}{2}R_s\left(\mathrm{i}_{qs}^2 + \mathrm{i}_{ds}^2\right) + \frac{3}{2}\omega_s L_m \mathrm{i}_{m0}\mathrm{i}_{qs} = P_{ls} + P_{as} \tag{7.2}$$

where, P_{ls} and P_{as} are the stator windings losses and the stator-part airgap power, respectively. From 7.1 and 7.2, the relation between P_{as} and P_{ar} can be deduced as follows:

$$P_{ar} = -s_g P_{as} \tag{7.3}$$

The airgap power comprises P_{as} and P_{ar}. The single-phase equivalent circuit of the generator rotor is shown in Figure 7.2. The amount of power delivered by DC link, P_{dc}, is the sum of the P_r and the converter losses, P_{lc}, and can be written as follows:

$$P_{dc} = P_{lc} + P_{lr} - s_g P_{as} \tag{7.4}$$

In general, P_{dc} must be zero to keep the DC-link voltage constant and provide an opportunity to eliminate the GSC. To this end, for any given power, the generator speed can be controlled such that equation 7.4 becomes zero. The control system in Figure 7.3 demonstrates the same concept. The speed reference is determined by a proportional-integrator (PI) controller such that the DC-link voltage remains constant.

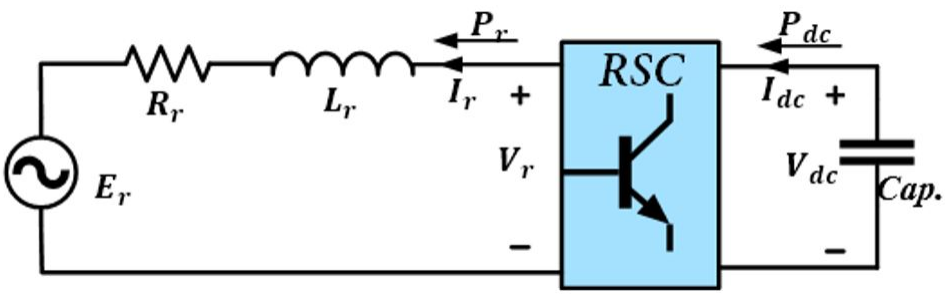

Figure 7.2. Single-phase equivalent circuit of the DFIG rotor

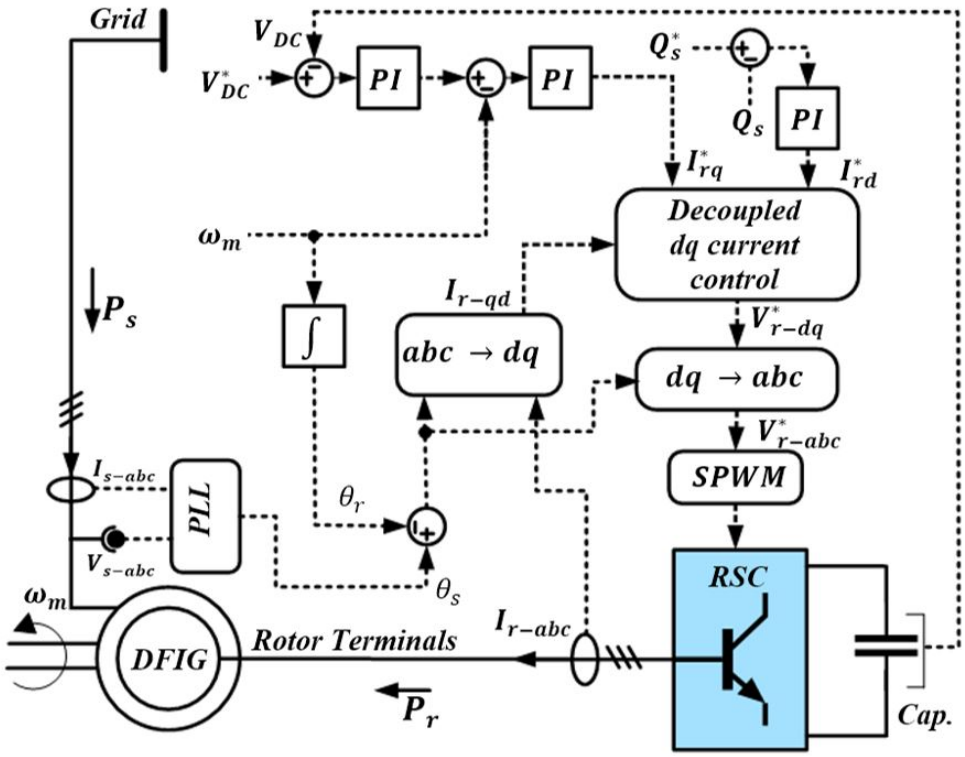

Figure 7.3. The active and reactive power control scheme of the proposed configuration

Reactive Power Control

Since in the proposed configuration, the DFIG is only connected to the electrical grid through its stator, controlling the stator reactive power is the only way to control the reactive power of the WECS. Reactive power control of DFIGs is well-known and easy and has been investigated extensively [34]–[37]. By using the feed-forward control loop to decouple the active and reactive power controls, the reactive power can be controlled by the direct component of the rotor current, as shown in Figure 7.3. Figure 7.4 demonstrates the relationship between the reactive power of the generator and the direct component of the rotor and stator current, which is calculated based on 3.38. To inject the reactive power into the grid, the direct component of the rotor current should be increased further to compensate for the magnetizing current of the generator.

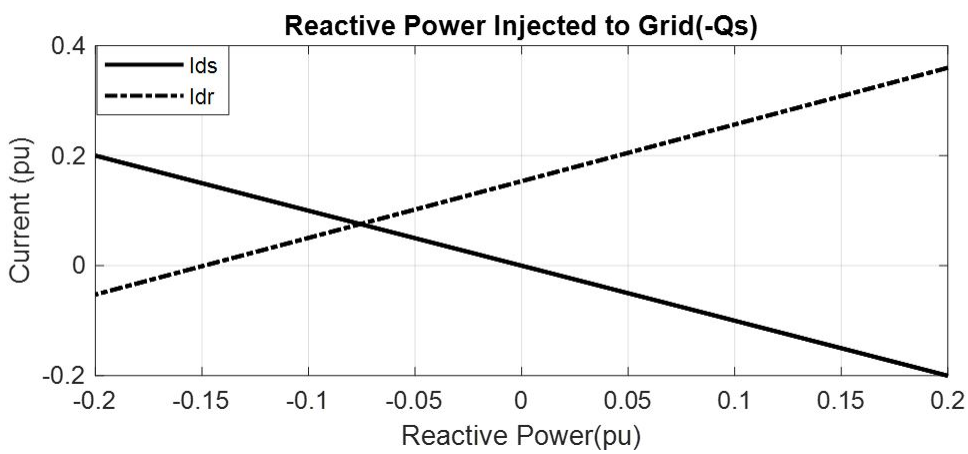

Figure 7.4. Rotor and stator direct component of current in various reactive currents

7.1.2 Design Considerations

In the steady state, when P_{dc} becomes zero to keep the DC-link voltage constant, the targeted generator slip, s_t, is small. In other words, the operating points are close to synchronous speed. This slip can be obtained by making Equation 7.4 zero, which results in:

$$s_t = \frac{P_{lc} + P_{lr}}{P_{as}} \tag{7.5}$$

The numerator in 7.5 shows the rotor winding loss and converter loss. As the slip is small, these terms are small positive values. The denominator is negative when the electric machine operates in generator mode. Therefore, the targeted slip s_t is a small negative value. Its negative sign dictates that the generator must operate at a super synchronous speed. The relatively small slip implicitly indicates that the generator does not need a large voltage at the rotor side. Since the losses of the rotor-side are relatively small for all operating points at different wind speeds, the DC-link voltage could be chosen as a small voltage.

Capacitor Selection

During transients or in the presence of disturbances, the capacitor on its own must handle the rotor voltage. The larger the capacitor, the lower the effects of the disturbances on the DC-link voltage. In low-voltage DC-links, a supercapacitor becomes suitable. In conventional wind turbines, the size of the capacitor is highly dependent on the bandwidth of current and dc-link voltage regulators. Commonly, the bandwidth of the current controller is chosen to be about 250-500 Hz, and the bandwidth of the voltage regulator, which is the second layer, is chosen to be less than $100Hz$. Therefore, the capacitor of the dc-link should be large enough to allow the GSC to maintain the dc-link voltage [132]–[135]. However, Since the dc-link regulator is the third layer of the controller in the proposed configuration, its bandwidth is chosen 1/10 or 1/5 of the speed bandwidth, and this controller should handle the DC-link voltage. Therefore, the amount of this capacitor is chosen such that:

$$C \geq \left(\frac{s_{max} P_n}{V_{dc}}\right) \frac{5\tau_{vd}}{\Delta V_{dc}} \tag{7.6}$$

where $\tau_d c$ is the time constant of the dc-link voltage regulator, and ΔV_{dc} is the maximum voltage variation on the dc link. s_{max} and P_n are the maximum slip and nominal power of the wind turbine.

Power Electronic Rating Selection

The switches are required to be sized according to the voltage and current rating. Therefore, a suitable rotor to stator winding turns ratio can help design the RSC better and result in properly rated switches. The voltage and current rating of the DFIG rotor winding at the rotor side are obtained as follows [37]:

$$V_r^{'} = nV_s \tag{7.7}$$

$$I_r^{'} = \frac{S_n}{\sqrt{3}V_r^{'}} = \frac{S_n}{\sqrt{3}nV_s} \tag{7.8}$$

where S_n is the rated apparent power of the DFIG, and n is the rotor to stator turns ratio of the generator. It is proven that the maximum voltage required for the rotor winding, which is the rated voltage of the RSC, is as follows [37]:

$$V_{con} = s_{max}V_r^{'} = s_{max}nV_s \tag{7.9}$$

where s_{max} is the maximum of the absolute value of the generator slip. Since the slip is small, the amount of V_{con} is also small. Therefore, increasing n leads to an increase in V_{con} and a reduction in $I_r^{'}$. With a fixed rotor winding copper volume, the rotor losses remain constant by increasing n. This value can be chosen based on the voltage and current rating of the power electronic switches.

Power Capability Curve

The power rating of the RSC can be achieved as follows:

$$S_{pu}^{r} = s_{max}\sqrt{(Q_{m-pu} - Q_{s-pu})^2 + P_{s-pu}^2} \tag{7.10}$$

The RSC rating power depends on s_{max}, which is dependent on the rotor winding and power converter losses and the maximum reactive power injected into the grid (Q_{s-pu}). The proposed configuration is capable of injecting or absorbing reactive power to/from the grid.

Two main limitations of the generator power are stator and rotor limits. The power capability curve of the generator can be achieved in Figure 7.5. Similar to SG's power capability curve, the maximum stator current limits the active and reactive power within a circle centered at the origin. However, the rotor current limit is a circle centered at $(0, Q_m)$. This means that when Q_s is negative (injecting reactive power to the grid), the rotor circuit should provide not only a magnetizing current but also an additional reactive term. In this case, similar to the conventional SG, the generator operates in over-excitation mode. When the magnetizing current partially or fully is supplied through the stator, the generator operates in under-excitation mode.

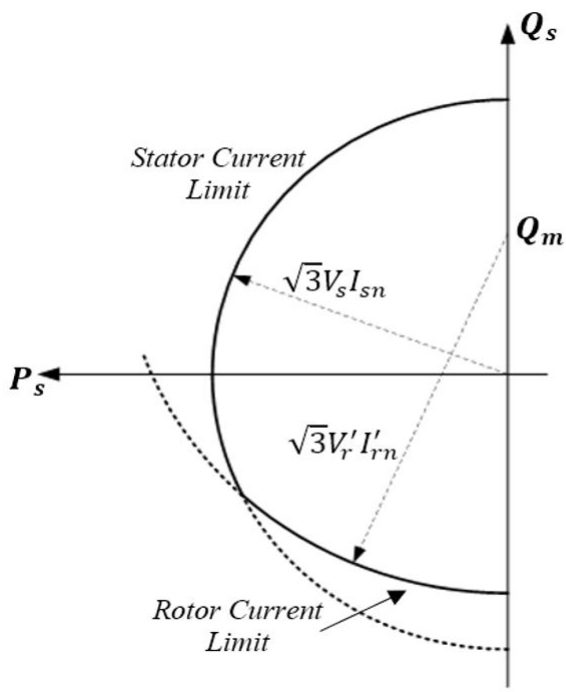

Figure 7.5. Power capability curve of the generator

7.2 Simulation and Discussion

The wind turbine parameters are provided in Table 3.1. The loss of the DFIG rotor can be calculated to be about 1.5% where s_{max} is about 2.5%. Since the stator line voltage is $690\,V$, the rated rotor line voltage and rotor current at the turns ratio of $n = 15$ are calculated as $10350\,V$ and $100\,A$, respectively. However, the maximum voltage required for the

rotor, depending on the maximum slip percentage, is $10350 \times 0.025 = 259\,V$. Therefore, the DC-link voltage required to establish the excitation voltage is $2\sqrt{2/3} \times 259 = 425\,V$. From 7.10 and using the data in Table 3.1, the apparent power rating of the power converter can be calculated to be $40\,kVA$. However, this is an estimation by considering a margin for the DFIG slip. A system with more detail has resulted in a 2.7% ($39\,kVA$) rating.

The wind speed is set to vary from 5 to $11\,m/s$ as shown in Figure 7.6 (a). The normalized power coefficient in Figure 7.6 (b) shows that the MPPT is achieved at various wind speeds, harvesting the maximum power from the existing energy in the wind. The actual output power reached a maximum of $1460\,kW$ and a minimum of $200\,kW$, as shown in Figure 7.6 (c). Furthermore, the generator has been successfully controlled to track the maximum power of the wind. In this case, the control command influences the generator's rotational speed. Figure 7.7 (a) illustrates the generator speed and the possibility of controlling the

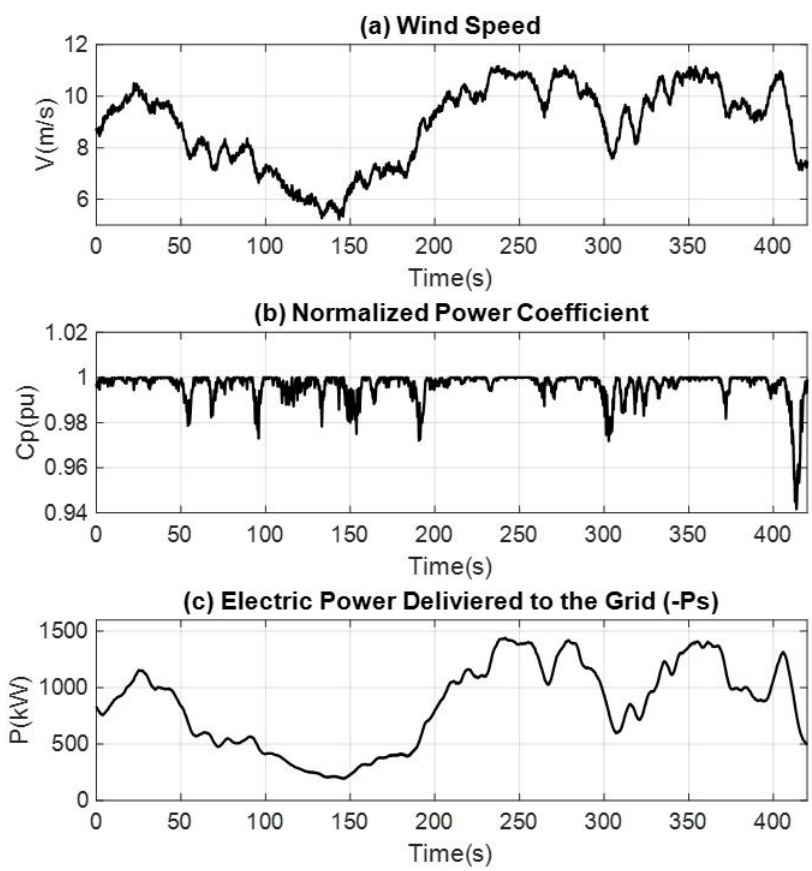

Figure 7.6. (a) Wind speed (b) normalized power coefficient (c) electrical power

generator speed precisely in a small window above the $1800\,rpm$ synchronous speed. This results in a -1.7% slip in the generation mode.

In this slip range, the rotor's active power is adjusted to provide the converter losses, as shown in Figure 7.7 (b). Furthermore, the reactive power of the rotor, which is proportional to the generator slip, is demonstrated in Figure 7.7 (b). Since the maximum apparent power of the generator rotor happens when the maximum active power and the maximum reactive power injected into the grid coincide. This coincidence happens around $250\,s$. As shown, the apparent power rating of the converter does not exceed $39\,kVA$ maximum.

Compared to conventional DFIG with two power converters at a rating power of $2 \times 30\%$ of the generator's rated power ($2 \times 450\,kVA$), this configuration only requires one converter at about 2.7% of rated power, a maximum of $39\,kVA$. The DC-link voltage profile is shown

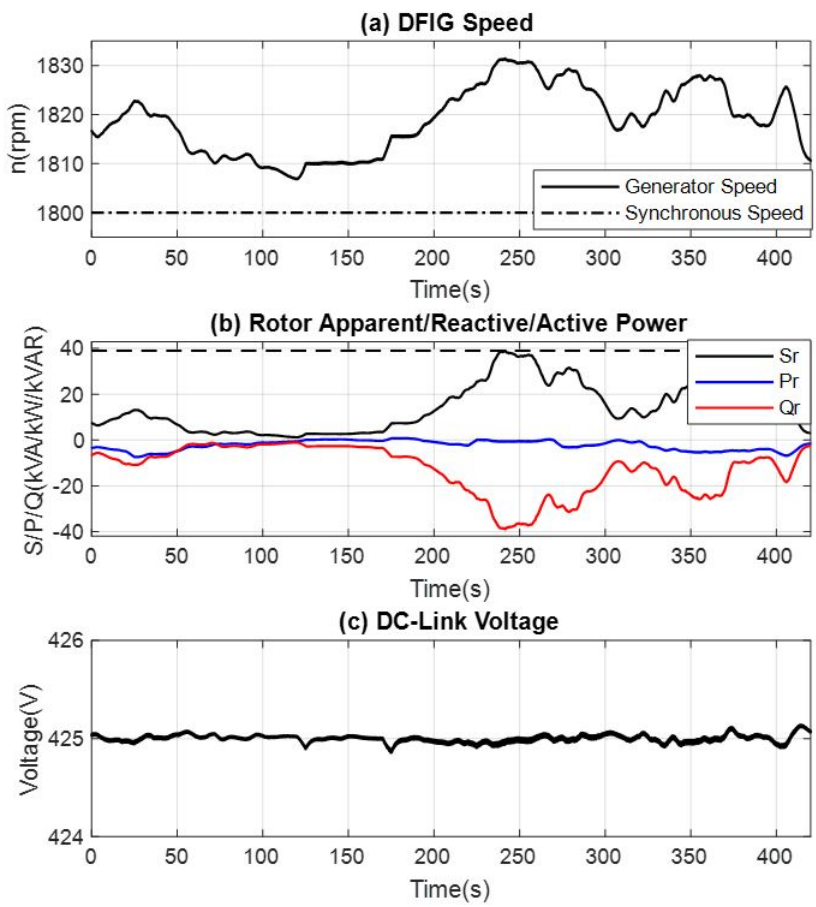

Figure 7.7. (a) Rotor speed (b) rotor active and reactive power (c) capacitor voltage

in Figure 7.7 (c). Since the amount of the generator slip is changing in a small range, the DC-link voltage required to inject the reactive power into the generator is smaller than that of the conventional DFIG. Therefore, the configuration is suitable for utilizing the supercapacitor at the rotor circuit. In addition, the capacitor is considered large enough ($20\,F$) to reduce the variation of DC-link voltage during an extreme change in wind speed. This figure demonstrates that the DC-link controller can maintain the DC-link voltage constant with small variations of less than $0.2\,V$ in extreme wind speed variations.

Accurate control over the slip of the generator results in a small fundamental component of the rotor voltage (Figure 7.8 (a)). The small rotor voltage and the resulting DC-link voltage reduce the voltage stresses of the power electronic devices, which leads to an increase in the reliability of the RSC and, subsequently, the whole system. Meanwhile, the smaller DC-link voltage leads to smaller switching losses of the power electronic devices, and increases efficiency, and reduces the thermal stresses of the converter. Figure 7.8 (b) shows the three-phase rotor currents, which vary directly proportional to wind speeds. The direct and

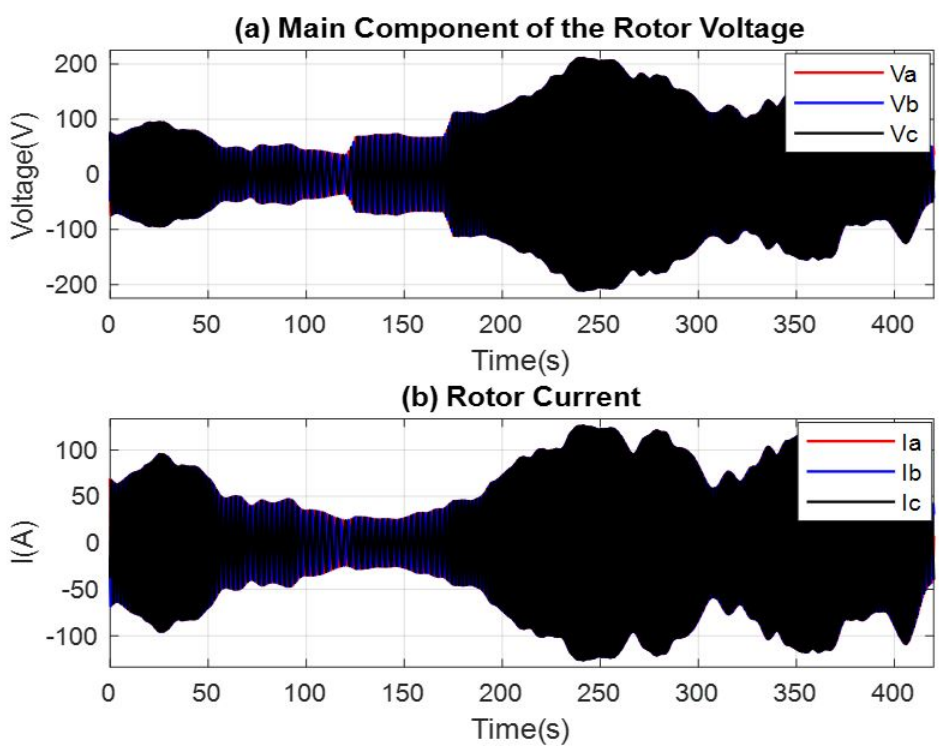

Figure 7.8. (a) Main component of the rotor voltage (b) rotor current

quadrature components of the rotor current are shown in Figure 7.9 (a). The active power is controlled by controlling the generator torque (Figure 7.9 (c)) or the quadratic current as i_{qr}. As shown, the torque and i_{qr} are proportionally varying with the wind speeds. The reactive power injected into the grid (Figure 7.9 (b)) is controlled following the reference of i_{dr}.

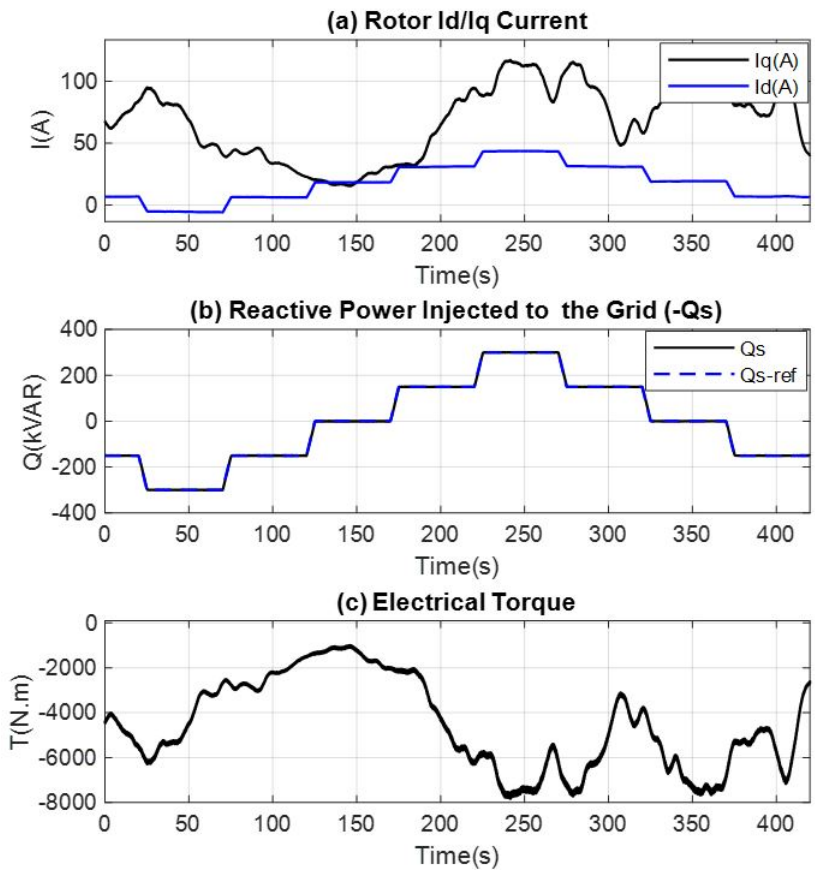

Figure 7.9. (a) Rotor current (b) electrical torque

It is proven that the controller is effectively capable of controlling the active and reactive power of the system. The drivetrain of the wind turbine also provides a unique dynamic in that the interface torque controller produces a command for the hydraulic pump displacement. As a result, the pressure on the system varies. Figure 7.10 (a) demonstrates the displacement of the pump, which is controlled to achieve the optimal aerodynamic power. The pressure of the fluid shown in Figure 7.10 (b) varies with the wind speed. Table 7.1 compares the proposed configuration with a conventional gear-box driven DFIG in a 1.5 MW

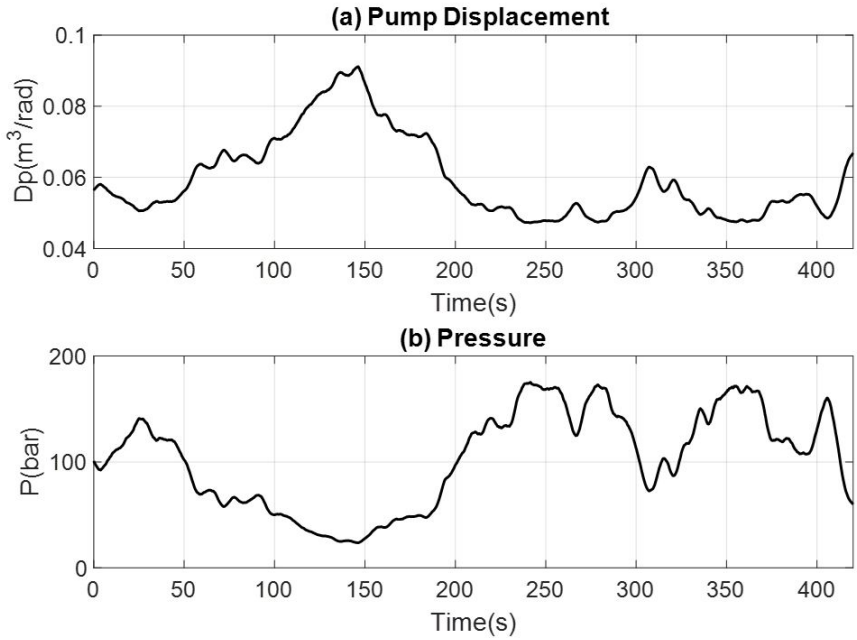

Figure 7.10. (a) Pump displacement (b) pressure of the pipeline

wind turbine. In conventional DFIG, the slip of the generator is chosen ±30%. Therefore, the DC-link voltage should be chosen such that both GSC and RSC be able to operate properly ($V_{dc} \geq 2\sqrt{2/3} \times 690 = 1100\,V$) [134]. However, this amount is calculated $425\,V$ for the proposed configuration. This also indicates that the voltage stress of power electronic devices in the proposed configuration is much less. The current stress of semiconductor devices is obtained $1150\,A$ for conventional DFIG compared to $125\,A$ for the proposed configuration. Assuming the stator of the conventional DFIG operates at unity power factor, RSC should handle the maximum active power of the rotor and magnetizing current, and the GSC should also handle the portion of active power passing through the rotor and the reactive power needed to inject to the grid. Therefore, in a conventional DFIG, The RSC and GSC rating power can be calculated as 412 and $457\,kVA$, respectively. However, the size of the RSC is much smaller for the proposed configurations, and the GSC is eliminated. The size of the DC-link capacitor is in a 1.5 MW conventional DFIG is about $16-21mF$ [132]–[135]. In the proposed configuration, by choosing the bandwidth of the DC-link voltage regulator 1/10 of

that of the speed regulator, which is $10\,Hz$, and allowing 5% voltage variation, the size of the capacitor should be larger than $16.6\,F$.

Table 7.1. Comparison of 1.5 MW conventional DFIG with the proposed configuration

Parameter,	**Conventional DFIG**	**Proposed Configuration**
V_s	$690\,V$	$690\,V$
P_s	$1.5\,MW$	$1.5\,MW$
n	1	15
V_{dc}	$1100\,V$	$425\,V$
I_{RSC}	$1150\,A$	$125\,A$
S_{RSC}	$412\,kVA$	$40\,kVA$
S_{GSC}	$457\,kVA$	NA
C	$20\,mF$	$20\,F$

7.3 Summary

This chapter proposed a new structure for SS-WECS that eliminated the need for the GSC. The system uses a supercapacitor and only one converter, RSC, to supply the power to the rotor. This new structure controls the DC-link voltage by controlling the speed of the generator. Eliminating the GSC, its filter, and transformer (if any) reduces the system's overall cost and increases the system's efficiency and reliability. Furthermore, controlling the speed around the synchronous speed provides the opportunity to limit the rotor voltage and enables the utilization of a supercapacitor. The proposed configuration is capable of controlling the active and reactive power with the need of only one converter, RSC, with a power rating of 2.7%. Compared to a conventional induction generator, the proposed configuration is capable of injecting reactive power into the grid.

8. HYBRID ENERGY STORAGE INTEGRATION WITH SS-WECS

In previous chapters, several configurations of SS-WECSs were introduced utilizing a new generator excitation with incorporated flywheel storage. This chapter characterizes a hybrid energy storage system (HESS) required to support the new generator excitation system developed for DFIG in the SS-WECSs. The goal is to improve the power quality while significantly reducing the generator excitation power rating and component counts. The rotor excitation circuit is modified to add the storage to its DC link directly. The output power fluctuations can be attenuated solely by utilizing the RSC, making it self-sufficient from the grid connection. The storage characteristics are identified based on several system design parameters, including the system inertia, inverter capacity, and energy storage capacity.

8.1 The Proposed Configuration

Unlike conventional gearbox-driven DFIG-based WECSs in which the DFIG shaft is mechanically coupled to the wind turbine shaft, the hydraulic drivetrain can control the generator speed by decoupling the shafts of the wind turbine and the generator. As a result, the power flowing through the RSC can be controlled independently of the wind speed and turbine's angular velocity by controlling the generator speed [123]. Therefore, the generator's speed and power passing through generator rotor windings can be controlled independently of the wind speed. Consequently, the GSC can be eliminated, and only the RSC can supply the rotor terminals in conjunction with storage, as shown in Figure 8.1. The RSC can independently control the generator's speed to attenuate output power fluctuations in this configuration.

8.1.1 Control Method of HESS

In the proposed configuration, the RSC controls the output power and HESS simultaneously. In other words, the low-frequency part of the mechanical power, P_s^* is injected into the power grid, and the energy storage at the rotor side absorbs the high-frequency component.

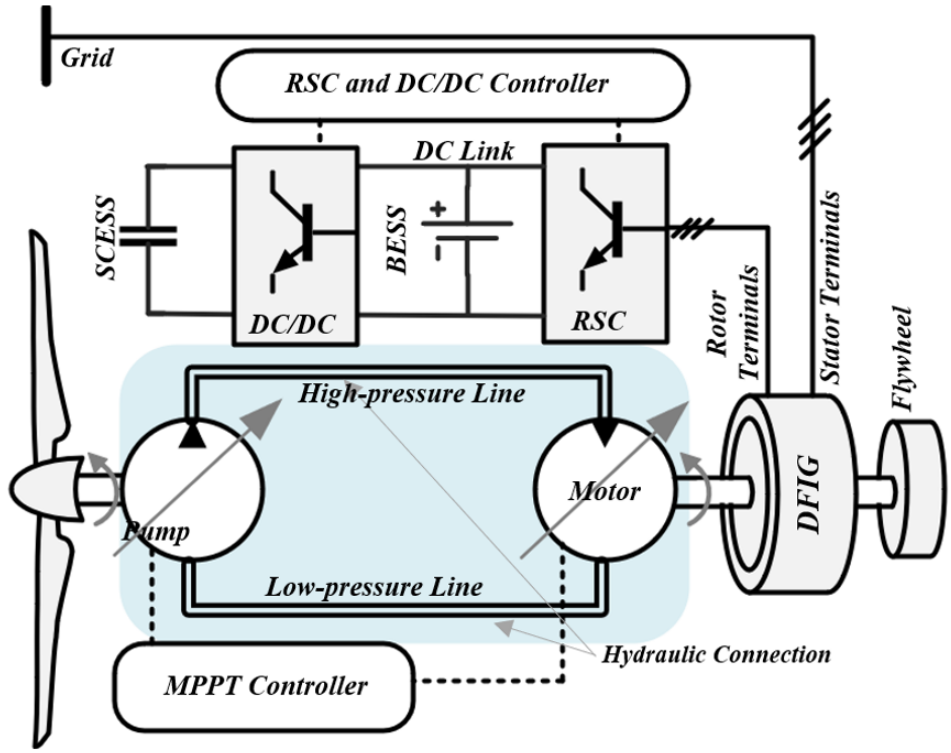

Figure 8.1. Configuration of the split-shaft wind energy conversion system

The diagram of the control strategy is shown in 8.2. In this figure, the SoC-feedback control shown defines the reference output power and maintains the SoC of the BESS and SCESS within its limits. The rotor and stator power equation are calculated in the stator-flux orientated (SFO) frame when the quadrature stator flux is zero, $\lambda_{qs} = 0$ and $\lambda_{ds} = L_m I_{m0}$, as follows:

$$P_r = \frac{-3}{2} s_g \omega_s L_0 \mathrm{i}_{m0} I_{qr} \tag{8.1}$$

$$P_s = \frac{3}{2} \omega_s L_0 \mathrm{i}_{m0} I_{qr} \tag{8.2}$$

$$Q_s = \frac{3}{2} \omega_s L_m \mathrm{i}_{m0} I_{ds} \tag{8.3}$$

In this framework, the active and reactive powers are controlled by the quadrature and direct components of the rotor current, respectively. Since the power of the rotor of DFIG is proportional to the generator's slip, the power rating of RSC is defined by the maximum

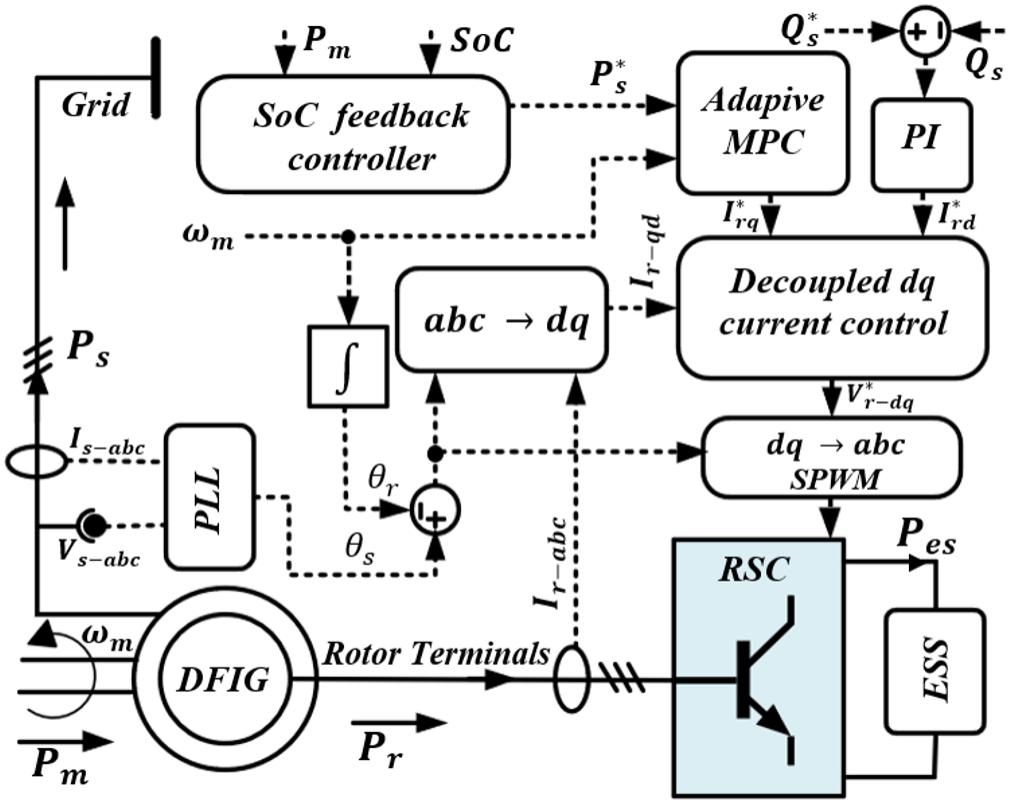

Figure 8.2. The overall view of the system controller

slip of the generator. Therefore, the speed of the generator should be controlled to remain within the maximum slip range. For example, if the converter size is chosen to be 10% of the wind power, the slip of the generator must be within $\mp$10%. To this end, the Model-based Predictive Controller (MPC) block in Figure 8.2 prevents the generator speed violation in case of sudden significant wind speed variations.

Adaptive MPC

The MPC controller in the control strategy shown in Figure 8.2 is employed to control only the speed of the generator to reduce the computational burden of the MPC and make it suitable for real-time implementation. Furthermore, the SoC of the storage is controlled by a SoC-feedback controller, and the reactive power is controlled in a decoupled dq vector control. Therefore, the only states considered in the MPC are the rotor speed and current

of the converter. Using the equations of the system, the system model of these two states is rewritten as follows:

$$\begin{bmatrix} s\omega_m \\ sI_{qr} \end{bmatrix} = \begin{bmatrix} \frac{1}{J_m\omega_m}\left(P_m + \frac{3}{2}\omega_s L_0 \mathrm{i}_{m0}(1-s_g)I_{qr}\right) \\ \frac{1}{T_c}\left(I_{qr}^* - I_{qr}\right) \end{bmatrix} \tag{8.4}$$

Since 8.4 presents a nonlinear system, the adaptive MPC controller is employed. The output of the system is P_s which is controlled to follow the reference power, P_s^*, defined through the SoC feedback controller. Therefore, the objective function of the system is considered as follows:

$$C = \sum_{\mathrm{i}=1}^{n_p} \left(\alpha_p \left(P_s(\mathrm{i}+k \mid k) - P_s^*(\mathrm{i}+k \mid k)\right)^2 + \rho_\epsilon \epsilon_k^2\right) \tag{8.5}$$

Such that:

$$P_s^{min} \leq P_s \leq P_s^{max} \tag{8.6}$$

$$\omega_m^{min} \leq \omega_m \leq \omega_m^{max} \tag{8.7}$$

$$-\epsilon \leq P_s(k+1 \mid k) - P_s(k \mid k-1) \leq \epsilon \tag{8.8}$$

where ϵ_k is the slack variable at control interval k (dimensionless) and ρ_ϵ is the constraint violation penalty weight (dimensionless), respectively. These parameters are utilized to soften the constraints and ensure MPC convergence. ϵ is defined as the limit of the power fluctuation rate in each time sample. Accordingly, the minute-by-minute power fluctuation of the power injected into the power grid is limited by system operators [136], [137]. Herein, the maximum of this rate is considered $\gamma_{min} = 2\%$. However, the amount of ϵ should be calculated based on γ_{min} and sample time, T_d, as follows:

$$\epsilon = \frac{\gamma_{min}}{60} T_d \tag{8.9}$$

Generally, the MPC controller follows the reference power calculated by the SoC feedback control and keeps speed and power fluctuations within the range. However, when the generator's speed exceeds its constraints, the controller might not keep the power fluctuations within their limits but find an optimal solution. The controller must keep the generator speed in range; otherwise, the power fluctuations increase. In the case of a fixed-displacement pump/variable-displacement motor (VDM), the OMDC is employed to follow MPPT. In the case of variable-displacement pump/fixed-displacement motors (VDP), the OPDC is utilized to achieve MPPT.

8.1.2 Hybrid Energy Storage System (HESS)

Three energy storage types seemed suitable to incorporate energy storage into the proposed configuration while keeping the minimal size of supporting components, namely FESS, SCESS, and BESS. BESS and SCESS could be directly integrated into the DC-link of RSC. Also, FESS could be coupled directly to the shaft of the generator. The combination of BESS and SCESS has been investigated in many pieces of literature. Employing the supercapacitor alongside BESS is a suitable option to decrease the maximum power of BESS at the DC link. In this case shown in 8.3, the configuration allows for taking advantage of the supercapacitor capacity. Meanwhile, the DC-link voltage is stable due to the existence of the BESS, which allowed for a smaller inverter size [109], [110], [138].

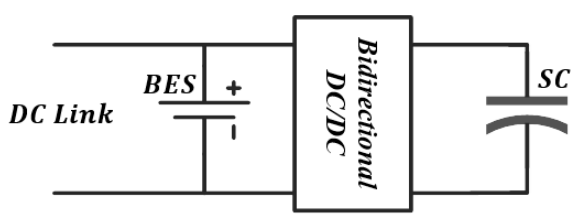

Figure 8.3. Super-capacitor semi-active topology

Super Capacitor Energy Storage System (SCESS)

The supercapacitor can provide ample charging and discharging current (high power) but has a lower energy-to-power ratio than battery energy storage [139], [140]. In other words, a supercapacitor has a quick charge and discharge time. However, hybrid energy storage, a combination of battery and supercapacitor, can provide a better power and energy requirement because of their complementary characteristics [141]. Supercapacitors can provide and absorb significant powers with fast dynamics. They are characterized by their high power capability due to the low internal resistance and low voltage [142].

In SCESS, the energy is stored through static electrical charges rather than the electrochemical process that happens in BESS. The SCESS is modeled as a large capacitor and a series resistor. The SoC of the SCESS is calculated similarly to BESS. A low-pass filter is employed to filter out the high-frequency component of the rotor power. The overall control approach to defining the power allocation of a supercapacitor is employing the low pass filter alongside a rule-based control approach to ensure the proper and safe operation of the SCESS. The energy of the supercapacitor is calculated based on the following equations:

$$E_s = \frac{1}{2} C V_s^2 \tag{8.10}$$

where C and V_s are the capacitance and the voltage of the supercapacitor. The voltage of the DC link is stable with slight variations because of the BESS. The minimum voltage of the supercapacitor (V_s^{min}) is limited to limit the range of the power converter gain. Thus, the energy of SCESS is calculated as follows:

$$E_s = \frac{1}{2} C (V_s^2 - V_s^{min^2}) \tag{8.11}$$

Allowing a minimal supercapacitor voltage, the supercapacitor capacity is utilized to a more considerable extent. However, the DC-DC converter should have a more extensive voltage gain range. A reasonable choice is that the minimum voltage is limited to half of the

maximum voltage that the supercapacitor (V_s^{max}) can handle. In this case, three-quarters of the supercapacitor's total capacity is available to be used.

$$\Delta E_s = \frac{3}{4}(\frac{1}{2}CV_s^m ax^2) \tag{8.12}$$

Flywheel Energy Storage System (FESS)

The combined inertia of the generator and hydraulic motor could slow down the acceleration and deceleration of the generator. This demonstrated that increasing the system inertia through a FESS on the generator shaft could decrease the maximum storage power and demand a low-power high-energy storage type, e.g., a battery. In general, the main components of a FESS include rotor, motor/generator, power electronic converter, bearing, and housing [61]. The cost of the high-speed flywheel could be five times more than the low-speed FESS. In high-speed FESS, the composite material is used for the rotor, and electromagnetic bearings are utilized to reduce the friction loss of the bearing. Unlike the high-speed FESS, the rotor is commonly built with steel using a mechanical bearing in low-speed FESS [61], [62]. Also, the housing compartment should be strong enough to withstand a high-speed rotor's burst. In low-speed FESS, the motor/generator and the power electronics can be a large portion of the cost of the whole storage system. To further decrease the storage cost, the SS-WECS can be employed with DFIG. Compared to the conventional FESS shown in Figure 8.4, the proposed configuration in Figure 8.1 allows eliminating the motor/generator and the dedicated power electronic by directly connecting the flywheel to the shaft of the wind turbine generator. The added flywheel behaves as the intrinsic inertia of the generator, and it does not need any control strategy. Therefore, the control system is more straightforward, and the configuration is cheaper.

BESS Model and Energy Management

A reduced-order model of the battery energy storage is utilized to create a baseline for some of the characteristics observed from a storage unit. The BESS State of Charge (SoC)

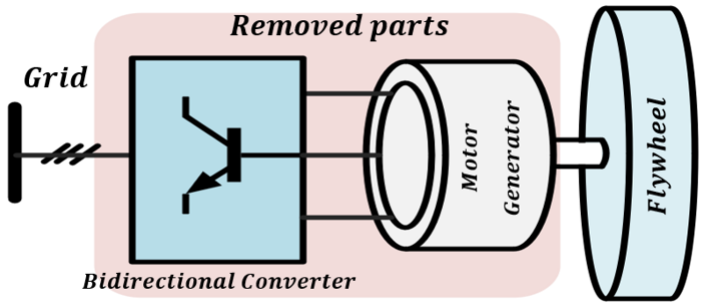

Figure 8.4. Conventional flywheel energy storage system

can be calculated based on Coulomb counting [143]. The SoC of the storage and the dynamic of the storage are calculated as follows:

$$SoC(t) = \begin{cases} SoC(t_0) + \frac{\eta_{es}}{E_{es}h} \int_{t_0}^{t} P_{es}\, dt & P_{es} \geq 0 \\ SoC(t_0) + \frac{1}{E_{es}h\eta_{es}} \int_{t_0}^{t} P_{es}\, dt & P_{es} < 0 \end{cases} \tag{8.13}$$

$$\Delta SoC(t) = \begin{cases} \frac{\eta_{es} P_{es}}{E_{es}h} & P_{es} \geq 0 \\ \frac{P_{es}}{E_{es}h\eta_{es}} & P_{es} < 0 \end{cases} \tag{8.14}$$

The SoC feedback control (shown in 8.5) is employed to manage the SoC of the BESS within its limits. In this method, the mechanical power (P_m) that reaches the hydraulic motor fluctuates with the variation of wind speed. An offset power, P_o is defined to attenuate these fluctuations. In other words, the mechanical power has many fluctuations, and the output power is desired to be smooth. The power difference is the amount of exchange power with the storage unit. The offset power is proportional to the level of SoC as shown in Figure 8.5 [144] and is obtained as follows:

$$P_o = \frac{k_P}{k_E s} P_{es} - k_P SoC_o \tag{8.15}$$

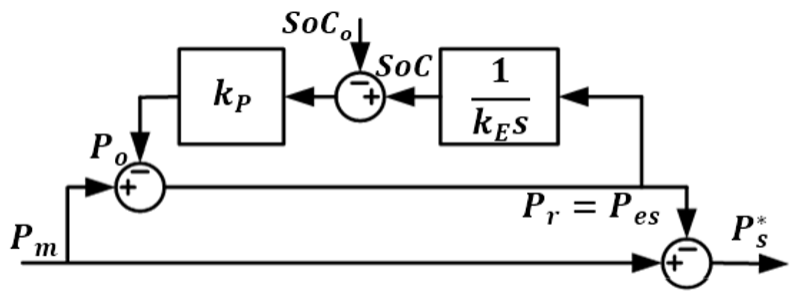

Figure 8.5. SoC-feedback control strategy

Using 8.15 and the control diagram in Figure 8.5, the storage and grid power references are obtained as follows:

$$P_e s = \frac{T_f s}{T_f s + 1}\left(P_m + k_P SoC_o\right) \tag{8.16}$$

$$P_s^* = \frac{1}{T_f s + 1}\left(P_m - k_E s SoC_o\right) \tag{8.17}$$

where $T_f = k_E/k_P$. This strategy is modeled as a first-order low-pass filter with a time constant of T_f. The time constant is dependent on the storage capacity. The larger the capacity of the storage, the larger the time constant T_f. The value of T_f is identified by determining the k_P such that the SoC of the storage remains within predefined limits. Therefore, k_P can be adjusted as follow:

$$k_P = \frac{P_{m,max} - P_{m,min}}{SoC_{max} - SoC_{min}} = \frac{P_n}{SoC_{use}} \tag{8.18}$$

Meanwhile, given a time constant, the size of storage capacity can be determined as follow:

$$E_{es} = \frac{P_{m,max} - P_{m,min}}{h(SoC_{max} - SoC_{min})} T_f = \frac{k_P T_f}{h} \tag{8.19}$$

In 8.19, h converts the unit of E_{es} to kWh. The offset of SoC, SoC_o, is chosen as SoC_{min}. If SoC_o is considered zero, the SoC of the storage changes from 0 to SoC_{use}. The SoC of the storage can be calculated as follows:

$$SoC(s) = \frac{P_m}{k_P(T_f s + 1)} + \frac{SoC_o}{T_f s + 1} \tag{8.20}$$

From 8.20, it can be seen that when the P_m becomes zero, $SoC(0)$ become SoC_o.

The SoC feedback control shown in Figure 8.4 does not consider the effects of the generator and hydraulic motor inertia. Since in the configuration shown in Figure 8.1, the electrical power transferred to the ESS is attenuated by the inertia of the generator, the SoC feedback control is adapted to incorporate the impacts of the generator inertia as shown in Figure 8.6. The difference between P_m and P_o is called P_{ri}. This power, P_{ri}, is the power that flows toward the generator's rotor and consists of two elements as follows:

$$P_{\mathrm{ri}} = P_r + P_{\mathrm{i}} \tag{8.21}$$

where, P_r and P_{i} are the power at rotor wingdings' terminal and the power stored in the inertia of the generator, respectively. Therefore, the swing equation of the generator can be rewritten as follows:

$$P_{\mathrm{i}} = P_{\mathrm{ri}} - P_r = J_m \omega_m \omega_m^{'} \tag{8.22}$$

Since the stator power, P_s, varies slowly compared to P_{ri} and ω_m, it can be considered constant. Therefore, by taking the derivative of 8.1 and 8.2, the derivative of generator speed can be calculated as follows:

$$P_r^{'} = \frac{P_s}{\omega_s} \omega_m^{'} \tag{8.23}$$

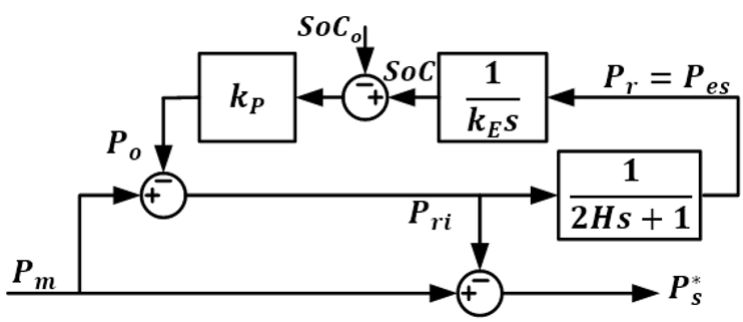

Figure 8.6. SoC feedback control strategy incorporated the generator inertia

By substituting 8.22 into 8.23 and rearranging the equation the P_r can be obtained as follows:

$$P_r = \frac{1}{\frac{J_m \omega_m \omega_s}{P_s} s + 1} P_{ri} \tag{8.24}$$

The term $\frac{J_m \omega_m \omega_s}{P_s}$ is dependent on the operating point of the generator, which makes the Equation 8.24 nonlinear. However, this term is considered constant in this subsection. The inertia constant of the generator is $H = \frac{J_m \omega_s^2}{2P_n}$. Therefore, the inertia constant of the generator can be obtained as $2H \approx \frac{J_m \omega_m \omega_s}{P_s}$. Using the block diagram shown in Figure 8.6, the power injected into the grid and storage power are obtained as follows:

$$P_{es} = \frac{T_f s}{T_f s(2Hs + 1) + 1}(P_m + k_P SoC_o) \tag{8.25}$$

$$P_s^* = \frac{1}{T_f s(2Hs + 1) + 1}(P_m - k_E sSoC_o) \tag{8.26}$$

To evaluate the effect of T_f and H on the power of energy storage, P_{es}, Bode diagrams for 8.16 and 8.25 are shown in Figure 8.7.

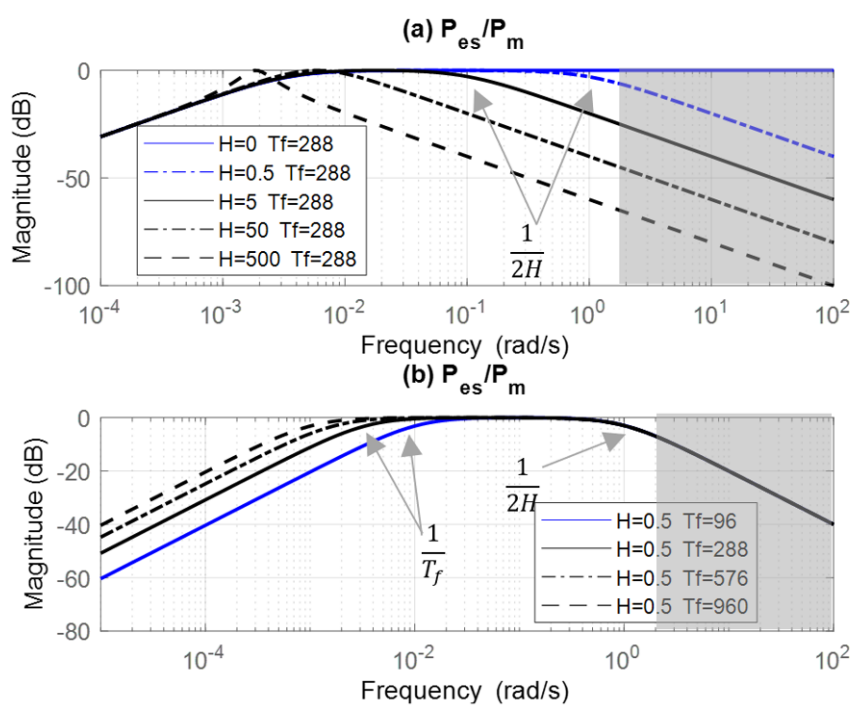

Figure 8.7. Bode diagram of P_{es}/P_m (a) for various H (b) for various T_f

In this figure, when $H = 0$ as in 8.7, the P_{es}/P_m is simply a first-order high-pass filter. In other words, the high-frequency components of the power are delegated to energy storage. However, for the non-zero inertia of the generator, P_{es}/P_m becomes a band-pass filter. The lower cut-off frequency of this band-pass filter is $\omega_{c1} = \frac{1}{T_f}$. However, the upper cut-off frequency is dependent on the inertia of the generator as $\omega_{c2} = \frac{1}{2H}$. This shows that the high-frequency components of the mechanical power oscillations are not transferred to energy storage and are absorbed to an extent by the generator's inertia.

In Figure 8.7 (a), the effect of inertia on energy storage is shown and T_f is considered constant. It can be observed that changing H mostly changes the upper cut-off frequency. In Figure 8.7 (b) the impacts of the storage capacity (T_f) on power of energy storage are shown and H is considered constant. Changing T_f shifts the lower cut-off frequency. The dark shaded area in these figures is where the inertia of the wind turbine has sufficiently attenuated the wind power variations. Therefore, further attenuation in this area is unnecessary.

Figure 8.8 demonstrates the bode diagram of the transfer function of P_s/P_m calculated in

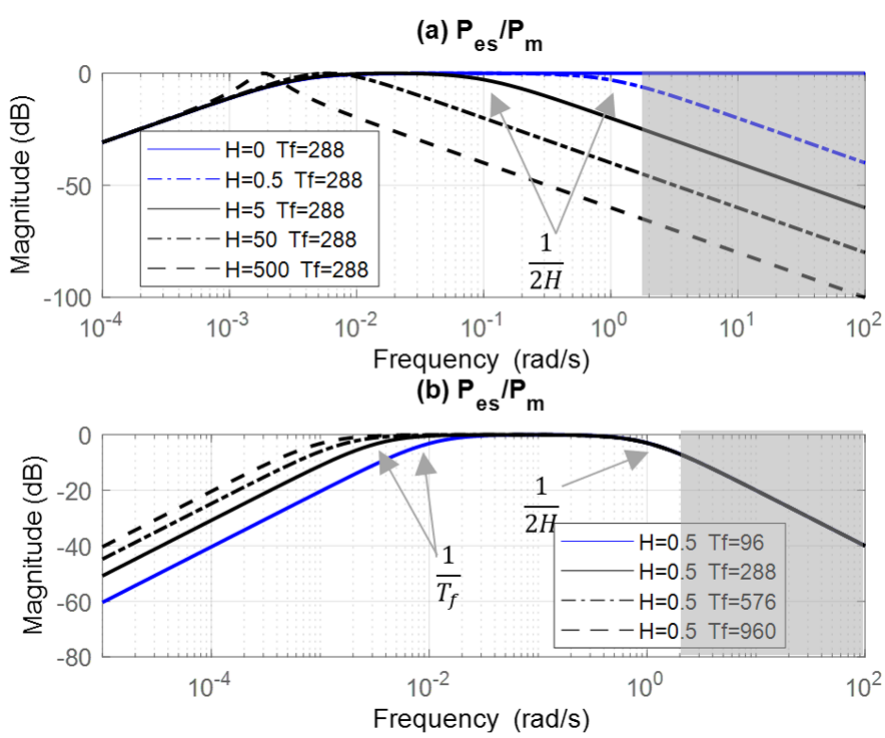

Figure 8.8. Bode diagram of P_s/P_m (a) for various H (b) for various T_f

8.17 and 8.26. As shown in Figure 8.8 (a), except for very large inertia, increasing the inertia of the generator helps to decrease only the very-high-frequency component of P_s, which are attenuated enough by T_f. Therefore, increasing the inertia of the system can affect P_{es} more than P_s. On the other hand, increasing T_f attenuates the lower-frequency components of the injected power into the grid as shown in Figure 8.8 (b).

8.2 Detailed Simulation

The proposed configuration is modeled to evaluate its feasibility. Accordingly, a detailed model of each element is obtained in MATLAB, with the initial parameters listed in Table 3.1. In this section, the direct component of the stator current is controlled to keep the reactive power zero ($Q_s = 0$). Using the steady-state equations of the hydraulic drivetrain, the correlations of the states (ω_p, ω_m and P_f) and control inputs (D_m and D_p) with the wind power (P_w) and electrical output power (P_s) for both configurations in Figure 8.1 are obtained in Table 8.1.

Table 8.1. General relationship

Parameter,	**VDP**	**VDM**
ω_m	$\propto P_m/P_s$	$\propto P_m/P_s$
ω_p	$\propto \sqrt[3]{P_m}$	$\propto \sqrt[3]{P_m}$
P_f	$\propto P_s$	$\propto \sqrt[3]{P_m^2}$
D_m	$const.$	$\propto P_s\sqrt[3]{1/P_m^2}$
D_p	$\propto \sqrt[3]{P_m^2}/P_s$	$const.$

Therefore, both configurations are simulated with the same wind profile shown in Figure 8.9 (a), and their performances were compared. Figure 8.9 (b) demonstrates the normalized power coefficient of the wind turbine, which is similar in both cases. In both cases, the mechanical power that reached the hydraulic motor and the electrical power injected into the grid are shown in Figure 8.10 (a). Due to the inertia of the wind turbine, the harvested power P_m is attenuated slightly compared to the wind power. Furthermore, the fluctuation of the output power (P_s) are attenuated. Most of the variations in power are absorbed by the rotor of the generator. Therefore, the generator speed varies proportionally based on the

amount of harvested power ($\propto P_m/P_s$) as shown in Figure 8.10 (b).

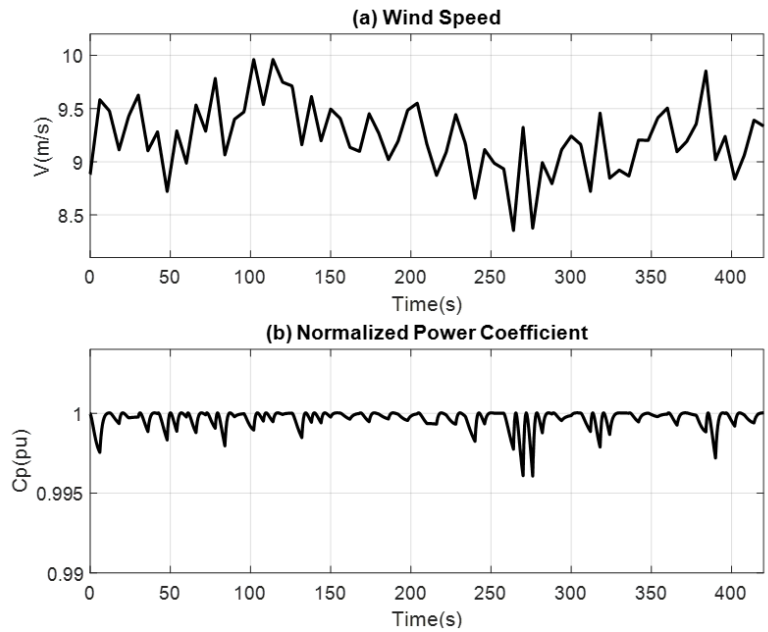

Figure 8.9. (a) Wind speed considered in the detailed analysis (b) normalized power coefficient of the wind turbine

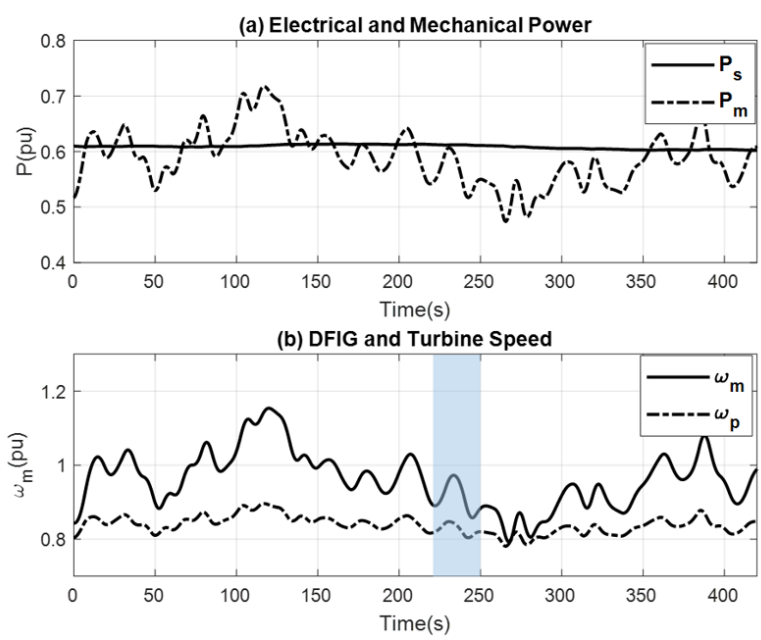

Figure 8.10. (a) The mechanical power (P_m) and the power injected into the power grid (P_s), (b) generator and turbine speed.

The relationship between the turbine speed and the wind power shows that the variation of the turbine speed is less than the variation of the generator speed at a given wind speed profile and harvested power because $\omega_p \propto \sqrt[3]{P_m}$.

The power that passes through the generator rotor circuit is shown in Figure 8.11 (a). This power is proportional to the rotor speed in the steady-state condition. The energy storage connected to the rotor of the generator is needed to provide excitation power. Therefore, the SoC of the storage can be controlled through the rotor power, as shown in Figure 8.11 (b). Figure 8.12 demonstrates a zoom-in of one phase of the rotor current and voltage in a 30 second window.

Since $I_{dr} = 0$, the amplitude of the rotor current is proportional to the active power only. However, the voltage of the rotor is proportional to the speed of the generator. Therefore, given the output power, P_s, the amplitude of the rotor current remained constant, and its frequency is proportional to the generator speed. Generally, both configurations behave the same from the electrical point of view for a given wind profile and the system parameters. In other words, the output power, or P_s, the rotor power, or P_r, SoC, and voltage and current

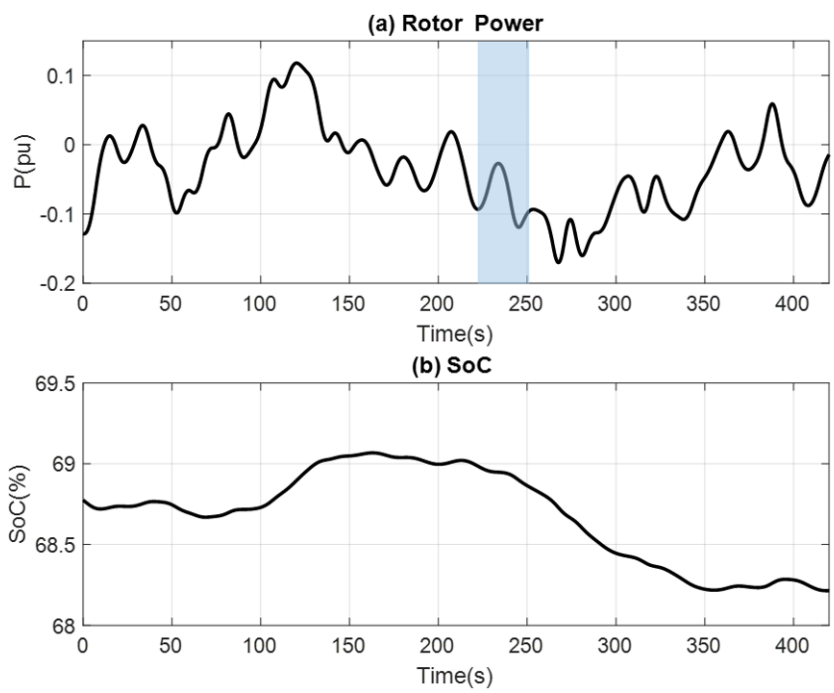

Figure 8.11. (a) Power of generator rotor (b) state of the charge of the storage

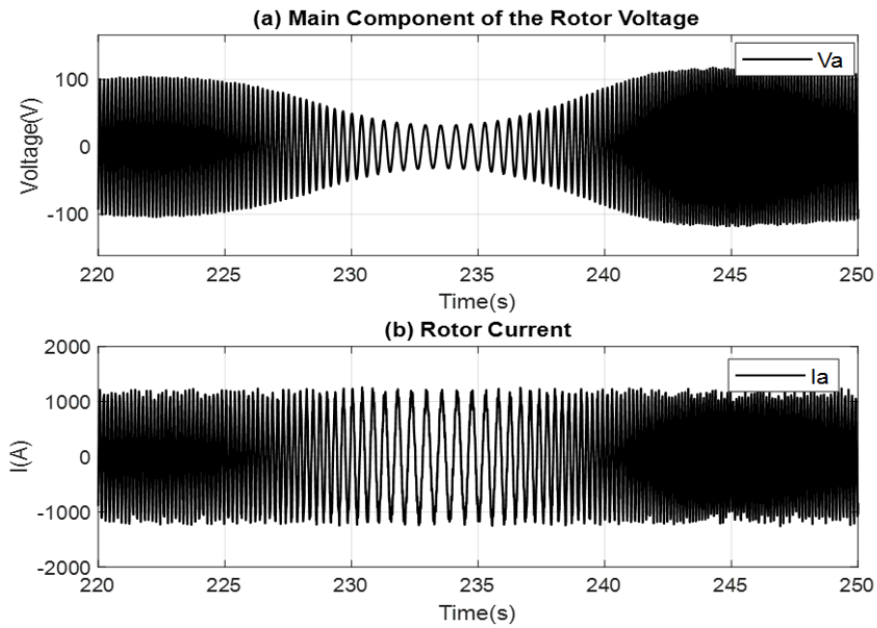

Figure 8.12. (a) The main component of the rotor voltage (b) the current of the rotor

of the RSC are the same in case 1 and case 2 configurations. The speeds of the pump and hydraulic motor are also dependent on the harvested wind power and output power which are the same in both cases.

As shown in Figure 8.13, the displacement of the hydraulic machinery and their operating pressures are different in both cases. As demonstrated in Figure 8.10, it is observed that when P_m increases, the displacement of the pump also increases to capture the maximum power in case 1 governed by $D_p \propto \sqrt[3]{P_m^2}$. In the contrary, the displacement of the hydraulic motor decreases when P_m increases governed by $D_m \propto \sqrt[3]{1/P_m^2}$. On the other hand, the pressure of the fluid for case 1 is proportional to the stator power and remained constant. However, there is a small fluctuation observed during the transient. In case 2, the pressure of the fluid increases when the captured power increases. This is evidenced by the governing equation $P_f \propto \sqrt[3]{P_m^2}$. Therefore, case 1 and case 2 configurations provide different drivetrain approaches.

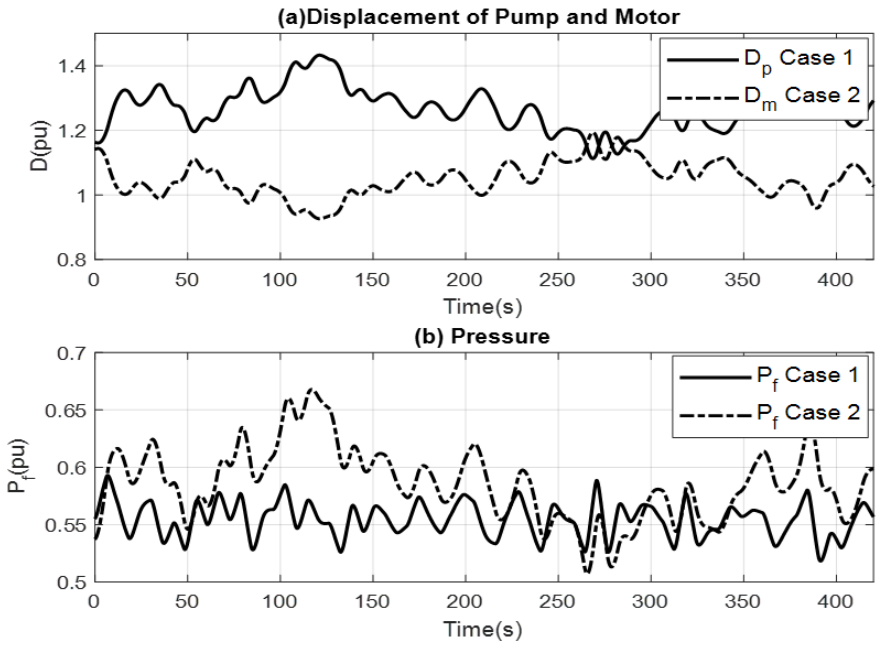

Figure 8.13. (a) Displacement of the pump and motor (b) pressure of the transmission fluid. The per-unit values do not exceed the actual displacement of the hydraulic machinery

8.3 Discussion

In this section, a 1.5 MW SS-WECS is simulated. The size of the converter is considered 40% with 120-kWh energy storage. The inertia of the generator is 80 $kg.m^2$. The losses of power transmission are considered negligible. Since it is shown that both configurations of case 1 and case 2 generated similar electrical power, only case 1 is studied in this section. The wind speed variation records at the turbine hub in 24 hours are shown in Figure 8.14 (a). The nominal wind speed of the wind turbine is 11 m/s, with a 3 m/s cut-in wind speed. The MPC control command is shown in Figure 8.14 (b). The simulation results of the system for the output power are shown in Figure 8.15. The active power generated from the system and the mechanical power are in Figure 8.15 (a). This figure demonstrates a significant quality improvement as power fluctuations are reduced by utilizing the energy storage and suitable control technique.

At point A in Figure 8.15 (b), the difference between P_s and P_m reaches 40% of P_s, and the generator's speed becomes 1.4 pu (Figure 8.16). The controller limits the generator

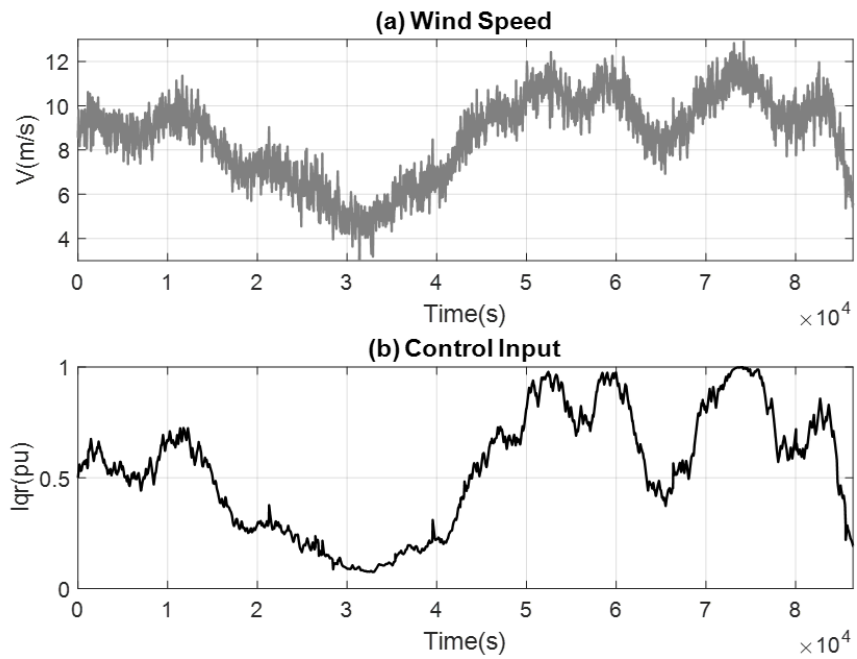

Figure 8.14. (a) Wind speed during one day (b) control input defined by MPC

speed and consequently increased the P_s.

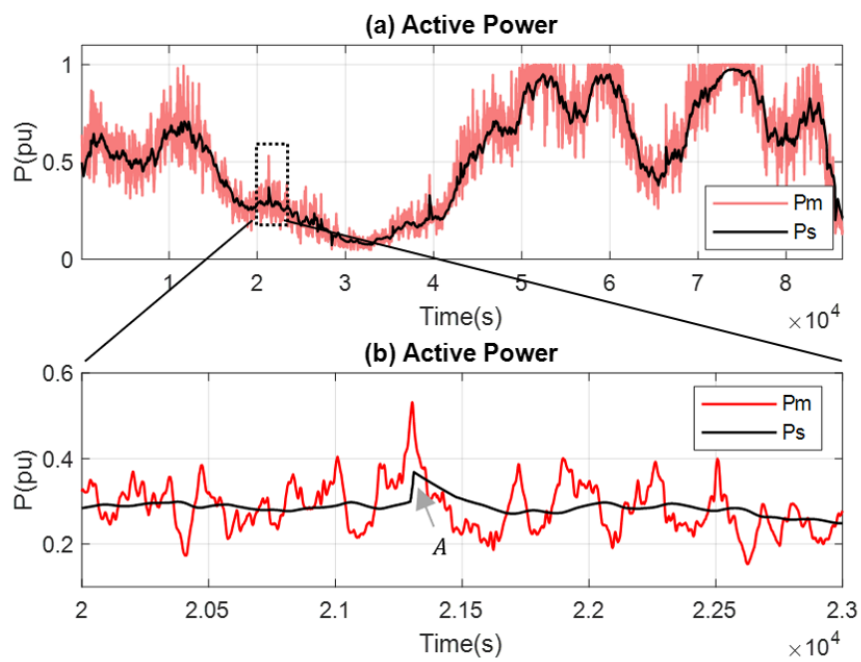

Figure 8.15. The system's active power injected into the power grid (a) during an entire day (b) in a zoomed-in window of time

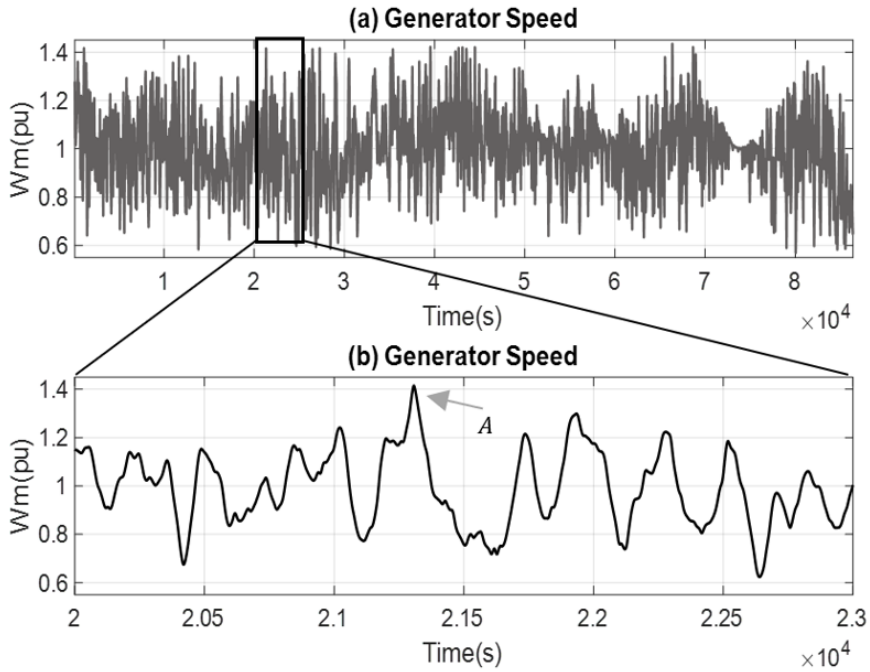

Figure 8.16. The generator speed (a) during an entire day (b) in a zoomed-in window

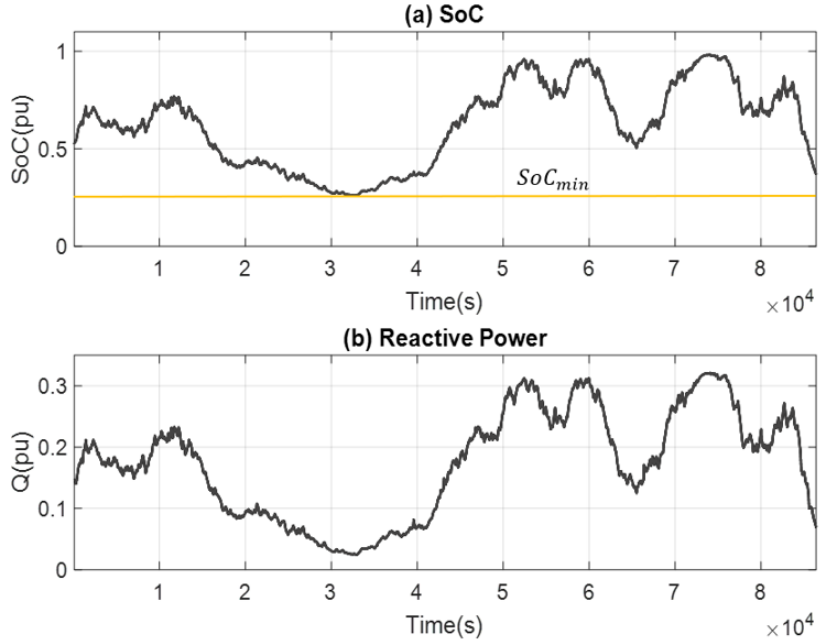

Figure 8.17. (a) SoC of the storage during an entire day (b) reactive power of the wind turbine (the turbine set to operate with 0.95 power factor)

Figure 8.16 demonstrates that the proposed controller can maintain the generator speed within limits. In case the generator speed exceeds its limits, the converter cannot produce the voltage to support the excitation needed, and the generator control could be lost. Therefore, the constraint violation penalty weight in 8.24 is set larger for the speed variable. The storage SoC is handled by the SoC-feedback control strategy and remains within the 20-95% range, as shown in Figure 8.17 (a).

The generator is controlled to operate with a power factor of 0.95 capacitive, as shown in Figure 8.17 (b). The minute-by-minute power fluctuations of the mechanical and electrical powers are demonstrated in Figure 8.18. This figure demonstrates a significant fluctuation

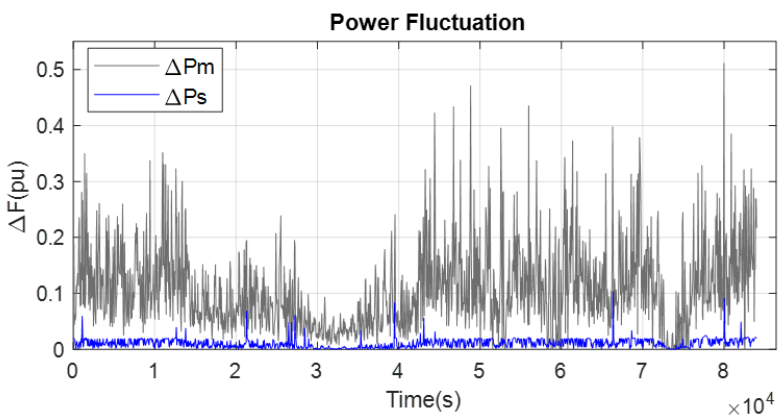

Figure 8.18. The minute-by-minute fluctuation of mechanical power of the hydraulic motor (P_m) and the electrical power injected into the grid (P_s)

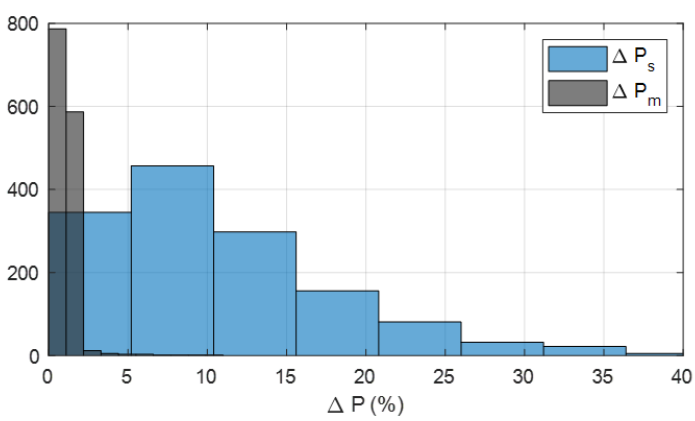

Figure 8.19. Histogram of fluctuation of the mechanical power of the hydraulic motor (δP_m) and the electrical power injected into the grid (ΔP_s)

reduction through the proposed drivetrain configuration and the selection of storage. The histogram of the mechanical and electrical power fluctuations (Figure 8.19) indicates that most electric powers have less than 2% fluctuation and are on target to meet the expectations. However, this percentage can be a variable to quantify the power quality for the desired performance. Accordingly, an indicator is defined as the probability of electrical power fluctuations which are less than a desired γ_{min}%, i.e., $\zeta = p(\Delta P_s \leq \gamma_{min})$. Utilizing the ζ indicator, the effect of different storage capacities, different inverter sizes, and different generator inertia on the output electric power and the power of storage can be evaluated.

8.3.1 Analysis of Storage Capacity and Inverter Size

The converter size and energy storage size directly impact the amount of power that the storage can provide. It is considered that the converter size varies from 20% to 50% of the nominal power, and the storage capacity varied from $40 - 400\,kWh$. Figure 8.20 (a) demonstrates how ζ is influenced by these variations. As the figure shows, in small storage sizes (e.g., 40 and $80\,kWh$), the amount of ζ is small, and changing the inverter size does not improve the power quality. In these cases, the SoC feedback controller attenuates the mechanical power P_m with small time-constants, T_f. Therefore, the output power, P_s, changes considerably while the controller tries to track the reference power P_s^*.

On the other hand, when the size of the storage increases, the amount of ζ increases as well, and the output power variations are reduced. This trend has been demonstrated through the Bode analysis in Figures 8.7 and 8.8. These figures show that the cut-off frequency of the low-pass filter decreases as T_f increases. For large storage capacities, the larger inverter sizes result in larger ζ. However, the power attenuation of the system slightly decreases at a larger storage size. The reasons are the larger time constant of the SoC-feedback control and consequently slower power reference P_s^* variations. This enhances the probability of meeting the speed constraints. The effect of inverter size on the storage's maximum power is shown in Figure 8.20 (b). As the figure shows, the larger the inverter, the larger the power from energy storage. The size of the inverter is proportional to the maximum slip of the generator. However, the energy storage size does not change the

amount of storage power. It is observed that the maximum power fluctuation (Figure 8.20 (c)) correlates with the inverter size and slightly changes with the storage size.

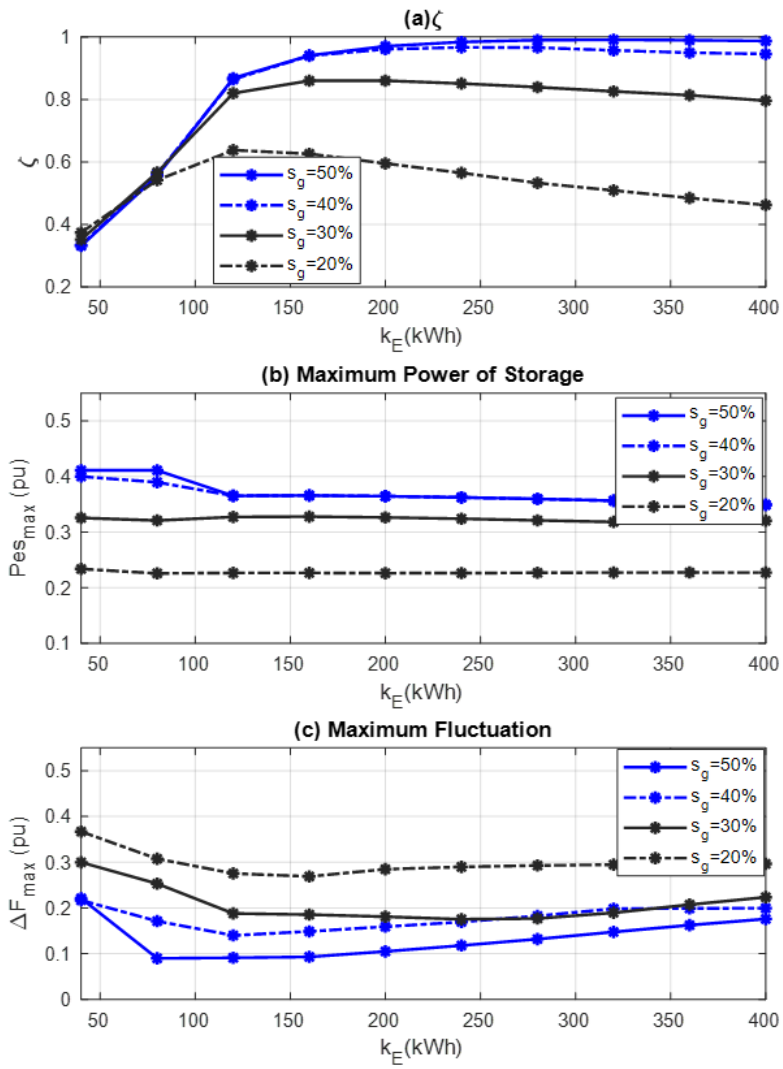

Figure 8.20. (a) ζ (b) maximum power of storage (c) maximum fluctuation of the output power

8.3.2 Analysis of Generator Inertia

The combined inertia of the generator and hydraulic motor can slow down the acceleration and deceleration of the generator shaft. This prevents the reach of speed limits in most cases. Figure 8.21 (a) shows the effect of inertia on ζ. It is observed that when the inertia of the

generator increases, the output power fluctuations decrease. It is also observed that the maximum power of the storage decreases while the inertia increases, Figure 8.21 (b). This demonstrates that increasing the system inertia through a flywheel energy storage on the generator shaft can decrease the maximum storage power and demand a low-power high-energy storage type, e.g., a battery. It is observed in Figure 8.21 (c) that the maximum fluctuation of the output power P_s decreases at higher inertia. On the other hand, increasing the storage capacity shows no impact on the maximum fluctuation and maximum storage power (Figure 8.21). For instance, the inertia constant of 22 seconds results in optimal energy storage of 160 kWh (for 0.1 h) and a 0.3 pu inverter. A hybrid combination of battery and supercapacitor is a suitable option in this case.

According to the impacts observed through storage capacity, inverter size, and generator inertia, suitable storage types can be discussed as follows:

- It is observed that the maximum power passing through terminals of the generator rotor windings determines the size of the inverter and correlates with the maximum generator slip.

- Changing the energy storage capacity (e.g., utilizing BESS and SCESS) does not decrease the maximum fluctuation of the output power. However, the FESS can be more effective in reducing the maximum fluctuation of the output power.

- Increasing the inertia of the generator reduces the size of the inverter and attenuates power fluctuations. Therefore, it is recommended to utilize a two-pole generator in such systems. This allows taking full advantage of the generator inertia constant, H.

- Providing additional inertia by employing a FESS coupled directly to the generator shaft is feasible. This can increase the inertia constant further and decreases the inverter size and power rating of the storage. Another advantage of this method is that the FESS responds intrinsically without any delay, does not need additional components, and has no computational burden.

- To decrease the maximum power of BESS at the DC link, employing the supercapacitor alongside BESS is a suitable option. In this case, the configuration in Figure 8.3

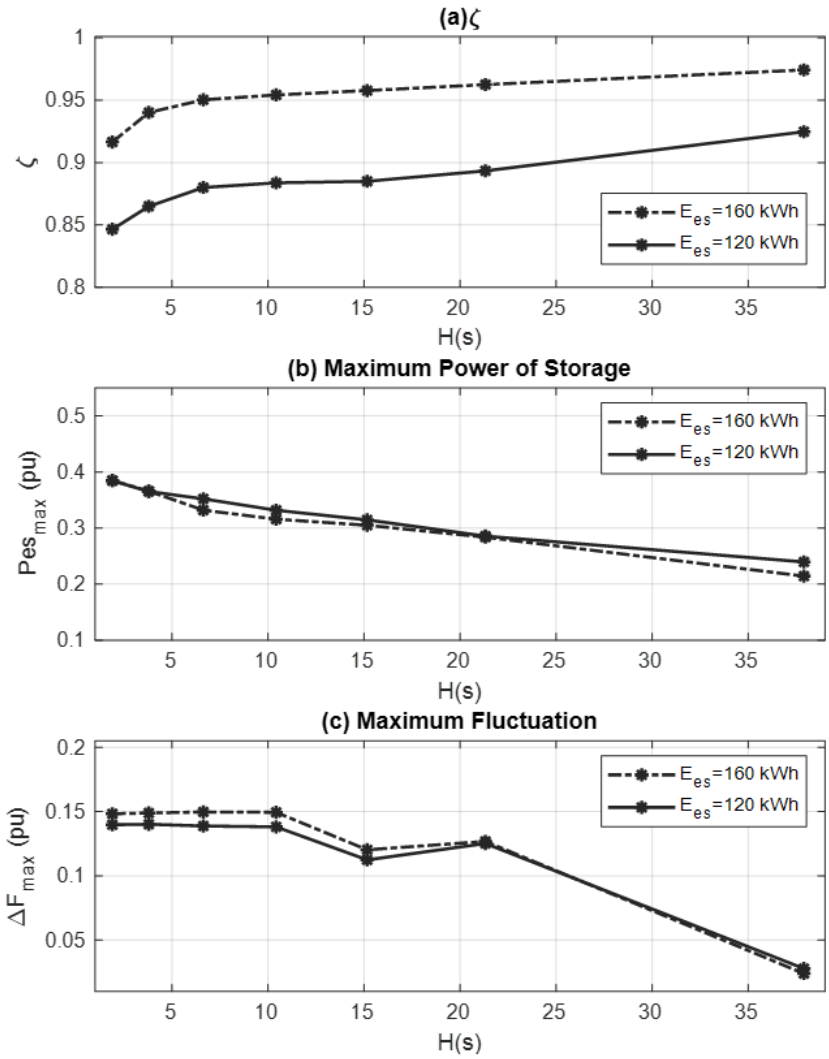

Figure 8.21. (a) ζ (b) maximum power of storage (c) maximum fluctuation of the output power

improves the supercapacitor capacity. Meanwhile, the DC link voltage is stable due to the existence of the BESS, which allows for a smaller inverter size.

8.4 Summary

This chapter introduced a method to integrate HESS with the DFIG-based SS-WECS. The goal was to improve the power generation profile. In this system, HTS was employed to decouple the generator shaft from the wind turbine shaft. Using the SS-WECS, the GSC was eliminated while providing a possibility to integrate HESS at the DC-link. The SoC feedback

strategy was utilized to manage the storage energy and adjust the output power. An MPC was then utilized to control the output power to reduce its fluctuation while the generator's speed constraints were satisfied. Then, the effects of increasing the size of the storage and the inertia of the system on the size of the components were evaluated. Furthermore, it was shown that increasing the inertia of the system resulted in utilizing storage with less nominal active power. The proposed system had the potential to decrease the system's cost and reduce the LCOE because it utilized only one power converter that controlled the DFIG and attenuated the output power fluctuation through charging and discharging the storage. This configuration incorporated hybrid energy storage and required no extra converter.

9. OPTIMIZATION OF HYBRID ENERGY STORAGE FOR SS-WECS

In the previous chapter, an SS-WECS is proposed that incorporated a HESS while keeping the minimal size of supporting components. This HESS consists of Flywheel Energy Storage System (FESS), Super-capacitor Energy Storage System (SCESS), and Battery Energy Storage System (BESS). BESS and SCESS are directly integrated into the DC-link of RSC, and FESS is coupled directly to the generator's shaft. Characteristics of these storage units are different. For instance, BESSs are suitable for low power with high energy capacity applications. However, FESS and SCESS can provide high power in a short time, but their energy capacities are much smaller than BESS [109], [110]. In this chapter, the optimal size of the HESS is calculated using the response surface method (RSM) to attenuate the output power fluctuations. Furthermore, with the same Level of Smoothness (LOS), A storage cost analysis compares the proposed HESS with its counterpart.

9.1 Optimization of HESS

Optimizing the size of the HESS employed in the configuration proposed in the previous chapter, which comprises three types of energy storage, is essential. Since each energy storage has a different lifetime, optimizing the annualized cost of the storage is more logical. Therefore, the annualized cost of storage is considered the objective function, which is defined as follows:

$$C = \sum_{\mathrm{i}}^{3} \left(\frac{C_{\mathrm{i}}^{inv} + \sum_t \left(\frac{C_{O\&M}^{\mathrm{i}-t}}{(1+r)^t} \right)}{N_{\mathrm{i}}} \right) \tag{9.1}$$

where i is an index for each energy storage, and t indicates the year. N_{i} and C_{i}^{inv} are the lifetime and investment costs, respectively. $C_{O\&M}^{\mathrm{i}-t}$ is the operation cost of ith energy storage at year t. The objective function of the HESS sizing is well defined mathematically. On the other hand, the purpose of the optimization is to find the optimal size of the HESS, such that the LOS (defined as the probability of the minute-by-minute output power fluctuation

less than 2%) is greater than 95% over the simulation time. This can be expressed as follows:

$$\hat{\zeta} = f_{\zeta}(E_b, H, S_g) > 0.95 \tag{9.2}$$

The smoothness level, ζ, depends on the parameters of the HESS and the maximum slip of the generator, and it is a statistical function. The cost of each storage is based on the year 2018, expressed in US dollars.

9.1.1 HESS Cost Model

BESS Cost Model

The capital cost of the Lithium-ion battery is reported to be $271\,\$/kWh$ in 2018 for a 4-hour battery [58], [59]. However, in this paper, the ratio of the battery capacity to the battery power is not necessarily 4 hours. To obtain the cost coefficient of the BESS, the battery pack data for the electric vehicle have been used [145]. Then, the estimated cost is obtained as follows:

$$\frac{C_b^{inv}}{P_b}\left(\frac{\$}{kW}\right) = \alpha_b + \beta_b \frac{E_b}{P_b} \tag{9.3}$$

The maintenance and operation costs of the battery are considered negligible at a rate of $10\,\$/kW - year$. The battery is expected to last ten years [58], [59].

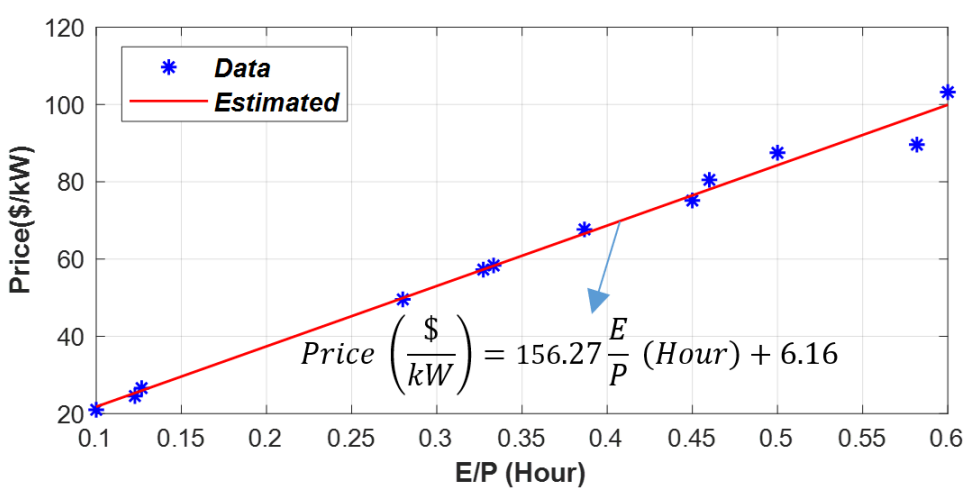

Figure 9.1. Cost estimation of battery based on the data in [145]

SCESS Cost Model

Super-capacitors can use multiple modules to scale the necessary power and energy capacity. Given the low energy density of super-capacitors, their cost is not competitive with the $\$/kWh$ of batteries. However, on the $\$/kW$ basis, they are more competitive than batteries due to their high-power density. Therefore, they are suitable for short-time storage. Herein, the super-capacitor is employed to smooth the battery power. The capital cost of the super-capacitor is reported $32,500\,\$/kWh$ in [58], [59] and $10,000\,\$/kWh$ in [146]. Herein the capital cost of the $10,000\,\$/kWh$ is considered. The lifetime of the super-capacitor is more than 1,000,000 cycles or 16 years. The super-capacitors fixed operation and maintenance cost is about $1\,\$/kW - year$ [58], [59].

FESS Cost Model

Obtaining the cost of FESS is challenging due to the lack of data in the literature. In [58], [59], the capital cost of the FESS, including the power conversion system, is reported in a wide range of $600 - 2400\,\$/kW$ for a $0.25 - hour$ duration of storage, which is equivalent to $2400 - 9600\,\$/kWh$. In these references, the overall cost of the FESS is estimated to be $4320 - 11520\,\$/kWh$. The lower estimation of the cost is for low-speed FESS. The overall cost of the FESS is estimated to be in the range of $1000 - 8800\,\$/kWh$ in [61]. However, the low-speed flywheels, which rotates at less than 10000 revolutions-per-minute (rpm), are usually made out of steel and can provide power in thousands of kilowatt for a short time [147]. These reports include the capital cost of the power electronic converters and the motor. However, our proposed configuration does not need the motor/generator and the dedicated power electronic converter. In [147], the capital cost of the flywheel rotor is calculated to be $523 - 573\$/kWh$ for a high-speed FESS in which the two-rim rotor is made of two composite materials. In [148], the estimated capital cost of the rotor is about $2\,\$/kWh$.

Since the capital cost of the flywheel rotor is estimated in a wide range of $2 - 11520\,\$/kWh$ in the reports, a new approach is taken to estimate the capital cost of the FESS and capital cost of the rotor, bearing, and the housing. Herein, a low-speed rotor is considered to be

connected to the shaft of the DFIG directly. A solid disc of steel or aluminum is chosen for the rotor [149]. Therefore, the inertia and mass of a solid disc can be obtained as follows:

$$J_f = \frac{\pi h}{2} \rho r_f^4 \tag{9.4}$$

$$M_f = \pi h \rho r_f^2 \tag{9.5}$$

where r_f and h are the radius and thickness of the solid disc, respectively. ρ is the density of the stainless steel. J_f and M_f are the inertia and mass of the disc. According to these equations, the energy content and specific energy (energy per one unit of mass) can be obtained as follows:

$$E_f = \frac{\pi h}{4} \rho r_f^4 \omega_m^2 \tag{9.6}$$

$$E_f / M_s = \frac{1}{4} r_f^2 \omega_m^2 \tag{9.7}$$

The cost of the rotor can be calculated based on these equations as follows:

$$C_r(\$/kWh) = \frac{M_r C_s}{\lambda_t E_r} = \frac{4C_s}{\lambda_t r_f^2 \omega_m^2} \tag{9.8}$$

where C_s and C_r are the cost per kilogram of the rotor's material and the rotor's cost per kWh. The coefficient λ turns the unit of energy to kWh ($\lambda_t = 2.77778e-7$). Based on the relative cost of different materials in [149], the cost of storage per unit of energy for a generator speed of 3600 rpm can be obtained as shown in Figure9.2. Accordingly, the cost of the rotor for steel-4340 is minimum due to the lower cost of the material. According to 9.8, the larger the radius of the disc, the lower the cost of the rotor. The cost of the rotor made out of steel-4340 for various generator speeds is calculated and shown in Figure 9.3. The material used in the rotor decreases when the speed of the rotor increases to obtain the same amount of energy content. At a 1-meter radius, the cost of the rotor is 15, 60, and 240 $\$/kWh$ for 7200, 3600, and 1800 rpm, respectively.

The thickness of the rotor does not affect the cost per kWh of the rotor. Since the speed of the rotor is low, the radial tensile of the rotor is not an issue. Therefore, the thickness of

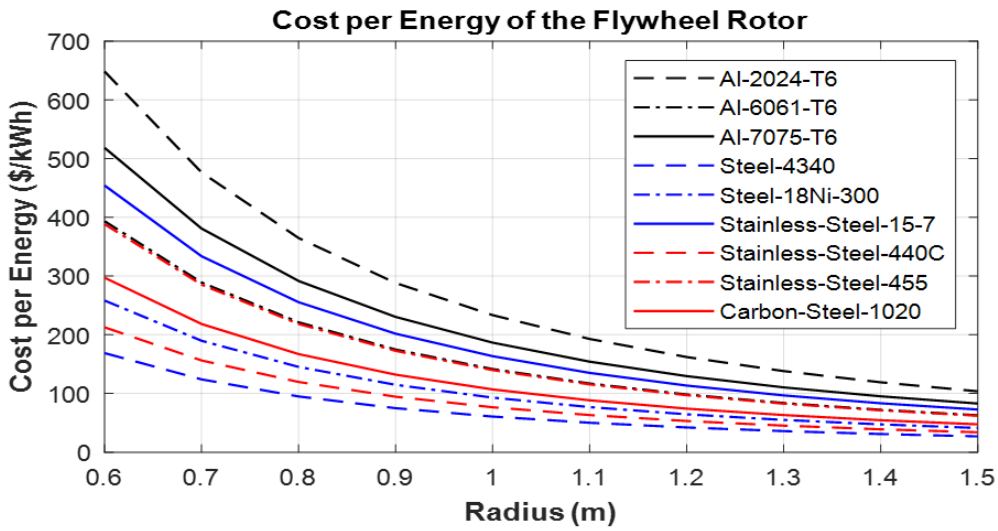

Figure 9.2. Cost per kWh for different materials at 3600 rpm speed

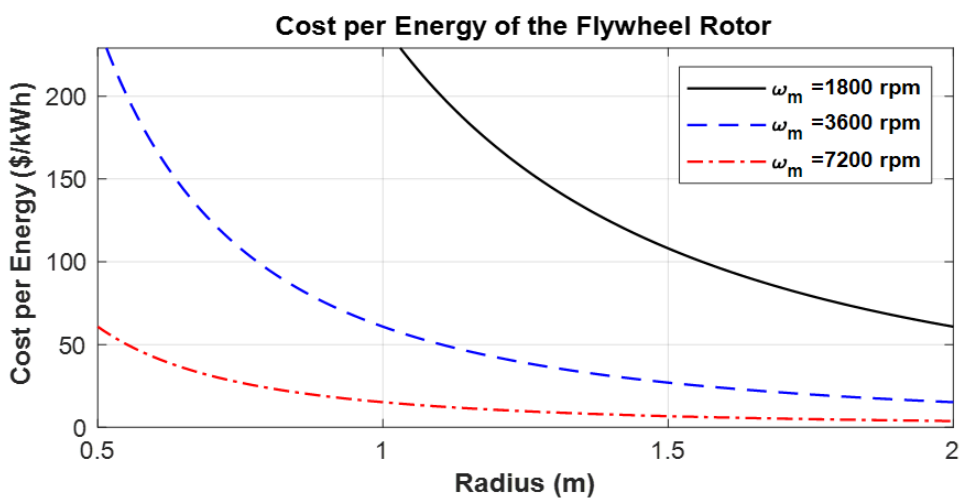

Figure 9.3. Cost per kWh of steel-4340 for various speeds

the rotor is chosen as a percentage of the rotor radius. For a 3600-rpm rotor and 1.5-MW DFIG, the cost of inertia constant (H) can be obtained for different thickness ratios to the rotor's radius, as shown in Figure 9.4. For 3600 rpm, the cost of the rotor is calculated as $60\,\$/kWh$. The flywheel's cost is three times the estimated value, $240\,\$/kWh$, because of housing and bearing. Since there is no power electronic converter and motor generator, the operation and maintenance of the system are considered negligible. The life of the storage is considered 20 years.

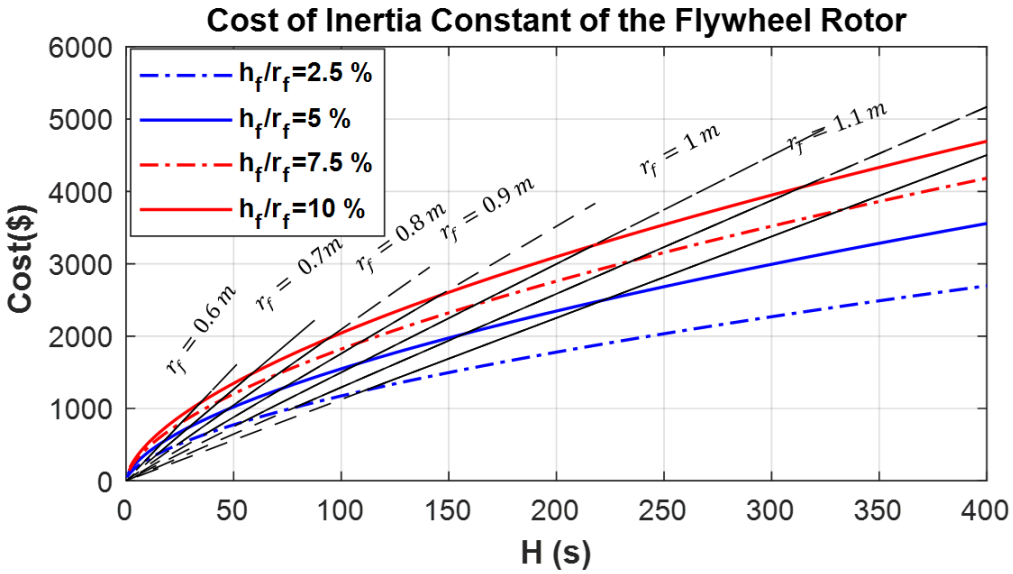

Figure 9.4. Inertia constant cost of the rotor for various h_f/r_f

Power Conversion System Cost

The power conversion system in the proposed configuration comprises a DC/AC inverter named RSC to control the DFIG and charge and discharge the battery and a DC/DC converter to control the power of the supercapacitor. The cost of the power converter is considered 288 $\$/kW$ for a lithium-ion battery [58], [59]. Commonly, this power converters consist of DC/DC and AC/DC stages. Since the RSC is a single-stage power converter, the RSC and DC/DC converter cost is 144 $\$/kW$.

9.1.2 Optimization Method

The HESS in the proposed configuration consists of three types of storage: flywheel, battery, and supercapacitor. These three storage systems seem suitable because the battery can be connected to the RSC without additional power converters, and the flywheel can be directly connected to the DFIG rotor. The purpose of the optimization is to minimize the annualized cost of the storage such that the smoothness level is greater than 0.95%, $\zeta > 0.95$. The objective function is expressed in 9.1, but the constraints of such optimization are stochastic variables and cannot simply be stated in mathematical equations. Therefore,

the HESS sizing in such a system involves the interactions of many variables in a non-linear and complicated system. Using the classical methods to optimize the HESS is not entirely practical since it needs many simulations runs and is time-consuming. A statistical-experimental method such as the Response Surface Method (RSM) could be a better option to overcome these limitations [150], [151].

Response Surface Method (RSM)

RSM combines statistical and mathematical approaches to optimize stochastic processes. Commonly, this approach is employed to estimate a stochastic cost function by a low-order polynomial, mostly second order, on a small subregion of the domain. The cost function and coefficients of the polynomial are estimated for several observation points using the least square approach. Then, the suboptimal point is obtained mathematically using the formulized cost function. This optimal point is used as a center for a new subregion of interest to end up the optimum point. In this approach, the subregion should be chosen small enough to estimate the response surface by a low-order polynomial. At the same time, the subregion should be large enough to prevent a large number of simulation (or experimental) runs. Choosing the number of points depends on the order of the polynomial and the number of variables of interest. For example, in this paper, the level of smoothness is estimated as a quadratic function by three factors: battery capacity, inertia time constant, and the maximum slip of the generator. Each factor can be defined in three or five levels to calibrate the quadratic function effectively. Herein, the three-level Central Composite Designs (CDDs), also known as Box-Wilson designs, are employed. The faced-pictured CDDs are shown in Figure 9.5. Each design consists of a factorial design (the corners of a cube) with the center and star points, which allow estimating the quadratic function. The center point is repeated several times to estimate the quadratic function better. These points are enough to estimate the $(n+1)(n+2)/2$ coefficients of a quadratic function with n factors.

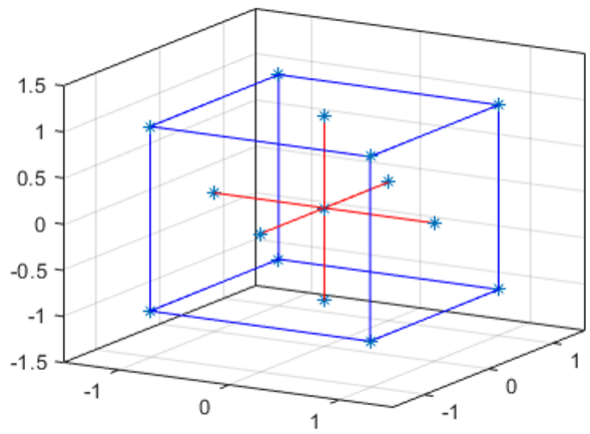

Figure 9.5. CDDs for a 3-factor quadratic function

Overview of the Optimization Approach

The overall flowchart of the optimization is shown in Figure 9.6. Since the optimization region is large, randomly choosing the start point can increase the steps of the optimization process. Thus, a starting point, the center of CDDs with more nuanced points, is chosen by simulation 15 points with an extensive CDDs network over the whole region. It is considered to have a battery capacity of 60-140 kWh, inertia constant of 50-500 s, and a maximum generator slip of $5 - 30\%$. The surface response of the configuration is complicated, and estimating a complex surface with a quadratic function can have a significant error. Still, the optimal point of this surface can be a good point (the center point of the CDDs) to start from there.

Based on the first starting point, the CDDs points are defined in a smaller subregion. Then, the simulation data of these points gather, and the optimal point in the subregion is obtained. Then this point is chosen as the center of the new CDDs, and this center point, as the optimal point of the subregions, moves toward the optimal point in the whole region. When the stopping criteria become satisfied, the optimization process ends. The stopping criteria are chosen as follows, as recommended in [152]: 1) the estimated optimal response does not change significantly, 2) the cost of the optimal response does not change significantly and continues to decrease, 3) real ζ (not estimated one) remain above the predefined amount (herein 0.95).

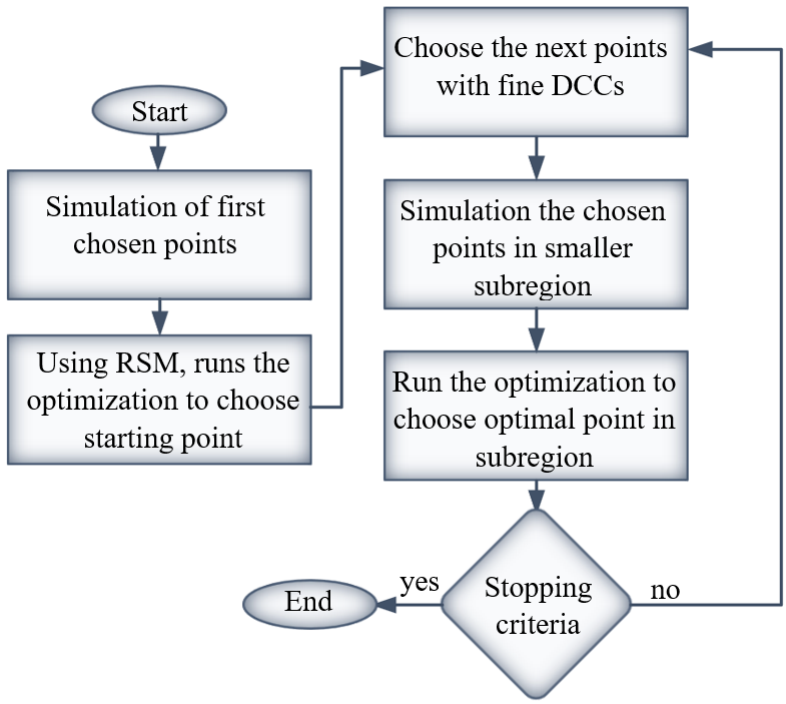

Figure 9.6. Optimization diagram

9.2 Results and Discussion

The proposed configuration is modeled to evaluate its feasibility. Accordingly, a detailed model of each element is obtained in MATLAB, with the initial parameters [121]. In general, there are six parameters to be defined: battery power (P_b), battery capacity (E_b), inertia constant (H), supercapacitor power (P_s), supercapacitor capacity (E_s), and maximum slip of the generator (s_g^{max}). Among these six parameters, the inertia (H), battery size, and the generator maximum slip are considered independent parameters. First, using the supercomputer, we simulate the split-shaft wind energy conversion systems with different operating points by sweeping inertia (H), battery size, and the generator maximum slip. Figure 9.7 demonstrates the smoothness level $\zeta = p(\Delta P < 2\%)$ for the simulating points shown by stars on each surface. Figure 9.8 shows the maximum power passing through the rotor of the DFIG, which is the sum of the power from the battery and supercapacitor. Figure 9.9 and Figure 9.10 demonstrate the supercapacitor capacity and power, respectively.

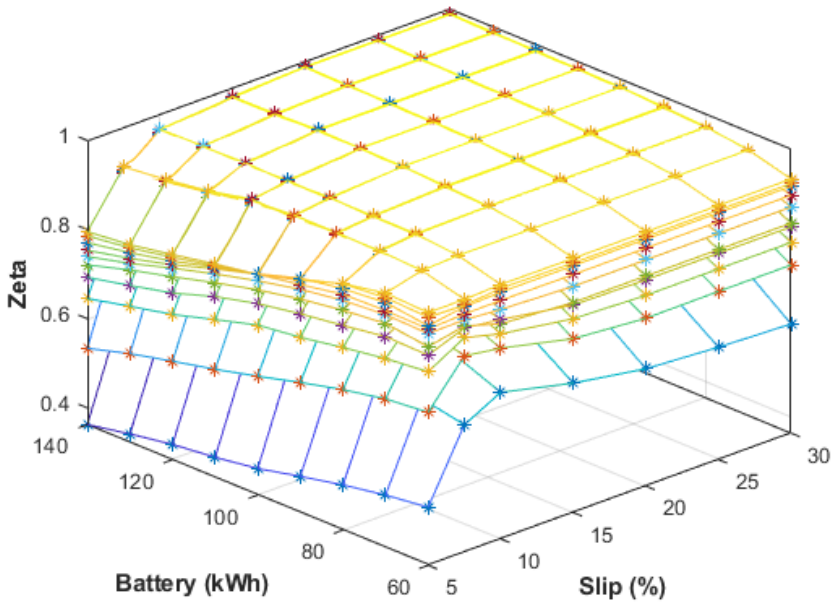

Figure 9.7. The smoothness level (ζ) for different operating points. Each surface belongs to a set of points with defined inertia constant

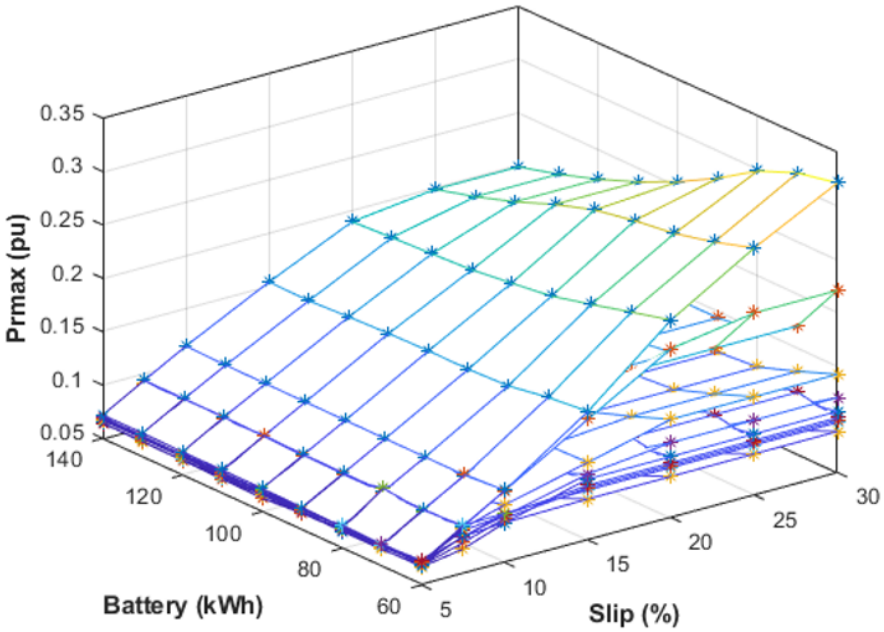

Figure 9.8. The power at the rotor of DFIG at different operating points. Each surface belongs to a system with defined inertia constant

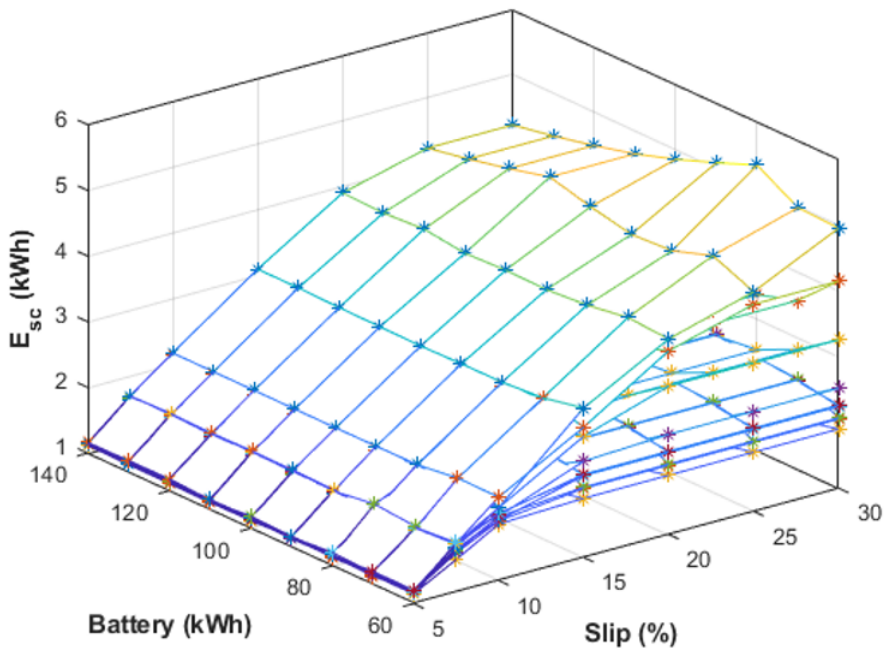

Figure 9.9. The Super-capacitor capacity for different operating points. Each surface belongs to a set of points with defined inertia constant

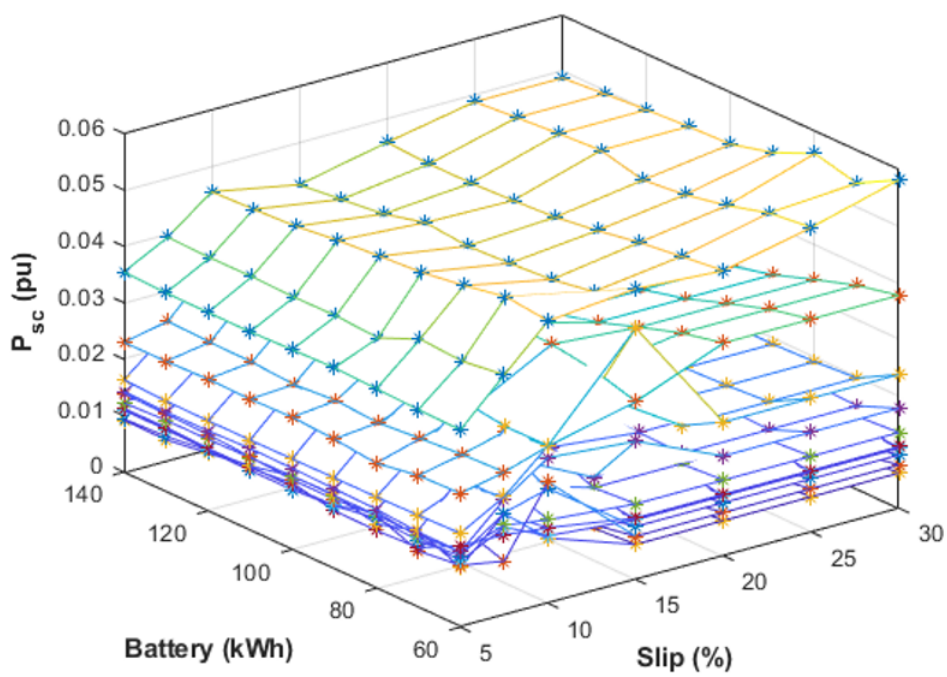

Figure 9.10. The power of supercapacitor for different operating points. Each surface belongs to a set of points with defined inertia constant

Using the optimization method explained in Figure 9.6, the components of HESS are optimized to sustain the power required and minimize the storage cost. The results are tabulated in Table 9.1. According to the table, the optimum annualized storage cost is 5411 \$/year. Also, the iteration of the optimization is shown in Table 9.2. This optimization method helps to reach the optimal point with fewer iterations. The trajectory of the overall cost of the storage in each optimization iteration is shown in Figure 9.11. This figure demonstrates a rapid convergence rate. The red point at iteration 2 shows that the real ζ is less than 0.95. Thus, the third stopping criterion does not satisfy, and the optimization process continues to reach the optimal point at iteration 10.

Table 9.1. Optimal Energy Storage

$E_b(kWh)$	**H(s)**	$S_{max}(\%)$	$P_b(kW)$	$E_{cap}(kWh)$	$P_{cap}(kW)$
90.25	325.64	8	107	0.88	21.44

Table 9.2. Iteration of the Optimization

Iteration	$E_b(kWh)$	$H(s)$	$S_{max}(\%)$	$Cost(\$)$
1	100	275	17.5	6737.36
2	83.31	322.33	13.53	5687.12
3	88.28	312.33	12.53	6083.85
4	90.95	302.33	11.53	5919.71
5	91.29	304.87	10.53	5770.81
6	92.72	310.42	9.53	5662.25
7	97.72	306.7	8.53	5571.42
8	100.24	316.7	7.73	5524.02
9	95.25	311.63	7.91	5446.54
10	**90.25**	**321.63**	**7.94**	**5411.12**
11	89.99	325.64	8.05	5446.08

For the optimized size of storage obtained in iteration 10 and listed in Table 9.1, a wind speed profile of Figure 9.12 (a) is applied to measure the wind turbine performance. The generated mechanical and electrical powers are shown in Figure 9.12 (b), and it is shown that the electric output power fluctuations have been attenuated noticeably. Also, battery SoC and generator speed are shown in Figure 9.12 (c) and Figure 9.12 (d), respectively. The

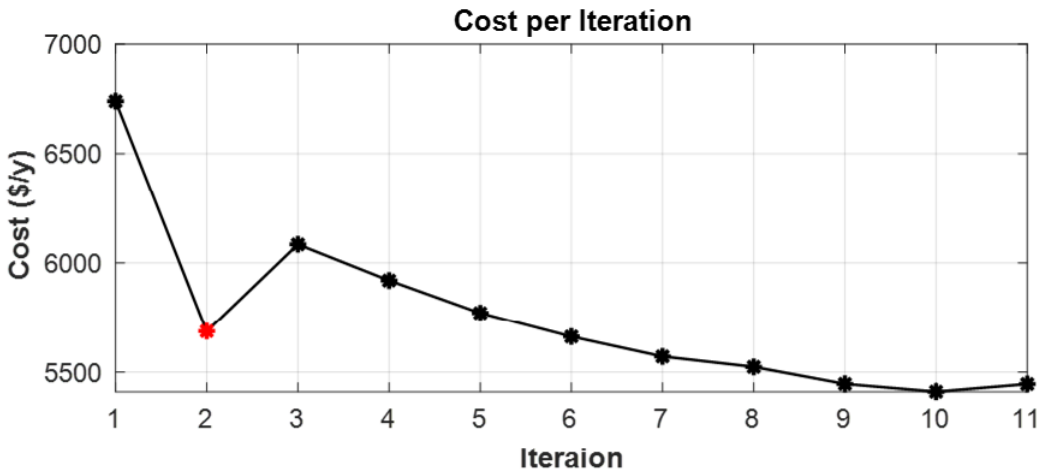

Figure 9.11. The overall cost function per iteration

inertia of the flywheel attenuates the speed variation of the generator considerably, and the controller was able to manage the speed within its limits (less than 7.94%).

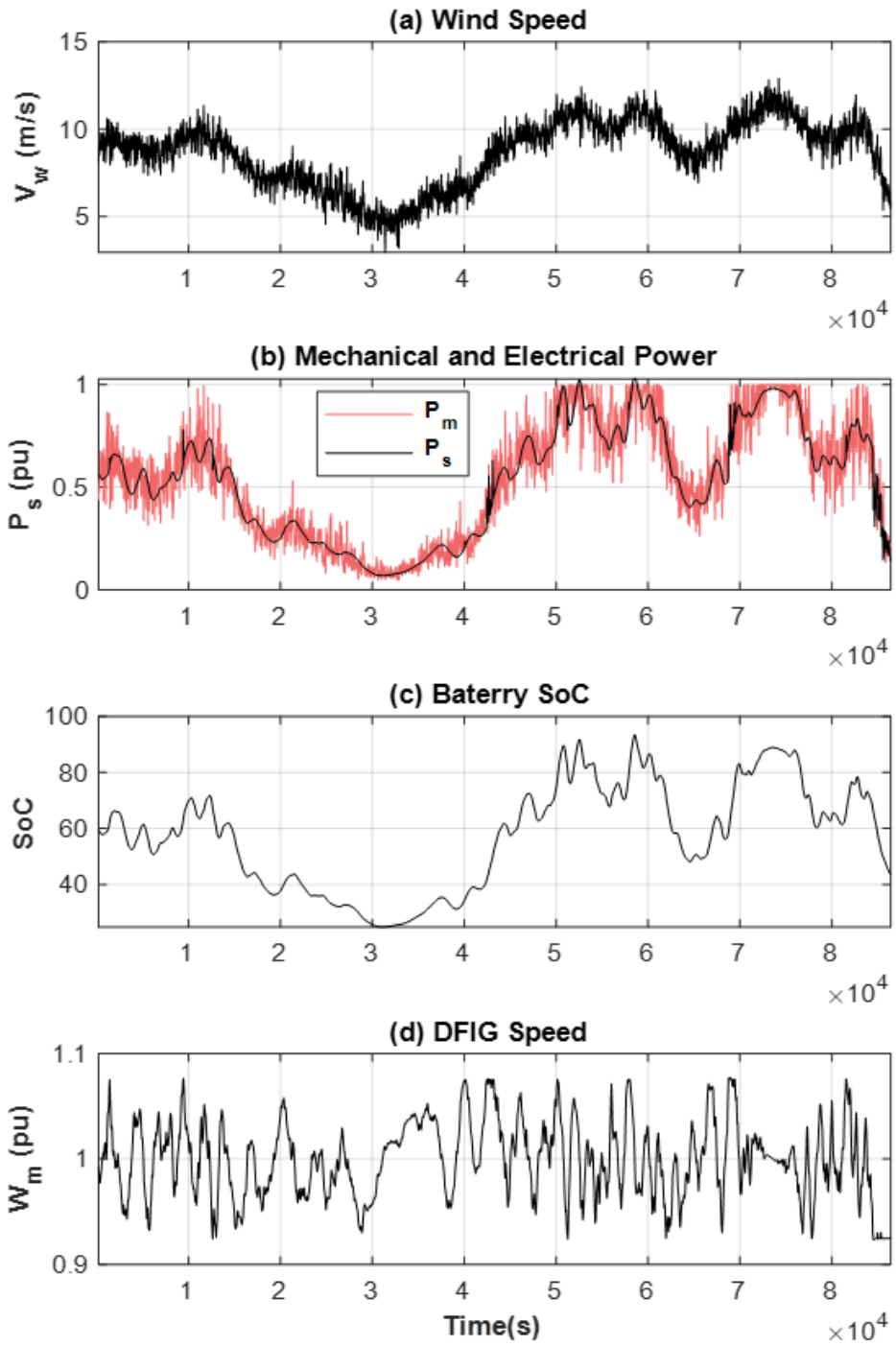

Figure 9.12. (a) wind speeds over 24 hours (b) DFIG mechanical power and electrical power injected into the grid (c) SoC of battery (d) the speed of DFIG

9.2.1 The Effect of the Smoothness Level on HESS Size and Cost

The annualized storage cost is shown in Figure 9.13 for a different level of smoothness. It is shown that the cost of storage increases exponentially as the level of smoothness increases. It can be inferred that the smoothness level one ($\zeta = 1$) is not a practical approach.

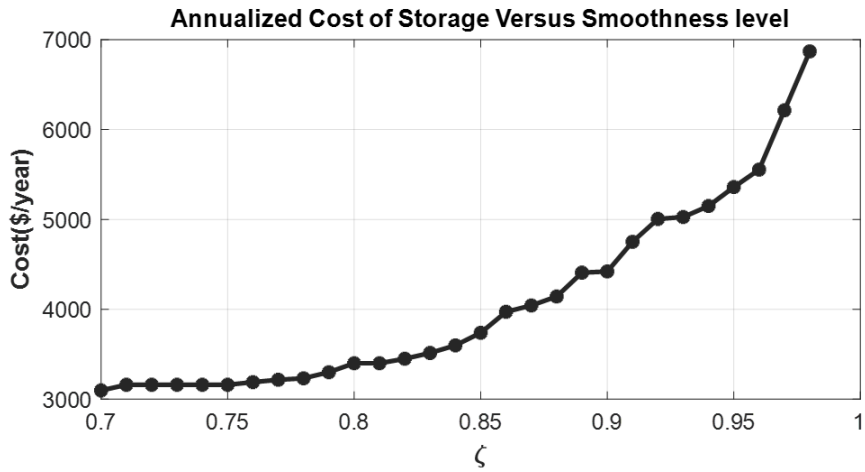

Figure 9.13. The annualized cost of the storage for different levels of smoothness

9.2.2 The Comparison of HESS Cost

To benchmark the result of the HESS optimization, the proposed configuration is compared with three different HESS. These three scenarios are as follows:

- In the **first scenario**, the proposed storage configuration consists of a flywheel, battery, and supercapacitor.
- In the **second scenario**, the flywheel is removed, and only the battery and supercapacitor are employed.
- In the **third configuration**, a battery-supercapacitor in hybrid storage is installed at the Point of Common Coupling (PCC). Thus, the power electronic converter required for the battery consists of AC/DC-DC/DC units, which cost twice the converter employed in the proposed configuration.

The cost associated with these three scenarios is shown in Figure 9.14. Accordingly, the annualized storage costs are \$54,111, \$15,001, and \$18,693 per year for scenarios 1, 2, and 3, respectively. The breakdown cost of each unit in each scenario is shown in Figure 9.14 and tabulated in Table 9.3. The relative costs of HESS are 29%, 80%, and 100% for scenarios 1,2, and 3, respectively. The flywheel cost is only 29.7% of the overall annualized storage cost in the first scenario. However, it does have a noticeable effect on the performance of the hybrid storage and decreases the cost of storage to 29% of conventional storage cost. In the second scenario, there is no flywheel, and the HESS consists of a supercapacitor and battery, which are integrated with the split-shaft WECS and take advantage of the RSC and do not need an additional dedicated power converter.

The cost of the HESS in scenario 2 is about 80% of the cost of the HESS in scenario 3, and this cost-saving is mainly because of the reduction in the cost of a power electronic converter. The cost of the power electronic converters in the third scenario takes up 50% of the hybrid storage cost and is more significant than in scenario 2. The battery and supercapacitor costs in scenario 3 are slightly smaller than the cost of these parts in scenario 2. This is because the storage performance is not limited by the speed of the generator (slip limitation) in the third scenario. Since there is no flywheel in scenarios 2 and 3, these configurations require a larger capacity of the HESS to achieve the desired level of smoothness. The simulation and optimization results demonstrate that the proposed configuration could smooth the output power by a HESS with 29% of the cost of a conventional standalone HESS.

Table 9.3. Optimal Energy Storage

Scenario	**Cost (\$/y)**	**Battery cost(%)**	**H cost(%)**	**SC cost(%)**	**PCS cost(%)**	**Relative cost**
1	5411.1	41.6	29.7	10	18.7	0.29
2	15001	49.2	0	14.1	36.7	0.8
3	18693	37.4	0	11.8	50.8	1

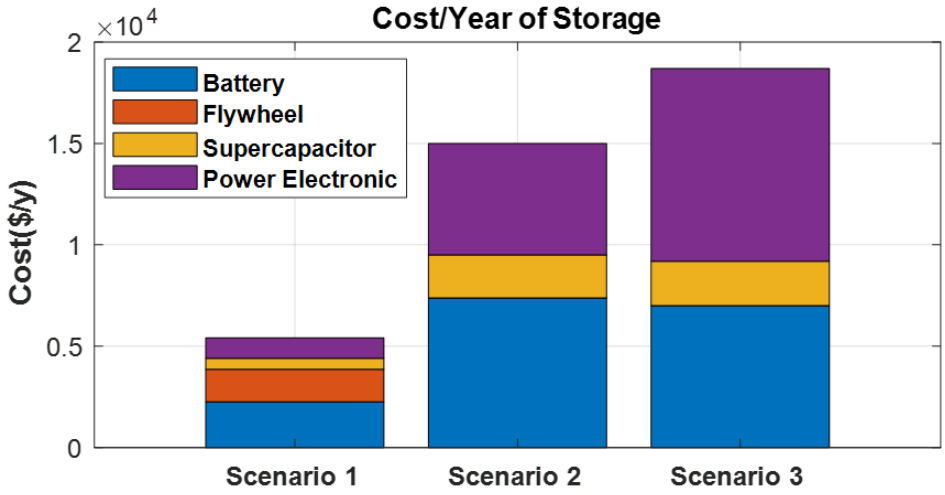

Figure 9.14. The annualized cost of the storage for various scenarios

9.3 Summary

In this chapter, an optimization process has been conducted to find the optimal size of the HESS employed in the previous chapter. The SCESS and BESS costs were calculated based on the data available in the literature. However, due to the lack of data about the cost of the flywheel, a methodology was employed to estimate the cost of the flywheel based on its material in this chapter. Then, the cost of each storage was formulated based on their specific properties. The response surface optimization technique was utilized to obtain the optimum hybrid storage size. The proposed optimization technique allowed for the optimization of various system configuration scenarios. The comparison of the proposed method with the conventional storage showed that the storage cost could be decreased by 29%.

10. LVRT CAPABILITY OF DFIG-BASED SS-WECS

This chapter investigates the LVRT capability of the DFIG-based SS-WECS proposed in chapter 7 [120], [121] that employed a reduced size rotor side converter. Four strategies based on the active crowbar (C), crowbar with series resistor-inductor (C-RL), Series Dynamic Resistor (SDR), and New-Bridge Fault Current Limiter (NBFCL) are adopted for the system, and the results and performance of these protection circuits are compared to show the LVRT capability of such a system.

10.1 LVRT Challenges for DFIG

The challenges that WECS has under fault and low-voltage cases are twofold: first, those are related to the requirements dictated by grid codes [114]–[117]; second, challenges associated with the protection of the system [80], [81].

10.1.1 Grid Code Requirements

According to recent grid codes [114]–[117], wind turbines should remain connected to the power grid during the voltage dip and withstand a particular voltage dip for a specific time before the trip off. This is because an unnecessary disconnection might degrade voltage restoration after faults and severely affect the transient and steady-state stability of power system operation [118]. Moreover, some transmission system operators expect the power generation unit to inject reactive power into the grid during a fault to improve voltage recovery. The expected reactive power depends on the voltage dip amount and can be different for different transmission operators [116].

10.1.2 Protection Measures

On the other hand, DFIG has the disadvantage of high vulnerability to grid disturbances, especially low voltage and short circuit cases [80], [81]. Due to the direct integration of the DFIG stator to the power grid, large currents are drawn to demagnetize the machine when a short circuit or voltage sag happens at the grid side. These transient demagnetizing currents

that last several cycles induce a large voltage in rotor windings. As a result, high rotor currents are generated in the rotor windings, which in turn flow towards the back-to-back power converters and may cause damage to the RSC. It is worth mentioning that the thermal time constant of the DFIG itself is large enough, and DFIG can handle the fault transient current.

Moreover, the wind power harvested by the wind turbine cannot be transferred into the power grid during faults due to the current restraints of the generator and power converter. This unbalanced power can increase the generator speed and lead to the loss of generator control. Consequently, after the clearance of the fault, the converter cannot provide the voltage needed to control the generator. Additionally, this increase could lead to a rise in the rotor power and increase the dc-link voltage. This overvoltage can exceed the rating of the converter and dc-link capacitor and damage them [80], [81].

10.2 Proposed LVRT for Hydraulic Wind turbine

Since the size of the converter in the SS-WECS is reduced enormously, and the GSC is eliminated, meeting the required LVRT capability could be challenging. Figure 10.1 demonstrates this system with the four protection circuits. Herein, the performance of these protection circuits is evaluated. Despite the fact that all four protection circuits are shown in this figure, only one of them becomes activated. Therefore, the switches $S_1 - S_5$ are employed to activate the protection circuit under study.

The DFIG speed should be controlled to remain close to the synchronous speed and prevent overvoltage of the DC link during the fault. To this end, the hydraulic machinery displacement is controlled such that the amount of power transferred to the DFIG is decreased. Accordingly, only a portion of wind power (γ) is transferred to the generator, and the surplus power is transferred to the rotor of the wind turbine and increases its kinetic energy. This energy can be returned to the grid after the fault is cleared. This control strategy is shown in Figures 10.2 and 10.3. If the speed of the turbine rotor exceeds the nominal value, the pitch angle controller shown in Figure 10.4 is activated to limit the turbine speed.

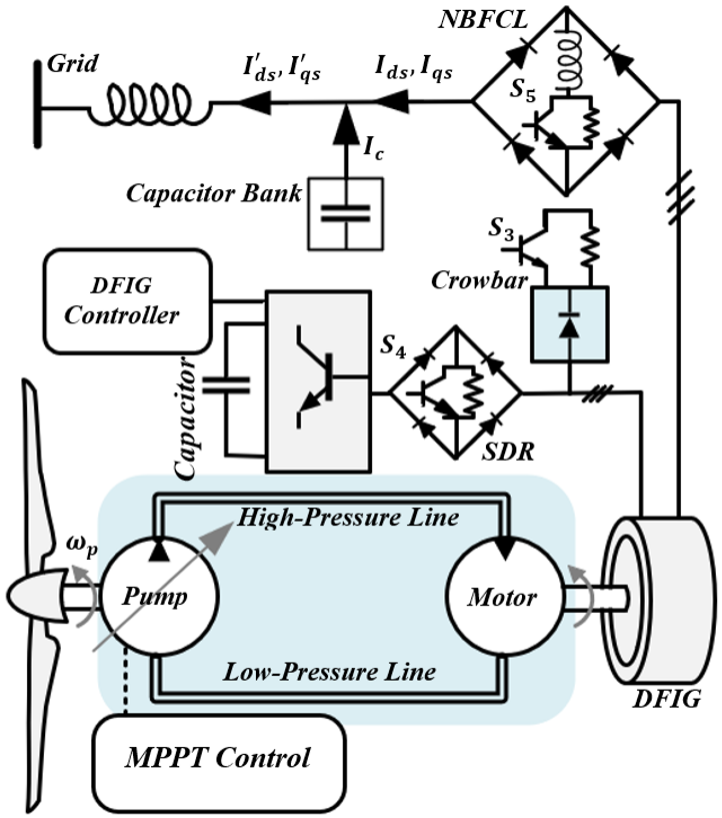

Figure 10.1. Configuration of the SS-WECS with all protection circuits

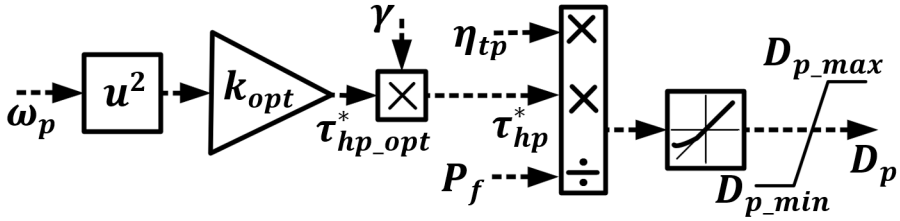

Figure 10.2. Displacement control of the hydraulic pump

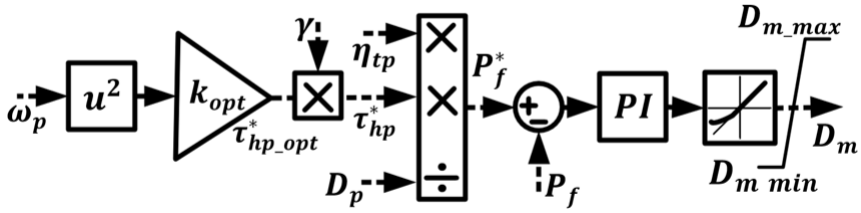

Figure 10.3. Displacement control of the hydraulic motor

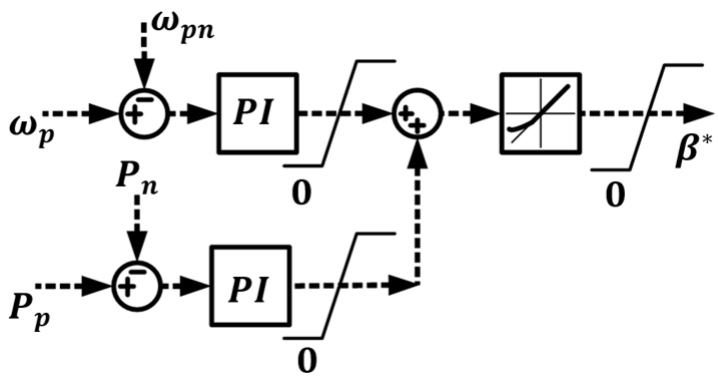

Figure 10.4. Pitch angle control

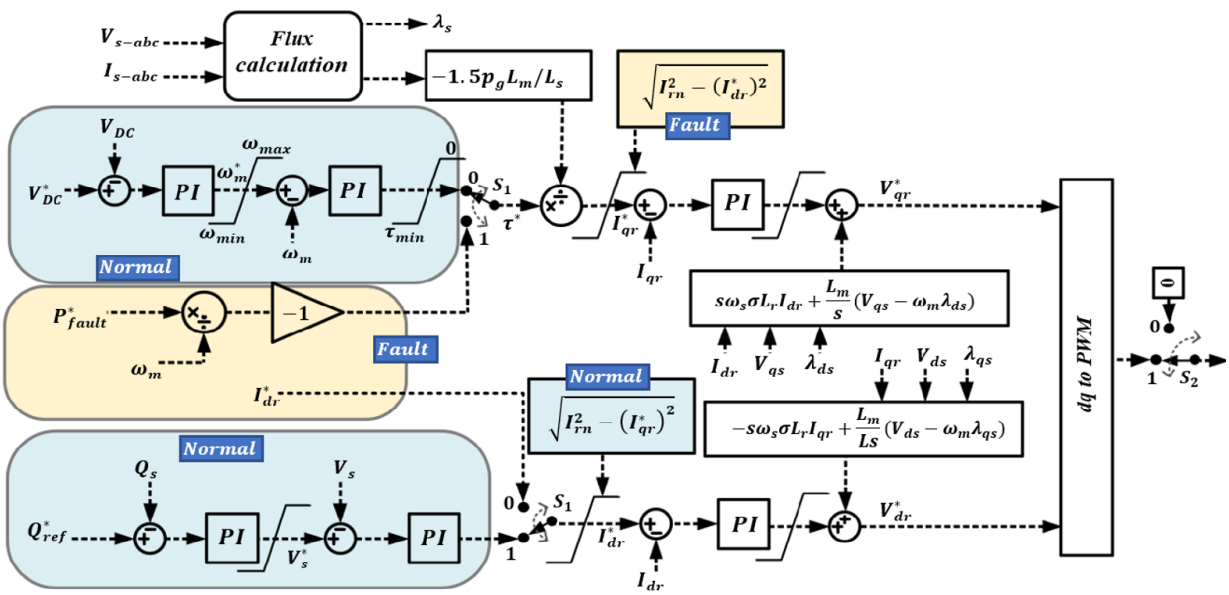

Figure 10.5. DFIG Controller for normal and fault operation (blue shaded part is for normal operation and orange ones are for the fault operation)

10.2.1 Overcurrent and Overvoltage Protection

DFIG controller is shown in Figure 10.5 for both regular and during-fault operations. The blue shaded blocks (labeled normal) are for the typical process, and the orange shaded blocks (labeled fault) are activated during faults. In this paper, the performance of crowbar, C-RL, SDR, and NBFCL are explored individually, as shown in Figure 10.1. The logic for switching $S_1 - S_5$ switches, shown in Figure 10.1 and Figure 10.5, is demonstrated in Figure 10.6. To understand this logic diagram better, Table 10.1 shows the state of each switch

in different protection circuits. In general, under a faulty situation, the position of switch S_1 changes from 1 to 0 for all protection strategies. However, switch S_2 is only used when the active crowbar (C) is activated to deactivate the RSC. Switch S_3 is activated whenever crowbar or C-RL are utilized, and the current exceeds the threshold current during the fault. Switches S_5 and S_6 are on during the fault when SDR and NBFCL are employed, and the current is above the threshold current, respectively. All proportional-integral (PI) controllers in the blue shaded block (regular operation) during the fault are forced to restart with a reference equal to the last measured value to achieve a soft restoration of the controller [93].

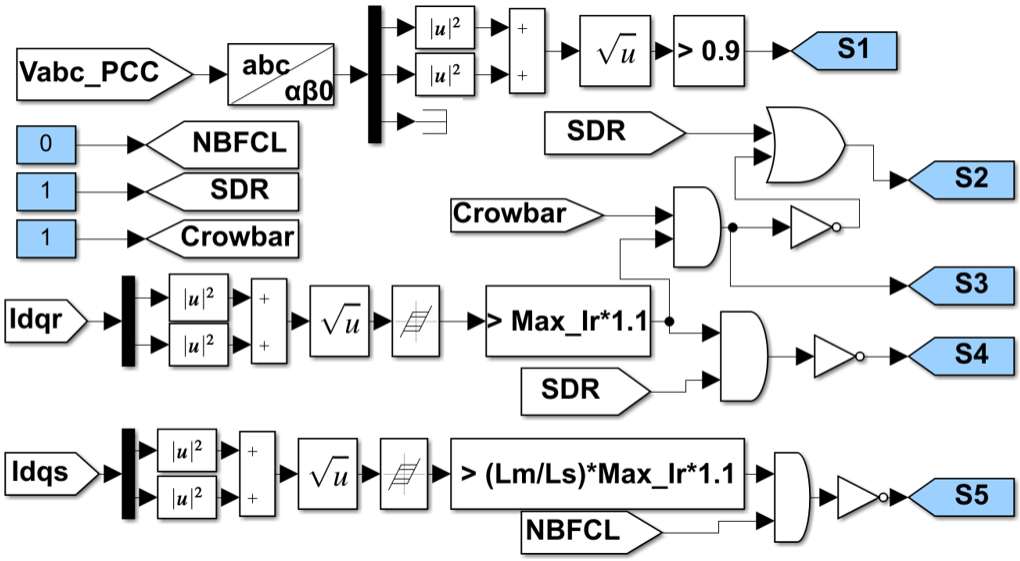

Figure 10.6. Logic diagram of all configurations

Table 10.1. States of Switches in Different Protection Circuits

Protection circuit	Switches with on or off state during fault	Switches turned on & off during fault
C	$S_4 = S_5 = off$	$S_2 = S_3 = on/off$
$C - RL$	$S_1 = S_2 = S_5 = off$	$S_3 = S_4 = on/off$
SDR	$S_1 = S_2 = S_3 = S_5 = off$	$S_4 = on/off$
$NBFCL$	$S_1 = S_2 = S_3 = S_4 = off$	$S_5 = on/off$

Active Crowbar (C)

This protection circuit is activated by turning on S_3 shown in Figure 10.1 during the fault whenever the rotor current exceeds the converter current rating. This switch is deactivated when the current is lower than the converter current rating. Furthermore, DFIG also draws a sizeable reactive power for magnetizing the machine after the fault clearance, during which the rotor current can increase again. Therefore, the active crowbar strategy is applied to protect the RSC after fault clearance to prevent the flow of magnetizing current toward the RSC. The amount of dynamic crowbar resistor is defined such that the DC-link voltage does not experience an overvoltage during the fault [94]. Furthermore, when the crowbar is activated, S_3 is deactivated to switch off the PWM signal of the RSC.

The direct and quadratic components of the current have limitations under normal and fault conditions. During the regular operation, the direct component of the rotor current is limited by $I_{dr}^* \leq \sqrt{I_{rn}^2 - (I_{qr}^*)^2}$ to ensure the active power delivery to the grid, which is defined by the I_{qr}^*. However, under fault, a minimum amount of reactive current is required to maintain the voltage, and the rest of the current capacity of the converter can be used toward the active power. Therefore, under fault, the quadrature component of the rotor current is limited to $I_{qr}^* < \sqrt{I_{rn}^2 - (I_{dr}^*)^2}$.

Crowbar and RL (C-RL)

In this protection approach, both crowbar and SDR are activated during the fault. The RSC remains connected to the rotor winding during the fault, and there is no need to turn off the RSC PWM. The value of the resistances is chosen such that the DC-link voltage during fault does not experience an overvoltage [98].

SDR

SDR is connected in series with the RSC. In normal conditions, switch S_4 is on. The switch turns off whenever the rotor current exceeds a predefined threshold during the fault.

The series inductor prevents the sudden change in rotor current. The amount of the optimal resistor is defined using simulation.

NBFCL

NBFCL is connected in series with the stator. The switch S_5 is turned off when the stator current goes beyond the predefined threshold.

Two crucial parameters I^*_{dr} and P^*_{fault} should accurately be defined because the first one determines the amount of reactive current injected into the grid. The second one defines the amount of active power injected into the grid during the fault. It is better to inject active power as much as the RSC allows without overloading the converter during the fault.

10.2.2 Reactive Current Reference Calculations

To calculate I^*_{dr}, the direct component of the stator, I'^*_{ds} (shown in Figure 10.1), should be calculated first. According to [116], this amount can be obtained based on the amount of voltage dip as follows:

$$I'^*_{ds} = \begin{cases} 0 & \Delta V > -0.1 \\ 2\Big(\Delta V + 0.1\Big) I_{sn} & -0.6 \leq \Delta V \leq -0.1 \\ -I_{sn} & \Delta V < -0.6 \end{cases} \tag{10.1}$$

where $\Delta V = \frac{V_s - V_{sn}}{V_{sn}}$, and V_{sn} is the nominal stator voltage. By using 3.32, and considering the equations of capacitor bank in dq frame, the dq components of the current that injected to PCC are obtained as follow:

$$\begin{bmatrix} I'_{qs} \\ I'_{ds} \end{bmatrix} = \begin{bmatrix} \frac{1}{L_s} - \omega_s^2 C & 0 \\ 0 & \frac{1}{L_s} - \omega_s^2 C \end{bmatrix} \begin{bmatrix} \lambda_{qs} \\ \lambda_{ds} \end{bmatrix} - \begin{bmatrix} \frac{L_m}{L_s} & 0 \\ 0 & \frac{L_m}{L_s} \end{bmatrix} \begin{bmatrix} I_{qr} \\ I_{dr} \end{bmatrix} \tag{10.2}$$

where $I_{qs}^{'}$, $I_{ds}^{'}$ are direct and quadrature components of the current injected into the Point of Common Coupling (PCC). Then, according to Figure 10.1, the reactive current injected into the grid is as follows:

$$Q_s^{'} = \frac{3}{2}\Big((\omega_s C - \frac{1}{L_s\omega_s})(V_{ds}^2 + V_{qs}^2) + \frac{L_m}{L_s}(V_{qs}I_{dr} - V_{ds}I_{qr})\Big) = Q_c - Q_m + Q_s \tag{10.3}$$

where $Q_c = \frac{3}{2}\omega_s C\Big(V_{ds}^2 + V_{qs}^2\Big)$ and $Q_m = \frac{3}{2}\frac{1}{L_s\omega_s}\Big(V_{ds}^2 + V_{qs}^2\Big)$ are the reactive power of the capacitor bank and magnetizing reactive power of the generator, respectively. It is assumed that the amount of reactive power of capacitor bank at the stator is designed such that it cancels out the magnetizing current of the generator:

$$Q_c = Q_m \Longrightarrow C = \frac{1}{\omega_s^2 L_s} \tag{10.4}$$

Therefore, the relationship between dq components of the rotor current and current at the PCC is obtained as follows:

$$\begin{bmatrix} I_{qs}^{'} \\ I_{ds}^{'} \end{bmatrix} = -\begin{bmatrix} L_m/L_s & 0 \\ 0 & L_m/L_s \end{bmatrix}\begin{bmatrix} I_{qr} \\ I_{dr} \end{bmatrix} \tag{10.5}$$

The size of the capacitor enables the DFIG complex to inject and absorb a similar amount of reactive power, as shown in Figure 10.7. Using 10.1, 10.4, and 10.5, the amount of I_{dr}^* can be obtained as follows:

$$I_{dr}^* = -\frac{L_s}{L_m}\begin{cases} 0 & \Delta V > -0.1 \\ 2\Big(\Delta V + 0.1\Big)I_{sn} & -0.6 \leq \Delta V \leq -0.1 \\ -I_{sn} & \Delta V < -0.6 \end{cases} \tag{10.6}$$

Generally, the reactive power capability of the DFIG is not symmetrical due to the required magnetizing current. However, employing capacitor bank results in symmetrical reactive power capability of the DFIG, as shown in Figure 10.7.

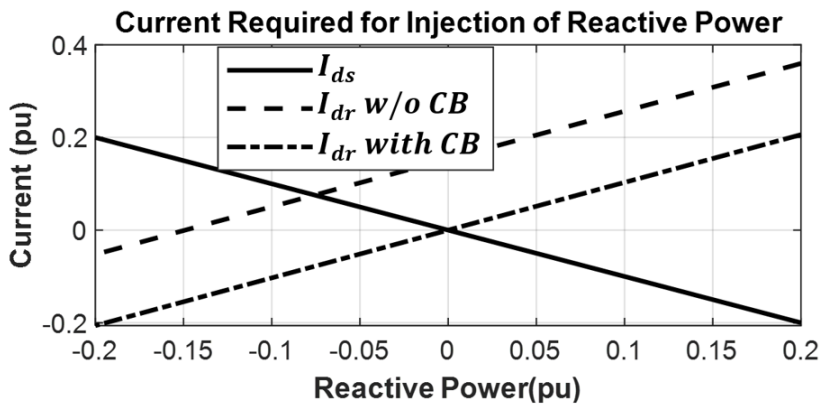

Figure 10.7. Rotor and stator direct component of current in various reactive currents

10.2.3 Active Power Reference Calculation

To calculate the reference of the active power during the fault, P^*_{fault}, first, the remaining current capacity of the RSC should be calculated. The maximum quadratic component of rotor current, I_{qr_max} can be obtained as follows:

$$I_{qr_max} = \sqrt{I_{rn}^2 - (I_{dr}^*)^2} \tag{10.7}$$

Therefore, using 10.6 and 10.7, the maximum active power that can be transformed to the grid during the fault is obtained as follows:

$$P_{s_max} = \frac{3}{2} V_{qs} I_{qs} = \frac{L_m}{L_s} V_s \sqrt{I_{rn}^2 - (I_{dr}^*)^2} \tag{10.8}$$

From the stability point of view and to prevent DC-link overvoltage and acceleration of DFIG, the output power of the hydraulic machinery needs to be adjusted to the amount that can be transferred to the grid. Accordingly, γ in Figure 10.2 and Figure 10.3 can be calculated as follow:

$$\gamma = min\Big(1, \frac{|P_{s_max}|}{\eta_t K_{opt} \omega_p^3}\Big) \tag{10.9}$$

Consequently, the reference power during faults can be adjusted as follows:

$$P^*_{fault} = \omega_m D_m P_f \eta_{tm} \tag{10.10}$$

10.3 Design of Experiment and Simulation Results

The SS-WECS can utilize variable displacement pumps at the turbine side or variable displacement motors at the generator side. Both configurations are simulated under a three-phase fault to analyze the ability of the reduced-size excitation system. The objective is to meet the US grid LVRT performance requirements. Accordingly, when the voltage at PCC drops to 15%, the generator and its supporting components should continue operation for 0.625 seconds. A fault is scheduled at $t = 4\,s$, which lasted for 0.625 seconds. The wind speed is considered $11\,m/s$ (nominal power) and remains constant for the LVRT analysis. Before the fault, the amount of the reactive power injected into the grid is zero, and the rest of the system is at their steady-state values.

10.3.1 LVRT in Variable-Displacement Pump (VDP) Configuration

First, to determine the optimal value for SDR and NBFCL resistors, the maximum current of the converter was obtained by simulation for different resistor values at different voltage phases, as shown in Figure 10.8. At a 0.6 per unit (pu) resistor, both curves in Figure 10.8 reached an optimal value.

Figure 10.9 (a) shows the PCC voltage profile considering all four cases of LVRT protection techniques. The PCC voltage shows a drop to 15% at time 4 s. The figure demonstrates a fast voltage recovery to its nominal value with no generator disconnection. With the NBFCL protection circuit, the stator voltage drops with a delay due to the voltage drop across the resistor at the stator side. The PCC reactive and active current components are shown in Figure 10.9 (b) and Figure 10.9 (c), respectively. During the fault, the amount of active current decreases, and 1 pu of reactive current is injected into the grid to maintain

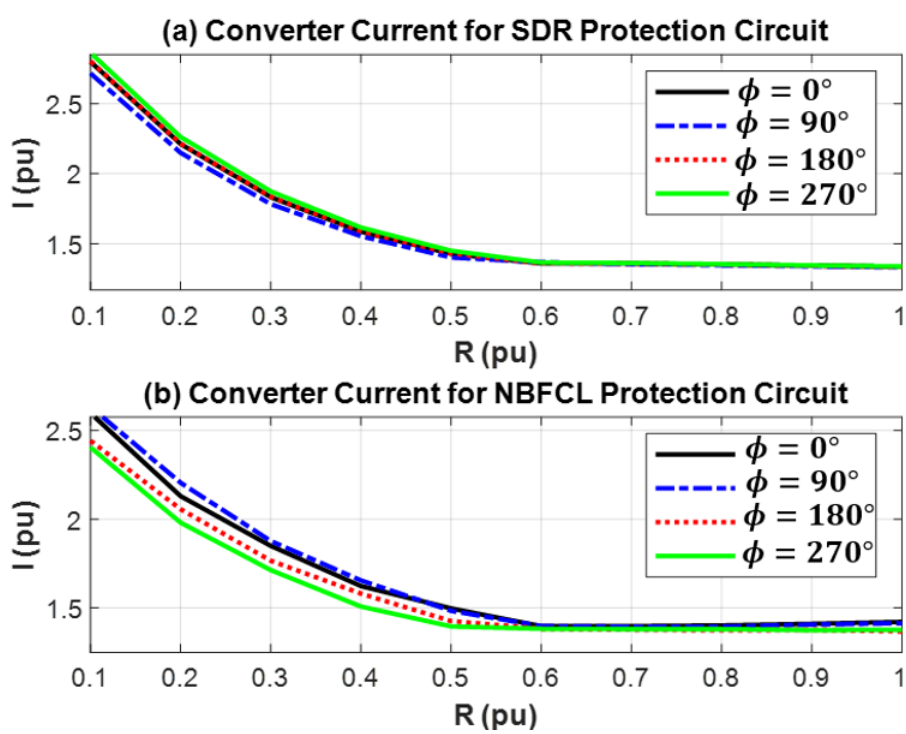

Figure 10.8. The maximum current of the converter for VDP Configuration with (a) SDR (b) NBFCL.

the voltage at PCC. These figures show that the transient fault current is damped in the NBFCL technique, but other methods remain oscillatory for about 200 ms.

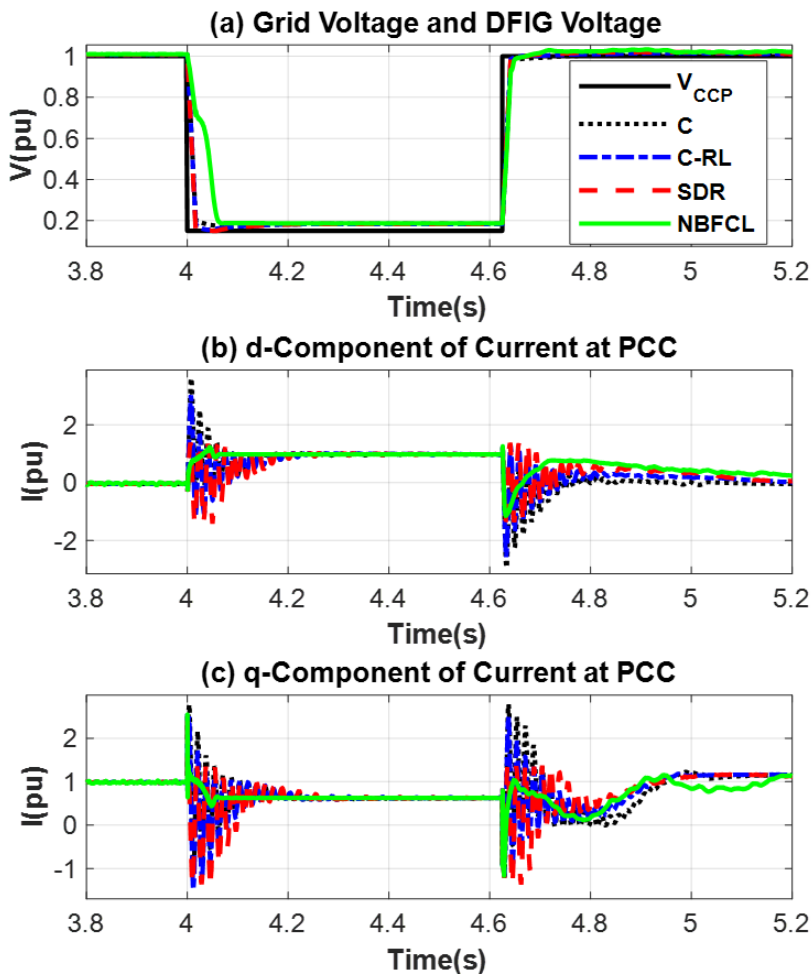

Figure 10.9. (a) Voltage at PCC and stator terminal (b) d-component of the current at PCC (c) q-component of the current at PCC for VDP Configuration

When the crowbar protection strategy is employed, the peak of fault current reaches its maximum. However, the current crest decreases in the partially controlled C-RL. This peak is limited further in SDR because of its fully controlled approach. However, the transient of the current cannot be eliminated due to the small size of the RSC.

The active power delivery to the PCC during fault for four protection circuits is shown in Figure 10.10 (a). At the beginning of the fault with the NBFCL protection, the amount of active power injected into the power grid is close to one pu. The main portion of this power is

transferred to the resistor in the NBFCL configuration. The protection circuits are activated again after the clearance of the fault. With crowbar configuration, the rotor excitation circuit becomes short-circuit, and the machine behaves as a Squirrel Cage Induction Generator (SCIG). Therefore, in this protection circuit, there is no control applicable to the rotor excitation during the fault. For this reason, it is observed that the active power remains close to 1 *pu* (Figure 10.10 (a)) but draw a large magnetizing reactive power (Figure 10.10 (b)) after the clearance of the fault. In the C-RL configuration, the magnetizing reactive power decreases due to the partially controlled approach, as shown in Figure 10.10 (b). This magnetizing reactive power is reduced further to zero in the SDR protection circuit. In general, the performance of the C-RL is a trade-off between crowbar and SDR configurations performance. The turbine speed starts increasing at the beginning of the fault and reaches a 5% overshoot, as shown in Figure 10.11 (a). Then, the turbine speed starts decreasing with a delay after the clearance of the fault. With the appearance of overshoot, the pitch angle control is activated to limit the speed, as shown in Figure 10.11(b). As a result of the displacement control and pitch angle control, the pressure of the fluid decreases during the

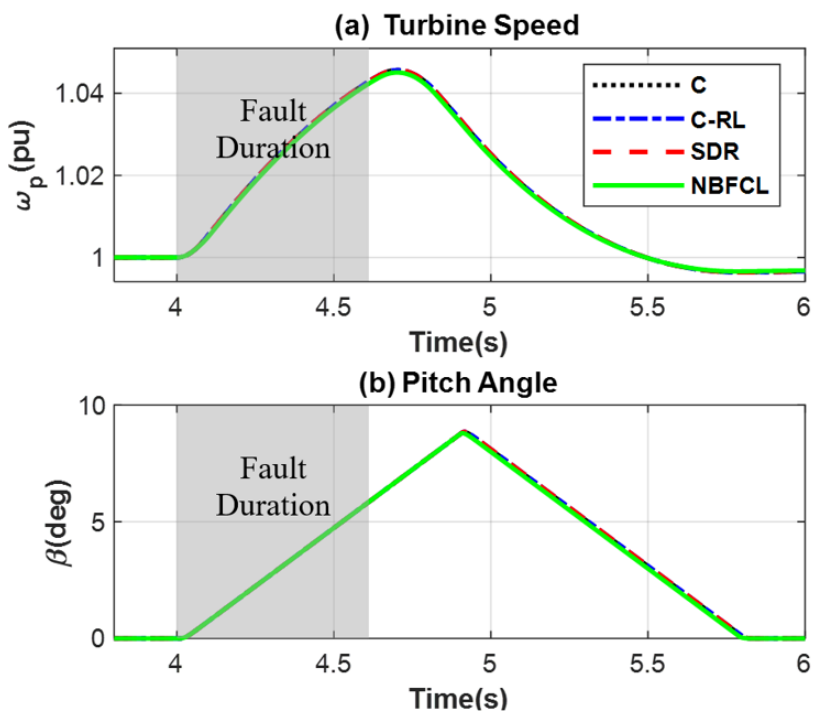

Figure 10.10. (a) Turbine speed (b) pitch angle for VDP Configuration

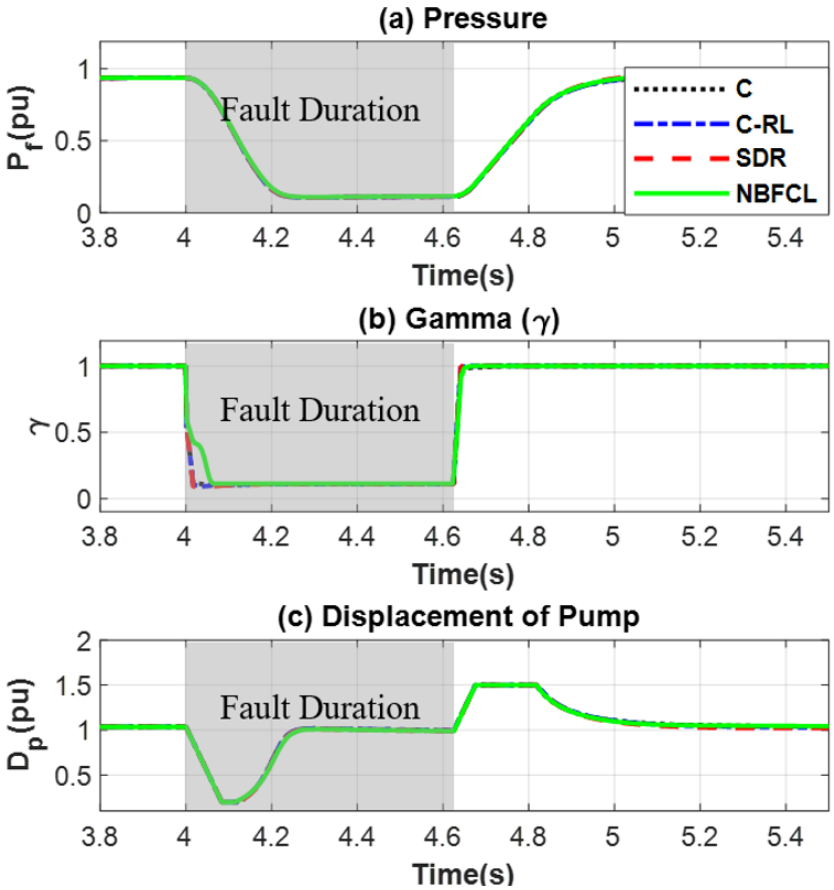

Figure 10.11. (a) Pressure, (b) γ (c) displacement of pump for VDP Configuration

fault (Figure 10.12(a)) to truncate the power at the hydraulic motor side. The fluid pressure starts increasing with a slight delay after the clearance of the fault. When the pressure is recovered, the speed of the turbine starts decreasing. The amount of γ factor is obtained for all configurations, as shown in Figure 10.12(b). Due to the voltage at the terminal of the DFIG, γ for NBFCL is slightly higher at the beginning of the fault. After the clearance of the fault, γ becomes one, and the displacement of the pump is controlled accordingly (Figure 10.12(c)).

The DC-link voltage for all configurations is shown in Figure 10.13(a). The variation observed at the DC-link voltage is the least when the SDR configuration is utilized. In general, these variations are within $\mp 7\%$ for all configurations. The generator speeds are shown in Figure 10.13 (b) for all protection circuits. As the figure shows, the fluctuation of the generator speed remains close to the synchronous speed. The NBFCL and SDR

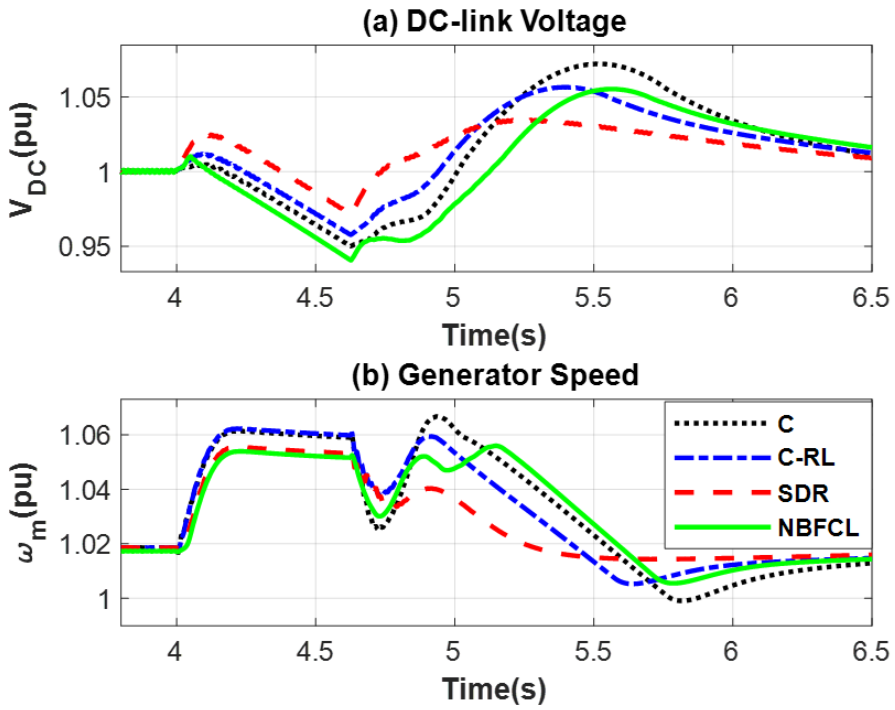

Figure 10.12. (a) DC-link voltage (b) the DFIG speed for VDP Configuration

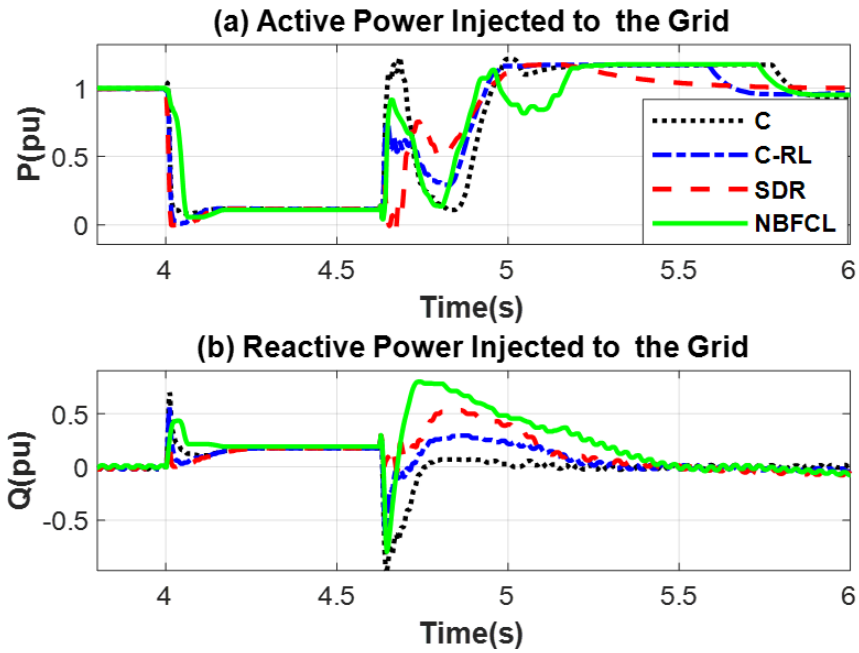

Figure 10.13. (a) Active power (b) reactive power for VDP Configuration

show the lower generator speed swing. Figure 10.14 demonstrates the current of the rotor and converter of a single phase in the three-phase system. During faults, the rotor current

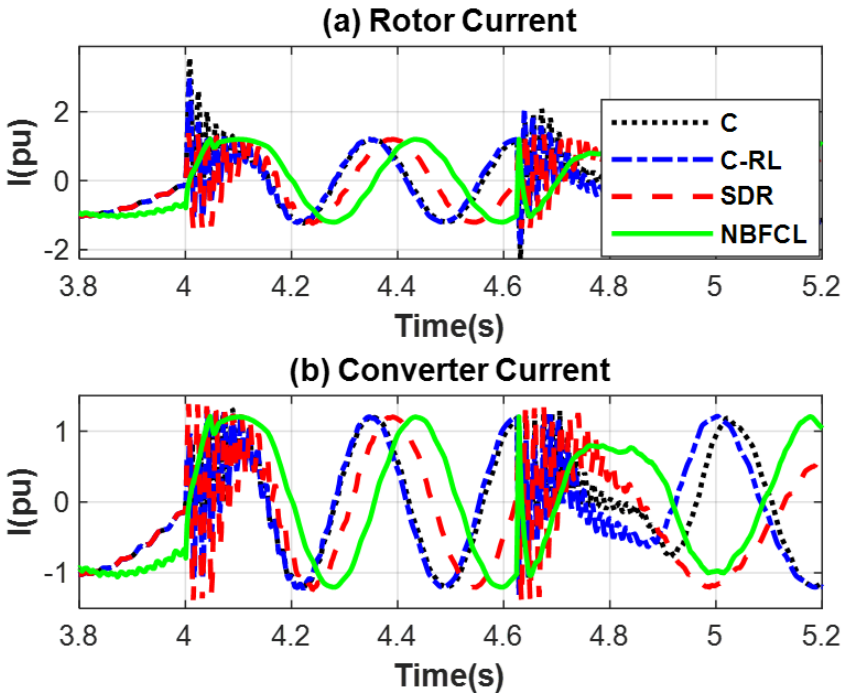

Figure 10.14. (a) Current of rotor winding (b) current of converter (c) current at PCC for VDP Configuration

reaches about 3.5 *pu* when the crowbar is used. The same current is reduced to 2.5 *pu* in the C-RL configuration. However, the converter is protected against overcurrent by a bypass route provided by the crowbar. The maximum current of the converter for all configurations reaches 1.4 *pu*, as shown in Figure 10.14(b). It can be observed that all configurations protect the system and provide the LVRT requirements. However, the SDR and NBFCL outperform the other methods. The SDR configuration can manage the reactive power of the generator after the clearance of the fault better, and the NBFCL decreases the oscillatory performance of the system during the fault.

10.3.2 LVRT in Variable-Displacement Motor (VDM) Configuration

Variable displacement motor directly accesses the generator speed control and indirectly influences the turbine rotational speed. Hence, the performance of the protection techniques selected for LVRT is different. The value of the fault-current-suppressing resistor needs to be optimized accordingly. Figure 10.15 shows the variation of the fault current concerning the fault current resistor values under SDR and NBFCL current limiting techniques, which gives similar results as Figure 10.8. In the SDR and NBFCL techniques, the converter current decrease sharply by increasing the resistor value up to 0.6 pu. However, the rotor current did not change significantly for the resistor above 0.6 pu.

In the case of the variable-displacement motor, the voltage of PCC drops to 15% at time $4\,s$, as shown in Figure 10.16 (a). The voltage of the stator for all configurations is demonstrated in Figure 10.16(a). The stator voltage is recovered to its nominal value immediately after the clearance of the fault. Similar to the VDP (shown in Figure 10.9(a)),

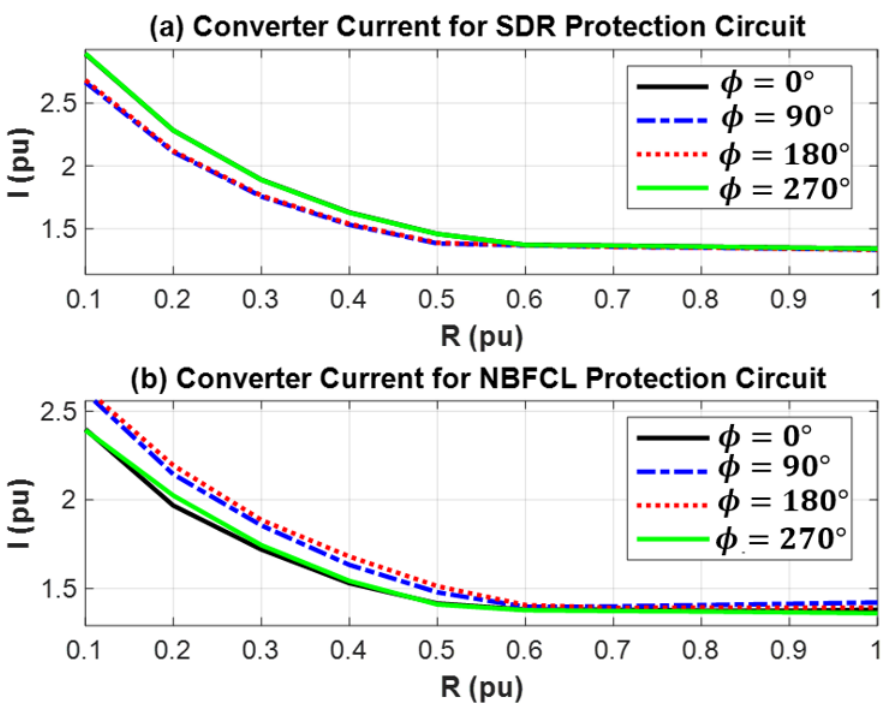

Figure 10.15. The maximum current of the converter for VDM Configuration with (a) SDR (b) NBFCL.

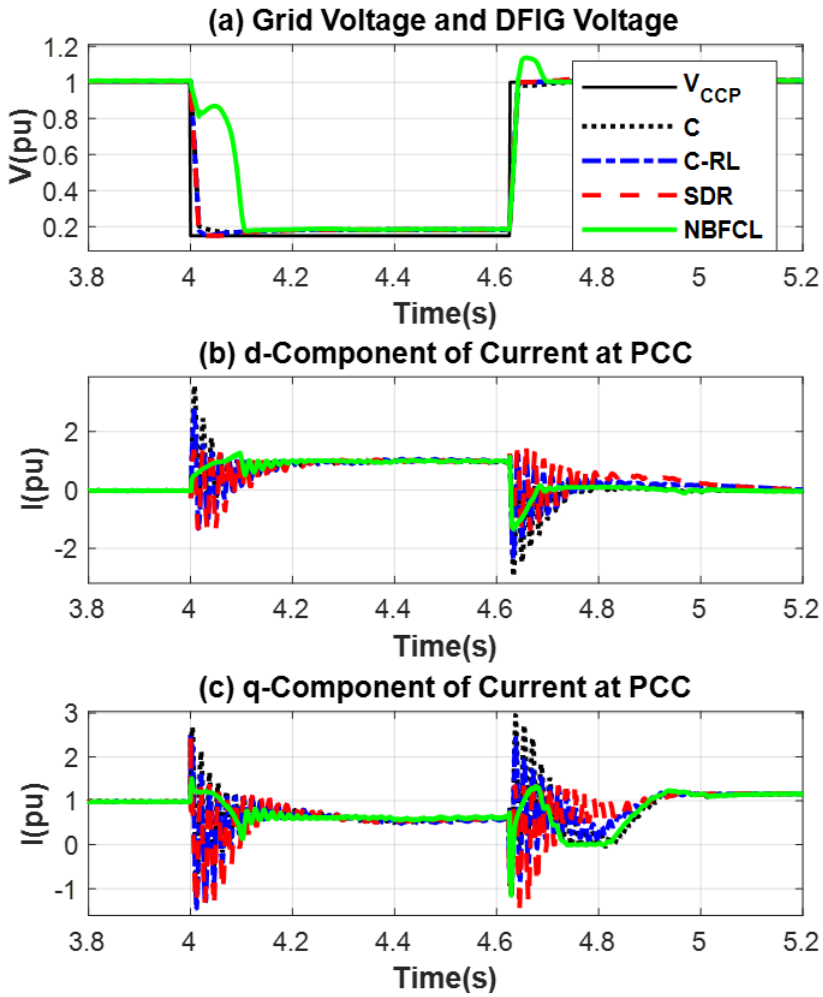

Figure 10.16. (a) Voltage at PCC and stator terminal (b) d-component of the current at PCC (c) q-component of the current at PCC for VDM Configuration

the stator voltage decreases with a delay in the NBFCL protection method (Figure 10.16(a)). The reactive currents at the PCC shown in Figure 10.16(b) reach one *pu* during the fault. Due to the limited capacity of the converter, the active current injected into the grid during the fault decreases, as shown in Figure 10.16(c). The active and reactive powers are shown in Figure 10.17. The performance of all configurations is similar to the case of the variable-displacement-pump drivetrain.

Immediately after the fault, the speed of the turbine starts rising and shows a 4% overshoot. This is shown in Figure 10.18(a). The speed starts decreasing as the fault cleared. Similarly, as the speed exceeds the nominal value, the pitch angle control is activated and

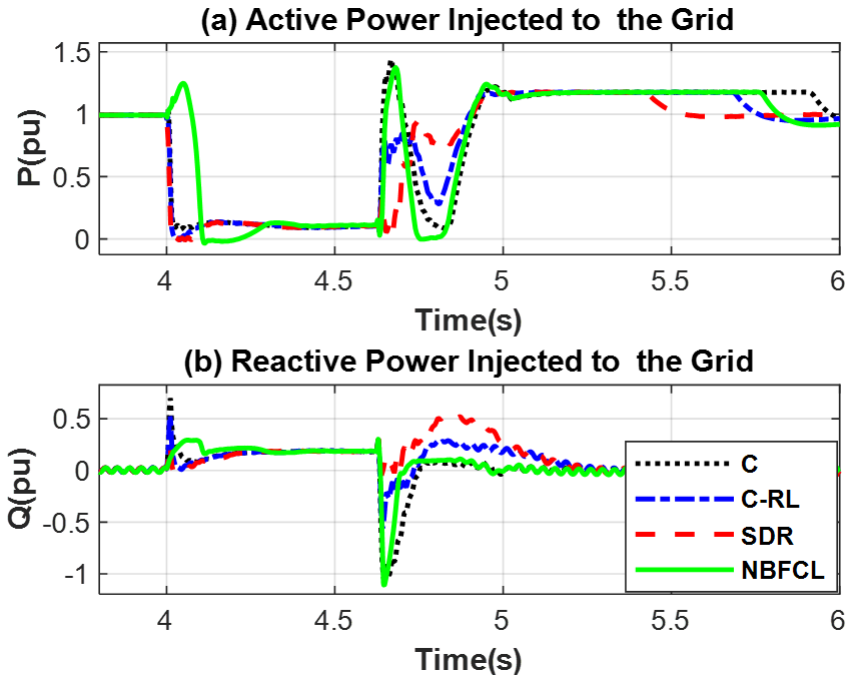

Figure 10.17. (a) Active power and (b) reactive power for VDM Configuration

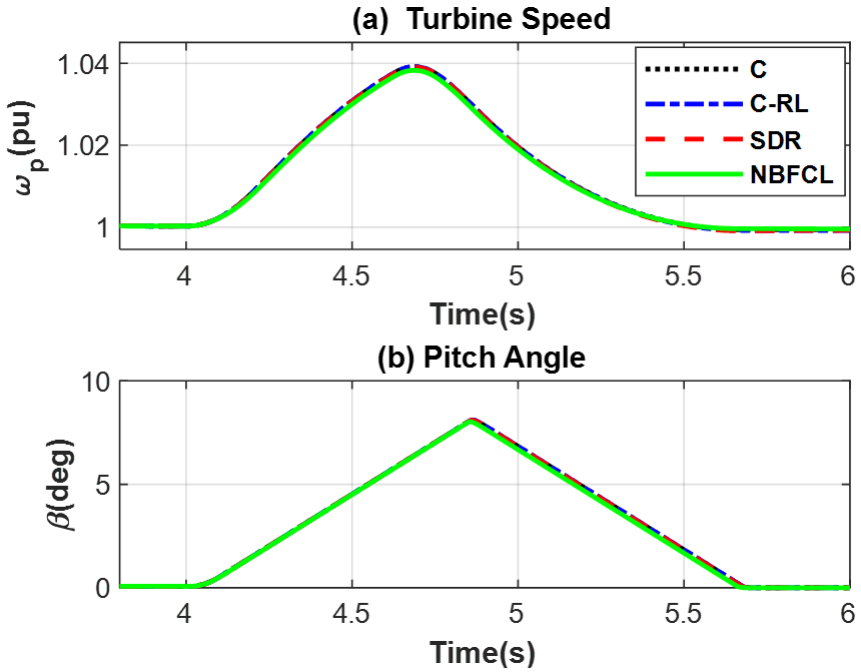

Figure 10.18. (a) Turbine speed (b) pitch angle for VDM Configuration

limits the speed, as shown in Figure 10.18(b). As a result of the displacement control and pitch angle control, the pressure of the fluid decreases during the fault (Figure 10.19(a))

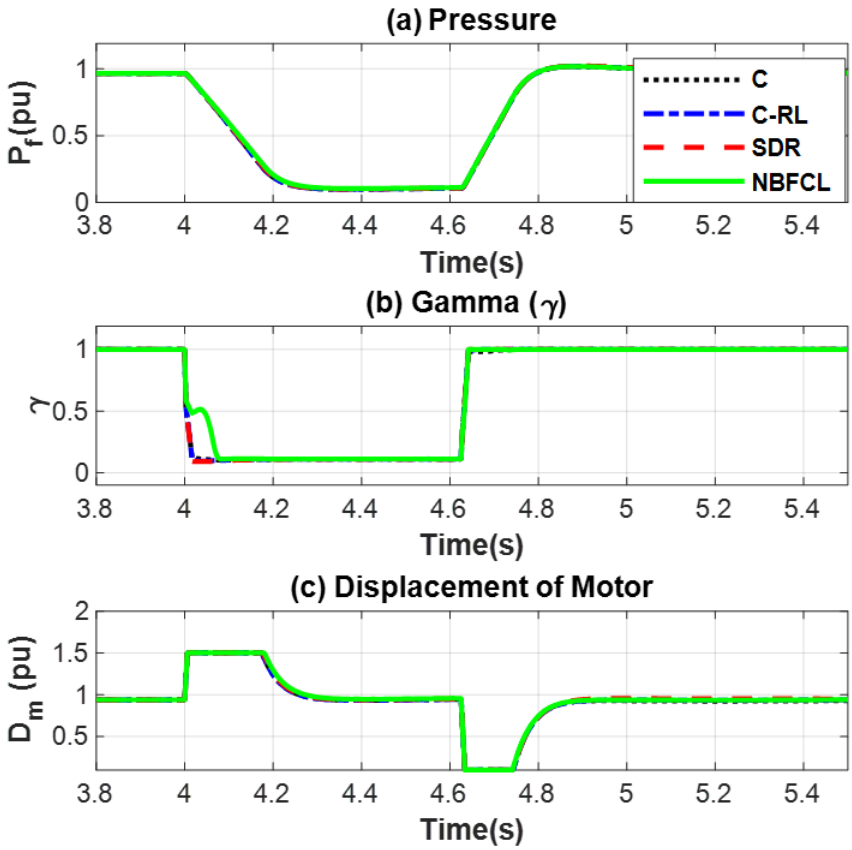

Figure 10.19. (a) Pressure (b) γ (c) displacement of pump for VDM Configuration

to truncate the power at the hydraulic motor side. The effect on the γ is shown in Figure 10.19(b) for all configurations. The control effort as the motor displacement for all LVRT control techniques is shown in Figure 10.19(c).

The DC-link voltage for all configurations is shown in Figure 10.20(a). A significant DC-link voltage fluctuation is observed in the VDM configurations compared with the VDP configurations, as previously shown in Figure 10.13(a). These variations remain within 8%. However, more minor variations are observed in the SDR configuration. The generator speed is shown in Figure 10.20(b).

Similarly, a more considerable generator speed variation is observed in VDM than the VDP configurations, limited to 9%. For the NBFCL protection circuit, the generator speed variation is less than other protection circuits. Figure 10.21 demonstrates the current of the

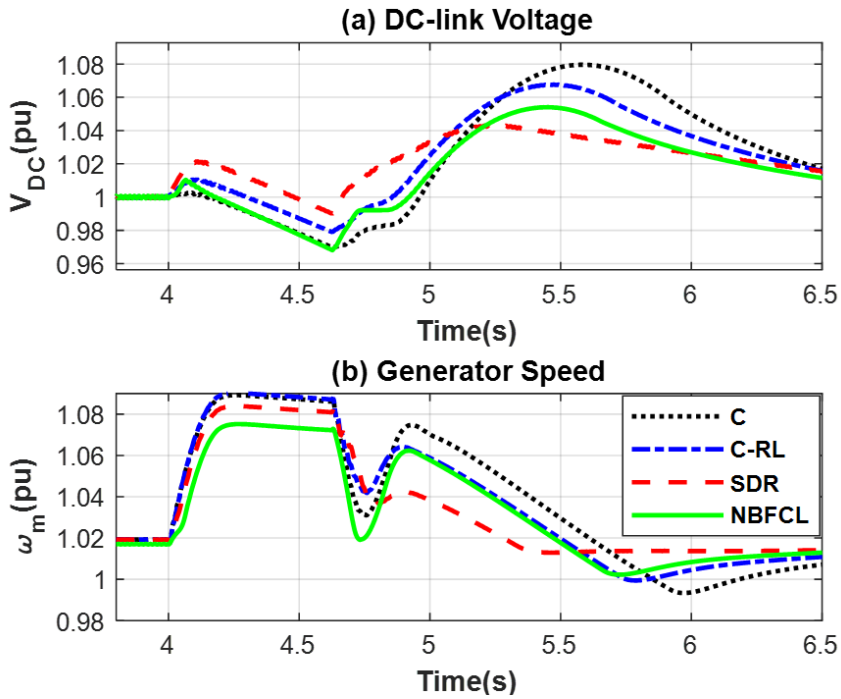

Figure 10.20. (a) DC-link voltage (b) the DFIG speed for VDM Configuration

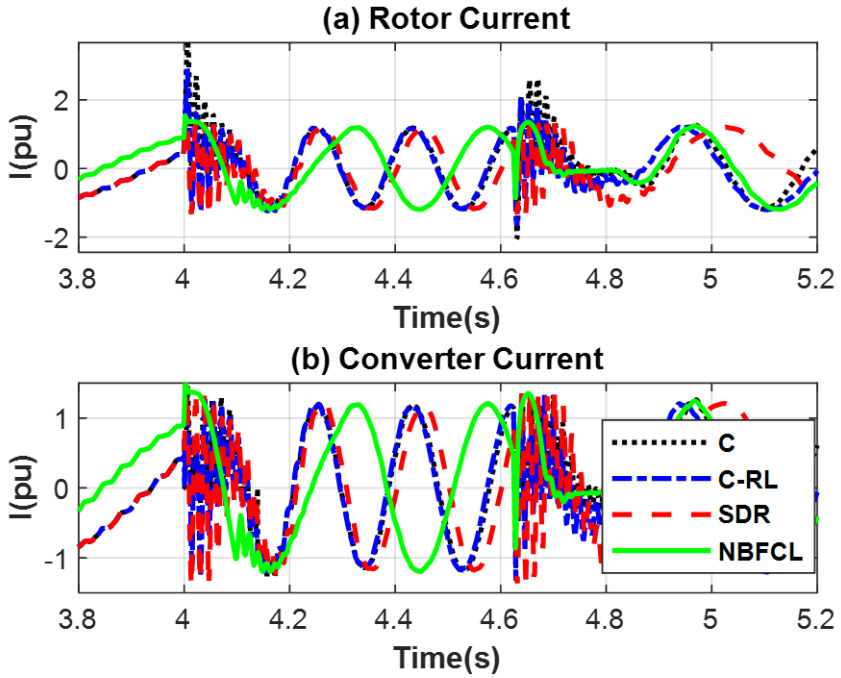

Figure 10.21. (a) Current of rotor winding (b) converter current for VDM Configuration

rotor and converter for one phase of the three-phase system. The current of the converter for all configurations is limited to $1.4\,pu$.

10.3.3 Converter Size Determination

The size of the converter depends on the minimum DC-link required to control the system and the maximum current of the RSC during the fault. The minimum DC-link voltage is correlated to the maximum slip of the DFIG during its operation. Herein in this paper. The dq frame is chosen such that all stator flux is aligned with the d axis. Therefore, $\lambda_{qs} = 0$ in steady-state. Neglecting the stator resistor ($R_s = 0$), the direct component of the stator voltage will be zero ($V_d s = 0$), and $\lambda_{ds} = V_{qs}/\omega_s$. By replacing this simplification in 3.34, the rotor voltage and minimum DC-link voltage can be achieved as follows:

$$\begin{bmatrix} V_{qr} \\ V_{dr} \end{bmatrix} = \begin{bmatrix} R_r & s\omega_s\sigma L_r \\ -s\omega_s\sigma L_r & R_r \end{bmatrix} \begin{bmatrix} I_{qr} \\ I_{dr} \end{bmatrix} + \frac{L_m}{L_s} \begin{bmatrix} sV_{qs} \\ 0 \end{bmatrix} \tag{10.11}$$

$$V_{dc} \geq 2\sqrt{V_{qr}^2 + V_{dr}^2} \tag{10.12}$$

Figure 10.22 demonstrates the minimum DC-link for various DFIG slips and stator voltages. This figure consists of three surfaces related to the different voltage levels 10.6. During Faults, the current of the rotor can be achieved based on 10.6 and 10.7, and the minimum DC-link voltage can be calculated. The maximum DFIG slip can be obtained by simulating the system at various fault voltages. On the other hand, in normal operation, the maximum slip of the generator is less than 2% [121], and the DC-link voltage calculated is less than the value required during the fault. The smaller the maximum slip of the DFIG, the smaller the DC-link voltage is required to ride through the fault and ensure the grid code. The boundary of the minimum DC-link voltage for different configurations is shown in Figure 10.22.

Based on the boundaries shown in Figure 10.22, the maximum slip and minimum DC-link voltage for all operating points and fault conditions are shown in Figure 10.23 and Figure 10.24. It is shown that the DFIG slip reaches a higher point for the VDM configuration than VDP one. Thus the minimum DC-link voltage is achieved higher for the VDM. Based

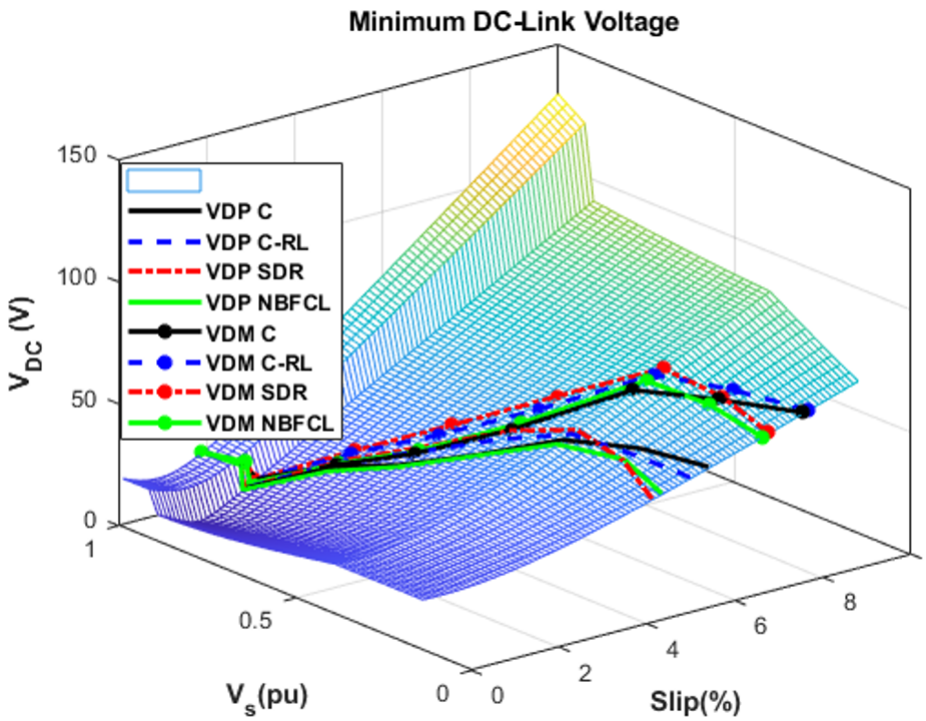

Figure 10.22. The minimum DC-link required at the different maximum slips

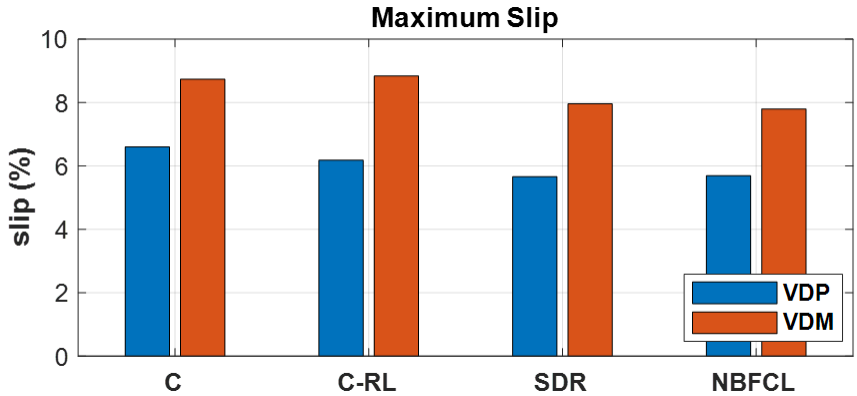

Figure 10.23. Maximum slip in all protection circuits

on these results, the RSC size for different protection circuits is obtained and shown in Figure 10.25. In general, the converter size is less than 6% and 8% for the VDP and VDM configurations, respectively. Therefore, the VDP configuration is a better choice in point of the size of the converter. Amongst drivetrain configurations, The VDP drivetrain has a better performance compared to VDM one. At the beginning of the fault, decreasing the pump

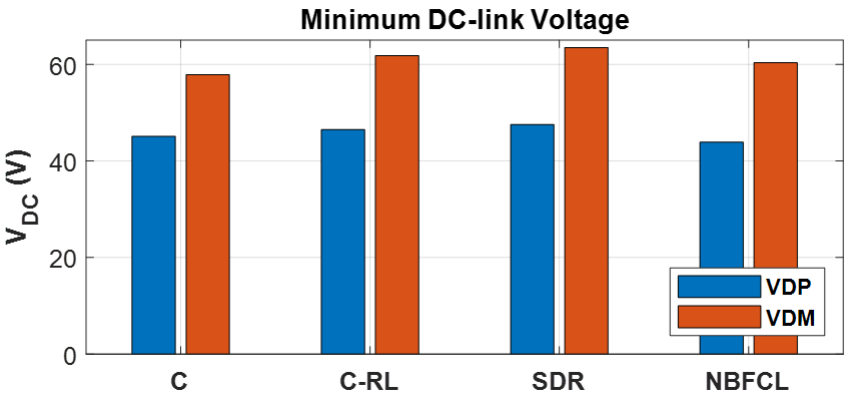

Figure 10.24. Minimum DC-link voltage required for all protection circuits

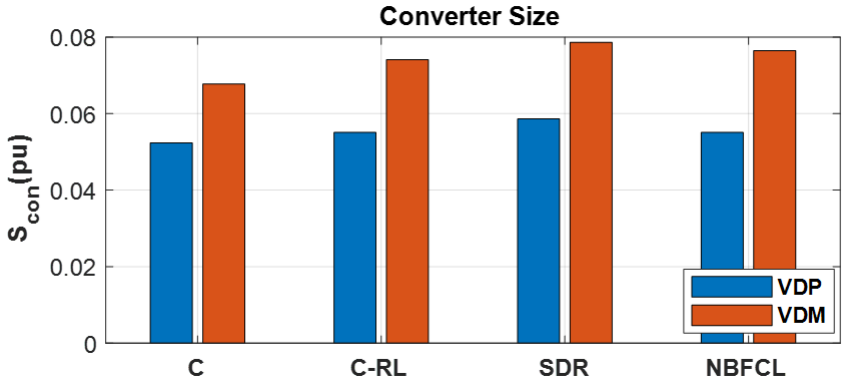

Figure 10.25. Converter size required for all protection circuits

displacement reduces the hydraulic power and increases wind turbine speed simultaneously. However, increasing the motor's displacement in VDM at the beginning of the fault first increases the output power, leading to a decrease in pressure and eventually an increase in wind turbine speed. This is the main reason for having a more significant slip variation in VDM. Amongst protection circuits, The NBFCL configuration is a suitable option to attenuate the system oscillation during the fault. The SDR is an acceptable option to control the reactive power after the clearance of the fault. All configurations need an RSC with a small size.

10.4 Summary

In this chapter, Low voltage ride-through capabilities of SS-WECS have been analyzed. A control technique was introduced to divert the energy from the generator to the wind turbine during the fault. This decreased the feeding of the fault by the generator. As a requirement, the DFIG was controlled close to the synchronous speed. The performance of four protection circuits, including a crowbar, C-RL, SDR, and NBFCL, were evaluated in two SS-WECS configurations, VDM and VDP. It was observed that the protection circuits did not significantly change the size of the converter. This allowed employing an RSC with 6% and 8% for VDP and VDM configurations, respectively. The system better managed the fault transients under NBFCL while it helped reduce the stator and rotor side transients. On the other hand, C-RL and SDR protection circuits better managed the active and reactive power generation controls. The protection circuits prevented the over current and over voltage of the RSC and DC-link capacitor. Therefore, the proposed system configuration successfully provided the required fault ride-through voltage profile with a reduced-size power converter.

11. CONCLUSION AND FUTURE STUDIES

11.1 Conclusion

In this research, we proposed a Doubly-Fed Induction Generator (DFIG)-based Split-Shaft Wind Energy Conversion System (SS-WECS). Instead of the gearbox employed in conventional wind turbines, SS-WECS utilizes a Hydraulic Transmission System (HTS) to drive the generator. In such a system, the weight of the nacelle could be decreased simply by relocating the generator and other subassemblies to the ground level. Therefore, the tower cost and the installation and maintenance costs were reduced enormously. Furthermore, unlike synchronous generators (SG), whose mechanical swing is defined by its primary mover power and damping factors, the speed of the DFIG can be controlled actively, and its active and reactive powers can be controlled in a decoupled manner.

One disadvantage of DFIG is that this generator needs two power converters with a size of about 30% of the generator's rated power. First, our research investigates the feasibility of the proposed structures to employ DFIG instead of the synchronous generator through analytical deduction and MATLAB simulation. The HTS allowed for decoupling the generator and wind turbine speed, consequently resulting in an independent control over the generator and wind turbine shaft speed. We designed a control method to use this degree of freedom to reduce the size and number of system components. Then, we proposed a method in which the size of both Rotor-Side Converter (RSC) and Grid-Side Converter (GSC) converters, the size of the transformer, and the DC-link voltage were reduced by 80%, 90%, and 85%, respectively.

Then, we proposed a SS-WECS to eliminate the Grid Side Converter (GSC), the required filter, and the grid-side transformer. The system uses a supercapacitor and only one converter with a power rating of 2.7% of the generator's rated power. The converter is only responsible for providing the generator rotor winding losses. Furthermore, controlling the generator speed around the synchronous speed provides the opportunity to limit the rotor voltage and enables the utilization of a low-voltage supercapacitor.

Next, we proposed a configuration that allows the integration of the flywheel energy storage system (FESS) into a wind turbine with minimal additional hardware to attenuate wind

power fluctuation, reduce the uncertainty of these power generation units, and have a more reliable, cost-effective wind energy. Conventionally, FESSs are connected either to the point of common coupling (PCC) or to the DC link of the back-to-back converter. These energy storage systems require an extra power electronic converter and electric motor-generator. Consequently, the cost of power production is increased, and the reliability of the system is decreased. In our works, the integrated energy storage removed the need for a dedicated power electronic converter and a motor/generator for the FESS due to the decoupling feature of the split-shaft wind turbine. Furthermore, two power quality control techniques based on fuzzy logic regulators were adapted, and simulation results demonstrated that both methods controlled the system properly. Furthermore, two MPPT control strategies, namely the optimal displacement control (ODC) and the virtual inertia adjustment, were investigated. The effect of virtually decreasing the inertia of the wind turbine was analyzed analytically by small-signal analysis. The results of utilizing virtual inertia showed an increase in the amount of harvested energy and increased system dynamics. It was also demonstrated that the output power fluctuations which were caused by intermittent wind speeds were eliminated effectively.

Then, a strategy is proposed to integrate the hybrid energy storage system (HESS), which consists of FESS, BESS, and SCESS with the proposed SS-WECS. In the proposed configuration, the FESS is connected the DFIG shaft directly, and the BESS is connected to the DC-link of the RSC without additional supporting hardware. Then, a control strategy was developed based on SoC feedback controller and MPC controller. The SoC feedback controller is adopted to manage the SoC of BESS and SCESS within the predefined limits. On the other hand, the adaptive MPC is responsible for maximizing the Level of Smoothness (LOS) while maintaining the DFIG speed constraints. Furthermore, the optimal size of the HESS is obtained using the response surface method (RSM) to attenuate the output power fluctuations. Furthermore, with the same level of smoothness (LOS), A storage cost analysis compares the proposed HESS with its counterpart. This configuration allows for reaching the predefined level of smoothness with hybrid energy storage at the cost of 30% of the conventional storage.

Also, we investigated the performance of this system under low voltage fault to evaluate

the system's Low Voltage Ride Through (LVRT) capability. We designed a control strategy to divert the extra power generated during the fault to wind turbine inertia by controlling the hydraulic machinery displacement. The results demonstrated this system could ride through short-circuit fault safely by choosing the proper size of the DC-link supercapacitor. In this configuration, Despite the small size of the RSC, the RSC was able to inject the desired reactive power during both normal and faulty situations. Furthermore, lower DC-link voltage allowed the use of less expensive capacitors and decreased the voltage stresses on power electronic devices. Therefore, reducing the generator excitation circuit size and employing a low-voltage supercapacitor in a WECS based on HTS can result in a more reliable, low-cost WECS.

11.2 Direction for Future Studies

As a direction for future studies, the configuration can be analyzed further in the following aspects:

11.2.1 Wind Prediction and Optimization of Hybrid Energy Storage

Due to the intermittent nature of wind speed forecasting and prediction of wind speeds or wind powers is important to establish optimal planning for power suppliers. For example, the accurate prediction of wind energy can reduce the size of energy storage systems, and by balancing the load and power provide better system stability and cheaper electricity. The main parameters considered for predictions are wind speed and wind power.

Wind speed prediction is essential for WECS operation. Most of the methods for forecasting wind speed, especially to deal with the uncertainties associated with wind speed, are based on neural networks [153]–[155]. Wind forecast can be divided into four subcategories: very short-term prediction (seconds-30 min), short-term (30 min-6 h), medium-term (6 h-1 day ahead), and long-term (1 day-1 week) forecasting approaches. Very short-term forecasting is useful for control application in ranges of seconds, and therefore their computational cost should be low enough to be used in online applications. In [155] a multi-layer Perceptron (MLP) is proposed to forecast very short-term wind speed. [156] employed an approach

based on wavelet and neural network and obtained more accurate results but it is required high computational cost. [157] proposed an approach based on a combination of MLP and Markov chains and obtained a better accuracy with a moderate computational cost. The authors of [158] used a hybrid method based on chaos phase reconstruction and NN to reduce the inaccuracy and conclude using a hybrid approach can result in better results than a single ANN for very short-term prediction. Several pieces of research have been conducted to predict short-term wind speed. In [159] different ANNs such as linear element network, BPNN, and RBFNN are investigated for 1 hour ahead prediction. this research concludes that there is no unique method can provide the best results in all cases. A feed-forward ANN method is proposed in [160] to predict the wind speed in a coastal area with complex topography. Increasing the time-horizon cause less accurate forecasting. Therefore, most approaches used to predict the medium-term and long-term wind speed are hybrid methods. Some of these approaches are wavelet decomposition and ANN [161], adaptive wavelet ANN [162], and MLP and the spatiotemporal evolution of weather [163].

Wind power forecasting can be categorized into three classes such as short-term, medium-term, and long-term predictions. Some of the most important researches in this topic are based on neuro-fuzzy, GA-BP NN, wavelet ANN or Adaptive Wavelet ANN, BPNN, Elman ANN, convolutional and recurrent ANNs, Boltzmann machine, artificial bee colony ANN, ANN combined with PSO or with PSO-FCM, or recurrent ANN [164]–[166].

In Chapters 8, an SS-WECS with an integrated HESS consisting of FESS, SCESS, and BBES was proposed. in Chapter 9, the optimal size of the HESS to achieve a certain LOS was calculated based on SRM. In this configuration a control strategy based SoC feedback controller and MPC was developed. In such a system, having the wind speed or wind power prediction allows that the MPC controls the system better and improve the performance of the system and reduce the optimal size of the HESS. Therefore, accommodating the prediction of wind speed or wind power with the proposed MPC can be potential topic to explore more.

11.2.2 Unsymmetrical Low Voltage Ride Through Analysis

Faults in which the balanced state of the system is disturbed are called unsymmetrical or unbalanced faults. Unsymmetrical faults involve only one or two phases, including 1) line to ground (LG), 2) line to line to ground (LLG), or 3) line to line (LL). In case of unsymmetrical faults, the current also has a negative sequence that remains over time and is undamped. Therefore, in this type of fault, the performance of the system can be more challenging and should be evaluated.

REFERENCES

[1] B. K. Bose, "Global warming: Energy, environmental pollution, and the impact of power electronics," *IEEE Industrial Electronics Magazine*, vol. 4, no. 1, pp. 6–17, 2010.

[2] B. K. Bose, "Global energy scenario and impact of power electronics in 21st century," *IEEE Transactions on Industrial Electronics*, vol. 60, no. 7, pp. 2638–2651, 2012.

[3] R. Wiser, E. Lantz, T. Mai, J. Zayas, E. DeMeo, E. Eugeni, J. Lin-Powers, and R. Tusing, "Wind vision: A new era for wind power in the United States," *The Electricity Journal*, vol. 28, no. 9, pp. 120–132, 2015.

[4] D. Gielen, F. Boshell, D. Saygin, M. D. Bazilian, N. Wagner, and R. Gorini, "The role of renewable energy in the global energy transformation," *Energy Strategy Reviews*, vol. 24, pp. 38–50, 2019.

[5] B. P. Center, "Annual energy outlook 2020," *Energy Information Administration, Washington, DC*, vol. 12, pp. 1672–1679, 2020.

[6] J. W. Shim, G. Verbič, K. Hur, and D. J. Hill, "Impact analysis of variable generation on small signal stability," in *2014 Australasian Universities Power Engineering Conference (AUPEC)*, IEEE, 2014, pp. 1–6.

[7] Y. V. Makarov, S. Lu, N. Samaan, Z. Huang, K. Subbarao, P. V. Etingov, J. Ma, R. P. Hafen, R. Diao, and N. Lu, "Integration of uncertainty information into power system operations," in *2011 IEEE Power and Energy Society General Meeting*, IEEE, 2011, pp. 1–13.

[8] A. M. Howlader, N. Urasaki, A. Yona, T. Senjyu, and A. Y. Saber, "A review of output power smoothing methods for wind energy conversion systems," *Renewable and Sustainable Energy Reviews*, vol. 26, pp. 135–146, 2013.

[9] P. Ralon, M. Taylor, A. Ilas, H. Diaz-Bone, and K. Kairies, "Electricity storage and renewables: Costs and markets to 2030," *International Renewable Energy Agency: Abu Dhabi, UAE*, 2017.

[10] A. A. Eladl, M. I. El-Afifi, M. A. Saeed, and M. M. El-Saadawi, "Optimal operation of energy hubs integrated with renewable energy sources and storage devices considering co2 emissions," *International Journal of Electrical Power & Energy Systems*, vol. 117, p. 105 719, 2020.

[11] I. Irena, "Renewable power generation costs in 2017. report," *International Renewable Energy Agency, Abu Dhabi*, 2018.

[12] M. Roggenburg, H. A. Esquivel-Puentes, A. Vacca, H. B. Evans, J. M. Garcia-Bravo, D. M. Warsinger, M. Ivantysynova, and L. Castillo, "Techno-economic analysis of a hydraulic transmission for floating offshore wind turbines," *Renewable Energy*, vol. 153, pp. 1194–1204, 2020.

[13] S. Sheng, "Report on wind turbine subsystem reliability-a survey of various databases (presentation)," National Renewable Energy Lab.(NREL), Golden, CO (United States), Tech. Rep., 2013.

[14] E. Artigao, S. Martín-Martínez, A. Honrubia-Escribano, and E. Gómez-Lázaro, "Wind turbine reliability: A comprehensive review towards effective condition monitoring development," *Applied energy*, vol. 228, pp. 1569–1583, 2018.

[15] J. Carroll, A. McDonald, and D. McMillan, "Failure rate, repair time and unscheduled o&m cost analysis of offshore wind turbines," *Wind Energy*, vol. 19, no. 6, pp. 1107–1119, 2016.

[16] N. Tazi, E. Châtelet, and Y. Bouzidi, "Using a hybrid cost-fmea analysis for wind turbine reliability analysis," *Energies*, vol. 10, no. 3, p. 276, 2017.

[17] T. Stehly, P. Beiter, and P. Duffy, "2019 cost of wind energy review," National Renewable Energy Lab.(NREL), Golden, CO (United States), Tech. Rep., 2020.

[18] C. Qin, E. Innes-Wimsatt, and E. Loth, "Hydraulic-electric hybrid wind turbines: Tower mass saving and energy storage capacity," *Renewable Energy*, vol. 99, pp. 69–79, 2016.

[19] J. Schmitz, M. Vukovic, and H. Murrenhoff, "Hydrostatic transmission for wind turbines: An old concept, new dynamics," in *Fluid Power Systems Technology*, American Society of Mechanical Engineers, vol. 56086, 2013, V001T01A029.

[20] M. Deldar, A. Izadian, and S. Anwar, "A decentralized multivariable controller for hydrostatic wind turbine drivetrain," *Asian Journal of Control*, vol. 22, no. 3, pp. 1038–1051, 2020.

[21] M. Deldar, A. Izadian, and S. Anwar, "Reconfiguration of a wind turbine with hydrostatic drivetrain to improve annual energy production," in *2015 IEEE Energy Conversion Congress and Exposition (ECCE)*, IEEE, 2015, pp. 6660–6666.

[22] A. Jarquin Laguna, "Steady-state performance of the delft offshore turbine," 2010.

[23] D. Rajabhandharaks and P. Hsu, "Optimal aerodynamic energy capture strategies for hydrostatic transmission wind turbine," in *2014 IEEE Conference on Technologies for Sustainability (SusTech)*, IEEE, 2014, pp. 140–147.

[24] B. Dolan and H. Aschemann, "Control of a wind turbine with a hydrostatic transmission—an extended linearisation approach," in *2012 17th International Conference on Methods & Models in Automation & Robotics (MMAR)*, IEEE, 2012, pp. 445–450.

[25] A. J. Laguna, N. F. Diepeveen, and J. W. Van Wingerden, "Analysis of dynamics of fluid power drive-trains for variable speed wind turbines: Parameter study," *IET Renewable Power Generation*, vol. 8, no. 4, pp. 398–410, 2014.

[26] H. T. Do, T. D. Dang, H. V. A. Truong, and K. K. Ahn, "Maximum power point tracking and output power control on pressure coupling wind energy conversion system," *IEEE transactions on Industrial Electronics*, vol. 65, no. 2, pp. 1316–1324, 2017.

[27] M. Chen, S. M. Santos, and A. Izadian, "Torque-assisting compressed air energy storage hydraulic wind drivetrains," in *2016 IEEE Power and Energy Conference at Illinois (PECI)*, IEEE, 2016, pp. 1–5.

[28] L. Wei, Z. Liu, Y. Zhao, G. Wang, and Y. Tao, "Modeling and control of a 600 kw closed hydraulic wind turbine with an energy storage system," *Applied Sciences*, vol. 8, no. 8, p. 1314, 2018.

[29] M. Vaezi and A. Izadian, "Energy storage techniques for hydraulic wind power systems," in *2014 International Conference on Renewable Energy Research and Application (ICRERA)*, IEEE, 2014, pp. 897–901.

[30] M. Saadat, F. A. Shirazi, and P. Y. Li, "Modeling and control of an open accumulator compressed air energy storage (caes) system for wind turbines," *Applied Energy*, vol. 137, pp. 603–616, 2015.

[31] P. Y. Li, E. Loth, T. W. Simon, J. D. Van de Ven, and S. E. Crane, "Compressed air energy storage for offshore wind turbines," *Proc. International Fluid Power Exhibition (IFPE), Las Vegas, USA*, 2011.

[32] Z. Liu, Y. Tao, L. Wei, P. Zhan, and D. Yue, "Analysis of dynamic characteristics of a 600 kw storage type wind turbine with hybrid hydraulic transmission," *Processes*, vol. 7, no. 7, p. 397, 2019.

[33] C. Ai, G. Zhou, W. Gao, J. Guo, G. Jie, Z. Han, and X. Kong, "Research on quasi-synchronous grid-connected control of hydraulic wind turbine," *IEEE Access*, vol. 8, pp. 126 092–126 108, 2020.

[34] J. B. Ekanayake, L. Holdsworth, X. Wu, and N. Jenkins, "Dynamic modeling of doubly fed induction generator wind turbines," *IEEE transactions on power systems*, vol. 18, no. 2, pp. 803–809, 2003.

[35] Y. Lei, A. Mullane, G. Lightbody, and R. Yacamini, "Modeling of the wind turbine with a doubly fed induction generator for grid integration studies," *IEEE transactions on energy conversion*, vol. 21, no. 1, pp. 257–264, 2006.

[36] B. Wu, Y. Lang, N. Zargari, and S. Kouro, *Power conversion and control of wind energy systems*. John Wiley & Sons, 2011.

[37] D. Aguglia, P. Viarouge, R. Wamkeue, and J. Cros, "Optimal selection of drive components for doubly-fed induction generator based wind turbines," in *Wind turbines*, IntechOpen, 2011.

[38] Z. Chen, J. M. Guerrero, and F. Blaabjerg, "A review of the state of the art of power electronics for wind turbines," *IEEE Transactions on power electronics*, vol. 24, no. 8, pp. 1859–1875, 2009.

[39] M. Chowdhury, N. Hosseinzadeh, and W. Shen, "Smoothing wind power fluctuations by fuzzy logic pitch angle controller," *Renewable Energy*, vol. 38, no. 1, pp. 224–233, 2012.

[40] M. Gholami, S. H. Fathi, J. Milimonfared, and Z. Chen, "Improving power smoothing and performance of pitch angle system for above rated speed range in wind power systems," *IET Generation, Transmission & Distribution*, vol. 13, no. 3, pp. 409–416, 2019.

[41] C. Luo, H. Banakar, B. Shen, and B.-T. Ooi, "Strategies to smooth wind power fluctuations of wind turbine generator," *IEEE Transactions on Energy Conversion*, vol. 22, no. 2, pp. 341–349, 2007.

[42] L. Ran, J. Bumby, and P. Tavner, "Use of turbine inertia for power smoothing of wind turbines with a dfig," in *2004 11th International Conference on Harmonics and Quality of Power (IEEE Cat. No. 04EX951)*, IEEE, 2004, pp. 106–111.

[43] T. Senjyu, Y. Ochi, Y. Kikunaga, M. Tokudome, E. B. Muhando, A. Yona, and T. Funabashi, "Output power leveling of wind generation system using inertia of wind turbine," in *2008 IEEE International Conference on Sustainable Energy Technologies*, IEEE, 2008, pp. 1217–1222.

[44] A. M. Howlader, N. Urasaki, T. Senjyu, A. Uehara, A. Yona, and A. Saber, "Output power smoothing of wind turbine generation system for the 2-mw permanent magnet synchronous generators," in *2010 International Conference on Electrical Machines and Systems*, IEEE, 2010, pp. 452–457.

[45] A. Uehara, A. Pratap, T. Goya, T. Senjyu, A. Yona, N. Urasaki, and T. Funabashi, "A coordinated control method to smooth wind power fluctuations of a pmsg-based wecs," *IEEE Transactions on energy conversion*, vol. 26, no. 2, pp. 550–558, 2011.

[46] L. Leclercq, B. Robyns, and J.-M. Grave, "Control based on fuzzy logic of a flywheel energy storage system associated with wind and diesel generators," *Mathematics and computers in simulation*, vol. 63, no. 3-5, pp. 271–280, 2003.

[47] G. Suvire and P. Mercado, "Active power control of a flywheel energy storage system for wind energy applications," *IET Renewable Power Generation*, vol. 6, no. 1, pp. 9–16, 2012.

[48] L. Jerbi, L. Krichen, and A. Ouali, "A fuzzy logic supervisor for active and reactive power control of a variable speed wind energy conversion system associated to a flywheel storage system," *Electric power systems research*, vol. 79, no. 6, pp. 919–925, 2009.

[49] G. O. Cimuca, C. Saudemont, B. Robyns, and M. M. Radulescu, "Control and performance evaluation of a flywheel energy-storage system associated to a variable-speed wind generator," *IEEE Transactions on Industrial Electronics*, vol. 53, no. 4, pp. 1074–1085, 2006.

[50] A. Rezaee Jordehi, "An improved particle swarm optimisation for unit commitment in microgrids with battery energy storage systems considering battery degradation and uncertainties," *International Journal of Energy Research*, vol. 45, no. 1, pp. 727–744, 2021.

[51] H. M. Hasanien, "A set-membership affine projection algorithm-based adaptive-controlled smes units for wind farms output power smoothing," *IEEE Transactions on Sustainable Energy*, vol. 5, no. 4, pp. 1226–1233, 2014.

[52] T. Penthia, A. K. Panda, P. R. Mohanty, and N. Patnaik, "Superconducting magnetic energy storage system with an improved nonlinear control approach for pulsed power applications," *International Transactions on Electrical Energy Systems*, vol. 30, no. 8, e12464, 2020.

[53] J. Pegueroles-Queralt, F. D. Bianchi, and O. Gomis-Bellmunt, "A power smoothing system based on supercapacitors for renewable distributed generation," *IEEE Transactions on Industrial Electronics*, vol. 62, no. 1, pp. 343–350, 2014.

[54] S. Choudhury, T. P. Dash, P. Bhowmik, and P. K. Rout, "A novel control approach based on hybrid fuzzy logic and seeker optimization for optimal energy management between micro-sources and supercapacitor in an islanded microgrid," *Journal of King Saud University-Engineering Sciences*, vol. 32, no. 1, pp. 27–41, 2020.

[55] A. Olabi, T. Wilberforce, M. Ramadan, M. A. Abdelkareem, and A. H. Alami, "Compressed air energy storage systems: Components and operating parameters–a review," *Journal of Energy Storage*, vol. 34, p. 102 000, 2021.

[56] A. Blakers, M. Stocks, B. Lu, and C. Cheng, "A review of pumped hydro energy storage," *Progress in Energy*, 2021.

[57] L. F. Cabeza, "Advances in thermal energy storage systems: Methods and applications," in *Advances in Thermal Energy Storage Systems*, Elsevier, 2021, pp. 37–54.

[58] K. Mongird, V. V. Viswanathan, P. J. Balducci, M. J. E. Alam, V. Fotedar, V. S. Koritarov, and B. Hadjerioua, "Energy storage technology and cost characterization report," Pacific Northwest National Lab.(PNNL), Richland, WA (United States), Tech. Rep., 2019.

[59] K. Mongird, V. Viswanathan, P. Balducci, J. Alam, V. Fotedar, V. Koritarov, and B. Hadjerioua, "An evaluation of energy storage cost and performance characteristics," *Energies*, vol. 13, no. 13, p. 3307, 2020.

[60] Y. Wang, L. Zhang, H. Hou, W. Xu, G. Duan, S. He, K. Liu, and S. Jiang, "Recent progress in carbon-based materials for supercapacitor electrodes: A review," *Journal of Materials Science*, vol. 56, no. 1, pp. 173–200, 2021.

[61] S. Choudhury, "Flywheel energy storage systems: A critical review on technologies, applications, and future prospects," *International Transactions on Electrical Energy Systems*, vol. 31, no. 9, e13024, 2021.

[62] A. G. Olabi, T. Wilberforce, M. A. Abdelkareem, and M. Ramadan, "Critical review of flywheel energy storage system," *Energies*, vol. 14, no. 8, p. 2159, 2021.

[63] W. Jing, C. H. Lai, S. H. W. Wong, and M. L. D. Wong, "Battery-supercapacitor hybrid energy storage system in standalone dc microgrids: Areview," *IET Renewable Power Generation*, vol. 11, no. 4, pp. 461–469, 2017.

[64] S. Hajiaghasi, A. Salemnia, and M. Hamzeh, "Hybrid energy storage system for microgrids applications: A review," *Journal of Energy Storage*, vol. 21, pp. 543–570, 2019.

[65] F. Li, K. Xie, and J. Yang, "Optimization and analysis of a hybrid energy storage system in a small-scale standalone microgrid for remote area power supply (raps)," *Energies*, vol. 8, no. 6, pp. 4802–4826, 2015.

[66] Z. Cabrane, M. Ouassaid, and M. Maaroufi, "Analysis and evaluation of battery-supercapacitor hybrid energy storage system for photovoltaic installation," *international journal of hydrogen energy*, vol. 41, no. 45, pp. 20 897–20 907, 2016.

[67] L. Barelli, G. Bidini, F. Bonucci, L. Castellini, A. Fratini, F. Gallorini, and A. Zuccari, "Flywheel hybridization to improve battery life in energy storage systems coupled to res plants," *Energy*, vol. 173, pp. 937–950, 2019.

[68] P. Glücker, K. Kivekäs, J. Vepsäläinen, P. Mouratidis, M. Schneider, S. Rinderknecht, and K. Tammi, "Prolongation of battery lifetime for electric buses through flywheel integration," *Energies*, vol. 14, no. 4, p. 899, 2021.

[69] P. Barra, W. de Carvalho, T. Menezes, R. Fernandes, and D. Coury, "A review on wind power smoothing using high-power energy storage systems," *Renewable and Sustainable Energy Reviews*, vol. 137, p. 110 455, 2021.

[70] W. Li, G. Joós, and J. Bélanger, "Real-time simulation of a wind turbine generator coupled with a battery supercapacitor energy storage system," *IEEE Transactions on Industrial Electronics*, vol. 57, no. 4, pp. 1137–1145, 2009.

[71] S. Nasri, B. S. Sami, and A. Cherif, "Power management strategy for hybrid autonomous power system using hydrogen storage," *International Journal of Hydrogen Energy*, vol. 41, no. 2, pp. 857–865, 2016.

[72] Z. Cabrane, M. Ouassaid, and M. Maaroufi, "Battery and supercapacitor for photovoltaic energy storage: A fuzzy logic management," *IET Renewable Power Generation*, vol. 11, no. 8, pp. 1157–1165, 2017.

[73] I. J. Cohen, D. A. Wetz, B. J. McRee, Q. Dong, and J. M. Heinzel, "Fuzzy logic control of a hybrid energy storage module for use as a high rate prime power supply," *IEEE Transactions on Dielectrics and Electrical Insulation*, vol. 24, no. 6, pp. 3887–3893, 2017.

[74] X. Feng, H. Gooi, and S. Chen, "Hybrid energy storage with multimode fuzzy power allocator for pv systems," *IEEE Transactions on Sustainable Energy*, vol. 5, no. 2, pp. 389–397, 2014.

[75] N. Chettibi, A. Mellit, G. Sulligoi, and A. M. Pavan, "Adaptive neural network-based control of a hybrid ac/dc microgrid," *IEEE Transactions on Smart Grid*, vol. 9, no. 3, pp. 1667–1679, 2016.

[76] F. Garcia-Torres, L. Valverde, and C. Bordons, "Optimal load sharing of hydrogen-based microgrids with hybrid storage using model-predictive control," *IEEE Transactions on Industrial Electronics*, vol. 63, no. 8, pp. 4919–4928, 2016.

[77] B. Hredzak, V. G. Agelidis, and M. Jang, "A model predictive control system for a hybrid battery-ultracapacitor power source," *IEEE Transactions on Power Electronics*, vol. 29, no. 3, pp. 1469–1479, 2013.

[78] M. Sabri, K. A. Danapalasingam, and M. F. Rahmat, "A review on hybrid electric vehicles architecture and energy management strategies," *Renewable and Sustainable Energy Reviews*, vol. 53, pp. 1433–1442, 2016.

[79] T. Li, L. Huang, and H. Liu, "Energy management and economic analysis for a fuel cell supercapacitor excavator," *Energy*, vol. 172, pp. 840–851, 2019.

[80] M. Dicorato, G. Forte, and M. Trovato, "Wind farm stability analysis in the presence of variable-speed generators," *Energy*, vol. 39, no. 1, pp. 40–47, 2012.

[81] A. A. B. M. Zin, M. P. HA, A. B. Khairuddin, L. Jahanshaloo, and O. Shariati, "An overview on doubly fed induction generators controls and contributions to wind based electricity generation," *Renewable and Sustainable Energy Reviews*, vol. 27, pp. 692–708, 2013.

[82] H. Xu, W. Zhang, H. Nian, and J. Li, "Improved vector control of dfig based wind turbine during grid dips and swells," in *2010 International Conference on Electrical Machines and Systems*, IEEE, 2010, pp. 511–515.

[83] F. K. Lima, A. Luna, P. Rodriguez, E. H. Watanabe, and F. Blaabjerg, "Rotor voltage dynamics in the doubly fed induction generator during grid faults," *IEEE Transactions on power electronics*, vol. 25, no. 1, pp. 118–130, 2009.

[84] D. Xiang, L. Ran, P. J. Tavner, and S. Yang, "Control of a doubly fed induction generator in a wind turbine during grid fault ride-through," *IEEE transactions on energy conversion*, vol. 21, no. 3, pp. 652–662, 2006.

[85] S. Xiao, G. Yang, H. Zhou, and H. Geng, "An lvrt control strategy based on flux linkage tracking for dfig-based wecs," *IEEE Transactions on Industrial Electronics*, vol. 60, no. 7, pp. 2820–2832, 2012.

[86] S. Hu, X. Lin, Y. Kang, and X. Zou, "An improved low-voltage ride-through control strategy of doubly fed induction generator during grid faults," *IEEE transactions on power electronics*, vol. 26, no. 12, pp. 3653–3665, 2011.

[87] Z. Xie, X. Zhang, X. Zhang, S. Yang, and L. Wang, "Improved ride-through control of dfig during grid voltage swell," *IEEE Transactions on Industrial electronics*, vol. 62, no. 6, pp. 3584–3594, 2014.

[88] D. Zhu, X. Zou, L. Deng, Q. Huang, S. Zhou, and Y. Kang, "Inductance-emulating control for dfig-based wind turbine to ride-through grid faults," *IEEE Transactions on power electronics*, vol. 32, no. 11, pp. 8514–8525, 2016.

[89] V. P. Suppioni, A. P. Grilo, and J. C. Teixeira, "Improving network voltage unbalance levels by controlling dfig wind turbine using a dynamic voltage restorer," *International Journal of Electrical Power & Energy Systems*, vol. 96, pp. 185–193, 2018.

[90] R. Sitharthan, C. Sundarabalan, K. Devabalaji, S. K. Nataraj, and M. Karthikeyan, "Improved fault ride through capability of dfig-wind turbines using customized dynamic voltage restorer," *Sustainable cities and society*, vol. 39, pp. 114–125, 2018.

[91] W. Guo, L. Xiao, and S. Dai, "Enhancing low-voltage ride-through capability and smoothing output power of dfig with a superconducting fault-current limiter–magnetic energy storage system," *IEEE Transactions on Energy Conversion*, vol. 27, no. 2, pp. 277–295, 2012.

[92] D. Ananth and G. N. Kumar, "Fault ride-through enhancement using an enhanced field oriented control technique for converters of grid connected dfig and statcom for different types of faults," *ISA transactions*, vol. 62, pp. 2–18, 2016.

[93] J. Morren and S. W. De Haan, "Ridethrough of wind turbines with doubly-fed induction generator during a voltage dip," *IEEE Transactions on energy conversion*, vol. 20, no. 2, pp. 435–441, 2005.

[94] J. Morren and S. W. De Haan, "Short-circuit current of wind turbines with doubly fed induction generator," *IEEE Transactions on Energy conversion*, vol. 22, no. 1, pp. 174–180, 2007.

[95] D. Li and H. Zhang, "A combined protection and control strategy to enhance the lvrt capability of a wind turbine driven by dfig," in *The 2nd International Symposium on Power Electronics for Distributed Generation Systems*, IEEE, 2010, pp. 703–707.

[96] M. K. Döşoğlu, "Crowbar hardware design enhancement for fault ride through capability in doubly fed induction generator-based wind turbines," *ISA transactions*, vol. 104, pp. 321–328, 2020.

[97] J. Liang, D. F. Howard, J. A. Restrepo, and R. G. Harley, "Feedforward transient compensation control for dfig wind turbines during both balanced and unbalanced grid disturbances," *IEEE Transactions on Industry Applications*, vol. 49, no. 3, pp. 1452–1463, 2013.

[98] J. Yang, J. E. Fletcher, and J. O'Reilly, "A series-dynamic-resistor-based converter protection scheme for doubly-fed induction generator during various fault conditions," *IEEE Transactions on Energy conversion*, vol. 25, no. 2, pp. 422–432, 2010.

[99] J. J. Justo, F. Mwasilu, and J.-W. Jung, "Enhanced crowbarless frt strategy for dfig based wind turbines under three-phase voltage dip," *Electric Power Systems Research*, vol. 142, pp. 215–226, 2017.

[100] H. Soliman, H. Wang, D. Zhou, F. Blaabjerg, and M. I. Marie, "Sizing of the series dynamic breaking resistor in a doubly fed induction generator wind turbine," in *2014 IEEE Energy Conversion Congress and Exposition (ECCE)*, IEEE, 2014, pp. 1842–1846.

[101] M. E. Hossain, "A non-linear controller based new bridge type fault current limiter for transient stability enhancement of dfig based wind farm," *Electric Power Systems Research*, vol. 152, pp. 466–484, 2017.

[102] M. Firouzi and G. B. Gharehpetian, "Lvrt performance enhancement of dfig-based wind farms by capacitive bridge-type fault current limiter," *IEEE Transactions on Sustainable Energy*, vol. 9, no. 3, pp. 1118–1125, 2017.

[103] A. Fereidouni, M. A. Masoum, T. Hosseinimehr, and M. Moghbel, "Performance of lr-type solid-state fault current limiter in improving power quality and transient stability of power network with wind turbine generators," *International Journal of Electrical Power & Energy Systems*, vol. 74, pp. 172–186, 2016.

[104] M. E. Hossain, "Low voltage ride-through capability improvement methods for dfig based wind farm," *Journal of Electrical Systems and Information Technology*, vol. 5, no. 3, pp. 550–561, 2018.

[105] O. P. Mahela, N. Gupta, M. Khosravy, and N. Patel, "Comprehensive overview of low voltage ride through methods of grid integrated wind generator," *IEEE Access*, vol. 7, pp. 99 299–99 326, 2019.

[106] M. Z. Jacobson and M. A. Delucchi, "A path to sustainable energy by 2030," *Scientific American*, vol. 301, no. 5, pp. 58–65, 2009.

[107] S. Chu, Y. Cui, and N. Liu, "The path towards sustainable energy," *Nature materials*, vol. 16, no. 1, pp. 16–22, 2017.

[108] E. Taherian-Fard, R. Sahebi, T. Niknam, A. Izadian, and M. Shasadeghi, "Wind turbine drivetrain technologies," *IEEE Transactions on Industry Applications*, vol. 56, no. 2, pp. 1729–1741, 2020.

[109] Y. Wang, L. Wang, M. Li, and Z. Chen, "A review of key issues for control and management in battery and ultra-capacitor hybrid energy storage systems," *ETransportation*, vol. 4, p. 100 064, 2020.

[110] M. Mahmoud, M. Ramadan, A.-G. Olabi, K. Pullen, and S. Naher, "A review of mechanical energy storage systems combined with wind and solar applications," *Energy Conversion and Management*, vol. 210, p. 112 670, 2020.

[111] S. Tohidi and M.-i. Behnam, "A comprehensive review of low voltage ride through of doubly fed induction wind generators," *Renewable and Sustainable Energy Reviews*, vol. 57, pp. 412–419, 2016.

[112] J. J. Justo, F. Mwasilu, and J.-W. Jung, "Doubly-fed induction generator based wind turbines: A comprehensive review of fault ride-through strategies," *Renewable and sustainable energy reviews*, vol. 45, pp. 447–467, 2015.

[113] H. Jadhav and R. Roy, "A comprehensive review on the grid integration of doubly fed induction generator," *International Journal of Electrical Power & Energy Systems*, vol. 49, pp. 8–18, 2013.

[114] A. Q. Al-Shetwi and M. Z. Sujod, "Grid-connected photovoltaic power plants: A review of the recent integration requirements in modern grid codes," *International Journal of Energy Research*, vol. 42, no. 5, pp. 1849–1865, 2018.

[115] Y.-K. Wu, S.-M. Chang, and P. Mandal, "Grid-connected wind power plants: A survey on the integration requirements in modern grid codes," *IEEE Transactions on Industry Applications*, vol. 55, no. 6, pp. 5584–5593, 2019.

[116] M. Tarafdar Hagh and T. Khalili, "A review of fault ride through of pv and wind renewable energies in grid codes," *International Journal of Energy Research*, vol. 43, no. 4, pp. 1342–1356, 2019.

[117] S. D. Ahmed, F. S. Al-Ismail, M. Shafiullah, F. A. Al-Sulaiman, and I. M. El-Amin, "Grid integration challenges of wind energy: A review," *IEEE Access*, vol. 8, pp. 10 857–10 878, 2020.

[118] P.-H. Huang, M. S. El Moursi, W. Xiao, and J. L. Kirtley, "Fault ride-through configuration and transient management scheme for self-excited induction generator-based wind turbine," *IEEE Transactions on Sustainable Energy*, vol. 5, no. 1, pp. 148–159, 2013.

[119] N. Jenkins, T. L. Burton, E. Bossanyi, D. Sharpe, and M. Graham, *Wind energy handbook*. John Wiley & Sons, 2021.

[120] R. Akbari and A. Izadian, "Reduced-size converter in dfig-based wind energy conversion system," in *2020 IEEE Energy Conversion Congress and Exposition (ECCE)*, IEEE, 2020, pp. 4217–4223.

[121] R. Akbari, A. Izadian, and R. S. Weissbach, "Quasi self-excited dfig-based wind energy conversion system," *IEEE Transactions on Industry Applications*, vol. 57, no. 3, pp. 2816–2824, 2021.

[122] W. K. Ahmed, "Mechanical modeling of wind turbine comparative study," *International journal of renewable energy research*, vol. 3, no. 1, pp. 94–97, 2013.

[123] R. Akbari, A. Izadian, and R. Weissbach, "An approach in torque control of hydraulic wind turbine powertrains," in *2019 IEEE Energy Conversion Congress and Exposition (ECCE)*, IEEE, 2019, pp. 979–982.

[124] W. Chen, F. Gao, X. Meng, A. Ren, and S. Zhou, "An offshore hydraulic wind turbine generator with variable-diameter rotor: Design, modeling and experiment," *Proceedings of the Institution of Mechanical Engineers, Part M: Journal of Engineering for the Maritime Environment*, vol. 231, no. 2, pp. 521–532, 2017.

[125] E. Dos Santos and E. R. Da Silva, *Advanced power electronics converters: PWM converters processing AC voltages*. John Wiley & Sons, 2014.

[126] D. Xiang, C. Wang, and Y. Liu, "Switching frequency dynamic control for dfig wind turbine performance improvement around synchronous speed," *IEEE Transactions on Power Electronics*, vol. 32, no. 9, pp. 7271–7283, 2016.

[127] R. T. Doucette and M. D. McCulloch, "A comparison of high-speed flywheels, batteries, and ultracapacitors on the bases of cost and fuel economy as the energy storage system in a fuel cell based hybrid electric vehicle," *Journal of Power Sources*, vol. 196, no. 3, pp. 1163–1170, 2011.

[128] T. Xisheng and Q. Zhiping, "Energy storage technologies and control methods of microgrid: A survey [j]," *Acta energiae solaris sinica*, vol. 33, no. 3, pp. 517–524, 2012.

[129] M. A. Abdullah, A. Yatim, C. W. Tan, and R. Saidur, "A review of maximum power point tracking algorithms for wind energy systems," *Renewable and sustainable energy reviews*, vol. 16, no. 5, pp. 3220–3227, 2012.

[130] M. Nasiri, J. Milimonfared, and S. Fathi, "Modeling, analysis and comparison of tsr and otc methods for mppt and power smoothing in permanent magnet synchronous generator-based wind turbines," *Energy Conversion and Management*, vol. 86, pp. 892–900, 2014.

[131] F. Jia, X. Cai, and Z. Li, "Fluctuating characteristic and power smoothing strategies of wecs," *IET generation, transmission & distribution*, vol. 12, no. 20, pp. 4568–4576, 2018.

[132] H. Nian, Y. Xu, L. Chen, and M. Zhu, "Modeling and analysis of dc-link dynamics in dfig system with an indicator function," *IEEE Access*, vol. 7, pp. 125 401–125 412, 2019.

[133] J. Hu, Y. Huang, D. Wang, H. Yuan, and X. Yuan, "Modeling of grid-connected dfig-based wind turbines for dc-link voltage stability analysis," *IEEE Transactions on Sustainable Energy*, vol. 6, no. 4, pp. 1325–1336, 2015.

[134] C. Liu, D. Xu, N. Zhu, F. Blaabjerg, and M. Chen, "Dc-voltage fluctuation elimination through a dc-capacitor current control for dfig converters under unbalanced grid voltage conditions," *IEEE Transactions on Power Electronics*, vol. 28, no. 7, pp. 3206–3218, 2012.

[135] D. Zhou and F. Blaabjerg, "Bandwidth oriented proportional-integral controller design for back-to-back power converters in dfig wind turbine system," *IET Renewable power generation*, vol. 11, no. 7, pp. 941–951, 2017.

[136] C.-L. Nguyen and H.-H. Lee, "Power management approach to minimize battery capacity in wind energy conversion systems," *IEEE Transactions on Industry Applications*, vol. 53, no. 5, pp. 4843–4854, 2017.

[137] Q. Jiang and H. Wang, "Two-time-scale coordination control for a battery energy storage system to mitigate wind power fluctuations," *IEEE Transactions on Energy Conversion*, vol. 28, no. 1, pp. 52–61, 2012.

[138] W. Jing, C. H. Lai, W. S. Wong, and M. D. Wong, "A comprehensive study of battery-supercapacitor hybrid energy storage system for standalone pv power system in rural electrification," *Applied Energy*, vol. 224, pp. 340–356, 2018.

[139] N. Mendis, K. Muttaqi, and S. Perera, "Management of low-and high-frequency power components in demand-generation fluctuations of a dfig-based wind-dominated raps system using hybrid energy storage," *IEEE transactions on industry applications*, vol. 50, no. 3, pp. 2258–2268, 2013.

[140] C. Krishna, "Managing battery and supercapacitor resources for real-time sporadic workloads," *IEEE Embedded Systems Letters*, vol. 3, no. 1, pp. 32–36, 2010.

[141] S. G. Jayasinghe, D. M. Vilathgamuwa, and U. K. Madawala, "Diode-clamped three-level inverter-based battery/supercapacitor direct integration scheme for renewable energy systems," *IEEE Transactions on Power Electronics*, vol. 26, no. 12, pp. 3720–3729, 2011.

[142] A. Lahyani, P. Venet, A. Guermazi, and A. Troudi, "Battery/supercapacitors combination in uninterruptible power supply (ups)," *IEEE transactions on power electronics*, vol. 28, no. 4, pp. 1509–1522, 2012.

[143] A. Fotouhi, D. J. Auger, K. Propp, S. Longo, and M. Wild, "A review on electric vehicle battery modelling: From lithium-ion toward lithium–sulphur," *Renewable and Sustainable Energy Reviews*, vol. 56, pp. 1008–1021, 2016.

[144] J. W. Shim, H. Kim, and K. Hur, "Incorporating state-of-charge balancing into the control of energy storage systems for smoothing renewable intermittency," *Energies*, vol. 12, no. 7, p. 1190, 2019.

[145] N. Lutsey and M. Nicholas, "Update on electric vehicle costs in the United States through 2030," *The International Council on Clean Transportation*, vol. 2, 2019.

[146] K. Kim, J. An, K. Park, G. Roh, and K. Chun, "Analysis of a supercapacitor/battery hybrid power system for a bulk carrier," *Applied Sciences*, vol. 9, no. 8, p. 1547, 2019.

[147] A. Rupp, H. Baier, P. Mertiny, and M. Secanell, "Analysis of a flywheel energy storage system for light rail transit," *Energy*, vol. 107, pp. 625–638, 2016.

[148] R. Okou, A. Sebitosi, and P. Pillay, "Flywheel rotor manufacture for rural energy storage in sub-saharan africa," *Energy*, vol. 36, no. 10, pp. 6138–6145, 2011.

[149] V. Kale and M. Secanell, "A comparative study between optimal metal and composite rotors for flywheel energy storage systems," *Energy Reports*, vol. 4, pp. 576–585, 2018.

[150] P. Kemper, D. Muller, and A. Thummler, "Combining response surface methodology with numerical methods for optimization of markovian models," *IEEE Transactions on Dependable and Secure Computing*, vol. 3, no. 3, pp. 259–269, 2006.

[151] J. García-Beleño and E. Rodríguez de San Miguel, "Integration of response surface methodology (rsm) and principal component analysis (pca) as an optimization tool for polymer inclusion membrane based-optodes designed for hg (ii), cd (ii), and pb (ii)," *Membranes*, vol. 11, no. 4, p. 288, 2021.

[152] H. G. Neddermeijer, G. J. Van Oortmarssen, N. Piersma, and R. Dekker, "A framework for response surface methodology for simulation optimization," in *2000 Winter Simulation Conference Proceedings (Cat. No. 00CH37165)*, IEEE, vol. 1, 2000, pp. 129–136.

[153] H. Liu, H.-q. Tian, X.-f. Liang, and Y.-f. Li, "Wind speed forecasting approach using secondary decomposition algorithm and elman neural networks," *Applied Energy*, vol. 157, pp. 183–194, 2015.

[154] H. Quan, D. Srinivasan, and A. Khosravi, "Short-term load and wind power forecasting using neural network-based prediction intervals," *IEEE transactions on neural networks and learning systems*, vol. 25, no. 2, pp. 303–315, 2013.

[155] R. Ak, V. Vitelli, and E. Zio, "An interval-valued neural network approach for uncertainty quantification in short-term wind speed prediction," *IEEE transactions on neural networks and learning systems*, vol. 26, no. 11, pp. 2787–2800, 2015.

[156] E. Safavieh, A. J. Ardakani, A. K. Laviani, S. Pourmousavi, S. Hosseinian, and M. Abedi, "A new integrated approach for very short-term wind speed prediction using wavelet networks and pso," in *Proceedings of the International Conference on Power Systems*, 2007.

[157] S. P. Kani and M. Ardehali, "Very short-term wind speed prediction: A new artificial neural network–markov chain model," *Energy Conversion and Management*, vol. 52, no. 1, pp. 738–745, 2011.

[158] S. Gao, L. Dong, X. Liao, and Y. Gao, "Very-short-term prediction of wind speed based on chaos phase space reconstruction and nwp," in *Proceedings of the 32nd Chinese Control Conference*, IEEE, 2013, pp. 8863–8867.

[159] G. Li, J. Shi, and J. Zhou, "Bayesian adaptive combination of short-term wind speed forecasts from neural network models," *Renewable Energy*, vol. 36, no. 1, pp. 352–359, 2011.

[160] K. Philippopoulos and D. Deligiorgi, "Application of artificial neural networks for the spatial estimation of wind speed in a coastal region with complex topography," *Renewable Energy*, vol. 38, no. 1, pp. 75–82, 2012.

[161] A. Meng, J. Ge, H. Yin, and S. Chen, "Wind speed forecasting based on wavelet packet decomposition and artificial neural networks trained by crisscross optimization algorithm," *Energy Conversion and Management*, vol. 114, pp. 75–88, 2016.

[162] B. Doucoure, K. Agbossou, and A. Cardenas, "Time series prediction using artificial wavelet neural network and multi-resolution analysis: Application to wind speed data," *Renewable Energy*, vol. 92, pp. 202–211, 2016.

[163] A. R. Finamore, V. Calderaro, V. Galdi, A. Piccolo, and G. Conio, "A wind speed forecasting model based on artificial neural network and meteorological data," in *2016 IEEE 16th International Conference on Environment and Electrical Engineering (EEEIC)*, IEEE, 2016, pp. 1–5.

[164] A. Tascikaraoglu and M. Uzunoglu, "A review of combined approaches for prediction of short-term wind speed and power," *Renewable and Sustainable Energy Reviews*, vol. 34, pp. 243–254, 2014.

[165] A. P. Marugán, F. P. G. Márquez, J. M. P. Perez, and D. Ruiz-Hernández, "A survey of artificial neural network in wind energy systems," *Applied energy*, vol. 228, pp. 1822–1836, 2018.

[166] S. Shamshirband, T. Rabczuk, and K.-W. Chau, "A survey of deep learning techniques: Application in wind and solar energy resources," *IEEE Access*, vol. 7, pp. 164 650–164 666, 2019.

A. APPENDIX

A.1 Supercomputer Programming for MATLAB Parallel Processing

MATLAB Parallel Computing Toolbox provides an opportunity to solve computationally and data-intensive problems using multicore processors, Graphics Processing Units (GPUs), and computer clusters. This MATLAB toolbox enables users to parallelize MATLAB applications using High-level constructs, parallel for-loops, particular array types, and parallelized numerical algorithms. The toolbox can be used with Simulink to run multiple simulations of a model in parallel. In this way, the full processing power of multicore desktops is used by executing applications on workers (MATLAB computational engines) that run locally. Furthermore, the same applications can be run on clusters or clouds (using MATLAB Parallel Server). These toolboxes can be used to execute matrix calculations that are too large to fit into the memory of a single machine. These toolboxes allow engineers in many fields to carry out many calculations simultaneously. In this way, significant problems and algorithms can often be split into smaller ones, and then they can be dedicated to workers to be solved simultaneously. The main advantages of parallel computing are saving processing time and solving big data problems by distributing tasks amongst workers and executing them simultaneously.

A.1.1 Indiana University Supercomputer Systems

Indiana University (IU) cyberinfrastructure consists of several robust, reliable supercomputing systems. These world-class research supercomputers enable researchers to carry out research experimentation and implementations that are computationally extensive, and they need large memory and processing power. IU super-computing systems include Big Red 200, Big red 3, Quartz, and Carbonate.

Each of these supercomputers is designed to be well-suited for specific applications. For instance, Big Red 200 is designed to support scientific and medical research and advanced research in artificial intelligence, machine learning, and data analysis with 640 compute nodes. This supercomputer has a theoretical peak performance of 7 petaFLOPS (1 petaFLOPS

=a quadrillion (10^{15}) floating-point operations per second (FLOPS)). Big red 3 is a supercomputer dedicated to large-scale, compute-intensive applications that can utilize the system's processing capability and high bandwidth network topology. This supercomputer has a theoretical peak performance of 934 teraFLOPS (1 teraFLOPS =10^{12} FLOPS). IU Quartz supercomputer has a theoretical peak performance of over 4.6 teraFLOPS with 92 compute nodes. Quartz is designed o deliver a large amount of processing capacity over long periods. IU Carbonate supercomputer system is designed to support data-intensive computing problems requiring large amounts of computer memory. This supercomputer has 72 general-purpose compute nodes.

A.1.2 Parallel Computing Toolbox

Parallel computing allows performing many calculations simultaneously by splitting them into smaller ones and running them simultaneously. First, some parallel computing concepts are explained as follows:

- Node: a standalone computer with one or more CPUs/GPUs. Several nodes can be networked to form a cluster or supercomputer.
- Thread: smallest set of instructions can be managed independently by a processor. On a multicore processor, multiple threads can be executed simultaneously
- Worker: a computational engine that runs in the background without a graphical desktop
- Parallel pool: a set of networked workers with automatic parallel computing support.

Using these parallel computing concepts, the commands in Table A.1 can be explained better. $maxNumCompThreads$ function is a function to define the number of Threads. $Parpool$ command creates a parallel pool of Matlab workers. However, using functions with parallel language automatically creates a parallel pool when necessary. Some parallel language functions or commands are listed in Table A.1, such as $parfor$ and $parsim$. $parfor$ commands is a parallel for-loop in Matlab to execute the code in for-loop simultaneously.

parsim command runs the simulation in parallel computing simulation. However, to run the simulation in parallel, some other functions and code commands are required to be used. First, the input data for all workers should be defined by Simulink. *SimulationInput* command. Then, parameters that should be swept during simulation should be defined by *setBlockParameter* command. The rest of the parameters and variables are constant for all simulations should be loaded to the MATLAB workspace of all workers. To this end, first, the *parfevalOnAll* function can be used to run some functions for all workers before the parallel simulations. Second, the *assignin* function can be used to load parameters and variables in the MATLAB workspace of all workers. *parfeval* function can be used to run a function in the parallel pool. *delete*(*gcp*('*create*)) function can be used to shut down a parallel pool. The *setVariable* command is used to assign a variable to the Simulink model.

Table A.1. MATLAB Codes

Command	**Explanation**
parpool	Creating Parallel Pool
parfor	Parallel for-loop code
parsim	Parallel simulation
maxNumCompThreads	To define the number of the threads
Simulink.SimulationInput	To set the simulation input for all worker
setBlockParameter	To set and sweep a parameter in parallel simulation
setVariable	To assign a variable
parfevalOnAll	To run a function before the simulation for all workers
assignin	To assign variables or objects to the base workspace of all workers
parfeval	To run a function in a parallel pool
delete(*gcp*(*nocreate*))	To shut down a parallel pool

VITA

Rasoul Akbari was born in Iran in 1988. He received the B.S. degree in electrical engineering from Bu-Ali Sina University, Hamedan, Iran in 2011. Then, he received M.S. degree in electrical engineering from the Sharif University of Technology, Tehran, Iran, in 2013. He strated his PhD program in 2018 under supervision of Dr. Afshin Izadian. He recieved PhD degree from Purdue University, Indiamapolis in 2022. His current research interests include renewable energy, wind energy conversion, and power electronic converters.

PUBLICATIONS

- R. Akbari and A. Izadian, ”Split-Shaft Wind Energy Conversion Systems Scalability and Components Selection,” in 2022 IEEE International Conference on Electro Information Technology (EIT), 2022: IEEE, pp. 125-130.

- R. Akbari and A. Izadian, ”Electrical Equivalent Circuit of Split-Shaft Wind Energy Conversion Systems,” in 2022 IEEE International Conference on Electro Information Technology (EIT), 2022: IEEE, pp. 103-108.

- R. Akbari and A. Izadian, ”Modeling and Control of Flywheel-Integrated Generators in Split-Shaft Wind Turbines,” Journal of Solar Energy Engineering, vol. 144, no. 1, 2022.

- R. Akbari, A. Izadian, and R. S. Weissbach, “Quasi self-excited DFIG-based wind energy conversion system,” IEEE Transactions on Industry Applications, vol. 57, no. 3, pp. 2816–2824, 2021

- R. Akbari and A. Izadian, ”Modelling and Control of Flywheels Integrated in Wind Turbine Generators,” in 2021 IEEE International Conference on Electro Information Technology (EIT), 2021: IEEE, pp. 106-11

- R. Akbari and A. Izadian, “Reduced-size converter in DFIG-based wind energy conversion system,” in 2020 IEEE Energy Conversion Congress and Exposition (ECCE), IEEE, 2020, pp. 4217–4223

- R. Akbari, A. Izadian, and R. Weissbach, “An approach in torque control of hydraulic wind turbine powertrains,” in 2019 IEEE Energy Conversion Congress and Exposition (ECCE), IEEE, 2019, pp. 979–982